

Advanced methodologies for modeling and assessment of SFR safety functions

Présentée le 12 décembre 2022

Faculté des sciences de base
Laboratoire de physique des réacteurs et de comportement des systèmes
Programme doctoral en énergie

pour l'obtention du grade de Docteur ès Sciences

par

Janos BODI

Acceptée sur proposition du jury

Prof. K. A. J. Mulleners, présidente du jury
Dr K. Mikityuk, Dr A. Ponomarev, directeurs de thèse
Dr A. Rineiski, rapporteur
Prof. F. Bertrand, rapporteur
Dr A. Vasiliev, rapporteur

"The horse is prepared against the day of battle: but victory is of the LORD"

Proverbs 21:31

Acknowledgements

The presented doctoral research was carried out within EU Project ESFR-SMART, which has received funding from the EURATOM Research and Training Programme 2014-2018 under the Grant Agreement No. 754501., providing financial support to the author and other researchers in the project.

Many people have contributed to different extent to the finalization of the doctoral work, for which I would like to express my gratitude.

First of all, I would like to thank my supervisor, Dr. Konstantin Mikityuk, for giving me the chance to join the Advanced Nuclear Systems (ANS) group at PSI, work, and gain experience in the field that I dreamed of. He was always available for discussions providing suggestions on the preparation of the reactor design or giving hints about modeling difficulties, which I have experienced many.

I would like to especially thank my co-supervisor, Dr. Alexander Ponomarev, as he helped me with TRACE modeling at the time when I was overwhelmed with the long input files and gave his opinions and suggestions on the core mechanics methodology development. Besides, I would like to thank him for checking all the draft conference and journal papers I sent him, with which I have been torturing him in the past years.

I want to thank the ANS group for the pleasant working environment and the interesting discussions, especially with Dr. Sandro Pelloni, Dr. Jiri Krepel, and all the exchange and master students who shared the office with me.

I would like to express my gratitude to Dr. Joel Guidez, with whom I worked in close collaboration with the ESFR conceptual design development, giving a great deal of support through his vast experience with Sodium-cooled Fast Reactors.

I am grateful for the opportunity of working with many students and researchers from the ESFR-SMART project, enriching my professional experience. Special thanks go to Dr. Evgeny Nikitin and Dr. Emil Fridman from HZDR for providing their Phenix Serpent input, saving significant time for me in the development of the core mechanics methodology.

I would like to thank also my jury members, Dr. Alexander Vasiliev, Prof. Frederic Bertrand, and Dr. Andrei Rineiski, for accepting the invitation, reading my thesis, and traveling to Lausanne for the exam.

Finally, I would like to thank my wife, Stephanie Bodi, who has been beside me throughout all the ups and downs of the past years, always cheering me and supporting me in so many ways, and my six months old son, little Janos, who allowed me to enjoy his cuteness when I needed a break from the writing of the thesis.

Abstract

The present doctoral work was performed to contribute to the conceptual design development and safety assessment of a Generation IV Sodium Fast Reactor (SFR) in the frame of the European Sodium Fast Reactor Safety Measures Assessment and Research Tools (ESFR-SMART) project. The contribution to the safety assessment is divided into two main areas. 1) To the development of new safety assessment methodologies using mainly Phenix and Superphenix reactor data, and 2) to the new safety measures assessment of the European Sodium Fast Reactor (ESFR). The safety assessment of ESFR was structured according to the safety functions the specific analyzed safety measure relates to, belonging mainly to the heat removal and reactivity control safety functions.

In the first part of the work, the conceptual design of the ESFR was synthesized by using the operational experience of former reactor designs and design options from reactor concepts currently under development. Based on these concepts, the safety measures were optimized and updated for use within the ESFR conceptual design. Within this part, a 3-Dimensional (3D) Computer-Aided Design model has been prepared, which served as the base for input preparation for much of the safety assessment within the research.

In the safety assessment, various calculation tools were involved, either already available for SFR analysis or newly developed methods as part of the doctoral work. The first of these newly developed tools is the currently available coupled TRACE-PARCS neutronic/thermal-hydraulic analysis toolset being further advanced by introducing a unique XS preparation technique at PSI. Through this development, increased accuracy 3D core power evaluation can be performed for transient simulations. The second tool developed in the research is the core mechanics analysis methodology, allowing general core distortion evaluation and the calculation of the resulting reactivity effect of the deformation. As part of the development, benchmark analysis or verification and validation work have been performed, testing the accuracy of the abovementioned techniques.

The ESFR safety measure analysis started with the various decay heat removal system (DHRS) assessment, which is one of the key new safety measures of ESFR, belonging to the reactivity control safety function. The decay heat removal capability of the new DHRSs were assessed, using the Protected Station Blackout (PSBO) accidental scenario, together with the general reactor behavior moving from forced to natural convection. In the study, each of the DHRS performance was evaluated as well as the system temperature evolution during the simulated accidental condition. Thus, it was assessed if the specific DHRS can keep the reactor from reaching the defined temperature limits or if certain modifications are required to achieve this, for which recommendations were made.

Finally, an unprotected loss of flow (ULOF) simulation has been performed, assessing the core behavior under such conditions. In the study, the low void effect core safety measure of ESFR was specifically targeted, corresponding to the reactivity control safety function. The sodium boiling progression has been assessed in the core for the reference SA design, as well as a modified design, affecting the vapor propagation in the SA.

Keywords: Sodium-cooled Fast Reactor (SFR), European Sodium Fast Reactor (ESFR), nuclear safety functions, TRACE, PARCS, Serpent, core deformation reactivity effect, ULOF

Abstrakt

Die vorliegende Doktorarbeit wurde durchgeführt, um im Rahmen des Projekts ESFR-SMART (European Sodium Fast Reactor Safety Measures Assessment and Research Tools) einen Beitrag zur konzeptionellen Entwicklung und Sicherheitsbewertung eines schnellen Natriumreaktors (SFR) der Generation IV zu leisten. Der Beitrag zur Sicherheitsbewertung gliedert sich in zwei Hauptbereiche. 1) Die Entwicklung neuer Methoden zur Sicherheitsbewertung, wobei hauptsächlich Daten aus den Reaktoren Phenix und Superphenix verwendet werden, und 2) die Bewertung neuer Sicherheitsmaßnahmen für den Europäischen Natriumschnellreaktor (ESFR). Die Sicherheitsbewertung des ESFR wurde nach den Sicherheitsfunktionen gegliedert, auf die sich die untersuchte Sicherheitsmaßnahme bezieht, die hauptsächlich zu den Sicherheitsfunktionen Wärmeabfuhr und Reaktivitätskontrolle gehören.

Im ersten Teil der Arbeit wurde die konzeptionelle Auslegung des ESFR unter Verwendung der Betriebserfahrungen früherer Reaktorkonzepte und der Auslegungsoptionen von Reaktorkonzepten, die derzeit entwickelt werden, zusammengefasst. Auf der Grundlage dieser Konzepte wurden die Sicherheitsmaßnahmen optimiert und für den Einsatz im ESFR-Konzeptentwurf aktualisiert. In diesem Teil wurde ein dreidimensionales (3D) computergestütztes Entwurfsmodell erstellt, das als Grundlage für die Vorbereitung der Eingaben für einen Großteil der Sicherheitsbewertung im Rahmen der Forschung diente.

Bei der Sicherheitsbewertung wurden verschiedene Berechnungswerkzeuge eingesetzt, die entweder bereits für die SFR-Analyse zur Verfügung stehen oder im Rahmen der Doktorarbeit neu entwickelt wurden. Das erste dieser neu entwickelten Tools ist das derzeit verfügbare gekoppelte neutronische/thermisch-hydraulische TRACE-PARCS-Analyse Toolset, das durch die Einführung einer einzigartigen XS-Präparationstechnik am PSI weiter verbessert wurde. Durch diese Entwicklung kann eine genauere 3D-Kernleistungsbewertung für transiente Simulationen durchgeführt werden. Das zweite in der Forschung entwickelte Werkzeug ist die Kernmechanik-Analysemethode, die eine allgemeine Bewertung der Kernverformung und die Berechnung der daraus resultierenden Reaktivitätswirkung der Verformung ermöglicht. Im Rahmen der Entwicklung wurden Benchmark-Analysen oder Verifizierungs- und Validierungsarbeiten durchgeführt, um die Genauigkeit der oben genannten Techniken zu testen.

Die Analyse der ESFR-Sicherheitsmaßnahmen begann mit der Bewertung der verschiedenen Nachwärmeabfuhrsysteme (DHRS), die eine der wichtigsten neuen Sicherheitsmaßnahmen des ESFR darstellen und zur Sicherheitsfunktion der Reaktivitätskontrolle gehören. Die Fähigkeit der neuen DHRS zur Nachwärmeabfuhr wurde anhand des Störfallszenarios "Protected Station Blackout" (PSBO) und des allgemeinen Reaktorverhaltens beim Übergang von erzwungener zu natürlicher Konvektion bewertet. In der Studie wurde die Leistung jedes einzelnen DHRS sowie die Entwicklung der Systemtemperatur während des simulierten Störfalls bewertet. So konnte festgestellt werden, ob das spezifische DHRS den Reaktor vor dem Erreichen der festgelegten Temperaturgrenzen bewahren kann oder ob bestimmte Änderungen erforderlich sind, um dies zu erreichen.

Schließlich wurde eine "Unprotected Loss Of Flow-Simulation (ULOF) durchgeführt, um das Verhalten des Kerns unter solchen Bedingungen zu bewerten. In der Studie wurde die Sicherheitsmaßnahme des ESFR-Kerns mit geringem Leereffekt besonders berücksichtigt, was der Sicherheitsfunktion der Reaktivitätskontrolle entspricht. Das Fortschreiten des Natriumsiedens im Kern wurde sowohl für die

Referenz-SA-Konstruktion als auch für eine modifizierte Konstruktion, die die Dampfausbreitung in der SA beeinflusst, bewertet.

Schlüsselwörter: Natriumgekühlter schneller Reaktor (SFR), europäischer schneller Natriumreaktor (ESFR), nukleare Sicherheitsfunktionen, TRACE, PARCS, Serpent, Kerndeformationsreaktivitätseffekt, ULOF

CONTENTS

ACKNOWLEDGEMENTS	I
ABSTRACT	II
ABSTRAKT	III
NOMENCLATURE	VIII
ABBREVIATIONS	VIII
PARAMETERS.....	X
INDICES	XI
CAPTION OF FIGURES.....	XII
CAPTION OF TABLES	XVII
CHAPTER 1 INTRODUCTION	1
1.1. NUCLEAR ENERGY WORLDWIDE	1
1.1.1. <i>Generation IV nuclear</i>	3
1.1.2. <i>Fast neutron reactors</i>	5
1.2. SODIUM-COOLED FAST REACTOR HISTORY	5
1.2.1. <i>SFR physics and working principle</i>	7
1.2.2. <i>European Sodium Fast Reactor</i>	8
1.3. MOTIVATION: NEED OF ESFR SAFETY MEASURES ASSESSMENT	11
1.3.1. <i>Reactivity control safety function</i>	12
1.3.1.1. Sodium void effect.....	12
1.3.1.2. Core deformation effect.....	16
1.3.2. <i>Heat removal safety function</i>	17
1.3.2.1. Reference design	17
1.3.2.2. DHRS-1 design	17
1.3.2.3. DHRS-2 design	19
1.3.2.4. DHRS-3 design	19
1.3.2.5. Modified secondary system design	21
1.3.3. <i>Containment safety function</i>	21
1.4. OBJECTIVES	23
1.5. STRUCTURE	24
CHAPTER 2 METHODOLOGIES OF RESEARCH	27
2.1. CAD METHODOLOGY	27
2.2. THERMAL-HYDRAULIC METHODOLOGY	28
2.2.1 <i>The TRACE code</i>	28
2.2.2. <i>Development of the TRACE model of ESFR</i>	29
2.3. NEUTRONIC METHODOLOGY	33
2.3.1. <i>Point kinetics</i>	33
2.3.2. <i>Spatial kinetics</i>	35
2.3.2.1. Methodology description	35
2.3.2.2. Reference SFR Superphenix core description.....	37
2.3.2.3. Description of the modeling.....	37
2.3.2.3.1. Serpent model.....	37
2.3.2.3.2. PARCS model.....	38

2.3.2.4. Static calculation results	39
2.3.2.4.1. K_{eff} evaluation of the simulated cases	39
2.3.2.4.2. Radial power map and relative error comparison of the simulated cases	40
2.3.2.4.3. Axial flux distribution evolution of inner core, outer core and breeder region SAs	44
2.4. CORE MECHANIC METHODOLOGY	46
2.4.1. Methodology overview	46
2.4.2. Sanity check of the coupled methodology	47
2.4.3. Verification of the mechanics part	51
2.4.4. Validation of the coupled methodology	52
2.4.4.1. Deformation calculation on the PHENIX core model	52
2.4.4.2. Neutronic calculation based on the deformed PHENIX core model	56
2.5. SUMMARY OF CHAPTER 2	58
CHAPTER 3 SAFETY FUNCTION: HEAT REMOVAL	60
3.1. PSBO SCENARIOS	61
3.2. ASSESSMENT OF ESFR DECAY HEAT REMOVAL WITH REFERENCE SECONDARY CIRCUIT DESIGN	62
3.2.1. TRACE models	62
3.2.1.1. DHRS-1	62
3.2.1.2. DHRS-2	63
3.2.1.3. DHRS-3	64
3.2.2. Simulation results for PSBO scenarios with no DHRS activated	65
3.2.3. Individual DHRS simulation results	69
3.2.3.1. Evaluation of heat removal capabilities with DHRS depending on air flowrate conditions	69
3.2.3.2. DHRS-1 system simulations	71
3.2.3.2.1. Application of auxiliary pump on DHRS-1 loop	71
3.2.3.2.2. DHRS-1 simulation results	72
3.2.3.3. DHRS-2 system simulations	74
3.2.3.3.1. DHRS-2 simulation results	74
3.2.3.3.2. DHRS-2 sensitivity study	76
3.2.3.4. DHRS-3 simulation results	79
3.2.4. Multiple DHRS cases	81
3.2.4.1. DHRS-1 and DHRS-3	81
3.2.4.2. DHRS-2 and DHRS-3	82
3.3. ASSESSMENT OF ESFR DECAY HEAT REMOVAL WITH UPDATED SECONDARY CIRCUIT DESIGN	83
3.3.1. Modified secondary circuit design	83
3.3.2. Simulation results for PSBO scenarios with no DHRS activated	86
3.3.3. DHRS-1 simulation results	89
3.3.4. DHRS-2 simulation results	91
3.4. CONCLUSIONS OF CHAPTER 3	93
CHAPTER 4 SAFETY FUNCTION: REACTIVITY CONTROL	97
4.1. ASSESSMENT OF ESFR UNDER ULOF CONDITIONS	97
4.1.1. ULOF accidental scenario	97
4.1.2. ULOF modeling	98
4.1.2.1. ESFR core description	99
4.1.2.2. Point kinetics model	100
4.1.2.3. TRACE model for ULOF study	101
4.1.3. Reference calculation results	102
4.1.4. Results for modified wrapper case	107
4.1.5. Comparisons and discussion	111
4.1.6. Sensitivity study of various core parameters	114

4.1.6.1. Reference case without inter SA gap heat exchange	114
4.1.6.2. Influence of the SA shielding and reflector design modification	116
4.1.6.3. Influence of the cooling group flow distribution modification	118
4.1.6.4. Influence of the fuel gap conductance modification	119
4.1.6.5. Influence of the sodium plenum reactivity worth modification	120
4.1.7. <i>Conclusions of Section 4.1</i>	122
4.2. ASSESSMENT OF SPX UNDER ULOF CONDITIONS WITH NEW METHODOLOGY	123
4.2.1. <i>ULOF simulation description</i>	123
4.2.2. <i>Model description</i>	123
4.2.3. <i>Transient results with sodium and Doppler feedbacks</i>	124
4.2.4. <i>Control rod shift simulations</i>	128
4.2.5. <i>Conclusion of Section 4.2</i>	133
4.3. ASSESSMENT OF CORE GEOMETRY DISTORTION EFFECT	134
4.3.1. <i>ESFR-SMART static core flowering calculations</i>	134
4.3.1.1. Core modeling and simulated scenarios.....	134
4.3.1.2. Neutronic calculations of the deformed ESFR geometries	135
4.3.2. <i>Transient core deformation simulation using the Phenix core design</i>	136
4.3.2.1. Transient modeling.....	136
4.3.2.2. Transient deformation results.....	138
4.3.3. <i>Phenix dynamic core deformation sensitivity study</i>	142
4.3.4. <i>Conclusions of Section 4.3</i>	145
CHAPTER 5 CONCLUSIONS AND RECOMMENDATIONS FOR FUTURE WORK.....	148
5.1. CHAPTER-WISE SUMMARY	148
5.2. MAIN ACHIEVEMENTS.....	149
5.3. RECOMMENDATIONS FOR FUTURE WORK	155
5.4. CONCLUDING REMARKS	156
APPENDIX A - ESFR-SMART REACTOR CONCEPT MAIN CHARACTERISTICS	158
APPENDIX B - ESFR-SMART WORKING DRAWINGS	160
APPENDIX C - CEFR CRP MODELING AND RESULTS.....	170
APPENDIX D - REACTIVITY DECOMPOSITION FIGURES FROM ULOF SENSITIVITY STUDY	190
BIBLIOGRAPHY.....	194
CURRICULUM VITAE.....	201

Nomenclature

Abbreviations

1D,2D,3D	One, two and three dimensional
ASTRID	Advanced Sodium Technological Reactor for Industrial Demonstration
AURN	Arrêt d’Urgence par (variation de) Réactivité Négative (Automatic emergency shutdown by negative reactivity)
BN-600,-800,-1200	быстрый натрий (fast sodium) 600, 800, 1200
BOC	Beginning Of Cycle
BWR	Boiling Water Reactor
CAD	Computer-Aided Design
CEFR	China Experimental Fast Reactor
CFR-600	China Fast Reactor 600
CG	Cooling Group
CP-ESFR	Collaborative Project on European Sodium Fast Reactor
CR	Control Rod
CRDL	Control Rod Driveline
CSD	Control and Shutdown Device
DFR	Dounreay Fast Reactor
DHR	Decay Heat Removal
DHRS	Decay Heat Removal System
DHX	Decay Heat Exchanger
DSD	Diverse Shutdown Device
Dyphtil THT	Dyphil Partially hydrogenated terphenyls (high temperature resistant oil)
EBR-1	Experimental Breeder Reactor 1
EFR	European Fast Reactor
EM	Electromagnetic
EM-10	9Cr-1Mo tempered martensitic steel
EOEC	End Of Equilibrium Cycle
ESFR	European Sodium Fast Reactor
ESFR-SMART	European Sodium Fast Reactor Safety Measures Assessment and Research Tools
EU	European Union
F2F distance	Face to face distance (subassembly width)
Gen IV	Generation IV
GIF	Generation IV International Forum
HZP	Hot Zero Power
IC	Inner Core
IHX	Intermediate Heat Exchanger
JEFF	Joint Evaluated Fission and Fusion File
KNS-37	Kompakter Natrium Siedekreislauf 37 (Compact sodium boiling cycle)
LWR	Light Water Reactor
MATLAB	Matrix Laboratory

MCNP	Monte Carlo N-Particle Transport
MOX	Mixed Oxide (plutonium/uranium fuel)
NASTRAN	NASA Structural Analysis
OC	Outer Core
PARCS	Purdue Advanced Reactor Core Simulator
PFR	Prototype Fast Reactor
PK	Point Kinetics
PSBO	Protected Station Blackout
PSI	Paul Scherrer Institute
PWR	Pressurized Water Reactor
SA	Subassembly
SFR	Sodium-cooled Fast Reactor
SG	Steam Generator
SK	Spatial Kinetics
SPX	Superphenix
std	Standard deviation
TE	Thermoelectric
TRACE	TRAC/RELAP Advanced Computational Engine
ULOF	Unprotected Loss Of Flow
US N.R.C.	United States Nuclear Regulatory Commission
USA	United States of America
XS	Cross-Section

Parameters

A	Neutron absorption rate	[1/cm ³ s]
A	Area	[m ²]
B	Magnetic field strength	[T]
E	Young modulus	[Pa]
F	Force	[N]
g	Gravitational constant	[m/s ²]
H	Pressure head	[Pa]
h	Height	[m]
I	Moment of inertia (Second moment of area)	[mm ⁴]
k _{eff}	Effective multiplication factor	[-]
L	Length	[mm]
P	Power	[W]
P	Neutron production rate	[1/cm ³ s]
T	Temperature	[K]
t	Time	[s]
x	Distance along x axis	[mm]
z	Distance along z axis	[mm]
η	Fraction of wetted perimeter	[-]
ρ	Density	[kg/m ³]
ρ	Reactivity	[pcm]
σ ₁	Flux error	[-]
σ ₂	Multiplication factor error	[-]
α	Void fraction	[-]
Φ	Neutron flux	[n/cm ² /s]

Indices

av	Average
d	Discharge
e	Electric
eff	Effective
i	Inlet
o	Outlet
P	PARCS
S	Serpent
th	Thermal
Tr	Transport cross-section

Caption of Figures

- FIGURE 1.** LOW CARBON ELECTRICITY PRODUCTION DISTRIBUTION BETWEEN DIFFERENT TECHNOLOGIES [2]
- FIGURE 2.** NUCLEAR FLEET AGE DISTRIBUTION AT DIFFERENT PARTS OF THE WORLD [2]
- FIGURE 3.** TIMELINE OF THE DIFFERENT GENERATION NUCLEAR REACTORS
- FIGURE 4.** SODIUM-COOLED FAST REACTOR (POOL TYPE) SCHEMATIC VIEW
- FIGURE 5.** THE GLOBAL VIEW OF ESFR WITH ALL MAIN COMPONENTS
- FIGURE 6.** CP-ESFR VS ESFR-SMART REACTOR DESIGN MODIFICATIONS
- FIGURE 7.** SCHEMATIC ILLUSTRATION OF THE FLOW PATTERN IN CASE OF SODIUM BOILING IN THE SA WITH REFERENCE (ON THE LEFT) AND MODIFIED (ON THE RIGHT) DESIGN OF THE HEXCAN [24].
- FIGURE 8.** DHRS-1 RELATED SYSTEM COMPONENTS
- FIGURE 9.** DHRS-2 RELATED SYSTEM COMPONENTS, INTEGRATED INTO THE SECONDARY CIRCUIT DESIGN
- FIGURE 10.** DHRS-3 CONCEPT WITH ITS OIL AND WATER CIRCUITS INTEGRATED INTO THE REACTOR PIT
- FIGURE 11.** SECONDARY CIRCUIT DESIGN WITH STRAIGHT TUBES
- FIGURE 12.** DIMENSIONS AND STRUCTURE OF THE REACTOR PIT DESIGN
- FIGURE 13.** SCHEMATIC VIEW OF THE ESFR MODELING IN THE TRACE SYSTEM CODE WITH ITS MAIN CIRCUITS AND COMPONENTS (FIGURE NODALIZATION FOR VISUALIZATION PURPOSES ONLY)
- FIGURE 14.** RADIAL AND AXIAL TRACE NODALIZATION OF THE PRIMARY CIRCUIT OF ESFR
- FIGURE 15.** COOLING GROUP ARRANGEMENT WITHIN THE REACTOR CORE
- FIGURE 16.** SIMULATION SEQUENCE OF THE SAMPLING METHOD
- FIGURE 17.** FISSILE CORE (LEFT) AND RADIAL BREEDER BLANKET (RIGHT) SA AXIAL STRUCTURE WITH SERPENT UNIVERSES
- FIGURE 18.** PARCS (LEFT) VS SERPENT (RIGHT) FUEL SA GEOMETRY DIVISIONS
- FIGURE 19.** CONVERGENCE OF THE MULTIPLICATION FACTOR AND ERROR ON FLUX FROM SUCCESSIVE CYCLES WHEN SAMPLING METHOD IS UTILIZED
- FIGURE 20.** SERPENT SA POWER MAP FOR REFERENCE CRITICAL CONFIGURATION
- FIGURE 21.** RELATIVE SA POWER DIFFERENCE BETWEEN PARCS AND SERPENT FOR REFERENCE CRITICAL CONFIGURATION
- FIGURE 22.** RELATIVE SA POWER DIFFERENCE BETWEEN PARCS AND SERPENT FOR SODIUM DENSITY CASE
- FIGURE 23.** RELATIVE SA POWER DIFFERENCE BETWEEN PARCS AND SERPENT FOR CRITICAL CONFIGURATION WITHOUT THE USE OF SAMPLING METHOD
- FIGURE 24.** SA POWERS RADIUS-WISE RADIAL DISTRIBUTION FOR REFERENCE CASE
- FIGURE 25.** INNER FUEL SA AXIAL FLUX PROFILE COMPARISON BETWEEN ORIGINAL PARCS AND PARCS WITH SAMPLING METHOD
- FIGURE 26.** OUTER FUEL SA AXIAL FLUX PROFILE COMPARISON BETWEEN ORIGINAL PARCS AND PARCS WITH SAMPLING METHOD
- FIGURE 27.** BREEDER FUEL SA AXIAL FLUX PROFILE COMPARISON BETWEEN ORIGINAL PARCS AND PARCS WITH SAMPLING METHOD
- FIGURE 28.** MAIN STEPS OF CORE DISTORTION CONVERSION INTO REACTIVITY EFFECT
- FIGURE 29.** GEOMETRY SPECIFICATION AND DETECTOR REGION DESCRIPTION OF THE 7-SA FUEL BUNDLE SIMULATION
- FIGURE 30.** SA GEOMETRIES FOR THE PRODUCTION RATE AND ABSORPTION RATE CALCULATIONS
- FIGURE 31.** AXIAL NEUTRON FLUX PROFILE SHIFT BETWEEN UNIFORMLY AND NON-UNIFORMLY DEFORMED ASSEMBLIES (HOTTER COLOR CORRESPONDS TO HIGHER FLUX)
- FIGURE 32.** CANTILEVER BEAM EXAMPLE, SIDE VIEW (LEFT) AND CROSS-SECTIONAL VIEW (RIGHT)
- FIGURE 33.** MODELING OF THE CORE DISTORTION WITHIN THE FINITE ELEMENT SOLVER FOR 6TH OF THE FULL CORE (UPPER CORE VIEW)

FIGURE 34. HETEROGENEOUS (LEFT) AND HOMOGENEOUS (RIGHT) SERPENT MODEL COMPARISON

FIGURE 35. 5TH ROW SA POSITION WHICH WAS USED FOR THE CALIBRATION OF THE YOUNG MODULUS OF THE SA MATERIAL

FIGURE 36. DISPLACEMENT OF THE MEASURED 5TH ROW SA IN COMPARISON TO THE EXPERIMENTAL RESULTS

FIGURE 37. SERPENT 2 MODEL BASED ON THE DEFORMED GEOMETRY OF THE REACTOR CORE, DIFFERENT COLORS CORRESPOND TO SEPARATE MODEL SECTIONS WITH DIFFERENT MATERIAL COMPOSITIONS

FIGURE 38. REACTIVITY EFFECT COMPARISON BETWEEN THE DATA PREVIOUSLY MEASURED [65] AND CALCULATED WITH THE PROPOSED METHOD

FIGURE 39. REACTIVITY EFFECT COMPARISON BETWEEN MEASUREMENT DATA [64] AND CALCULATED DATA POINT REGARDS TO THE EXPERIMENTAL DEVICE DISPLACEMENT AT PAD LEVELS

FIGURE 40. SCHEMATIC VIEW OF THE DHRS-1 SYSTEM IN THE TRACE MODEL, CONNECTED TO THE SECONDARY SODIUM LOOP (FIGURE NODALIZATION FOR VISUALIZATION PURPOSES ONLY)

FIGURE 41. SCHEMATIC VIEW OF THE DHRS-2 MODEL AND ITS CONNECTION TO THE SECONDARY SYSTEM IN TRACE (FIGURE NODALIZATION FOR VISUALIZATION PURPOSES ONLY)

FIGURE 42. SCHEMATIC VIEW OF THE DHRS-3 MODEL AND ITS CONNECTION TO THE PRIMARY SYSTEM IN TRACE (FIGURE NODALIZATION FOR VISUALIZATION PURPOSES ONLY)

FIGURE 43. EVOLUTION OF REACTOR POWER, PRIMARY AND SECONDARY MASS FLOW FOR DIFFERENT PSBO SCENARIOS WITHOUT ACTIVATION OF DHRS (AIR INLETS ARE CLOSED)

FIGURE 44. TEMPERATURE PROFILE OVER THE LENGTH OF THE SECONDARY CIRCUIT BEFORE TRANSIENT INITIATION AND 1500 S AFTER FOR THE “FEEDWATER” CALCULATION CASE

FIGURE 45. EVOLUTION OF SELECTED PRIMARY SYSTEM TEMPERATURE PARAMETERS DURING THE PSBO ACCIDENT WITHOUT ACTIVATION OF DHRS (SA OUTLET-TOP LEFT, IHX INLET-TOP RIGHT, IHX OUTLET-BOTTOM LEFT, VESSEL AVERAGE-BOTTOM RIGHT)

FIGURE 46. THE SIMPLIFIED TRACE MODEL OF ESRF FOR SENSITIVITY ANALYSIS (FIGURE NODALIZATION FOR VISUALIZATION PURPOSES ONLY)

FIGURE 47. SENSITIVITY STUDY ON THE DHRS-1 HEAT REMOVAL VERSUS THE APPLIED AIR FLOWRATE IN THE DHRS-1 CHIMNEY WITH THE REMOVED POWER BY THE DHRS VS DECAY POWER PRODUCED BY THE CORE (POWER RATIO)

FIGURE 48. DIFFERENT PUMP OPERATION OPTIONS WITH THE INDUCED FLOW IN THE DHRS-1 LOOP

FIGURE 49. DHRS-1 HEAT REMOVAL CAPABILITY USED AS AN INDIVIDUAL HEAT REMOVAL

FIGURE 50. PRIMARY SODIUM TEMPERATURES EVOLUTION DURING THE ACCIDENT USING ONLY DHRS-1

FIGURE 51. DHRS-2 HEAT REMOVAL CAPABILITY USED AS AN INDIVIDUAL HEAT REMOVAL MEANS

FIGURE 52. PRIMARY SODIUM TEMPERATURE EVOLUTION DURING THE ACCIDENT USING ONLY DHRS-2

FIGURE 53. TEMPORAL EVOLUTION OF THE SECONDARY SYSTEM SODIUM FLOWRATE

FIGURE 54. DHRS-2 POWER (TOP), PRIMARY SODIUM TEMPERATURE (MIDDLE), AND SECONDARY FLOWRATE (BOTTOM) EVALUATION BY USING 5% VERSUS 7% NOMINAL PUMP ROTATION SPEED

FIGURE 55. DHRS-2 POWER (TOP) AND PRIMARY SODIUM TEMPERATURE (BOTTOM) EVALUATION BY USING 50 KG/S AIR FLOW AT 600°C AND 550°C TEMPERATURES LIMITS AS SIGNAL FOR THE AIR INLET OPENING

FIGURE 56. DHRS-3 HEAT REMOVAL CAPABILITY USED AS AN INDIVIDUAL HEAT REMOVAL OPTION

FIGURE 57. PRIMARY SODIUM TEMPERATURE EVOLUTION DURING THE ACCIDENT USING ONLY DHRS-3

FIGURE 58. DHRS-1 INITIATION TIME COMPARISON BY DHRS-1 ALONE VERSUS DHRS-1 AND 3 TOGETHER

FIGURE 59. DHRS-2 INITIATION TIME COMPARISON BY DHRS-2 ALONE VERSUS DHRS-2 AND 3 TOGETHER

FIGURE 60. MODIFIED SECONDARY CIRCUIT DESIGN WITH DHRS-1 AND DHRS-2 WITH THE COMMON CHIMNEY FOR BOTH SYSTEMS [34]

FIGURE 61. OPTIMIZED LAYOUT OF THE SECONDARY CIRCUITS HAVING A CIRCULAR DISTRIBUTION AROUND THE PRIMARY SYSTEM [34]

FIGURE 62. LAYOUT COMPARISON OF THE OPTIMIZED CIRCULAR SECONDARY CIRCUIT AND THE REFERENCE SYSTEM ARRANGEMENT [34]

FIGURE 63. PSBO REACTOR BEHAVIOR ASSESSMENT WITHOUT THE USE OF DHRSS USING THE FEEDWATER AND NO FEEDWATER CASES

FIGURE 64. PRIMARY SODIUM TEMPERATURE COMPARISON BETWEEN REFERENCE (LEFT) AND MODIFIED (RIGHT) SECONDARY LOOP DESIGN FOR SA OUTLET, IHX INLET, IHX OUTLET AND VESSEL AVERAGE TEMPERATURES

FIGURE 65. DHRs-1 HEAT REMOVAL CAPABILITY COMPARISON BETWEEN MODIFIED AND REFERENCE SECONDARY CIRCUIT DESIGN USED AS AN INDIVIDUAL HEAT REMOVAL MEANS

FIGURE 66. PRIMARY AND DHRs-1 FLOWRATE COMPARISON BETWEEN REFERENCE AND MODIFIED SECONDARY LOOP DESIGNS

FIGURE 67. PRIMARY SODIUM TEMPERATURE EVOLUTION COMPARISON BETWEEN MODIFIED AND REFERENCE SECONDARY CIRCUIT DESIGN USING ONLY DHRs-1 HEAT REMOVAL

FIGURE 68. DHRs-2 HEAT REMOVAL CAPABILITY COMPARISON BETWEEN MODIFIED AND REFERENCE SECONDARY CIRCUIT DESIGN USED AS AN INDIVIDUAL HEAT REMOVAL MEANS

FIGURE 69. PRIMARY SODIUM TEMPERATURE EVOLUTION COMPARISON BETWEEN MODIFIED AND REFERENCE SECONDARY CIRCUIT DESIGN USING ONLY DHRs-2 HEAT REMOVAL

FIGURE 70. TEMPORAL EVOLUTION OF THE SECONDARY SYSTEM SODIUM FLOWRATE WITHIN THE MODIFIED SECONDARY CIRCUIT

FIGURE 71. ESFR-SMART CORE RADIAL LAYOUT WITH THE DIFFERENT BATCHES AND SA TYPES

FIGURE 72. INNER CORE AND OUTER CORE SA AXIAL REGION AND HEIGHTS

FIGURE 73. TRACE NODALIZATION DIAGRAM OF THE ULOF 42 CHANNEL MODEL

FIGURE 74. TEMPORAL EVOLUTION OF THE NORMALIZED POWER AND MASS FLOWRATE (ON THE LEFT) AND NORMALIZED POWER TO FLOW RATIO (ON THE RIGHT) FOLLOWING THE INITIATION OF THE TRANSIENT

FIGURE 75. PEAK POWER ASSEMBLY VOID FRACTION DISTRIBUTION AXIALLY VERSUS TIME PLOTTED FROM THE BOILING ONSET

FIGURE 76. REACTIVITY COMPONENTS USED IN THE POINT KINETICS MODEL VS. TIME

FIGURE 77. DECOMPOSITION OF SODIUM REACTIVITY EVOLUTION WITH RESPECT TO CGs AND AXIAL REGIONS (FUEL AND PLENUM) VS TIME

FIGURE 78. FUEL INNER SURFACE AND CLADDING INNER SURFACE TEMPERATURE EVOLUTION IN THE PEAK POWER CHANNEL AT THE FISSILE FUEL MIDDLE-HEIGHT NODE VS TIME

FIGURE 79. NORMALIZED POWER/MASS FLOWRATE (ON THE LEFT) AND NORMALIZED POWER TO FLOW RATIO (ON THE RIGHT) VS. TIME FOLLOWING THE INITIATION OF THE TRANSIENT

FIGURE 80. PEAK POWER ASSEMBLY VOID FRACTION DISTRIBUTION AXIALLY VERSUS TIME PLOTTED FROM THE BOILING ONSET

FIGURE 81. EVOLUTION OF THE REACTIVITY COMPONENTS USED IN THE POINT KINETICS MODEL VS. TIME

FIGURE 82. SODIUM REACTIVITY EFFECT EVOLUTION IN TIME DISTRIBUTED AMONGST THE DIFFERENT COOLING GROUPS AND FUEL/PLENUM REGIONS VS TIME

FIGURE 83. FUEL INNER SURFACE AND CLADDING INNER SURFACE TEMPERATURE EVOLUTION IN THE PEAK POWER CHANNEL AT THE FISSILE FUEL MIDDLE NODE HEIGHT VS TIME

FIGURE 84. LIQUID SODIUM VELOCITY AT THE CHANNEL INLET AND OUTLET FOR THE REFERENCE CASE (LEFT) AND THE MODIFIED DESIGN CASE WITH WINDOWS (RIGHT) WITHIN THE PEAK POWER SA VS TIME

FIGURE 85. PRESSURE EVOLUTION AT THE FISSILE TOP, SODIUM PLENUM, SHIELDING, AND CHANNEL TOP AXIAL NODES FOR THE REFERENCE CASE (LEFT) AND THE MODIFIED DESIGN CASE WITH WINDOWS (RIGHT) WITHIN THE PEAK POWER SA VS TIME

FIGURE 86. AVERAGE VOID FRACTION ALONG THE FUEL AND PLENUM REGIONS OVER ALL THE MODELLED CHANNELS FOR THE REFERENCE CASE (LEFT) AND THE MODIFIED DESIGN CASE WITH WINDOWS (RIGHT) VS TIME

FIGURE 87. NORMALIZED POWER/MASS FLOWRATE (ON THE LEFT) AND NORMALIZED POWER TO FLOW RATIO (ON THE RIGHT) VS. TIME FOLLOWING THE INITIATION OF THE TRANSIENT

FIGURE 88. EVOLUTION OF THE REACTIVITY COMPONENTS USED IN THE POINT KINETICS (LEFT) AND SODIUM REACTIVITY EFFECT EVOLUTION, DISTRIBUTED BETWEEN THE DIFFERENT CGS FOR FUEL AND PLENUM AXIAL REGIONS (RIGHT) VS TIME

FIGURE 89. FUEL INNER SURFACE AND CLADDING INNER SURFACE TEMPERATURE EVOLUTION IN THE PEAK POWER CHANNEL AT THE FISSILE FUEL MIDDLE NODE HEIGHT VS TIME

FIGURE 90. NORMALIZED POWER/MASS FLOWRATE (ON THE LEFT) AND NORMALIZED POWER TO FLOW RATIO (ON THE RIGHT) VS. TIME FOLLOWING THE INITIATION OF THE TRANSIENT FOR SA OUTLET GEOMETRY SENSITIVITY CASE

FIGURE 91. FUEL INNER SURFACE AND CLADDING INNER SURFACE TEMPERATURE EVOLUTION IN THE PEAK POWER CHANNEL AT THE FISSILE FUEL MIDDLE NODE HEIGHT VS TIME FOR SA OUTLET GEOMETRY SENSITIVITY CASE

FIGURE 92. NORMALIZED POWER/MASS FLOWRATE (ON THE LEFT) AND NORMALIZED POWER TO FLOW RATIO (ON THE RIGHT) VS. TIME FOLLOWING THE INITIATION OF THE TRANSIENT

FIGURE 93. FUEL INNER SURFACE AND CLADDING INNER SURFACE TEMPERATURE EVOLUTION IN THE PEAK POWER CHANNEL AT THE FISSILE FUEL MIDDLE NODE HEIGHT VS TIME FOR CG FLOW DISTRIBUTION SENSITIVITY CASE

FIGURE 94. NORMALIZED POWER/MASS FLOWRATE (ON THE LEFT) AND NORMALIZED POWER TO FLOW RATIO (ON THE RIGHT) VS. TIME FOLLOWING THE INITIATION OF THE TRANSIENT FOR THE FUEL GAP CONDUCTANCE SENSITIVITY CASE

FIGURE 95. FUEL INNER SURFACE AND CLADDING INNER SURFACE TEMPERATURE EVOLUTION IN THE PEAK POWER CHANNEL AT THE FISSILE FUEL MIDDLE NODE HEIGHT VS TIME FOR THE FUEL GAP CONDUCTANCE SENSITIVITY CASE

FIGURE 96. NORMALIZED POWER/MASS FLOWRATE (ON THE LEFT) AND NORMALIZED POWER TO FLOW RATIO (ON THE RIGHT) VS. TIME FOLLOWING THE INITIATION OF THE TRANSIENT FOR THE SODIUM PLENUM SENSITIVITY CASE

FIGURE 97. FUEL INNER SURFACE AND CLADDING INNER SURFACE TEMPERATURE EVOLUTION IN THE PEAK POWER CHANNEL AT THE FISSILE FUEL MIDDLE NODE HEIGHT VS TIME FOR THE SODIUM PLENUM SENSITIVITY CASE

FIGURE 98. SUPERPHENIX MODEL OF THE COUPLED TRACE/PARCS CODES FOR THE ULOF ANALYSIS

FIGURE 99. TEMPORAL EVOLUTION OF THE NORMALIZED REACTOR POWER FOR PK AND SK METHODS

FIGURE 100. TEMPORAL EVOLUTION OF THE AVERAGE FISSILE AND CORE AVERAGE SODIUM TEMPERATURE FOR THE PK AND SK SIMULATIONS

FIGURE 101. REACTIVITY INSERTION COMPARISON BETWEEN PK AND SK METHODS MEASURED FROM THE ULOF INITIATION POINT

FIGURE 102. COMPARISON OF THE TEMPORAL EVOLUTION OF THE POWER BETWEEN PK AND SK METHODS WITH REACTIVITY FEEDBACK DECOMPOSITION

FIGURE 103. RELATIVE POWER DIFFERENCE COMPARISON BETWEEN SK AND PK

FIGURE 104. SUPERPHENIX REACTOR CORE RADIAL STRUCTURE WITH THE ADJUSTED CONTROL RODS HIGHLIGHTED

FIGURE 105. TEMPORAL POWER EVOLUTION OF PK AND SK DURING THE TRANSIENT, WHICH STARTS AT 10 S

FIGURE 106. TEMPORAL REACTIVITY EVOLUTION OF PK AND SK DURING THE TRANSIENT, WHICH STARTS AT 10 S

FIGURE 107. TEMPORAL EVOLUTION OF THE INNER AND OUTER CORE AVERAGE AND CORE AVERAGE SODIUM TEMPERATURE OF PK AND SK DURING THE TRANSIENT, WHICH STARTS AT 10 S

FIGURE 108. RELATIVE POWER DIFFERENCE OF THE DIFFERENT SAs IN THE CORE FOR SK AND PK

FIGURE 109. MAXIMUM FUEL TEMPERATURE DIFFERENCE OF THE DIFFERENT SAs IN THE CORE FOR SK AND PK

FIGURE 110. ESFR-SMART CORE LOADING FOR THE FLOWERING DEFORMATION SIMULATION

FIGURE 111. MODEL OF THE DEFORMED ESFR CORE IN SERPENT 2 MONTE CARLO CODE

FIGURE 112. PHENIX REACTOR CORE MODEL USED WITH THE APPLIED PRESSURE LOADS ON THE SAs WITH THE DIAGONAL SA NUMBERING FOR THE SA MOVEMENT CHARACTERIZATION

FIGURE 113. DEFORMATION MAGNITUDE OF THE SAs FOR 1/12TH OF THE REACTOR CORE AT THE ASSESSED TIME POINTS

FIGURE 114. DIAGONAL ROW SA DEFORMATION (SA NUMBERING SHOWN IN FIGURE 112) TOGETHER WITH THE CORE DISTORTION REACTIVITY EFFECT EVOLUTION THROUGHOUT THE SIMULATED TIME FRAME

FIGURE 115. POWER EVOLUTION DURING THE MEASURED AURN EVENT ALIGNED WITH THE CALCULATED PHENIX CORE - DEFORMATION DUE TO SODIUM BOILING

FIGURE 116. DEFORMATION MAGNITUDE OF THE SAs FOR 1/12TH OF THE REACTOR CORE AT THE ASSESSED TIME POINTS FOR THE SENSITIVITY CASE WITH PADS IN CONTACT

FIGURE 117. DIAGONAL ROW SA DEFORMATION (SA NUMBERING SHOWN IN FIGURE 112) TOGETHER WITH THE CORE DISTORTION REACTIVITY EFFECT EVOLUTION THROUGHOUT THE SIMULATED TIME FRAME FOR THE SENSITIVITY CASE

FIGURE 118. POWER EVOLUTION DURING THE MEASURED AURN EVENT ALIGNED WITH THE CALCULATED PHENIX CORE DEFORMATION DUE TO SODIUM BOILING FOR THE SENSITIVITY CASE

Caption of Tables

TABLE 1. GENERATION IV REACTOR TECHNOLOGIES ACCORDING TO GENERATION IV INTERNATIONAL FORUM [6]

TABLE 2. SODIUM-COOLED FAST REACTORS WORLDWIDE [7]

TABLE 3. ESFR-SMART REACTOR CONCEPT MAIN CHARACTERISTICS

TABLE 4. LIST OF MAIN DESIGN MODIFICATIONS BETWEEN CP-ESFR AND ESFR-SMART REACTOR CONCEPTS

TABLE 5. SERPENT AND PARCS MULTIPLICATION FACTOR COMPARISON

TABLE 6. PRODUCTION AND ABSORPTION RATE MEASUREMENT FOR DIFFERENT GEOMETRY SA BUNDLES CALCULATED WITH SERPENT AND NORMALIZED TO FLUX

TABLE 7. K_{eff} COMPARISON BETWEEN DIRECT SERPENT OUTPUT AND CALCULATION FROM NEUTRON PRODUCTION AND ABSORPTION RATE

TABLE 8. VERIFICATION RESULTS AND SENSITIVITY ANALYSIS ON THE MESH SIZE OF THE FINITE ELEMENT SIMULATION

TABLE 9. COMPARISON OF RADIAL EXPANSION REACTIVITY EFFECTS BETWEEN HETEROGENEOUS AND HOMOGENEOUS SERPENT MODELS

TABLE 10. COMPARISON OF PIPE LENGTHS, SODIUM VOLUME AND BUILDING SURFACE AREA BETWEEN THE REFERENCE AND MODIFIED SECONDARY LOOPS

TABLE 11. COOLING GROUPS WITH THE CORRESPONDING SA NUMBERS AND SODIUM FLOWRATES WITHIN EACH GROUP

TABLE 12. MODELED REACTIVITY EFFECTS AND THEIR VALUE

TABLE 13. MODELED IC AND OC SA REGIONS IN TRACE WITH CORRESPONDING NODE NUMBERS

TABLE 14. APPLIED SENSITIVITY CASES WITH CHANGE DESCRIPTION

TABLE 15. ESFR-SMART CORE FLOWERING CORE DEFORMATION AND K_{eff} VALUES AS A FUNCTION OF APPLIED FORCE

CHAPTER 1

Introduction

The opening chapter of the thesis is subdivided into the following sections: Section 1.1 gives a brief overview of the status of nuclear energy technology used worldwide, followed by a short overview of the Generation IV (Gen IV) reactors expected to be deployed in the near future, ending with the general outline of fast neutron reactor principles. Section 1.2 expands on the description of a specific Gen IV reactor type, the Sodium-cooled Fast Reactor (SFR), by describing the historical context of the reactor, followed by the introduction of the ESFR reactor, which is the main subject of the current thesis. Section 1.3 gives a summary on the new safety measures to be assessed in the current thesis together with the motivation for the specific assessments, distributed according to the different safety functions. The objectives of the thesis are formulated in Section 1.5., and the chapter is finished with the overall structure of the thesis in Section 1.6.

1.1. Nuclear energy worldwide

Nuclear energy was first used for electricity generation in December 1951 in the USA with the Experimental Breeder Reactor (EBR-1), first lighting up four light bulbs at the reactor site. Since then it has gone through significant expansion and today there are more than 400 operating nuclear reactors, spread out in 32 different countries with the total capacity of around 400 GWe. These reactors give about 10% of the total electricity generated worldwide [1].

In light of the climate change problem, it is even more noteworthy that nuclear energy is a low-carbon emission energy source with the highest energy density. Therefore, it has the potential to be one of the major players to reduce humanity's carbon footprint without significant impacts on the quality of life within the western world providing a ray of hope to not to miss the climate goals by a significant margin. When energy produced by nuclear reactors is assessed within the low carbon electricity production mix, shown in Figure 1, it shows that around 28% of the total low-carbon electricity is from nuclear source, being the second largest producer behind hydro power [2].

Despite the fact that nuclear energy could mitigate or even solve climate change, its total share in power production is declining over time. According to projections, giving a low and a high case scenario for nuclear reactor capacity change, based on the low case scenario, by 2030 the total capacity could be reduced by around 7% [3]. This shows the current tendency, as in many countries the currently operating nuclear reactor fleet is ageing, especially in the western world, and the reactor closures can outpace the construction of new power plants. On the other hand, if the current political view would shift due to the increasing severity of climate change, and therefore an increased need to decarbonize the energy sector, nuclear power generation capacity could be increased by 30% until 2030 and by over 100% until 2050, according to the high case scenario [4].

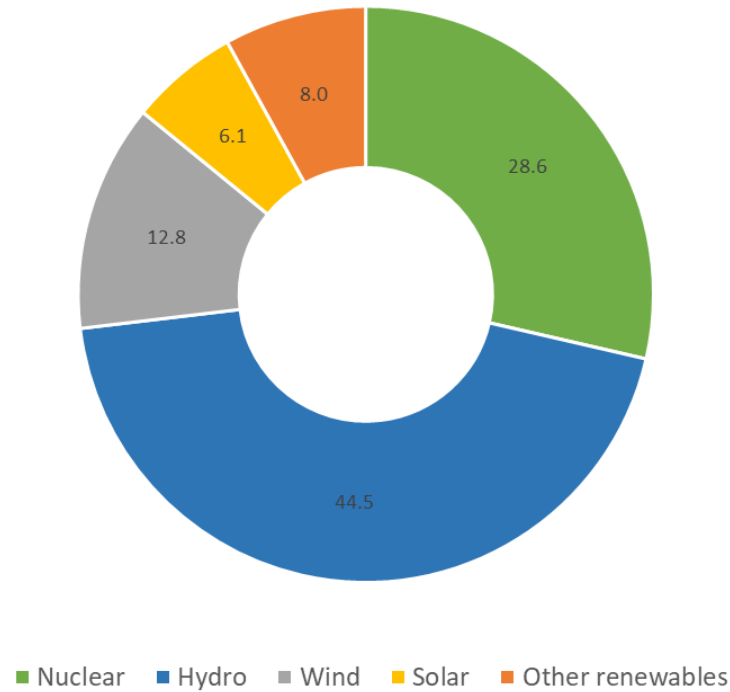


Figure 1. Low carbon electricity production distribution between different technologies [2]

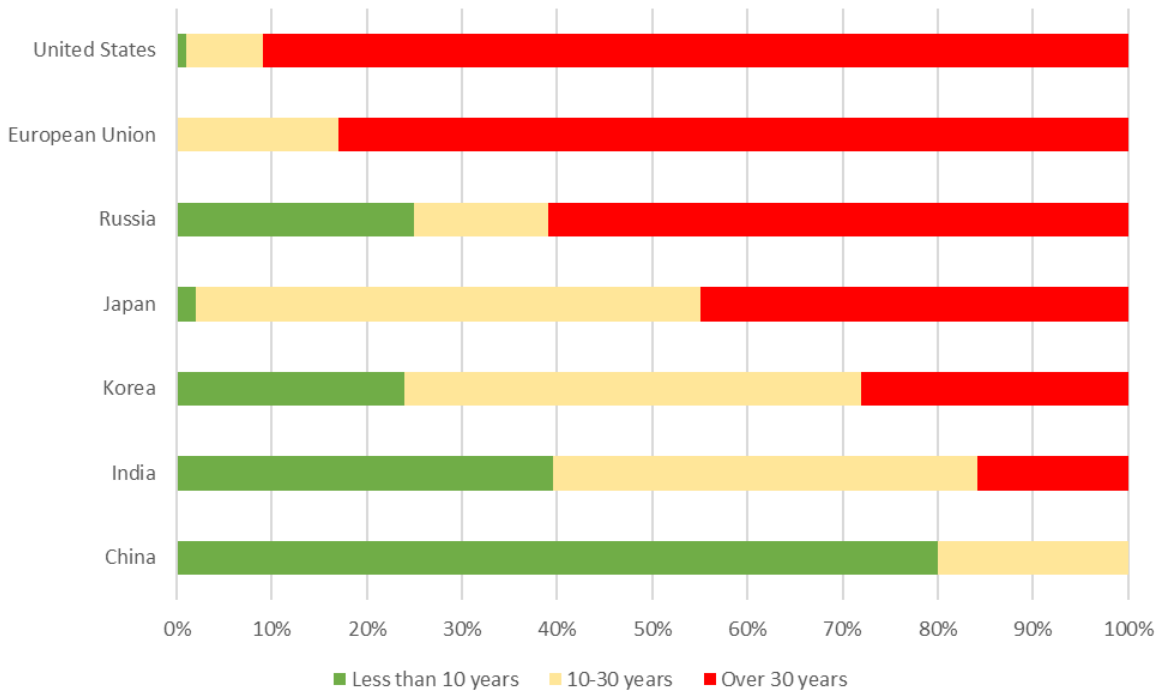


Figure 2. Nuclear fleet age distribution at different parts of the world [2]

The problem of the ageing reactor fleet is visualized in Figure 2, where it is clearly shown that in the western world, such as the United States, and the European Union over 80% of the currently operating reactors are older than 30 years, which is already over 160 reactors out of the ~440 currently operating.

To at least keep the presently available production capacity, either life time extension needs to be done for the ageing operating reactors or urgently deployment of new reactors needs to be initiated. Countries like China, India, Russia have significant near term deployment prospective, nevertheless, in many European countries and in the United States a lack of political support requires a different approach to maintain or increase the power generation by nuclear means. To achieve this, they need to tackle issues such as increased safety and more efficient nuclear waste treatment. Such goals are to be met by the next generation of nuclear reactors, called Generation IV type reactors, for which it is proposed that the safety is increased, the nuclear waste could be treated due to different operating principle and in general cost competitiveness should be increased compared to the conventional reactors of today.

1.1.1. Generation IV nuclear

Most of the operating nuclear reactors today are light water cooled reactors (LWRs), with two dominating reactors types, the pressurized water reactors (PWRs) and the boiling water reactors (BWRs). Around 370 of all operating nuclear reactors belong to these two categories [4], having the majority as PWRs with around 300 reactors currently in operation, leaving the rest, around 70 reactors, as BWRs. Although, the current reactor technology has a high safety standard, it lacks the possibility to efficiently utilize the U-238 isotope from the reactor fuel and it is reliant on the enriched U-235 isotope of the fuel for energy production. Furthermore, due to the usage of water as coolant in the reactors, there is only a relatively limited temperature range, around 300 °C, where the reactor can operate, and even these temperatures are only possible under high pressures (~16 MPa for PWRs and ~7.5 MPa for BWRs). Achieving higher temperatures would allow higher power conversion efficiency, and more diverse utilization possibilities, such as chemical process where very high temperature is required.

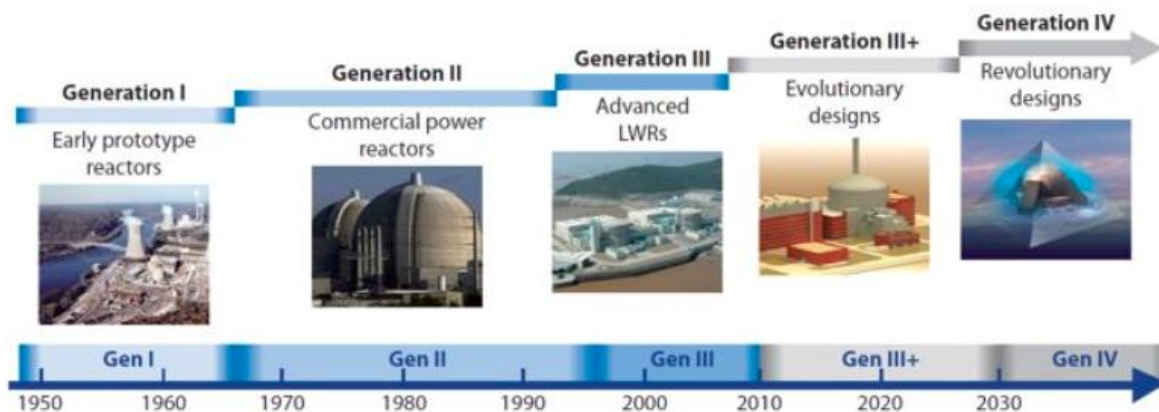


Figure 3. Timeline of the different generation nuclear reactors

In order to further develop the current reactor technology to overcome limitations stated above and to further increase the safety and cost effectiveness of the nuclear reactors, the so called Generation IV reactors are proposed to be developed and deployed in the near future. The proposed deployment timeline for these reactor types is presented in Figure 3, showing that in principle these reactors should start operating by the end of this decade. As the Figure shows, calling them “revolutionary designs”, these

reactors include significantly different design considerations than it is for today's conventional LWRs. Six specific reactor concepts are considered as part of the Generation IV designs, which were chosen by an expert group, called Generation IV International Forum (GIF), in the year of 2000. During this meeting the goal of these new reactor types were specified as follows [5]:

1. Increased sustainability.
2. Better economics.
3. Increased safety and reliability.
4. Greater proliferation resistance and physical protection.

These goals are to be achieved with various new design principles within each of the chosen reactor types. The mentioned six reactor technologies and some of their main features are presented in Table 1. The main differences compared to conventional reactors which should be highlighted are 1) the possibility to run the reactor with fast neutron spectrum within 5 proposed technologies out of the total 6. This allows a more efficient fuel utilization, paving the way to 2) use a closed fuel cycle, where the nuclear fuel is reprocessed and used again as feed fuel in a later stage. Besides, as the 3) coolant medium is usually not water but either liquid metal, helium or molten salt, 4) higher outlet temperatures can be achieved which broadens the possible applications of the reactor and higher power conversion efficiencies can be obtained. Moreover, larger margins to boiling of these coolants allow for operating the Gen IV reactors without pressurization, improving therefore the intrinsic safety compared to Light Water Reactors.

System	Neutron spectrum	Coolant	Outlet Temperature [°C]	Fuel cycle	Power output [MWe]
<i>VHTR (Very-high-temperature reactor)</i>	Thermal	Helium	900-1000	Open	250-300
<i>SFR (Sodium-cooled fast reactor)</i>	Fast	Sodium	500-550	Closed	50-150 300-1500 600-1500
<i>SCWR (Supercritical-water-cooled reactor)</i>	Thermal/fast	Water	510-625	Open/closed	300-700 1000-1500
<i>GFR (Gas-cooled fast reactor)</i>	Fast	Helium	850	Closed	1200
<i>LFR (Lead-cooled fast reactor)</i>	Fast	Lead	480-570	Closed	20-180 300-1200 600-1000
<i>MSR (Molten salt reactor)</i>	Thermal/fast	Fluoride salts	700-800	Closed	1000

Table 1. Generation IV reactor technologies according to Generation IV International Forum [6]

In the current study, the Sodium-cooled Fast Reactor technology is in the main focus, thus the further discussion will be concentrated on this.

1.1.2. Fast neutron reactors

As it was presented in the previous chapter, the majority of the Gen IV designs are to be operated in the fast neutron energy spectrum. The fast neutron spectrum is achieved by using a coolant medium, which does as little as possible moderation or slowing-down of the neutrons, allowing to maintain a high fraction of the initial neutron energy following the fission reaction. Using highly energetic neutrons to maintain fission chain reaction is beneficial in terms of 1) more efficient use of the fertile fuel (such as U-238), which has a higher probability of fission reaction using fast neutrons, and 2) burning of the minor actinides. The latter is due to the fact that the ratio of fission and capture reaction is greater in a fast reactor for plutonium and minor actinides than in a thermal reactor. Therefore, it is possible to fission the heavier transuranic elements into lighter fission products, which require a much shorter storage time, in the order of a few hundred years. With fast reactors, a beneficial neutron balance makes it also possible to breed fissile nuclear fuel from the fertile uranium isotopes, by transmuting efficiently the U-238 atoms to Pu-239. Due to this feature, it is possible to produce excess fissile material, which could be used to fuel other thermal or fast reactors. In principle it is possible to achieve breeding with a thermal reactor using a thorium cycle, thus having an efficient fuel usage, but the U-Th cycle has certain disadvantages (e.g. in terms of sustainability, neutron balance, and radiotoxicity) not to mention the fact, that the minor actinide burning is still not efficient with the thermal spectrum.

Based on the above mentioned features of a fast reactor, there are three main design options for the reactor to operate. These options are, 1) to use it as a net breeder, meaning that more fertile fuel is converted into fissile than the amount of fissile the reactor burns during its operation. 2) Iso-breeder, where the breeding ratio is equal to one, where the reactor burn as much fissile as it converts from fertile to fissile and 3) the burner concept, which burns more fissile than the amounts it produces. This third concept can be efficiently used to reduce the minor actinide content from the nuclear waste produced in LWRs.

There are various challenges in operating a fast reactors compared to LWRs, such as 1) the need to develop fuel and structural materials withstanding high neutron fluence as the burnup and fuel residence time is increased for better economical prospective. 2) Another safety related challenge is that the core configuration is not in its most reactive configuration, therefore other type of accidental scenarios, are to be also assessed, compared to LWRs, potentially leading to core meltdown and re-criticality. 3) A reactor with high energy neutrons, require higher amount of fissile fuel to be present in the reactor core to achieve criticality, as the probability of fission is reduced, leading to an increase in neutron flux, compared to conventional reactor types. As the highly energetic neutrons have a greater tendency to escape from the reactor core, coupled with the present higher neutron flux, the required neutron shielding to protect the surrounding structure and personnel from dangerous radiation dose or damage might be increased. These negative factors can be readily mitigated with available engineering solutions and these reactors can be safely operated, which is proven with over 400 years of operating experience with such technology.

1.2. Sodium-cooled Fast Reactor history

Sodium-cooled Fast Reactor technology is one of the Generation IV nuclear systems, proposed by the GIF expert group, and it has one of the highest technological readiness level from the proposed six concepts.

The technology was originally developed in the United States, operating the first reactor of this type from 24 of August 1951 in power operation and at the same year at 20 of December electricity has been produced by the power plant, making it the first reactor in the world which achieved such a milestone. The reactor used NaK as coolant and uranium metal fuel in the core, producing 1.4 MW thermal power or 0.2 MW electricity. Following the successful demonstration of power operation, multiple follow-up liquid metal cooled reactor projects have been launched in the US as well as in other countries.

In Table 2, an overview is presented of the different SFRs worldwide. This table shows various research or prototype SFRs ever operated, leading to a total SFR operating experience of over 400 reactor-years.

	MWe	MWth	Operation
USA			
EBR I	0.2	1.4	1951-63
EBR II	20	62.5	1963-94
Fermi 1	61	200	1963-75
SEFOR		20	1969-72
Fast Flux Test Facility		400	1980-93
UK			
Dounreay FR	15	65	1959-77
Prototype FR	250	650	1974-94
France			
Rapsodie		40	1967-83
Phenix	250	563	1973-2009
Superphenix	1240	3000	1985-98
Germany			
KNK 2	20	58	1972-91
India			
FBTR	13	40	1985-
PFBR	500	1250	under construction
Japan			
Joyo		50, 75, 140	1978-2007
Monju	280	714	1994-96, 2010
Kazakhstan			
BN-350	135	750	1972-99
Russia			
BR 5 Obninsk		5	1958-71
BOR 60 Dimitrovgrad	12	60	1969-
BR 10 Obninsk		8	1973-2002
BN-600 Beloyarsk 3	600	1470	1980-
BN-800 Beloyarsk 4	864	2100	2014-
MBIR	40	150	under construction
China			
CEFR	20	65	2010-
CFR600	600	1500	under construction

Table 2. Sodium-cooled Fast Reactors worldwide [7]

1.2.1. SFR physics and working principle

Sodium Fast Reactors, as the name suggest, are fast reactors using liquid sodium as the coolant medium to remove the heat from the reactor core.

Sodium as the coolant medium in a fast reactor has numerous advantages compared to other coolants. First of all, it is a weak neutron moderator, which required to keep the neutron spectrum at a high energy range. Secondly, liquid metals in general but sodium especially have high thermal conductivity providing a very efficient heat removal mean from the fuel assemblies even with reduced coolant flow rates. Sodium coolant has a relatively large density variation with temperature, therefore, the reactor can potentially safely shutdown and remove all residual heat from the reactor core even with natural convection flow. Lastly, sodium has a wide temperature margin between the melting temperature (98°C or 371K) and the boiling point (883°C or 1156K) at atmospheric pressure. This temperature difference permits the operation of the reactor at near atmospheric pressure, whereas in a LWR to keep the water in liquid phase at around 300°C requires significant overpressure (~7.5 MPa for BWR or ~16 MPa for a PWR). It is also worth to mention that sodium is a widely available resource and therefore is it a relatively cheap coolant compared to for example lead.

There are certain disadvantages also corresponding to sodium as coolant. The most notable issue with sodium is its chemical reactivity with air and water. This reactivity poses a serious hazard on the safety of the reactor and measures need to be taken to practically eliminate the risk of sodium fires or to reduce its consequence as much as possible. Due to this risk, an intermediate sodium circuit is used for SFRs which separates the activated sodium, as a result of the radiation around the reactor core, from the water/steam circuit. In this way, even in case of a sodium fire, due to some leak from the sodium to the water circuits, it is not categorized as a reactivity incident but as a normal fire without radioactive release.

There are two main arrangements of SFR components which are 1) pool type and 2) loop type designs. In a pool type design, such as the Phenix, Superphenix, BN-800, EBR-II, CFR-600 etc. reactors, the primary sodium coolant is contained within the main reactor vessel. In this way, the Intermediate Heat Exchangers (IHX) and primary pumps are situated beside the reactor core. On the contrary, for the loop type design, such as the Rapsodie, DFR, PFR, Monju, etc., the IHX and the primary pumps are outside of the main vessel of the reactor. Some of advantages of the pool type concept is the greater heat capacity available within the main vessel which is favorable in case of hypothetical accidental conditions, whereas a disadvantage would be the greater main vessel size requirement to fit the extra components into it. Recent developments on commercial size of SFR, i.e. those of Generation IV, mainly consider the pool type design.

The working principle of a pool-type SFR is shown in Figure 4. In the reactor vessel, the primary sodium is divided into hot and cold pools (or plenums). The cold sodium is sucked in by the primary pump and is pushed through the reactor core, where the generated power is removed by the sodium, resulting in coolant temperature increase. From the core, the sodium arrives to the hot pool from where it enters the IHX. The IHX provides the connection between the hot and cold primary sodium, where the hot sodium enters at the top of the device, and exchanges its heat with the secondary circuit sodium. After the heat exchange, the primary sodium leaves the IHX and enters the cold pool, from where the cycle repeats. The heated secondary sodium enters the steam generators (SGs), where the heat is exchanged with the tertiary water circuit, through a heat exchanger. After leaving the steam generator, the cold intermediate

sodium moves through the pump and flows towards the IHX for heat exchange with the primary sodium. From the tertiary circuit onwards, the reactor plant operation is identical to any conventional power plant, where the generated steam drives a turbine, which generates electricity through the rotation of the generator.

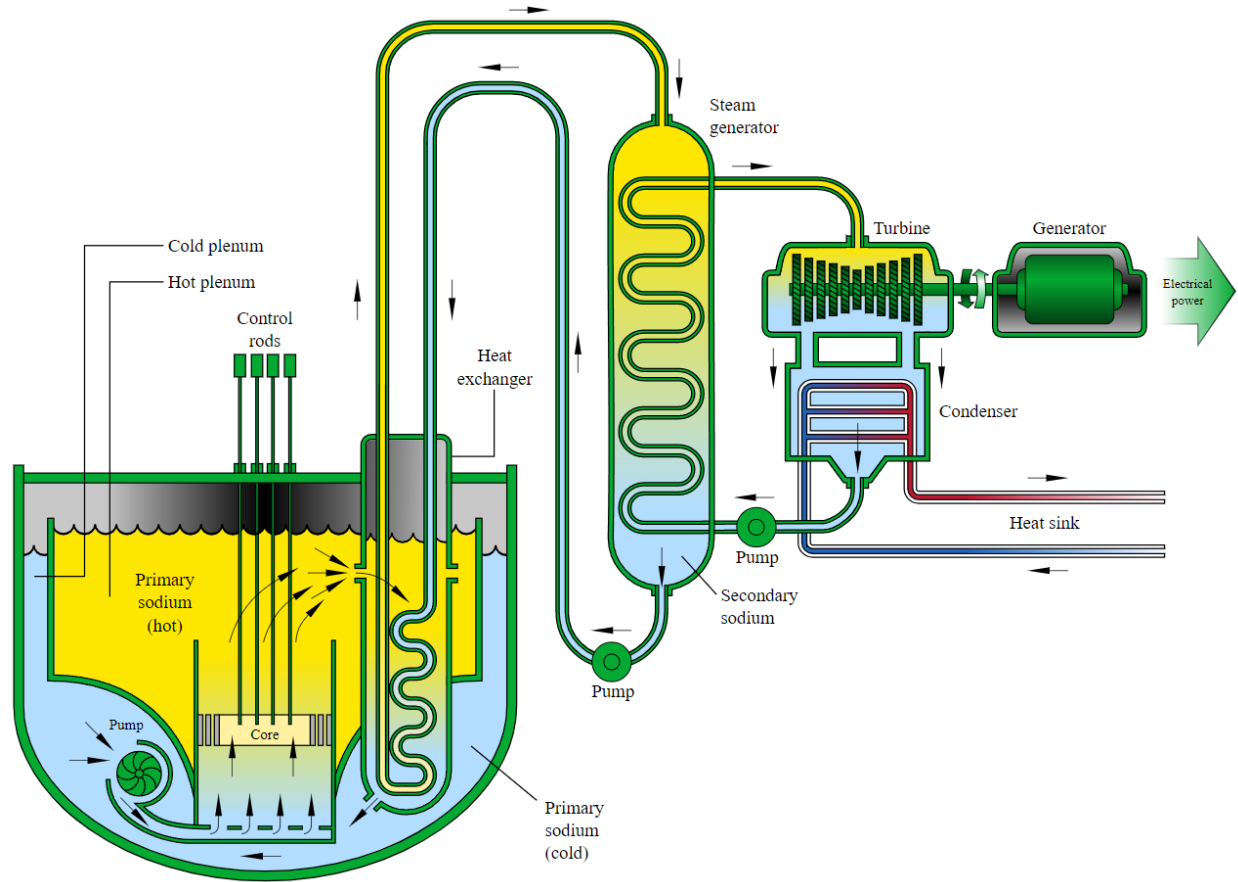


Figure 4. Sodium-cooled Fast Reactor (pool type) schematic view

1.2.2. European Sodium Fast Reactor

The main subject of the current thesis is the European Sodium Fast Reactor (ESFR) [8], which is a conceptual design of a pool-type, commercial size SFR, with the power output of 1500 MWe (3600 MWth), see general reactor details in Table 3. For the reactor core mixed oxide fuel is used, being the reference EU fuel type, due to the vast operating experience, high melting point, and low swelling properties. The reactor design accumulates the legacy of the previously operating SFRs, in particular the Phenix [9] and Superphenix [10] reactor designs. Although the main ideas and working principles of the aforementioned two reactors have been retained in the ESFR concept, numerous new design elements have been implemented, based on Superphenix successor project called the European Fast Reactor (EFR) [11], to increase safety, and reduce costs. Leveraging the EFR developments, in 2009, a new European project was launched, called Collaborative Project on European Sodium Fast Reactor (CP-ESFR) [12], which initiated the work on the ESFR. Following this project, the development of the reactor continued in 2017,

within the European Sodium Fast Reactor Safety Measures Assessment and Research Tools (ESFR-SMART) project [13]. Within ESFR-SMART, all the main characteristics of the reactor, such as the power output, overall dimensions, etc., has been kept but various new safety measures have been included in the design. In the following part of the Section, a design overview is going to be provided, which was developed as part of the PhD work.

As the ESFR is a pool-type SFR, it consists of a primary sodium circuit, which is immersed completely into a sodium pool, with all of its components, such as the intermediate heat exchanger, primary pumps, reactor core, etc. The primary circuit is connected to the secondary sodium loop, through the intermediate heat exchanger. Finally, through the steam generator units the secondary sodium is connected to the tertiary circuit, which is a steam-water circuit driving the turbines.

An overview of the reactor is shown in Figure 5. In the primary system, three primary pumps and six IHXs are located, connected to six secondary circuits placed around the reactor, each equipped with six steam generators. To guarantee that the residual heat is safely removed from the reactor during shutdown or an accidental scenario, three different decay heat removal systems (DHRS) have been allocated for this reactor design. These systems are completely independent from each other and can operate separately. The DHRS-1 and DHRS-2 both use secondary sodium for the heat removal, and both of them can operate in a completely passive manner, whereas the DHRS-3 is the pit cooling system and uses forced convection.

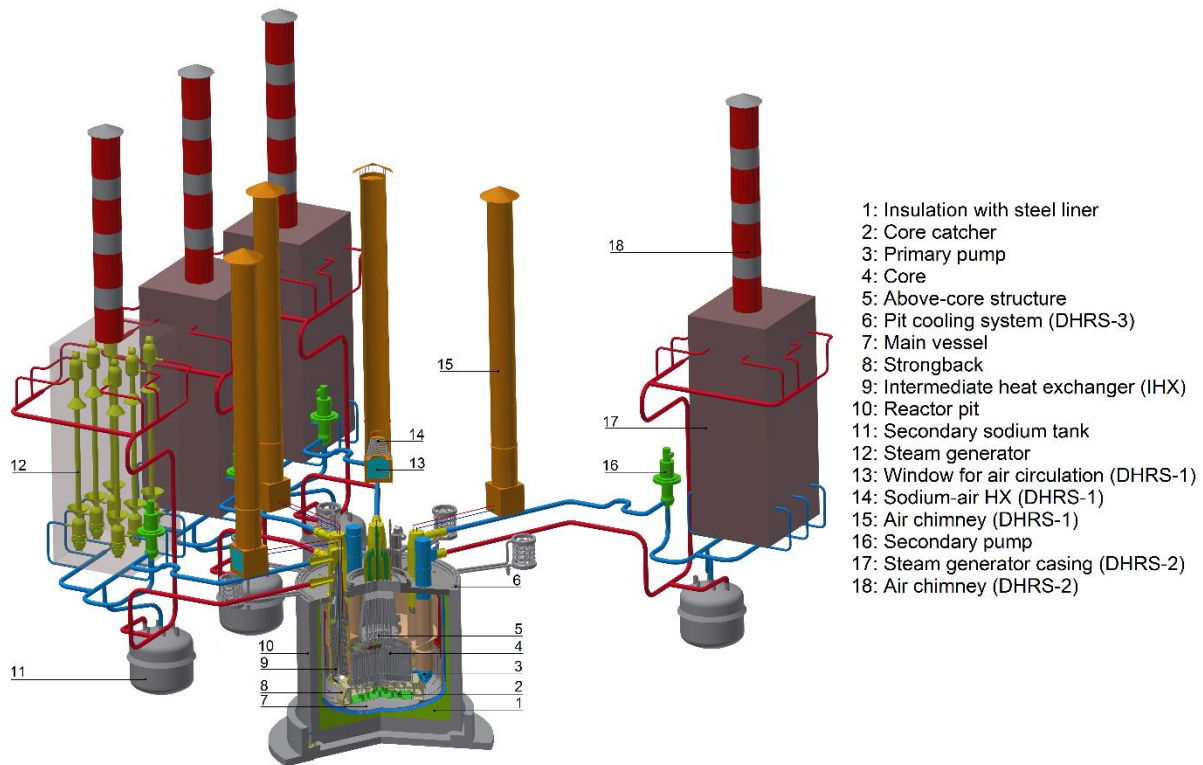


Figure 5. The global view of ESFR with all main components

General	
Thermal power (MWth)	3600
Net electrical power (MWe)	1500
Mass of sodium in main vessel, t	2350
Total pressure losses in primary system, bar	4.5
Cover gas above primary sodium free level	Argon
Pressure of cover gas, bar	1.15
Core	
Core inlet / outlet temperatures, °C	395 / 545
Type of fuel	(U,Pu)O ₂
Core outside diameter, m	~8
Core flowrate, kg/s	~18700
Core bypass flowrate, kg/s	~900
Core pressure drop (including inlet and outlet), bar	3.8
Core support pressure drop (diagrid), bar	0.7
IHX	
Number of IHXs	6
Power of one IHX, MW	600
Type	Tubular, counterflow
Pressure loss (primary), bar	0.25
Working fluids, primary / secondary	sodium / sodium
Primary sodium temperature at IHX inlet / outlet, °C	545 / 395
Secondary sodium temperature at IHX inlet / outlet, °C	530 / 345
Primary pumps	
Number of primary pumps	3
Type	mechanical, radial admittance, axial exhaust, anti-reverse-flow diode
Mass of one pump with motor, t	~164
Location	in reactor vessel
Nominal rotational speed, rot/min	450
Net positive suction head, / available, m	13
Pressure head, bar	4.5
Nominal flowrate, kg/s	6512
Halving Time, s	~10
Min Time from 100% to 25% of nominal speed, s	30
Secondary loops	
Number of secondary loops	6
Composition	1 IHX, 6 SGs, 1 secondary pump, 1 thermal pump, 1 purification system, 2 draining systems
Nominal flowrate per loop, kg/s	2541
Length of pipes with Ø 850 / Ø 350 mm per loop, m	~219 / ~90
Steam generator	
Number of steam generators per secondary loop	6
Type	modular, tubular, counterflow
Working fluids, secondary / tertiary	sodium / water
Power of one SG, MW	100
Water inlet / steam outlet temperature, °C	240 / 528
Steam pressure, bar	185
Steam flowrate per secondary loop, kg/s	287

Table 3. ESRF-SMART reactor concept main characteristics (extended Table is provided in Appendix A)

1.3. Motivation: need of ESFR safety measures assessment

As it was presented in the previous sections, Sodium-cooled Fast Reactor technology has the highest operating experience compared to other Generation IV reactor technologies, totaling to ~400 reactor-years. This vast experience and the number of previous reactor designs make it a good candidate to be developed and built in the near term future, which would be an important milestone in the development of advanced fast reactors. This fact, coupled with the ever greater urgency of acting to mitigate climate change, makes the SFR technology a great candidate to perform safety assessment and design studies to generate knowledge, essential for the deployment of such reactors.

Within the ESFR-SMART project various new safety measures have been adapted into the reactor design, based on previous experience with SFRs, operated in the past or currently being in operation. The reactor design was based on the outcome of the previous CP-ESFR project but further design improvements were adapted mainly from the operating experience of Phenix [9], Superphenix [10] and EFR design outcome [11]. In Figure 6 and Table 4, the design modifications are highlighted between CP-ESFR and ESFR-SMART projects, which are to be discussed in the following part of the Section together with the required modeling capability developments to assess the reactor design with greater accuracy than it was possible in the past.

Modified reactor component	Main modification between ESFR-SMART and CP-ESFR
Reactor core	The reactor core is established with a 6 batch burnup structure, with general neutronic core optimization. Besides, corium guide tubes are included at specific subassembly (SA) locations
Primary pump	The primary pump connection is moved from the strongback to the more conventional diagrid component
DHX	The dedicated decay heat exchanger has been removed from the primary circuit and instead a decay heat exchanger has been incorporated into the intermediate heat exchanger (IHX), using the secondary sodium for the cooling.
Guard vessel	The function of the guard/safety vessel has been taken over by the modified design of the reactor pit, including a steel liner on its surface. Therefore, the component has been removed from the design. Furthermore, within the new pit design an auxiliary decay heat removal system (DHRS) has been incorporated.
Reactor dome	Instead of the large reactor dome, the large components, immersed into the primary circuit, are welded on the reactor roof to maintain leak tightness in the case of an accident, causing overpressure in the primary system.
Secondary circuit	In the secondary circuit, an extra auxiliary pump is proposed to be fitted, a passively operating thermoelectric-pump, to improve natural circulation for the DHRSs.

Table 4. List of main design modifications between CP-ESFR and ESFR-SMART reactor concepts

The above-mentioned modifications were implemented as a response to the latest safety criteria, proposed following the Fukushima accident. The main principle in the design development was to use

simplified, passively operating safety measures. Further justification of the proposed the new safety measures must be done with application of the probabilistic safety analysis, in particular, to verify the appropriate application of the principle of redundancy with regard to equipment and systems, and to specify the requirement for the implementation of protective measures against the common cause failure to redundancy systems [14].

The new safety measures are considered within the technical requirements and must be assessed during safety analysis of the reactor in accord with the fundamental safety principles, defined by International Atomic Energy Agency (IAEA). The latter comprises three main pillars of the safe operation, which require that the fulfilment of the three fundamental safety functions for a nuclear power plant shall be ensured for any plant state: (i) control of reactivity; (ii) removal of heat from the reactor and from the fuel store; and (iii) confinement of radioactive material, shielding against radiation and control of planned radioactive releases, as well as limitation of accidental radioactive releases [15]. The safety analysis, which is going to be presented in the thesis, is divided into dedicated sections, according to the safety functions. In this sense, to keep the same structure as it is in the main part of the thesis, the newly implemented safety measures of ESFR are categorized into the three safety functions here also, namely: 1) Reactivity control safety function, 2) Heat removal safety function and 3) Containment safety function.

1.3.1. Reactivity control safety function

Fast neutron physics and core design of SFR imposes a specific inherent feature of the reactor core, that it is not at its most critical configuration at nominal operation. In particular, high positive reactivity effect of the sodium voiding for some designs, especially for large commercial size cores, is of a great concern. The possibility of the core compaction resulting in a positive reactivity insertion must be also eliminated. Regarding the fulfillment of the reactivity control safety function, in the thesis the work focuses on the new safety measures and calculation methods in relation to two specific issues, namely, 1) positive sodium void reactivity coefficient and 2) reactivity variations related to core geometry distortion.

1.3.1.1. Sodium void effect

Sodium-cooled Fast Reactors can be strongly affected by the boiling of the sodium in the reactor core. In traditional SFR core designs the sodium density decrease within the reactor core can result in positive reactivity insertion, which in turn can result in rapid power excursion. This is due to the fact that the density change of the sodium affects the neutron spectrum of the core.

Generally, the concern is when the sodium density is decreasing, i.e. the sodium temperature is increasing in the system, especially at the point where sodium boiling happens, which results in a large, sudden density decrease. As the sodium captures and scatters the neutrons of the system, the decrease of sodium isotope number density results in two effects, 1) increase neutron leakage and 2) harder neutron spectrum, the latter of which tends to be the dominating effect in traditional, large SFR cores. The harder neutron spectrum has an overall positive reactivity effect in an SFR, in contrast to an LWR, due to the increased fast fission factor from the U-238 and the increased reproduction factor mainly from the Pu-239. With the increase in the neutron energy, the parasitic absorption of the neutron in the U-238 is reduced, whereas the fast fission cross section is increased for U-238. For the Pu-239, there is an increase

as well in the fission cross section with increased neutron energy, but the main effect comes from the increase in the number of emitted neutrons per fission reaction. If this process is not mitigated, the continuous sodium boiling can fill the SA channel with vapor, leaving only a thin liquid layer on the pin surfaces (film boiling) and eventually reaching dry-out condition with the overheating of the fuel pins, culminating in pin failure.

The above-mentioned problem is an issue particularly for commercial size reactors, having a large reactor core. For reactors having smaller core even negative void effect is possible, such as in Rapsodie or Phenix [16]. This is due to the fact, that void effect has a negative contribution close to the periphery of the reactor core, as a result of the increased leakage from the core and for small reactor core, this effect can dominate the overall reactivity evolution. For increased size reactor core, the reduced neutron absorption due to spectrum hardening at the center of the core tends to have the dominating effect [16]. There are various ways to reduce the effect of sodium voiding in the core, starting with the more compact, hexagonal fuel pitch introduction, reducing the available sodium between the fuel SAs, this concept has been used for nearly all SFR designs. The next improvement in the path to reduce sodium void effect is the introduction of the low height to diameter fissile core region, so called pancake shape design, done for example within the European Fast Reactor (EFR) studies [11]. For more recent SFR core design, a low (or zero) void effect core has been proposed. This is achieved by introducing a so-called sodium plenum above the fissile core, on top of the previously mentioned core modifications, as in the currently operating Russian BN-800 [17] reactor the French ASTRID [18] reactor concepts. By doing so, when the sodium starts to boil at the top of the SAs, the vapor fills the plenum region, where therefore the neutron leakage out of the core is increased. Thus, in these reactors the global zero or even slightly negative void reactivity effect can be achieved, as the sodium voiding assessment shows in [18]. The analysis of the hypothetical accidental conditions, e.g. unprotected loss of primary mass flow (ULOF), followed by sodium boiling, reveals potentials to keep the core integrity and to provide a considerable grace time before the intervention of the safety systems and/or operator. In this accidental condition the primary pumps of the reactor are tripped, with a gradual flow reduction to the natural circulation level, combined with the failure of reactor shutdown by control rod insertion. Under such circumstances, a stabilized boiling was predicted which doesn't result in a power excursion and cladding dry out [19][20].

Within the ESR-SMART reactor concept, all the above-mentioned core design measures have been taken into account and the core concept developed within CP-ESFR [12] has been carried over to ESR-SMART applying further optimization on it [21]. In this sense, it uses a hexagonal SA pitch, achieving high power density with low sodium volume between the fuel pins. The active core height to diameter ratio has been kept low, having 1 m active core height with the diameter of ~5 m. Besides, the large sodium plenum region from CP-ESFR with further optimization to decrease the global sodium void effect has been kept also, having 60 cm plenum height. Another safety related core modification, which is unique for the ESR-SMART concept is the introduction of empty channels into the core, called corium discharge tubes (shown in Figure 6), at the center, inner/outer core periphery and outer core periphery regions. These channels are intended to provide a clear path for the melted core towards the core catcher, where it can be cooled long term, in case of a severe accident. With all the applied measures, careful safety assessment has to be done, to verify that such a low void effect core can keep a 3600 MWth, commercial size reactor safe during an accidental scenario. This is required as the previous reactor concepts were generally smaller in size and therefore less much affected with the sodium void reactivity problem.

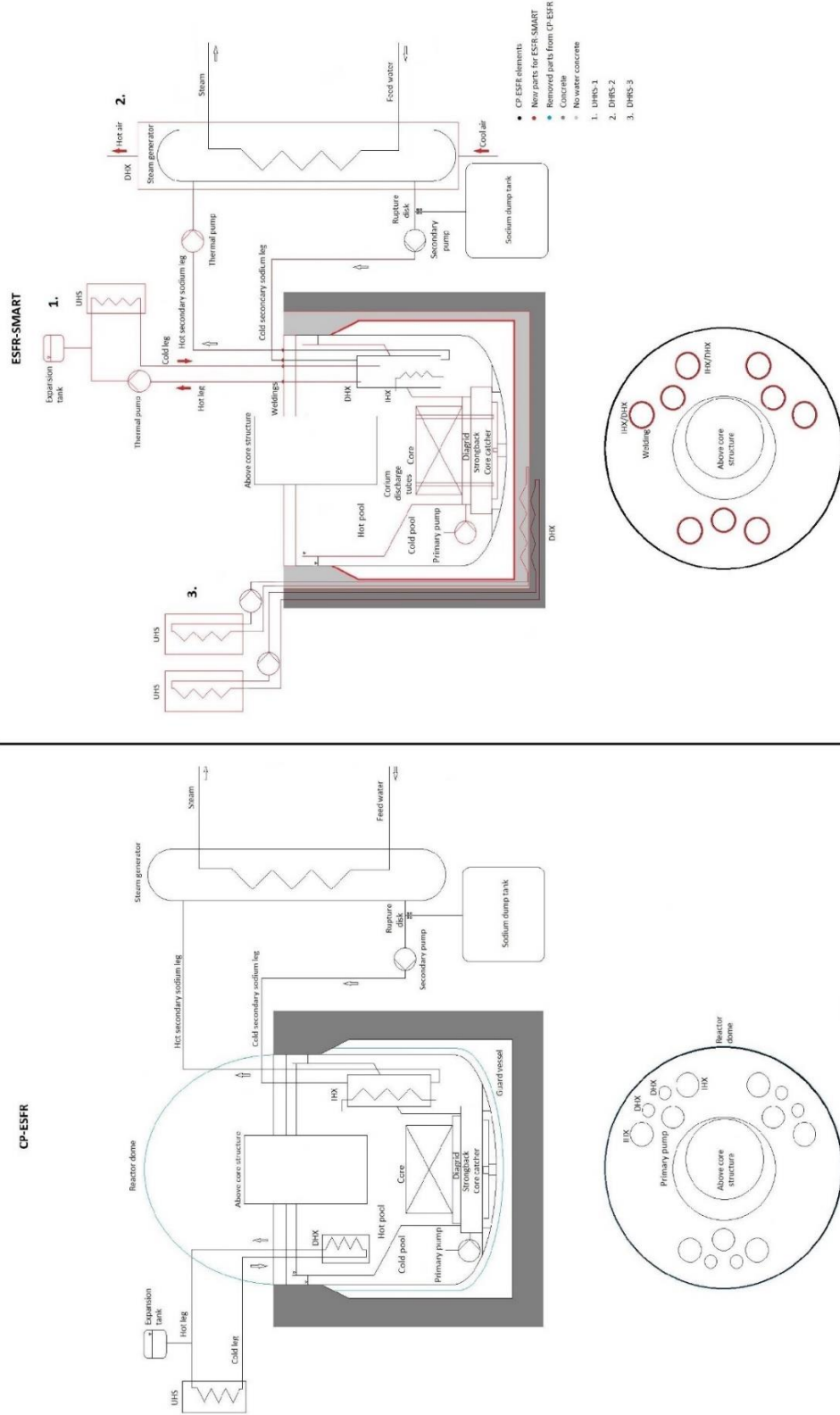


Figure 6. CP-ESFR vs ESR-SMART reactor design modifications

Another issue related to the boiling phenomenology is the possibility of flow blockage in the SA in case of sodium boiling. The sodium vaporization in the channel with high power release (i.e. occurring at core power level close to nominal power level) is characterized by a quick bubble growth period as it has high heat conductivity, low specific heat, and high vapor to liquid volume ratio [22]. Therefore, the bubble growth can potentially cyclically push out and suck back in the liquid sodium, reducing the effective sodium flow to close to 0, which can potentially lead to the SA being filled with sodium vapor at the fissile fuel region as the vapor propagates downwards. As the channel is increasingly being filled with vapor at the fuel region, the spectrum hardening effect starts to dominate the reactivity evolution rather than the increased leakage and thus under these circumstances the reactor core can have a positive overall void effect even with the usage of sodium plenum [24].

To overcome this issue, the assessment of a new feature has been proposed in the thesis on the SA wrapper tubes (hexcans). More specifically, windows are introduced on each side of the SA hexcan close to the top of the fuel region, shown in an earlier patent developed under the previous CP-ESFR project [24], with the aim to provide a path for the sodium flow in case the top of the SA is filled with sodium vapor, see in Figure 7. Such wrapper design supports the establishment of stabilized boiling phenomenon within the reactor core, meaning that boiling process stays in regions contributing to the reduction of the overall core reactivity. Thus, the sodium void propagation to the positive void effect fuel region is potentially reduced with the proposed modification. The application of this safety feature on the previous ESFR design has been analyzed in [25]. It was modelled as the SAs being connected to each other with pipes, having the geometry of the windows, specified in the patent. The improvement in the core behavior during an accident with sodium boiling has been stated. Thus it is of importance to perform a relevant safety assessment using a more accurate modeling of the core, in particular by introducing the inter-SA gap. As the inter-SA gap has a small bypass flow and in reality, the windows on the hexcans are connected to this region, the modeling approach can have an effect on the sodium vapor propagation within the reactor core, and requires the more accurate simulation technique used for the current work.

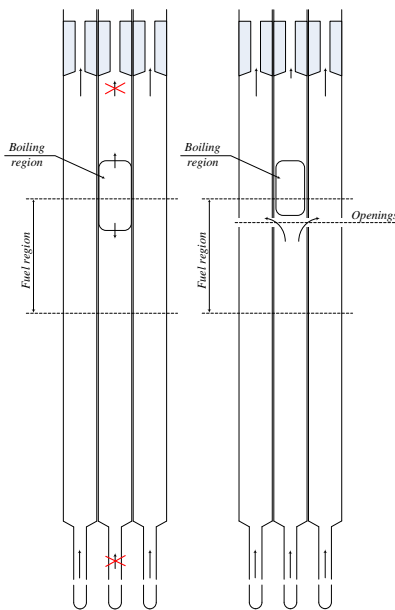


Figure 7. Schematic illustration of the flow pattern in case of sodium boiling in the SA with reference (on the left) and modified (on the right) design of the hexcan [24].

1.3.1.2. Core deformation effect

Core mechanical analysis is an infeasible part of the safety evaluation of a reactor during the design process, especially for fast reactors with higher fissile fuel content, such as an SFR. An incorrectly chosen SA constraint in the core can lead to the damage of the reactor as it has happened for the Experimental Breeder Reactor (EBR-I) [26] in the US. As part of this incident, due to a thermal gradient within the core, the fuel SAs bowed inwardly which introduced a positive reactivity insertion in the reactor core and a partial core meltdown has occurred. Since then, improvements have been made on the core constrain design [27]. Nevertheless, it is still an open issue, revealed by the more recent negative reactivity event (AURN) [28], which has happened four times during the operation of the Phenix reactor in France. Although the exact cause of the events is still not resolved, according to the current most probable explanation, the cause is related to the radial deformation of the reactor core. This deformation can happen due to several reasons, such as sodium boiling and bubble collapse causing pressure spikes. Thus, modelling of the distorted core geometries and evaluation of the corresponding reactivity is of a high importance for safety analysis of SFRs.

Generally, for the evaluation of the reactivity effect of the core distortion, different geometry simplification methods are used. A usual approach is to expand the reactor core uniformly in the axial and radial direction. This approach is sufficient to model quasi-static perturbations in the reactor core, such as the thermal expansion of the fuel assemblies due to the thermal power of the core. Nevertheless, when fast dynamic perturbations are evaluated, these uniform expansions of the reactor core provides only an envelope for the reactivity effect [29] and it can be modeled more accurately with a non-uniform deformation approach. Various approaches have been considered in the past decades to determine effect on core criticality the dynamic SA bowing. In the late 90's to account for the fluid structure interactions within the simulations posed a significant challenge, therefore the change of the SA bowing frequency could not be modeled accurately [28]. Since then significant development has been made in the computational tools and today it is possible model deformation of the reactor core for fast dynamic perturbations. Usually these approaches apply certain modeling simplifications, like using one-dimensional (1-D) beam finite element models to calculate the SA bending [28] or using a lumped core approach where the radii of the core is changed, differently for the separate axial regions, to account for the overall SA deformation within each axial region [30]. For certain approaches a two-dimensional (2-D) core calculation is performed for the assessment of local perturbations [31], resulting in accurate SA wise local deformation but for three-dimensional (3-D) calculations with high non-uniformity, the assessment on the actual fuel SA displacement is still seldom performed.

In this thesis a new method is proposed to evaluate the reactivity variation in fast transients, such as initiated by a local pressure spike, using a 3-D whole reactor core model in neutronics with the geometry obtained from the mechanical simulation with a finite element solver. The neutron transport in the detailed distorted core geometry is solved with the Monte Carlo method, thus the reactivity effect of the deformation is derived. This approach allows treatment of nearly all realistic deformed geometries, i.e. resulting from local perturbation sources, and corresponding accurate evaluation of the core reactivity benefiting from the capabilities of the Monte Carlo method. With the use of the described method, it is possible to assess the reactivity change due to SA bowing or flowering of the ESFR-SMART core design and compare it to validated Phenix flowering results, assessing the effect of the different core designs related to the core deformation reactivity change. More importantly, a postulated sodium boiling induced

core deformation on an SFR core is assessed in the work. It is performed by applying the sodium vapor collapse induced pressure spikes on the SA surfaces, obtained from sodium boiling calculations, simulating the dynamic movement of the SAs and the corresponding reactivity effect variation.

1.3.2. Heat removal safety function

The heat removal safety function is addressed with assessment of the related safety measures proposed within the ESFR-SMART project for the new ESFR concept. Various DHRs are assessed and their capability is evaluated to remove the residual heat following the reactor shutdown, either as part of normal operation or caused by an accidental scenario. During the assessment performed in frame of the thesis, the modifications applied on the reference secondary circuit design and their impact on the flow pattern and heat removal capability of the systems were studied.

1.3.2.1. Reference design

Decay heat removal (DHR) is of key importance for any reactor type as it ensures that the reactor can be kept safely after its shutdown, which can occur not only during normal operation for maintenance and refueling processes, but also during an accidental scenario. At normal conditions, decay heat is removed using the steam/water circuit. In an SFR, it is usually backed up by two safety qualified DHR systems. Therefore, the assessment of such systems is essential, especially when newer reactor types are considered where higher degree of passively safe design is intended. It is especially true for SFRs, where the pin failure and fuel melt down occurred due to lack of cooling, may result in full core disruptive accident, which may be followed by a re-criticality event.

The passive operating principles of DHRs, as well as high level of redundancy, have been present in various previous SFR designs, such as Phenix, Superphenix and EFR and is also present in more recent designs such as the ASTRID conceptual design, the Russian BN-800 or the Chinese CEFR, just to mention a few. Similarly to the sodium void effect challenge, commercial size reactors carry greater challenge to keep them sufficiently cooled during an accidental scenario as a result of the high decay heat production. There is a threshold of ~500 MWth reactor core, for which the DHR can be done merely by thermal radiation through the reactor vessel towards the pit and cooling only the pit with forced convection [16] as it was possible e.g. for the Phenix reactor (though other DHR means were also included in the design). This DHR path (thermal radiation through the reactor vessel) was already not sufficient for Superphenix, having 2990 MWth nominal power output [16]. For the ESFR concept, the Phenix, Superphenix and EFR DHRs have been used as the basis for the two main DHR means with certain further improvements to increase robustness, efficiency and to decrease the cost of the systems. Furthermore, a third auxiliary heat removal system has been also included in the design, which is unique to the current ESFR concept, linked to the Phenix and EFR pit cooling methodology.

1.3.2.2. DHRs-1 design

The DHRs-1 is one of the two main DHR means of ESFR, shown in Figure 8. The idea of the main DHRs, capable of cooling down the primary system, has been taken from Superphenix, EFR and CP-ESFR designs, where there was an independent heat exchange unit immersed into the primary sodium. In order to

reduce the number of penetrations into the primary system, increasing the risk of sodium leak in case of accidental overpressure, and to reduce the costs of the units, the concept was modified according to another Superphenix DHRS. This DHRS in Superphenix used the secondary sodium as a working fluid with a secondary sodium/atmospheric air heat exchanger to evacuate the heat originating from the primary system. The problem with that DHRS was that in the event of losing the secondary sodium from the main loop, the DHRS was no longer capable to maintain its function. Therefore, for ESR-SMART this system has been re-designed, still using the secondary sodium for the DHR operation but the system is now connected directly to the IHX units. In this way, it is possible to maintain the cooling function even if the secondary sodium loop is drained, as the remaining sodium in the IHX is sufficient to circulate sodium in the DHRS-1 loop. Therefore, as the DHRS has been significantly modified compared to the previous designs, it is important to assess that sodium circulation in the loop can be achieved with sufficient flowrate and the heat removal capability can maintain the long term cooling of the primary system. This analysis was done in the thesis.

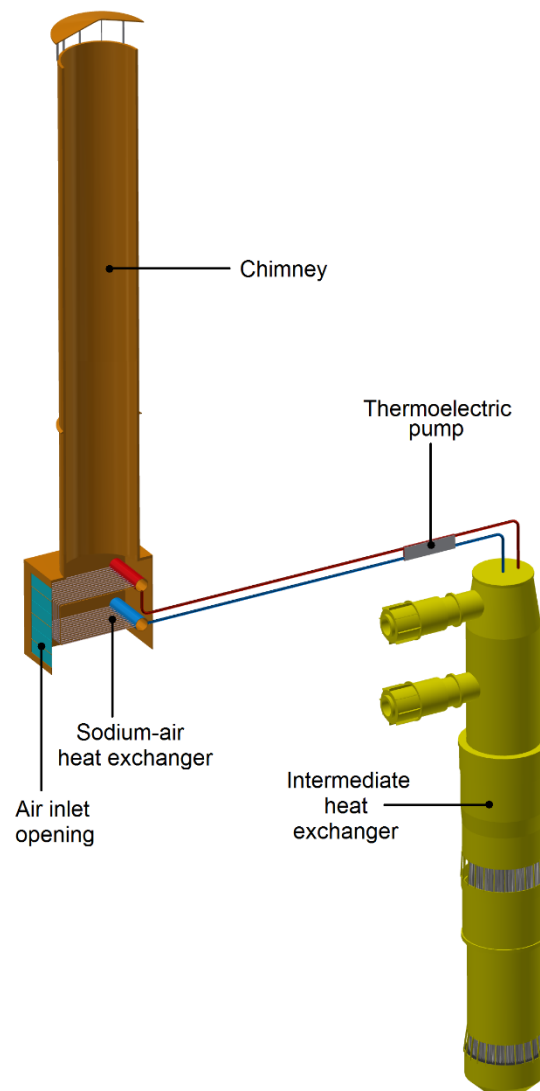


Figure 8. DHRS-1 related system components

1.3.2.3. DHRS-2 design

To increase the redundancy of the DHRSs, another main system was considered, based on the design used in the Phenix reactor. In this design, the casing of the SG units could be opened and cooled by the flow of atmospheric air, removing the heat from the outer surface of the SG tubes. In the Phenix reactor the utilized SG units were of hairpin type, meaning that there were numerous bends on the tubing [9]. During the operation of the reactor there have been various water leaks to the sodium, creating sodium/water interaction in the SG casing at the superheater section due to thermal fatigue [9]. To reduce this issue, in more recent SFRs the choice of SGs is rather the straight pipe design, used on the EFR concept, BN-600 or PFBR reactors [16]. In the EFR concept, the outer surface of a SG unit was proposed as one of the decay heat removal means, using forced convection air circulation [11]. In this proposal there was only 1 SG unit per secondary loop, monolithic option, making it necessary to remove a whole secondary circuit from operation if a water leak appears in a SG. For ESFR-SMART, the Phenix and EFR concept has been developed further for the DHRS-2 (Figure 9), as modular SGs are proposed to be used (6 per secondary circuit in the current design), using atmospheric air circulation within the SG casing, containing the 6 units, to remove the heat from the secondary sodium. From the EFR concept, the use of the straight tube SG type has been retained. This design offers an easier manufacturability and therefore steady quality, resulting in fewer failures and decreased costs. Furthermore, in case of a SG unit failure, the modular option allows a quick and easy replacement of the faulty unit, without affecting the plant as a whole.

The assessment of the system is required for the safety analysis of the reactor concept as there have been significant changes compared to the previous designs. The DHRS-2 is one of the main units to remove the decay heat, even when DHRS-1 is not available, therefore there is a strong motivation for the performance assessment of the system. Furthermore, both DHRS-1 and DHRS-2 includes thermoelectric pumps in the design concept, able to provide a limited pressure head supporting the establishment of natural circulation in the sodium loops, the feasibility of which needs to be assessed.

1.3.2.4. DHRS-3 design

In nearly all SFRs, there is a safety vessel around the main vessel of the reactor, having the function to contain the sodium in the event of a primary vessel leak. To reduce cost and remove the possibility of a safety vessel failure incident, in the EFR concept, the reactor pit has been designed to contain the primary sodium in the case of the primary vessel leak [11]. Therefore, it was possible to eliminate the use of the safety vessel from the design. In ESFR-SMART this concept has been further developed, as instead of the using only water loops for the cooling of the concrete in the pit, which is the usual approach, another cooling system, using high temperature resistant oil have been introduced in the design. The justification for this is the fact that by removing the safety vessel, there is a more efficient heat radiation towards the pit and therefore higher amount of heat can be removed. In addition to the concrete cooling during normal operation, these water and oil cooling circuits form together the DHRS-3 unit, shown in Figure 10. The DHRS-3 system is an auxiliary decay heat removal option of ESFR. It complements the operation of the DHRS-1 or DHRS-2, and it is not designed to manage heat removal at accidental conditions by itself. As in previous SFR designs the reactor pit was only cooled through the concrete, it is an interesting task to characterize the heat removal performance without the use of a safety vessel and oil cooling circuits being directly positioned to the metallic liner. This task is solved in the thesis.

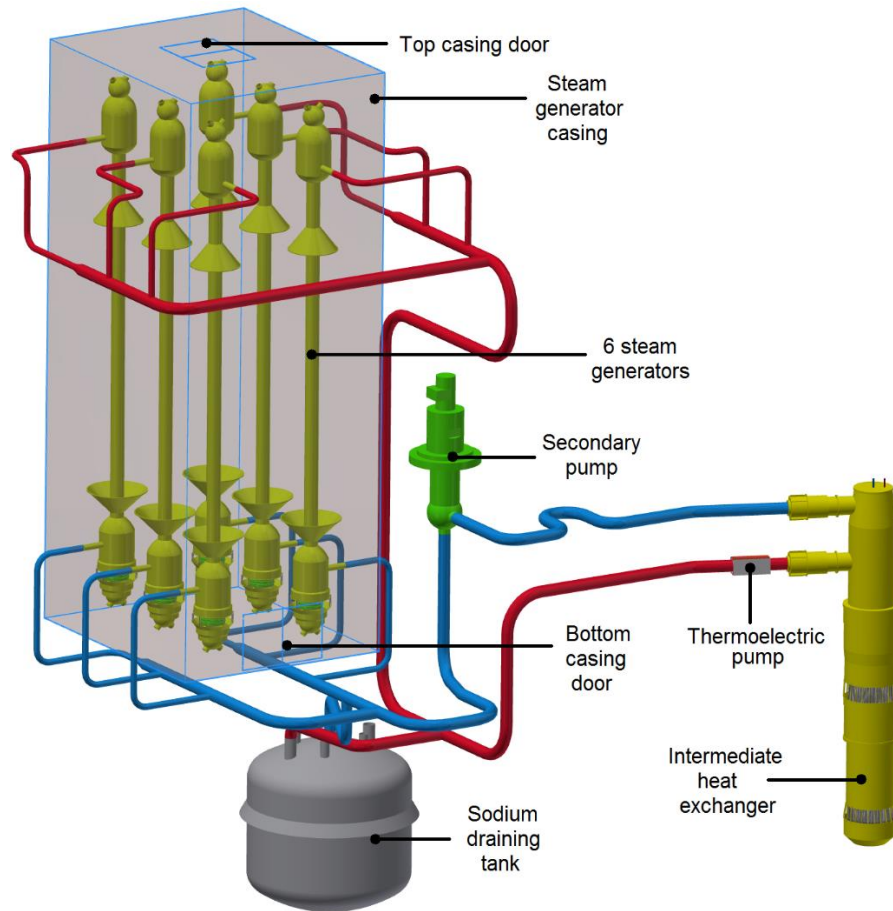


Figure 9. DHRS-2 related system components, integrated into the secondary circuit design

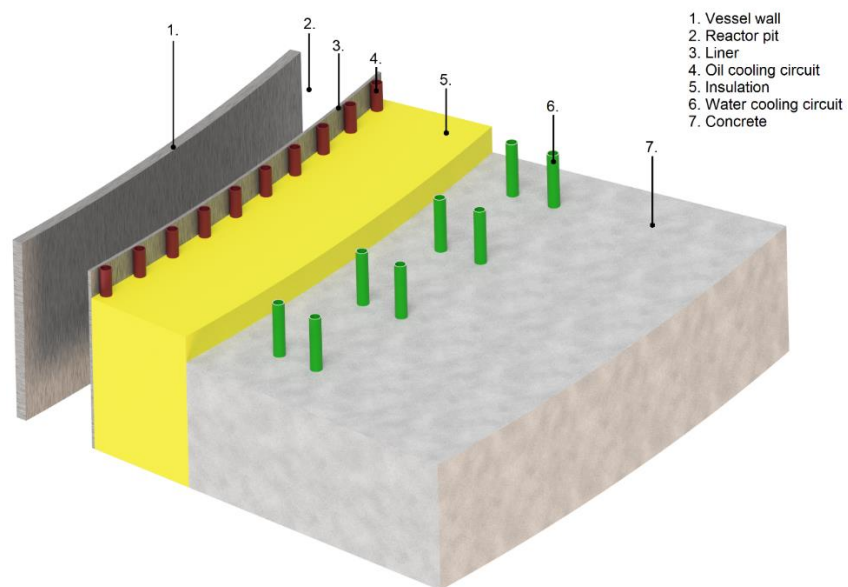


Figure 10. DHRS-3 concept with its oil and water circuits integrated into the reactor pit

1.3.2.5. Modified secondary system design

In traditional SFRs, there are long pipes with large bends to accommodate thermal expansion on the secondary sodium circuit. This layout causes problems related to the pipe fixing points as during earthquakes the pipes can get stuck in these points and potentially break. Moreover, this design involves higher chances of sodium leaks as the number of bends and the overall length of the circuit is large. In the Superphenix reactor feedback it is recorded that the flexible pipe design suffers the above mentioned problems during operation [10]. The sodium pipes on Superphenix had lyres to account for the thermal expansion between cold and operational states. These lyres resulted in large pipe lengths, which give rise to an overall large weight of the system, requiring supports in which the pipes would inevitably need to slide. This requirement opposes the anti-seismic standards, which would require the pipes to be firmly maintained during an earthquake. To fulfill both requirements, a rather complex system was installed, which could not perform as well as the engineers hoped for [10]. Besides, there were issues with the thermal insulation of the pipes, leading to difficulties in detecting sodium leaks, coupled with high number of false alarms during the operation [10][32]. Due to these negative feedbacks in terms of capital costs and safety, having the risk of rupture of the piping stuck in their support, in the ESFR-SMART concept an improved secondary circuit design is proposed with straight piping, using bellows for the accommodation of the thermal expansion. This option has been taken from the BN-1200 reactor, where this is the proposed solution for the secondary circuit design [33]. Thermal expansion compensating bellows have been already used in reactor components like Phenix heat exchanger but for the actual secondary circuit it has not been utilized so far, therefore further R&D is required to validate that the element can be used for such purpose also [34].

Following the design work of this updated secondary circuit, the effect on the DHRS performance has to be evaluated, as the shorter piping can affect the behavior of the system, especially in terms of the natural circulation establishment. Therefore, an updated model and new assessment of the systems are included in the presented research.

1.3.3. Containment safety function

In a traditional pool-type SFR, the primary circuit is enclosed with the main vessel, which is enclosed in another vessel called a guard or safety vessel. The safety vessel was mandatory requirement for SFR firstly because in case of the main vessel rupture the core and other primary components must stay immersed in sodium and secondly because the escaping coolant contacting the reactor pit concrete could cause a radioactive sodium fire which is an important safety concern. In the ESFR-SMART project, the option proposed in EFR has been followed, discussed within the DRHS-3 concept above, where the usage of such safety vessel was reconsidered and a modified design was used, showed in Figure 12 [8]. Within this concept, there is no the safety vessel, but the reactor pit is prepared to contain the leaking sodium in case of a severe accident. Instead of the safety vessel the pit design include a metallic liner on an insulation layer, which supposed to take over the safety vessel's function. Behind the insulation layer, the reactor pit concrete is located. The cooling of the reactor pit, to maintain the concrete temperature below 70 °C, is maintained with the DHRS-3, described previously.

As the DHRS-3 has the task mainly to cool the concrete of the reactor pit and keep it below the set limiting temperature, the assessment of this function is part of the current study, as it is directly related to the structural integrity of the reactor pit. More details are given in Section 1.3.2.4 “DHRS-3 design”.

There are further measures included in the ESR-SMART reactor concept, which were not assessed in this work but for consistency, as some of them belongs to the containment safety function, a list of these is provided below:

- An internal spent fuel storage space is included around the reactor core to cool the Inner and Outer core SAs taken out of the active core following their final irradiation cycle, similarly to the Phenix design.
- An in-vessel core catcher is included in the reactor under the core, made of molybdenum, as it is in the Russian BN-800 SFR, for the hypothetical accident with reactor core meltdown.
- A metallic roof of about 80 cm thickness is proposed to close the main vessel, based on the previous EFR project outcome, to increase neutron shielding capability and provide strong mechanical resistance. A mechanical seal is insuring the roof leak tightness at component penetrations (IHXs, primary pumps) and, in addition, these components are welded to the roof over their perimeters to assure total leak tightness during reactor operation, even in the most severe accidental cases. With the same objective, the tightness of the rotating plugs is assured by an eutectic seal frozen during reactor operation. These measures allow excluding the reactor dome and therefore gaining economical benefits.

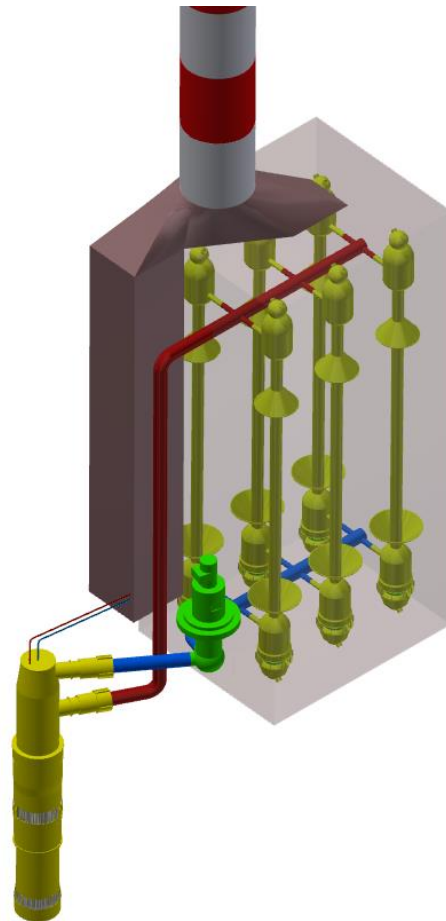


Figure 11. Secondary circuit design with straight tubes

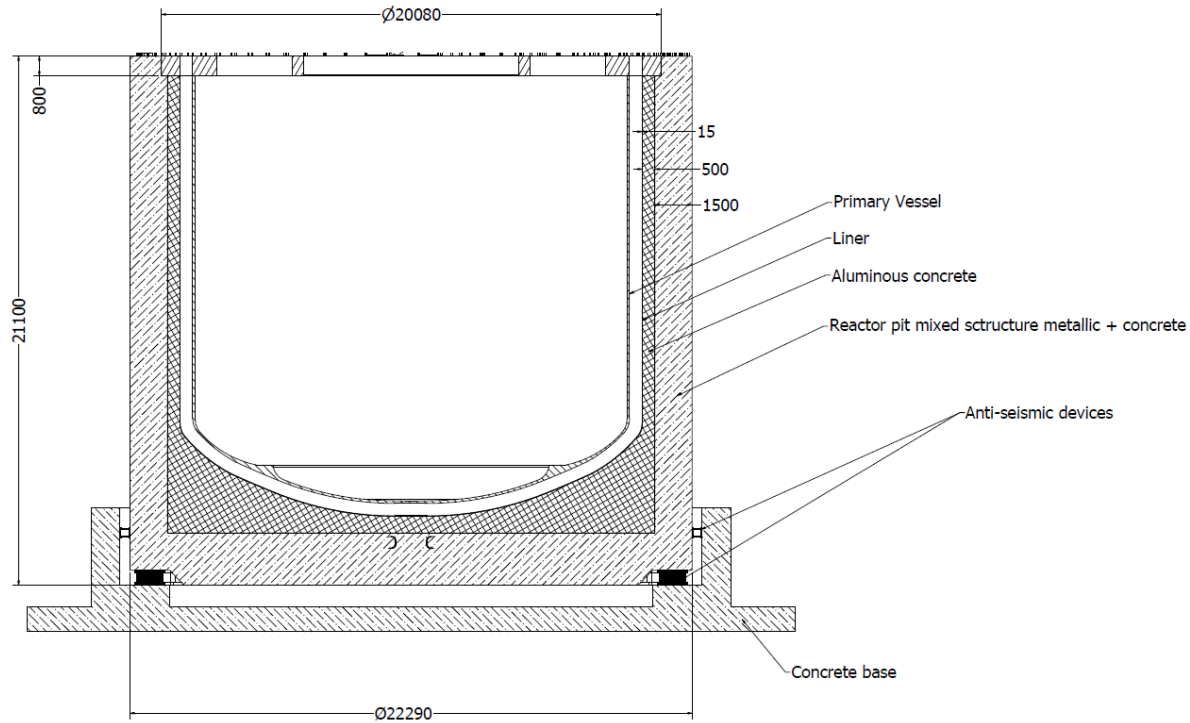


Figure 12. Dimensions and structure of the reactor pit design

1.4. Objectives

As presented in the previous Section (1.3), in the ESFR-SMART concept, the design development was built on the vast operating experience of previous SFR designs, aiming at synthesizing current state of the art SFR technological knowledge together with the optimization of the currently available technical solutions.

The present doctoral work was performed to contribute to the conceptual design development and safety assessment of a Gen IV SFR in frames of the EU ESFR-SMART project. The high-level objectives of the thesis are:

- Develop and when possible validate innovative methodologies for safety assessment of Gen IV SFRs, including creation of Computer-Aided Design drawings for the reactor components, coupled modeling of neutron transport using Monte Carlo and deterministic methods, core and system thermal hydraulics, including sodium single- and two-phase flows, and core thermal mechanics.
- Assess European Sodium Fast Reactor safety measures and more generally safety functions using the developed methodologies.

For the safety assessment of the conceptual design options, various tools have been used in the thesis. Some of these codes are already available for nuclear safety studies, such as the TRACE thermal-hydraulic system code, modified at PSI for SFR applications or Serpent 2 Monte Carlo code for neutronic analysis. Besides these codes, there are areas where further methodology development is performed or a completely new methodologies are established within the thesis.

To this end, the currently available coupled neutronic and thermal-hydraulic dynamic analysis tool (TRACE-PARCS) is further developed in the thesis by introducing a hybrid hybrid spatial kinetics sampling method for preparation of one-group cross sections, allowing acceleration of dynamic calculations.

Besides, a new core mechanics assessment methodology is developed and validated for accurate simulation of core deformation reactivity effect, supporting safety analysis of events resulting in core deformation. By doing so, the accuracy and scope of the safety assessment of SFRs is extended.

In the study, various new or optimized safety measures proposed in the ESFR-SMART project and related to the reactivity control, heat removal and containment safety functions are evaluated.

In this sense, the decay heat removal capability of the new DHRs is assessed, revealing if the applied design option is sufficient for long-term cooling of a commercial-size ESFR at a required temperature level under a protected accidental scenario in forced and natural convection conditions. By doing so, requirements for design modification are proposed where needed. Besides, the overall behavior of the ESFR is studied with the critical temperature evolutions, assessing the available safety margins at various components.

Lastly, perhaps the most penalizing accidental condition, an Unprotected Loss of Flow (ULOF) simulation, is performed, using the newly developed computational tools. This type of accident generally results in sodium boiling, as the flow is gradually reducing to natural convection level with a produced power level governed by the various reactivity feedback effects of the reactor. The aim of this exercise is to assess the low void effect core design in its capability to ensure safe reactor cool down under such conditions and to assess design improvements to further extend safety margins.

In connection to the sodium boiling phenomenon, the pressure spikes induced by sodium vapor collapse are assessed and their core deformation capability is estimated. By doing so, the SA bowing dynamic is analyzed, providing data for potential future design of an improved core restrain system. This SA bowing dynamic is compared to available Phenix experimental data from a negative reactivity event, during which the power has been registered, and the suspected cause for the event is SA flowering, which generally has a similar dynamic as the applied pressure spikes on the model. Furthermore, the core deformation related reactivity effect is evaluated, to see if it poses further threat to the reactor operation under ULOF.

1.5. Structure

The current doctoral thesis is organized into 5 Chapters.

Following the first Chapter, providing the introduction of the work, in Chapter 2 the methodologies of the research are presented. The Chapter starts with the description of the Computer-Aided Design tool and the various uses it has been applied to within the doctoral work. Following that, the description of the utilized TRACE thermal-hydraulic code is provided, showing the specificities required for the SFR safety analysis. The detailed TRACE model is also described, which was used later in Chapter 3 for the assessment. In the next Section, the various ways, used in the work, to calculate the reactor power during the accidental conditions are presented, namely the point kinetic method used in TRACE and the proposed new hybrid spatial kinetics sampling method. Lastly, a core mechanic methodology is described

in the final Section of the Chapter, with the verification and validation work used for the methodology development.

In Chapter 3, the heat removal safety function related analysis is given. The Chapter starts with the description of the various DHRSs in the design, giving further details compared to the description in Chapter 1. After that, the simulated accidental scenario is described, which was used for the DHRS assessment. The study starts with reference simulations, where no DHRS were modeled, to obtain the reactor behavior under such conditions. Thereafter, the various DHRS operation cases have been assessed, describing the performance and operational behavior of the units. In the second part of the Chapter, the previously mentioned study has been performed again, using an optimized secondary circuit design, thus the impact of the design modification on the plant and DHRS behavior has been assessed.

In chapter 4, the reactivity control safety function has been studied, using various SFR designs, utilizing the proposed advanced methodologies. In the first Section of the Chapter, a ULOF accidental condition has been simulated using a simplified version of the ESFR TRACE model. In the Section, the sodium boiling progression is analyzed and various approaches are studies to mitigate this effect. In the second Section, the proposed hybrid spatial kinetics sampling methodology is benchmarked against the established point kinetics method as part of a Superphenix ULOF transient simulation until boiling onset, as well as through a control rod movement transient calculation. Lastly, the proposed core mechanics methodology has been applied on the ESFR core, calculating the effect of a core deformation at various static deformed points. Finally, the same method was applied on the Phenix reactor core, simulating a transient core deformation using a sodium boiling like core deformation initiation.

Finally, in Chapter 5 the conclusions of the presented doctoral work are provided as well as the recommendations for future work.

CHAPTER 2

Methodologies of research

For the reactor analysis presented in this work, various computational codes and methodologies have been used to allow the multiphysics simulations necessary for the evaluation of such complex systems as a nuclear reactor. This chapter presents the main codes and methodologies which have been used for the safety assessment. In this sense, the description starts with the modeling method for the 3D reactor concept, followed by the different simulation tools description for the thermal-hydraulic, reactor neutron kinetics and core mechanics analysis.

2.1. CAD methodology

The concept of the ESFR reactor within the framework of the ESFR-SMART project was developed using a computer aided design (CAD) system. A full 3D model of the reactor was created with its primary, secondary, and tertiary systems. The methodology of CAD application allowed the precise pre-dimensioning of the reactor components and structures, and served as a tool for preparation of consistent inputs for different simulation tools.

The modeling was performed using the Autodesk Inventor 3D CAD software, which is developed by Autodesk Inc., for 3D design development, visualization, simulation and design documentation [35]. It allows to virtually build any product concept, e.g. a reactor, testing the fit and manufacturability before it is created physically.

The development of the ESFR conceptual design was considerably facilitated by use of the CAD system, while the design did undergo a number of changes and improvements through the whole project timeframe. The model development was initiated starting from the analysis of the design of ESFR reactor components, provided within the former CP-ESFR project [36], and considered a number of major improvements to achieve economical and safety goals, described in section 1.3.

The application of CAD for the development of the concept provided the following distinctive features:

- 1) Continues check of the components arrangement, i.e. that the constituent parts fit well into each other;
- 2) Quick update of the component dimensions and design features;
- 3) Dimensioning of the components basing on particular limitations and criteria.

The convenience and effectiveness of this approach can be demonstrated by an example for the modification of the secondary circuit design, where straight tubing with bellows was proposed instead of the previous long tubes with bends for thermal expansion. In this way, the minimum tube lengths were reached as all the connected elements were real time aligned according to the new design. Thus, potential inconsistencies could be seen and resolved immediately. Another example to the usefulness of the method is how the reactor pit sizing was achieved. The requirement was to have the pit as small as possible so that in case of a sodium leak from the main vessel, the sodium still remains at such height that

circulation can be maintained through the openings of the IHXs. On the other hand, enough space needs to be provided for a robot to perform the regular inspection of the vessel and liner surfaces. As the available sodium volume could be obtained from the model with high accuracy, the sizing of the pit could be precisely determined.

Overall, the developing environment of CAD allowed to minimize considerably the probability of error propagation into the conceptual design.

For the thesis work, it provided detailed input information for the following domains:

- 1) Within the thermal-hydraulics modeling, such data as the sodium volumes in the SAs, the volumes of the hot and cold plena, hydraulic diameters, flow areas, tube diameters, etc. were extracted directly with dedicated means of the CAD system and used for preparation of the complex thermal hydraulic model, thus following the design specifications in a very detailed way.
- 2) It also has a crucial role in the core mechanics studies, as the homogenized 3D model of the reactor core is prepared as input for the deformation calculations within the CAD software.
- 3) In the neutronic domain, following the core mechanic deformation calculations the deformed shape reactor geometry is processed directly for the Serpent 2 Monte Carlo simulation, in order to calculate the K_{eff} of the deformed shape core state.

In conclusion, the developed CAD model (briefly presented in Appendix B) contributed to nearly every analysis work within the project. It facilitated the creation of the database on materials and structure dimensions to be distributed to different partners, as well as providing parts of the 3D model for example for CFD analysis of the hot pool. With this, most of the parameters were calculated automatically avoiding an individual data preparation. Apart from the research domain, a very specific example, which was important for the project presentation, is noteworthy. The production of the movie on safety improvements proposed in ESFR-SMART became possible as the conceptual design drawings and 3D model of the reactor were available [37].

2.2. Thermal-hydraulic methodology

2.2.1 The TRACE code

To model the thermal hydraulic behavior of the ESFR reactor, the TRACE thermal hydraulic system code [38] was utilized. TRACE has been developed by the US NRC and was originally used as a best estimate tool for the analysis of steady state and transient behavior of light water reactors. It is a two-fluid, six equation thermal hydraulic code, having the capability to model both liquid and vapor phases of the coolant separately allowing accurate two-phase flow calculations.

In recent years, several modifications have been implemented at the Paul Scherrer Institut (PSI) [39] to extend the capabilities of the code simulating advanced fast reactors, i.e. SFRs. This capability has been extensively used in this work, as the analysis of DHRS systems performance and ULOF transient conditions was performed with the aid of this tool.

For the modeling of transient sodium boiling, the two-fluid model with new closure relations is used. The approach is based on the same main conservation equations as coded for two-phase water flow and modifies only the closure relations and equations-of-state. Particularly, the thermal physical two-phase properties of sodium are calculated according to [40]. The simplified two-phase sodium flow regime map used in the modified TRACE distinguishes single-phase liquid and single-phase vapor convection regimes with annular film boiling regime in-between. The following correlation is used to calculate the fraction of the perimeter wetted by liquid sodium for all regimes:

$$\eta = \frac{1}{1+500e^{250(\alpha-1)}} \quad (1)$$

where α represents the void fraction. This correlation predicts that η is equal to 1 for α less or equal to about 0.95 moreover, in the interval from 0.95 to 1 η is smoothly reducing to 0. For the dry-out criterion, the value of 0.957 was chosen according to the recommendation given in [41]. Thus, the η value describes a transition from the annular film boiling regime to the single-phase vapor convection regime. In the modified code, the Rehme model [42] is used for the liquid-to-wall friction factor calculation for the wire-wrapped bundles, whereas for all other configurations the Churchill model [43] is utilized. As for the vapor-to-wall friction factor calculation, it is achieved by using the Churchill model [43] for all configurations. In all cases, for the liquid phase the calculated friction factor is multiplied by the value of η whereas for the vapor phase by the value of $(1-\eta)$. Liquid-to-wall and vapor-to-wall heat exchange coefficients are evaluated based to the model described in [44] for the liquid phase whereas for the vapor phase the Dittus-Boelter model is used. The Interfacial area density evaluation is built on the geometrical representation of the annular film boiling pattern using the value of η in accordance with the SABENA code [45] and suggested in [41]. Similarly, the Interfacial heat transfer and friction coefficients calculation is performed as it is in the SABENA code [45] and suggested in [41]. A validation has been performed on incorporated sodium boiling model in TRACE, using the KNS-37 sodium boiling experiment, which has been reported in [46].

2.2.2. Development of the TRACE model of ESFR

Using the previously presented 3D CAD model, the reactor was reproduced in TRACE on a detailed manner to represent the operation of the power plant according to the designed specifications. The reactor model is built from 3D or 1D components such as vessel, pipe, valve, pump, etc. These units include the geometrical details from the corresponding components of the actual reactor design, according to the CAD drawings.

In Figure 13, the overview of the full TRACE model is given with all of its main components including the 1) primary, 2) secondary and 3) tertiary systems. In this detailed model, the primary system includes a vessel to which all the components are connected, such as the 3 primary pumps, the 6 IHXs, 12 vessel cooling pipes, 504 fuel assemblies, see Appendix B, Drawing.1. To each of the IHX, a secondary system is connected through a heat structure component. In the secondary system the secondary pump drives the sodium through the 6 SG units per circuit. Each SG unit is finally connected to a simplified tertiary system,

where constant feedwater flow is supplied and evaporated within a pipe, which is connected to the SG through a heat structure component.

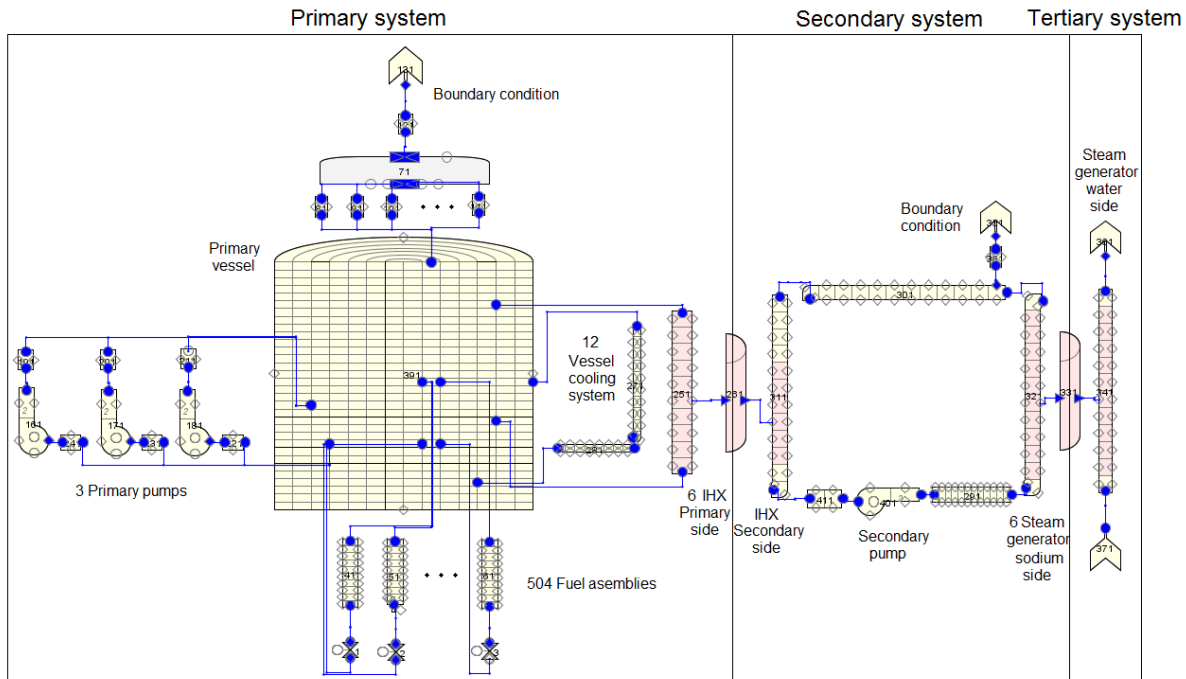


Figure 13. Schematic view of the ESRF modeling in the TRACE system code with its main circuits and components (Figure nodalization for visualization purposes only)

Within the primary system modeling, the reactor vessel is divided into 311 axial zones, 7 radial zones and 12 azimuthal zones, shown in Figure 14. The axial distribution was established according to the reactor core region nearly the whole height of the reactor vessel, allowing a detailed axial temperature distribution analysis throughout the whole reactor height. The 7 radial zones are distributed according to certain physical borders posed by the structures situated in the primary system, such as the reactor vessel wall, vessel cooling reservoir wall, inner vessel walls, which separates the hot and cold sodium pool, outer core region and inner core region boundaries. Azimuthally, the reactor was divided into 12 sections according to the components situated in the section. In this sense, one section includes an IHX, in the following section there is a pump component and beside that there is again an IHX, according to the actual design. Beside these three sections there is a fourth section which is filled with sodium. Due to symmetry this arrangement repeats three times adding up to the 12 section nodalization. It is of importance to mention, that for every zone specific flow characteristics, such as hydraulic diameter, porosity, flow perimeter and area were derived from the CAD model (see Section 2.1).

To model the reactor core, each of the 504 SA of the active core were modeled individually as 1D channel (pipe component), shown by the blue path lines at the middle of Figure 14. These channels have the geometry and flow parameters (flow areas, hydraulic diameters, etc.) calculated from the CAD model for every axial segment of the SA height (inlet and outlet sections, fuel rod bundle, sodium plenum, etc.). The bottom of the channel is connected to the vessel in the region which models the diagrid structure under the core. Between the vessel and channel connection a valve is situated to adjust the individual SA flow rate according to the power output and pre-specified cooling group (CG), thus modeling the physical orificing of the SAs. This adjustment is driven by control logic, set up in the model input, therefore it

automatically adjusts the valve flow area to the specific flow rate of a given CG group. In Figure 15, the 5 different CGs are shown, each group having its pre-specified flow rate. The outlet section of the channel is connected to the part of reactor vessel representing the hot plenum region.

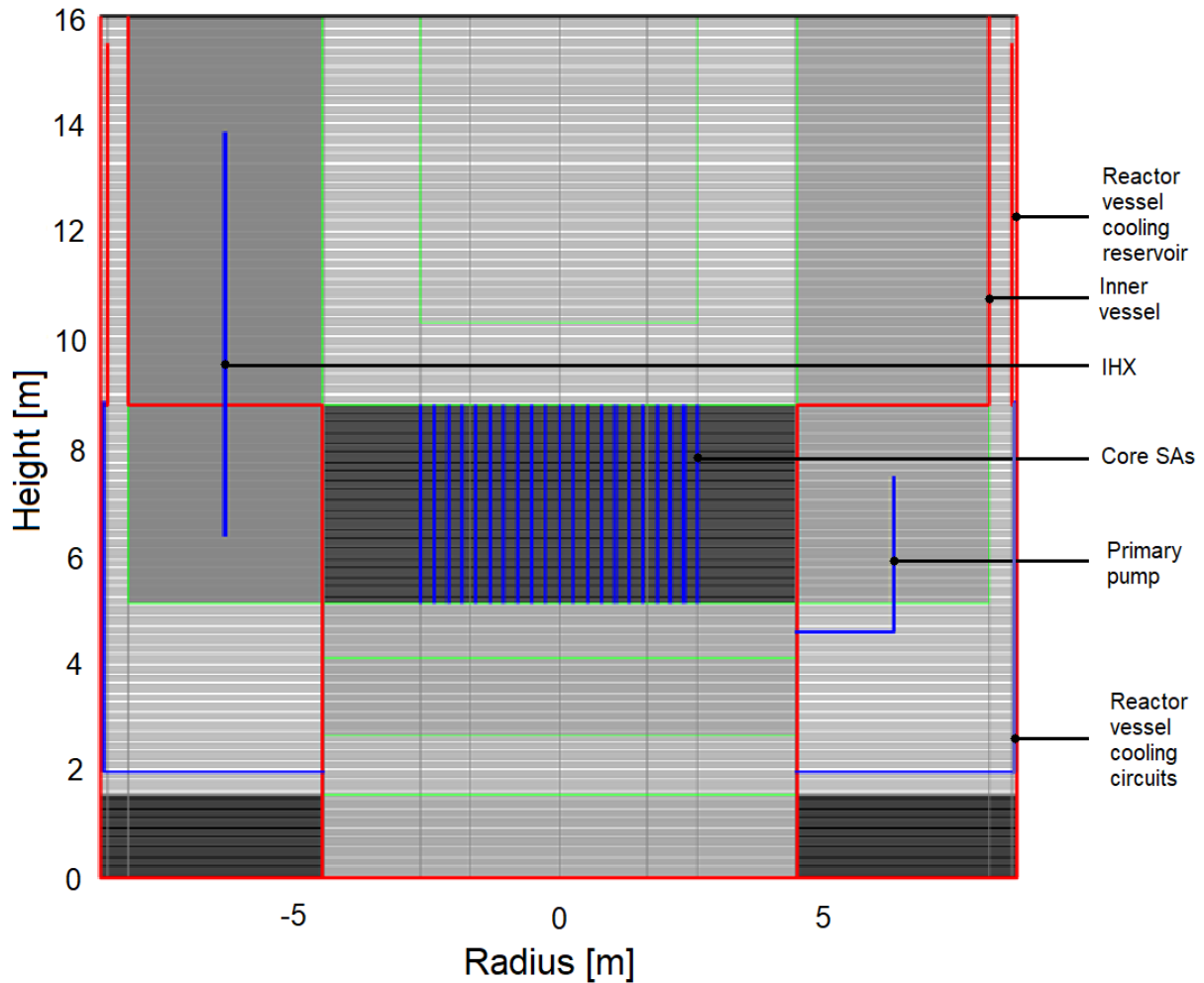


Figure 14. Radial and axial TRACE nodalization of the primary circuit of ESRF

The coolant flow through the primary circuit is delivered by the three primary pumps included in the model, shown in Figure 14. The total flowrate provided by the pumps in nominal conditions is ~ 19600 kg/s, equally distributed between the 3 pumps. This flow is then directed towards the part of the vessel which models the diagrid. From the diagrid the flow is distributed into 3 directions. The bulk of the sodium flows through the SAs of the reactor core to cool the fuel elements with ~ 18700 kg/s flow. Around 400 kg/s sodium is flowing into the inter SA gap, surrounding the SAs. Lastly, the rest of the sodium flow, ~ 500 kg/s, is directed downwards, supplying the vessel cooling system with cold sodium, shown in Figure 14.

As the hot, ~ 545 °C, sodium leaves the SAs, it enters into the hot pool part of the vessel, also containing the above core structure, where, at the top of the hot sodium, a pressure boundary condition is set to 0.15 MPa. The hot sodium is then enters the IHX, where the sodium cools down while it flows through a pipe component connected to the cold, ~ 395 °C, sodium pool of the vessel, from which the sodium enters

the pumps and the cycle repeats. Within the IHX the hot sodium is cooled, as they are in contact with the countercurrent secondary sodium flow through a pipe with a geometry corresponding to the 5022 tubes, defined in the CAD model. As it is shown in Figure 13, the heat transfer connection between the pipe with the primary and the secondary sodium is established with the use of a heat structure. For the steady state conditions the power evacuated from the primary system through the one IHX equals to 600 MW.

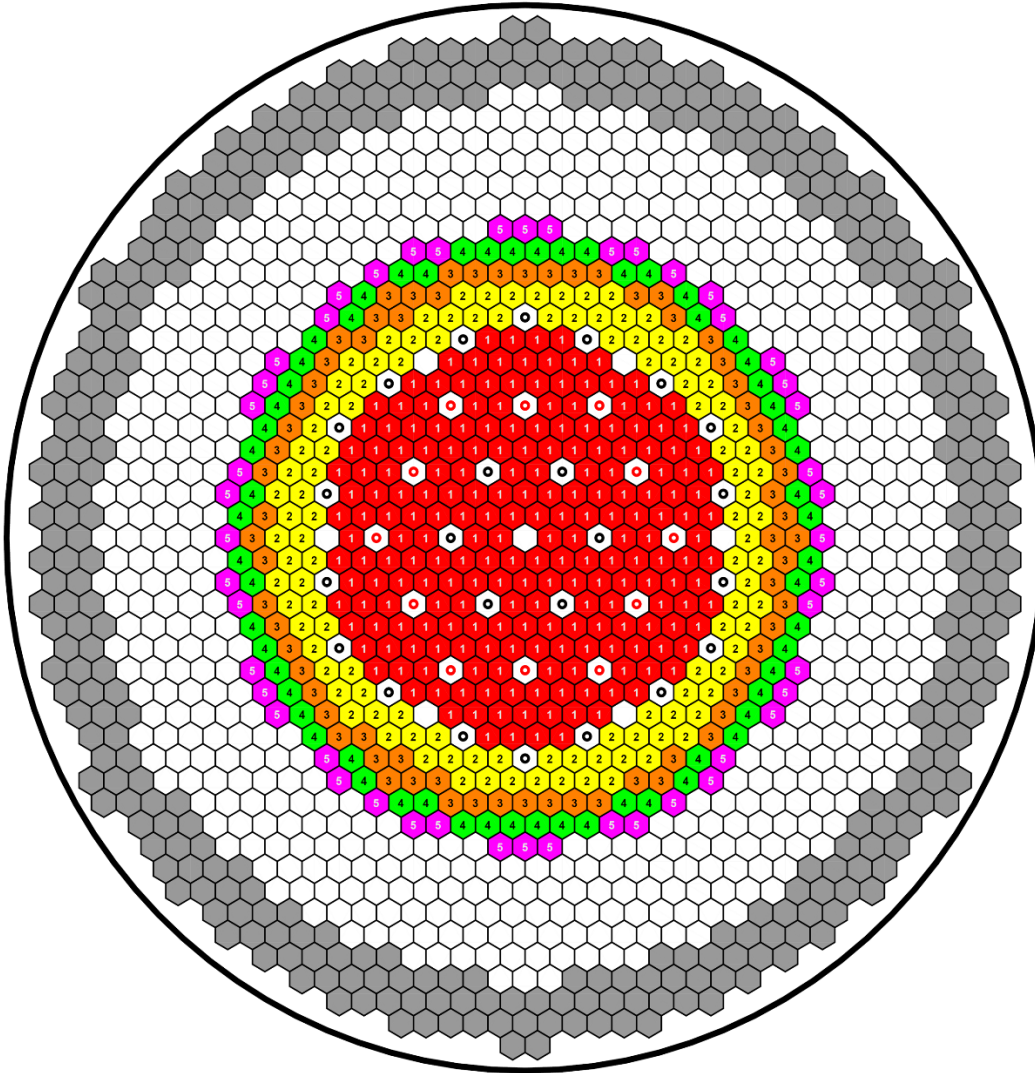


Figure 15. Cooling group arrangement within the reactor core

In each of the six secondary circuit, the sodium is pumped towards the SG units, with the pumping of ~ 2500 kg/s. At the highest elevation of the secondary circuit, at the SG connection, a pressure boundary condition of 0.1 MPa is established. The sodium temperature when it enters the SG is at $\sim 530^\circ\text{C}$, which is cooled to $\sim 345^\circ\text{C}$ as it flows through the SG unit, producing steam. The SG unit is modeled on the same way as the IHX, meaning that there is a countercurrent flow of sodium in one pipe and water in another. The pipe geometry for the water is set to account for the 364 water tubes.

The tertiary circuit is simulated in a simple fashion where a constant feedwater flow of ~ 48 kg/s is set to enter the water pipe. As the water turns into steam, it leaves the circuit via a pressure boundary condition of 18.5 MPa. For every secondary system, there are six of these SG units modeled with 100 MW nominal cooling capacity.

To heat up the sodium in the reactor and produce steam in the tertiary circuits, the core power was specified in time tables with a constant steady state power level of 3600 MW. The power distribution corresponding to the End-Of-Equilibrium-Cycle (EOEC) was obtained in neutronic simulations [47] with the Serpent 2 code. To reproduce the power distribution in the core accurately, each fuel SA has individual axial power profile derived from [47].

First, the model was tested to reproduce steady state conditions of the ESFR reactor, demonstrating targeted design performance. Next, the thermal-hydraulic model was extensively used for the evaluation of the DHRs implemented in the reactor design, for which the results are going to be presented in Chapter 3.

2.3. Neutronic methodology

In this work to determine the reactor power evolution during a ULOF transient two different approaches have been used: 1) the point kinetic approach, utilized for the ESFR ULOF transient simulation; and 2) a hybrid spatial kinetics sampling approach, which has been developed as part of the current work, applied on the Superphenix ULOF test exercise.

2.3.1. Point kinetics

The point kinetics approach [38] is the built-in method in TRACE to calculate the reactor power evolution in the course of a transient simulation. The method is based on solving the point reactor kinetic equations, with which the change in reactor power can be calculated through the separation of the space and time functions. The properties of the system is then averaged in energy, angle and space through the use of weighting functions and by solving the resulting ordinary differential equations the time behavior of the system can be evaluated. The space dependent perturbation of neutron density function is neglected in the model, only the amplitude variation is obtained [48]. Although the method has limitations in simulating certain transients with strong local perturbations, its capability for calculating ULOF, with sodium boiling in the core, has been presented in [49].

The required input parameters by TRACE for the calculation, are the kinetic parameters such as the effective delayed neutron fraction, delayed neutron decay constant, prompt neutron lifetime, etc. The reactivity variation vs time is also required as input and it is calculated, with the aid of the control logic developed in the model, based on the reactivity feedback coefficients.

The employed reactivity feedback coefficients and kinetic parameters were calculated using the Serpent 2 Monte Carlo code on the End of Equilibrium Cycle (EOEC) core state [23]. The following reactivity feedback effects were considered in the modeling (more details on the feedback coefficients are going to be given in Section 4.1.):

1) Fuel Doppler effect. In the model, individual Doppler constants were used in four different regions of the reactor core, allowing a detailed spatial representation of the reactivity effect related to fuel temperature change.

2) Core axial expansion. The axial core expansion was modeled by calculating the expansion of the cladding, under the assumption that at an EOEC core the cladding and fuel are in contact with each other, and the cladding temperature drives the axial core expansion.

3) CR position change. The effect considers change of the CR position in the core as a result of a number of counterbalancing effects, such as expansion of the CRDL, core support structure, vessel wall or other, depending on the design. In the current ESFR model, the CR position change in the core is calculated according to both the CRDL expansion, which is, in a simplified manner, considered to be driven by the temperature evolution of the outlet plenum, and variation of the fuel height due to the axial expansion of the fuel.

4) Core radial expansion (diagrid plate expansion). The core radial expansion is typically represented by SA pitch increase, as result of the temperature variation of the diagrid plate. In a simplified manner, the effect is linked to the core inlet temperature. For relatively short transient, i.e. ULOF, the effect may be neglected, as the inlet temperature is not affected considerably during the simulated time, while for the ULOHS transient, the negative reactivity due to diagrid expansion drives a significant power drop [50].

5) Sodium density effect including voiding. The sodium density related effect is modelled composed of two components. The first one is calculated based on the sodium density variation prior to boiling, and the second one relates to the contribution due to voiding. Traditionally, there is only one sodium reactivity coefficient used in point kinetics calculations for the whole range of sodium densities to obtain the reactivity effect during the transient. For more complex, low void effect reactor core designs, this approach is not sufficient as the effect in some regions is strongly non-linear on density. In a previous study [51], a new method was developed to account for this non-linearity of the density feedback coefficient, which is especially relevant for the sodium plenum region. This approach was also implemented in the current research accounting for the evolution of the sodium feedback coefficient with the following equation (2):

$$C_{Na} = C_{Na,Density} + (C_{Na,Void} - C_{Na,Density}) \times Void\ signal \quad (2)$$

where, C_{Na} is the overall sodium reactivity coefficient, $C_{Na,Density}$ is the sodium density coefficient, $C_{Na,Void}$ is the sodium void coefficient, and the *Void signal* is the void fraction within the node. The spatial distribution of every coefficient is given individually for each CG of the core, divided into 20 axial zones in the fuel region and 7 zones in the plenum region. Here, the fuel region refers to the fissile and fertile regions, together corresponding to the active core with a positive global contribution. The calculation is performed for every axial node in every SA with the corresponding coefficients, which are then summed together into a global sodium reactivity effect.

In the modeling, all reactivity effects are independent of each other, therefore, effects such as deterioration of fuel Doppler effect due to sodium voiding are not being considered in the simulation.

The above described point kinetic methodology is going to be used for the ULOF simulation of the ESFR core, presented in chapter 4.

2.3.2. Spatial kinetics

Within this study efforts were made for a hybrid stochastic-deterministic spatial kinetics (SK) method development using sampling XS correction technique (hybrid SK sampling), in which the advantages of the Monte Carlo methods, such as the possibility to simulate any arbitrary geometry with high level of fidelity, were combined with the computational speed of a nodal diffusion code [52]. With this method certain limitations of the previously presented point kinetic calculation scheme could be overcome, providing a way for more accurate neutronic results for cases where there is a strong spatially dependent perturbation in the reactor core, as for example a control rod ejection would be. Therefore, an effective way for coupled thermal-hydraulic/neutron kinetics reactor transient calculations is obtained, with increased application domain, compared to the thermal-hydraulic simulations with point kinetics power evolution.

For the method development, the Superphenix [10] reactor core was used, for which static calculations were performed, first with a reference calculation tool and later with the proposed hybrid SK sampling method comparing the results to determine the achieved accuracy. In the present work, Serpent 2 continuous energy multipurpose reactor physics Monte Carlo code, developed at the VTT Technical Research Center of Finland [53], was used as a reference calculation tool. Monte Carlo codes employ stochastic methods to obtain solution for the transport equation which means that particle interactions are tracked in the modeled system based on known probabilities or cross sections (XS).

There are various reasons why Serpent was chosen as the reference Monte Carlo code. Firstly, as previously demonstrated by several studies [54][55][56], it provides useful features such as the homogenized group XS data library generation which is necessary for the current work demonstration. Another relevant advantage of Serpent, reported in [57], is a relatively high performance in point of computational time, with respect to some other Monte Carlo codes (e.g. MCNP [58]). This superior feature is facilitated mainly by using two applied methods. First, Serpent uses Woodcock delta tracking method [53] in contrast to the usual ray tracing of the particles with which the free path length of the particle is recalculated every time it crosses a material region. Second, Serpent uses unionized energy grid which is reconstructed from the continuous energy cross sections in order to increase the speed of the calculation [53]. As a drawback of the latter method, there are higher requirements for memory usage which can be a potential issue for certain calculations, such as burnup calculations.

2.3.2.1. Methodology description

The developed calculation method compared to the reference Monte Carlo calculations was a nodal diffusion solver (PARCS) [59] coupled with the Sampling XS correction technique to adjust the transport XS in order to obtain results closer to the reference calculation. This adjustment assumed that Serpent does not calculate completely accurately the transport XSs [54][60], coupled with inaccuracies inherent to the diffusion approximation. In the proposed method, 1 energy group XS is generated for multiple axial layers for every SA of the reactor core separately. This procedure was developed as a response to a previous study [61], where it was shown that a 24 or 33 energy group XS, generated for only certain representative SAs, might not be always adequate for nodal diffusion calculations. This problem might not be valid for the currently analyzed reactor core as it is in the beginning of cycle stage, meaning that there is no big variation between the SAs material composition. Nevertheless, it is adequate to introduce the methodology of interest.

For the described methodology a script was developed, which initially conducts a base PARCS calculation. Following this first calculation, an initial multiplication factor is obtained together with the nodal flux values for the reactor core for each axial node of each SA. As a next step, differences between PARCS and Serpent fluxes are calculated (equation 3, 4). These flux and the multiplication factor values are then compared to the reference calculation, equation 5 and 6 respectively, to register the difference.

$$\Delta\phi_i = |\phi_i^P - \phi_i^S| \quad (3)$$

$$\mu = \frac{\sum_i^N \Delta\phi_i}{N} \quad (4)$$

Where ϕ_i^P and ϕ_i^S are the PARCS and Serpent flux values respectively for each zone, while N is the total number of the different zones.

$$\sigma_1 = \sqrt{\frac{\sum_i^N (\Delta\phi_i - \mu)^2}{N(N-1)}} \quad (5)$$

$$\sigma_2 = |k_{eff}^P - k_{eff}^S| \quad (6)$$

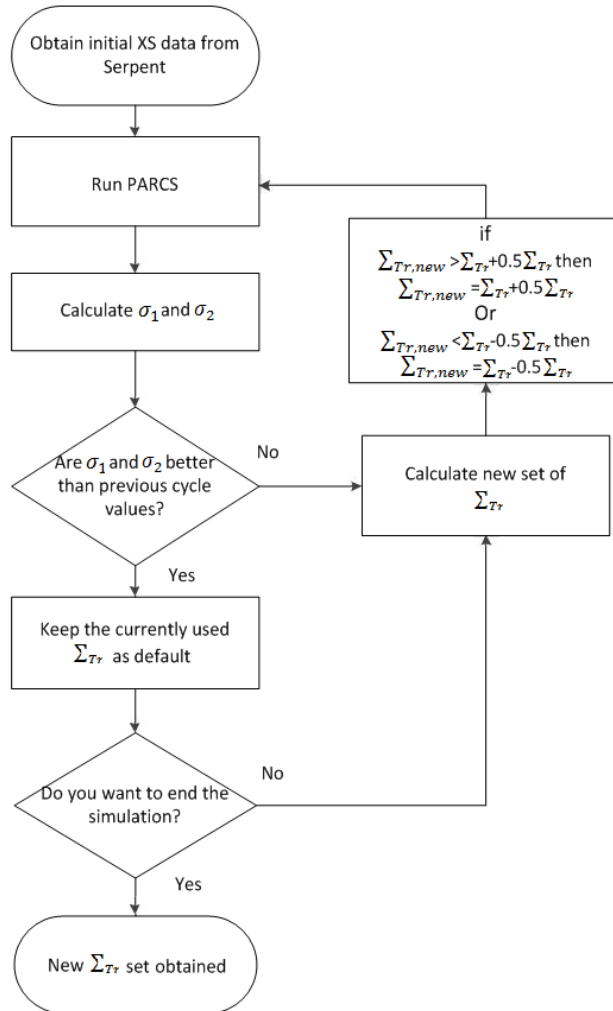


Figure 16. Simulation sequence of the Sampling method

Upon obtaining flux and multiplication factor deviation, σ_1 and σ_2 , the script randomly changes the transport cross section for each node with uniform distribution by a maximum of 1.5%, which is the limit between subsequent iterations, and runs again the simulation. This cycle continues until the end of the predetermined number of iterations, where, if σ_1 and σ_2 are reduced between subsequent iterations, the newly modified transport cross sections become the new default data for the next iteration. The total allowable transport XS change through all cycles cannot exceed 50% compared to the original Serpent value, which imposes a limit on the total change of the XS data. This calculation scheme is shown in Figure 16.

2.3.2.2. Reference SFR Superphenix core description

The current analysis uses the benchmark core model [62] of Superphenix, French sodium fast reactor core, which has been in operation in France from 1981 until 1996. The core at start-up configuration (fueled with fresh fuel) contains about 360 fissile fuel SAs and generates thermal power of 2990 MW resulting in electric power of 1240 MW.

The core model, with 120°-symmetry in plane, contains 7 different SA types. More specifically, there are 190 inner core, 168 outer core, 225 radial breeder blanket, 21 control rod, 3 shutdown rod, 18 diluent and 294 radial shielding SAs. The reactor was fed by MOX fuel where the fissile isotopes content in the inner and outer core region were about 16% and 19.7%, respectively. The axial structure of the fissile SA of inner and outer core and the fertile SA of radial breeder blanket is shown in Figure 17.

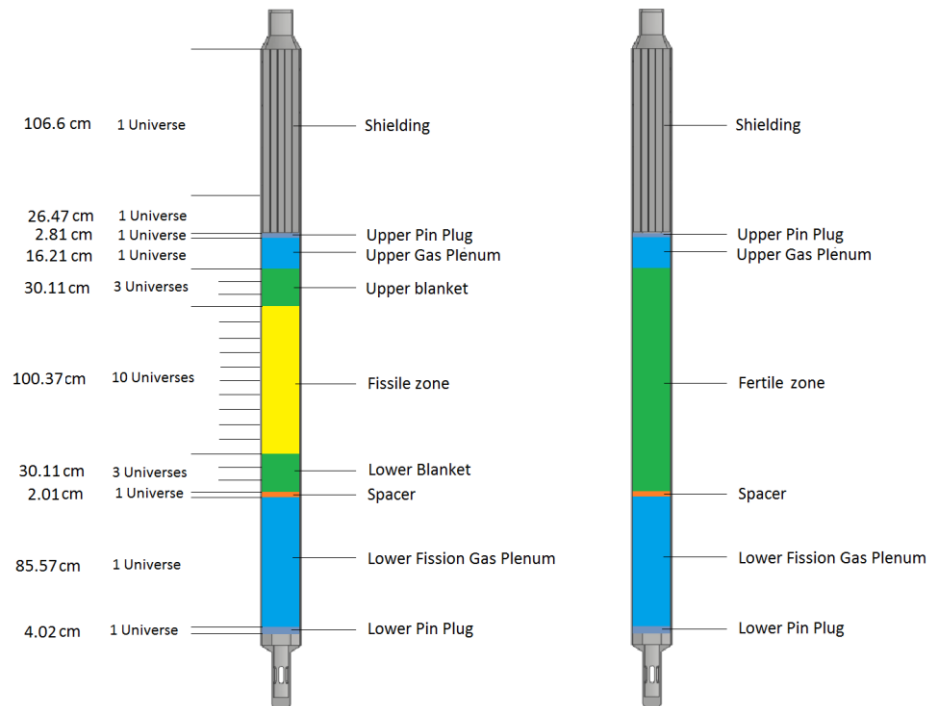


Figure 17. Fissile core (left) and radial breeder blanket (right) SA axial structure with Serpent universes

2.3.2.3. Description of the modeling

2.3.2.3.1. Serpent model

The Serpent model employed in the simulations is based on the reference critical core configuration, described in the benchmark assessment [62], where the control rods were inserted into the core by 400 mm, whereas the shutdown rods were completely withdrawn. For the requirements of present analysis, modifications have been introduced on the model, namely, the number of universes for which XSs are generated have been increased so that region-wise XSs could be obtained individually for number of axial layers of interest and all fuel SAs separately. Figure 17 shows the Serpent SA axial partitioning with the corresponding universes. The model dimensions correspond to the reference hot zero power (HZP) conditions assuming the core geometry at sodium inlet temperature of 673K [62].

Two additional configurations have been set up to model Doppler and sodium density reactivity feedback effects:

- 1) In the Serpent input, for the Doppler case, the XS library temperature of the fissile and fertile material isotopes was increased from 600K to 1500K.
- 2) To quantify the reactivity effect of the sodium density change, a sodium heat-up by 400K (increase of sodium temperature from the nominal 673K to 1073K) has been considered for all SAs of the inner core, outer core and radial breeder blanket in all axial regions corresponding to fuel height and above.

In the current modeling only these two feedback effects were considered, as the aim of the study was to demonstrate the efficiency of the proposed new method, rather than focusing on the accuracy of the reactor model. For an actual safety assessment, further and more detailed reactivity feedback effects are to be considered.

2.3.2.3.2. PARCS model

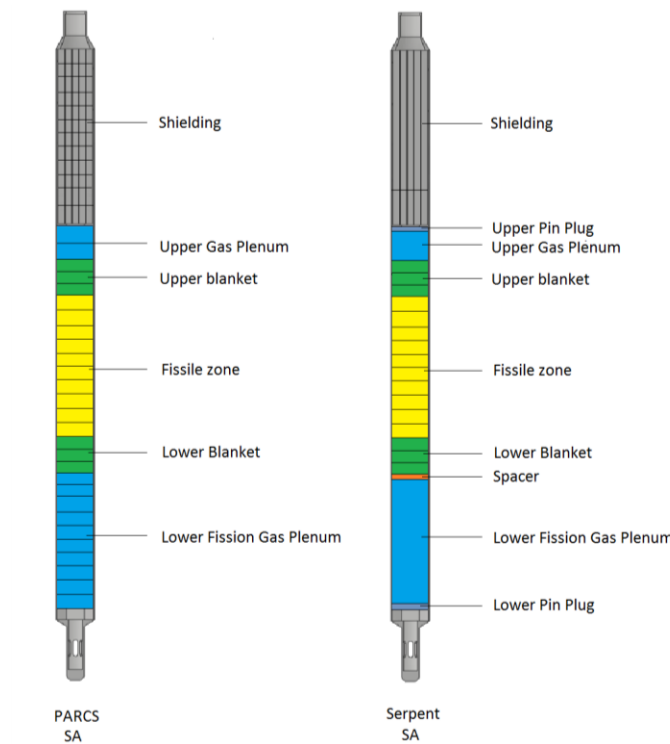


Figure 18. PARCS (left) vs Serpent (right) fuel SA geometry divisions

The PARCS model was created on basis of the Serpent core model ensuring a correspondence between them, applying some necessary simplifications. While the Serpent SA input employs a detailed axial structure containing various regions with several heights, some simplifications had to be applied on the PARCS model as unified axial mesh height had to be used for all SAs. In this sense, all the SAs are divided up into 40 axial layers with the node height of about 10 cm, Figure 18. In the radial direction, the calculation nodes of the model correspond to SA cells in the diagrid with the pitch equal to 18.02 cm following the same arrangement utilized in the Serpent model. As the core exhibits 120° symmetry, 307 SAs have been modeled, each with individual one-group homogenized XS for all calculation nodes.

2.3.2.4. Static calculation results

The sampling script (see Section 2.3.2.1) was set to run 10000 iterations for the XS adjustment process to ensure that the resultant transport XS set reproduces the Serpent simulation results as close as possible. It was found that most of the XS change happens in the first few 100 iterations as the results are converging to the reference value and further improvement in both multiplication factor and flux deviation is increasingly difficult. This provides a possibility to significantly decrease the time required for the process as only 1000 iterations includes ~98% of all XS changes in the current calculation. Considering ~5 s per iteration time requirement, the whole XS adjustment could be done in ~1.4 hours.

For the analysis three cases have been assessed: 1) the reference critical core configuration and two other cases, where the most important reactivity feedback effects have been included, 2) the Doppler and 3) sodium density feedback effects.

2.3.2.4.1. K_{eff} evaluation of the simulated cases

Table 5 presents the results of multiplication factors for different core configurations in reference Serpent and corresponding PARCS simulations. One of the criteria for accepting a new transport cross section in the method is that the difference between Serpent's and PARCS' k_{eff} values is reduced from a preceding iteration or being less than 7 pcm, therefore the reactivity difference between the results is small, between 1 and 7 pcm.

Core configuration	k_{eff} value		[pcm]
	Serpent (std=1.6pcm)	PARCS	
Reference critical, without cross section correction method	0.99895	1.00312	416
Reference critical	0.99895	0.99889	6
Doppler effect	0.98862	0.98857	5
Sodium density effect	0.99969	0.99970	1

Table 5. Serpent and PARCS multiplication factor comparison

From the 10000 repeating cycles performed by the hybrid SK sampling method for the optimal XS search, the number of successful iterations was around 400, Figure 19. The Figure shows that even when the

multiplication factor has converged to the Serpent value, within 7 pcm, after around 70 successful iterations, the difference between flux in PARCS nodes and flux in corresponding Serpent universes kept on decreasing. This indicates that other parameters than multiplication factor is also needed to be analyzed to obtain a representative picture on the performance of the correction method.

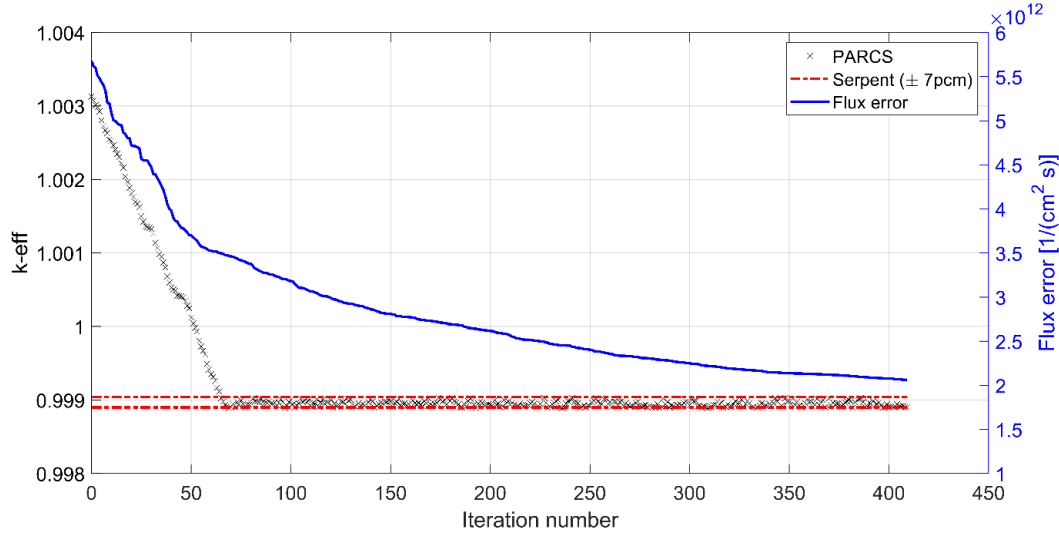


Figure 19. Convergence of the multiplication factor and error on flux from successive cycles when sampling method is utilized

2.3.2.4.2. Radial power map and relative error comparison of the simulated cases

To obtain a more illustrative picture on the performance of the hybrid SK sampling method, the radial power distribution of the core and the axial flux profile have been compared for some representative SAs between the two solutions. Figure 20 demonstrates the SA power map obtained for the reference critical core configuration with Serpent. The highest power SA are located between the periphery of the inner and outer core with the peaking SA power at around 10 MW. The power of the fissile SAs at the outer core periphery does not exceed 5-6 MW while the neighboring SAs, the radial breeder blanket, colored mainly in dark blue, have significantly lower power level, around 0.01 to 0.5 MW per SA.

In Figure 21, a power comparison is presented between the hybrid SK sampling and reference stochastic methods for the reference core configuration. A power peaking factor was introduced in the plots based on the inner and outer core power so that the deviations for the higher power SAs are pronounced to receive a higher importance. More specifically, as about 99% of the produced power comes from the inner and outer core of the reactor, a normalization factor has been introduced (equation 7) which has twofold effect. On the one hand, it pronounces the error on SAs with power higher than the average calculated from the inner and outer core (equation 8). On the other hand, it decreases the importance of the error values on the SAs under the average SA power, which could potentially show significant power deviation, especially for the lowest power periphery breeder SAs, whereas the absolute power difference is in the order of a kW. Thus, a more representative picture is obtained on the relative error of the hybrid SK sampling calculation.

$$P_{av}^P = \frac{\text{Total core power}}{\text{No. of power generating SAs}} \quad (7)$$

$$\text{Error} = \frac{(P^P - P^S)}{P^S} * \frac{P^P}{P_{av}^P} * 100 \quad (8)$$

Where P^S is the actual SA power obtained from the Serpent simulation, P^P is the SA power from the PARCS simulation and P_{av}^P is the average power calculated from the inner and outer core. After applying the aforementioned peaking factor on the figure, the highest relative power difference for the inner core is 1.36%. However, the biggest relative error is in the outer core region, close to the control rods and the region periphery with the value of 2.2%. While the utilization of the power peaking factor pronounces the error in the higher than average power zones, it decreased the error values in the lower power region to less than 0.1%, as only about 1% of the total power is produced in the breeder region.

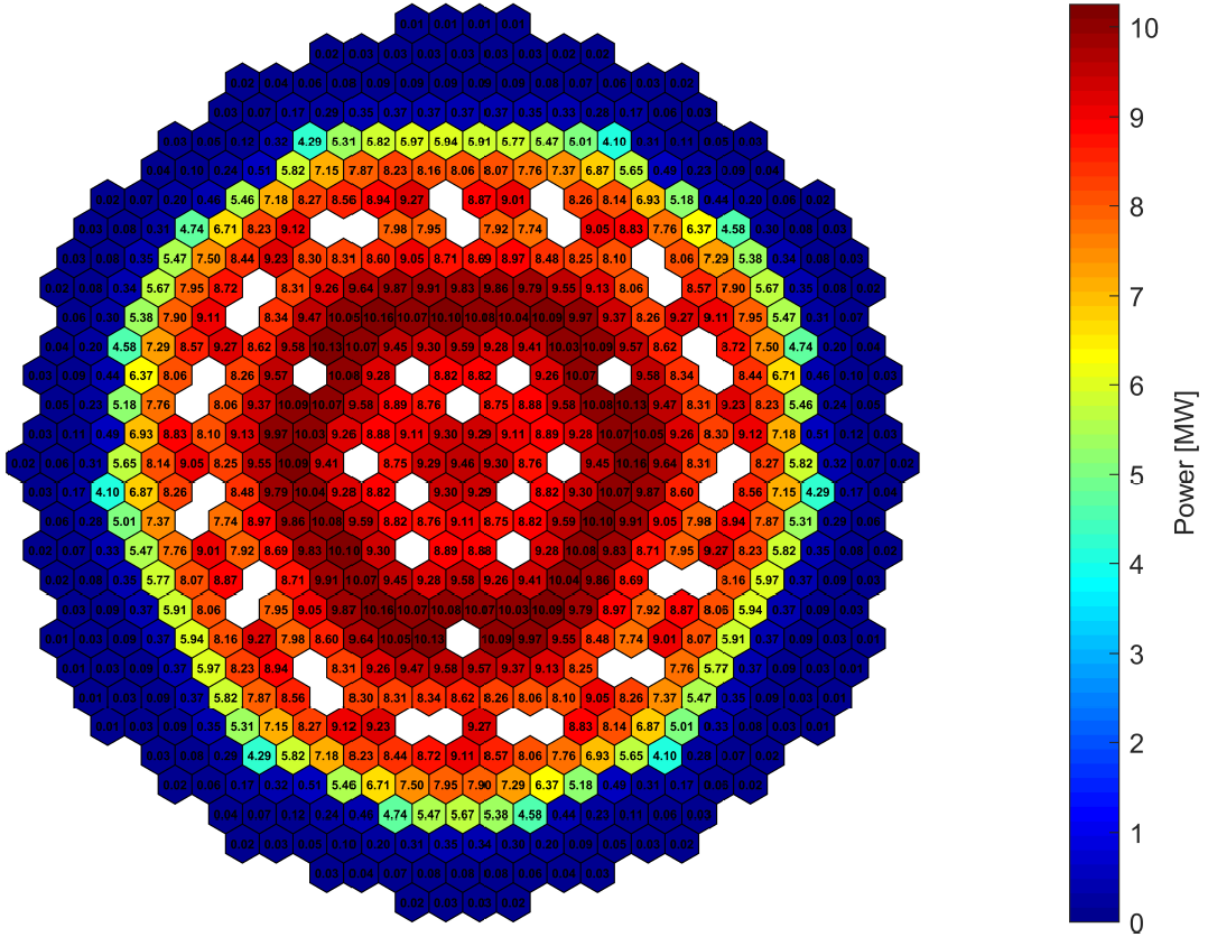


Figure 20. Serpent SA power map for reference critical configuration

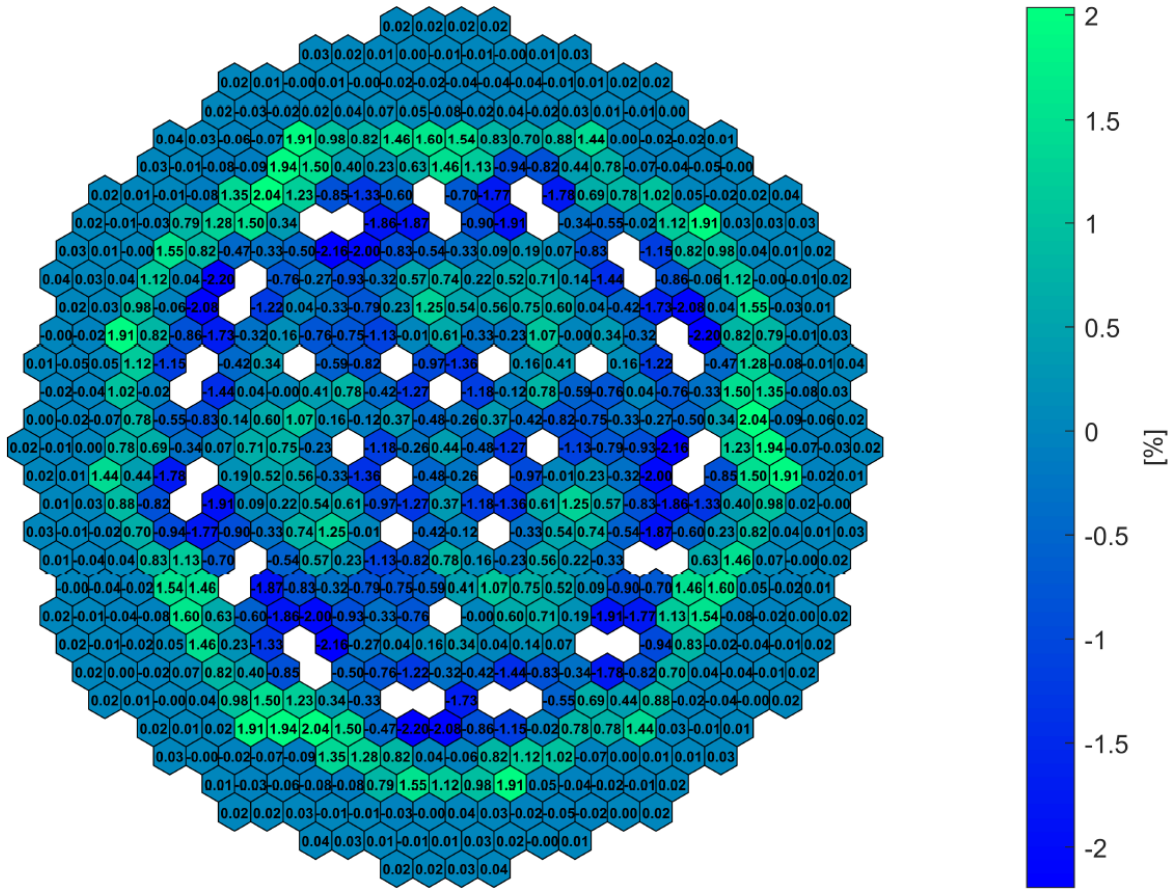


Figure 21. Relative SA power difference between PARCS and Serpent for reference critical configuration

In Figure 22, the relative SA power difference between the results of two solutions calculated for the sodium density case is depicted. Overall, the observed differences are close to each other for both the reference and the sodium density case. This similarity in the error range stays true for the modeled Doppler case also, which means that the perturbation applied on the reactor core does not have a significant effect on the accuracy obtained by using the hybrid SK sampling method.

Figure 23 illustrates relative SA power difference between PARCS and Serpent for the reference case when sampling was not used on the PARCS results. In the middle of the core, the Serpent SA power is up to 6% higher than that for PARCS which is significantly higher difference considering that it belongs to the highest power SAs. Another highly differing power region can be observed around the periphery of the outer core, close to the breeder region. Here the SA power is overestimated in PARCS by up to 5.5%. Considering this wave like power difference, it can be concluded that the PARCS results with the original cross section set does not follow well the power profile of the core. By comparing it to the original Serpent power map (Figure 20 or Figure 24), it can be seen that PARCS flattens the dips and peaks in the power distribution.

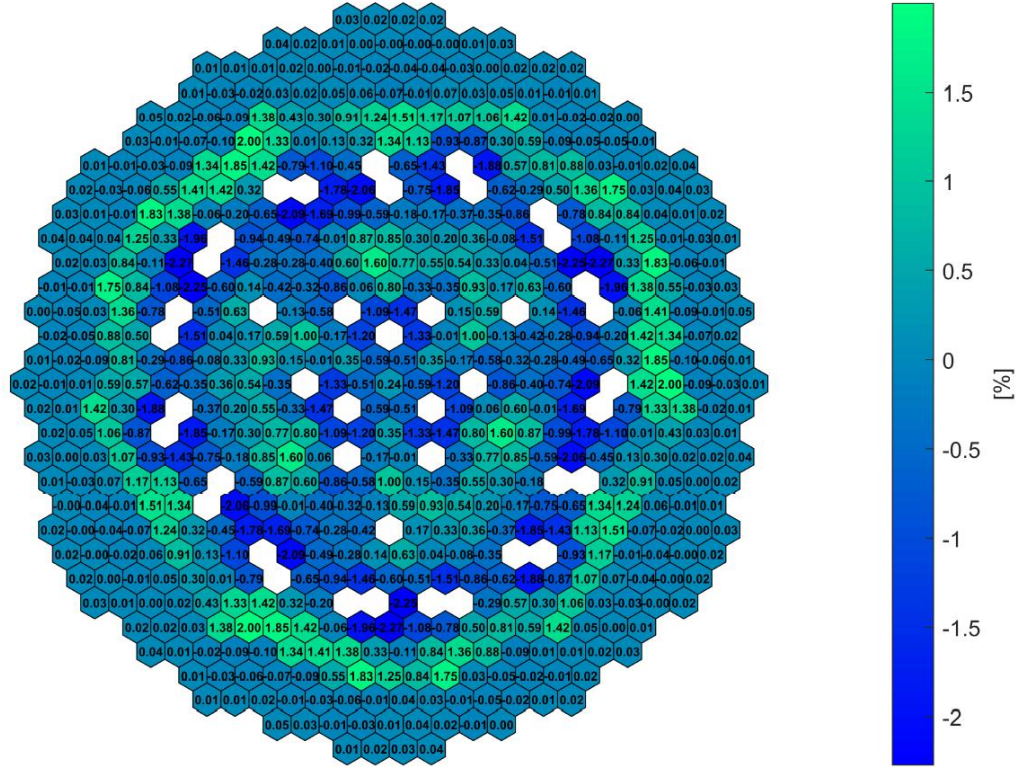


Figure 22. Relative SA power difference between PARCS and Serpent for sodium density case

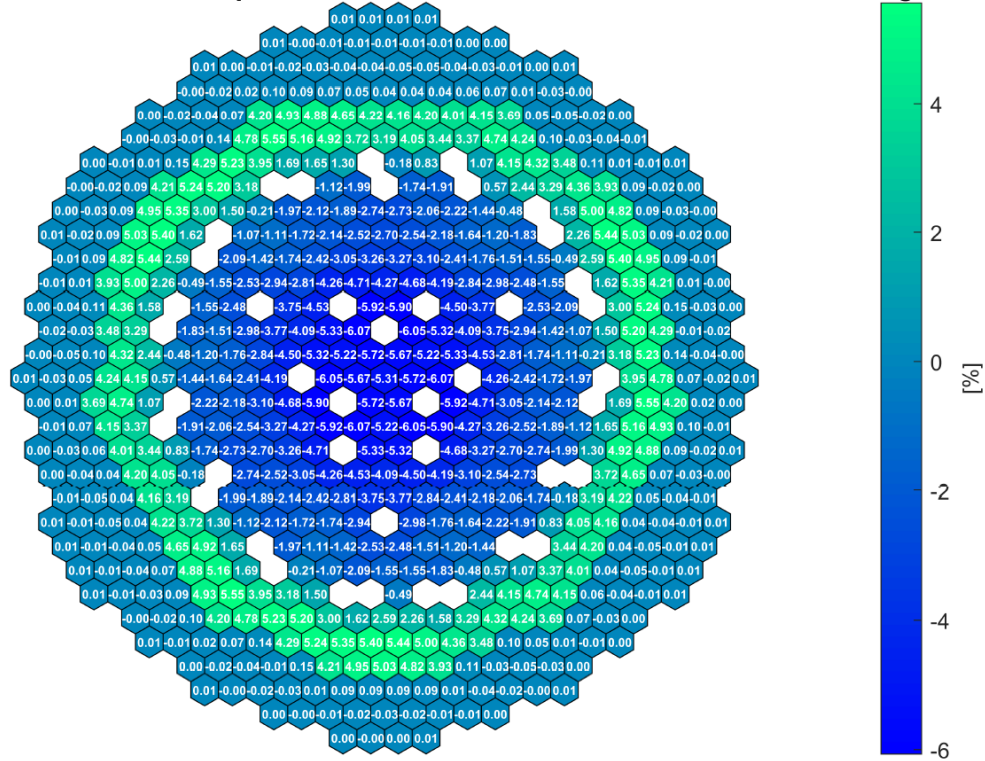


Figure 23. Relative SA power difference between PARCS and Serpent for critical configuration without the use of Sampling method

Figure 24 provides the radial distribution of SA powers. In this figure, as the core is 120° symmetric, the data for only one third of all SAs are plotted, according to the core radius where the SA is situated. Due to the presence of the control rods in the core, small dips in the power level can be observed around radius 50 and 150 cm. The SA power level noticeably decreases towards the periphery of the fissile core, reaching close to zero values at breeder region.

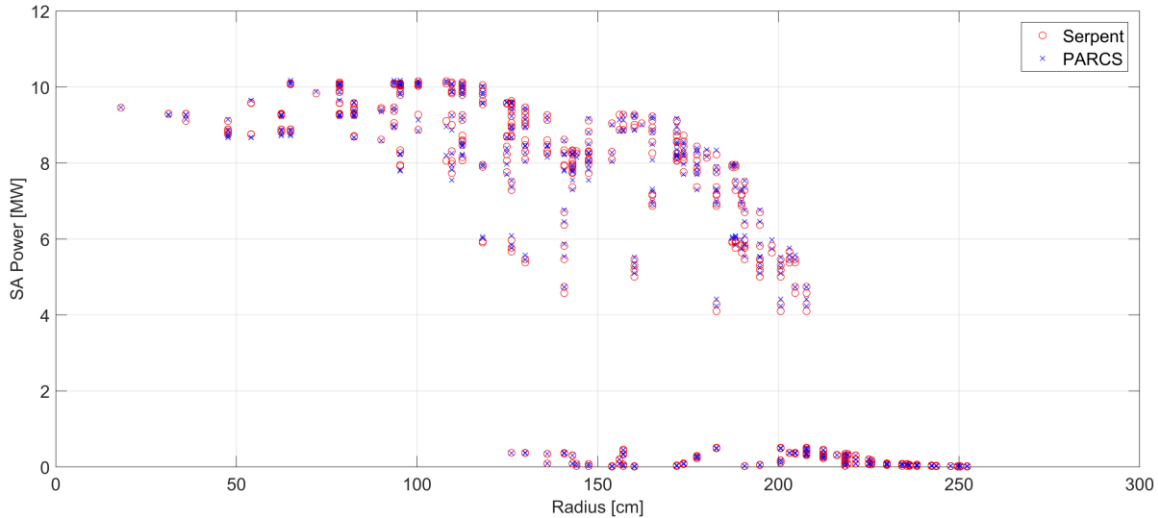


Figure 24. SA powers radius-wise radial distribution for reference case

2.3.2.4.3. Axial flux distribution evolution of inner core, outer core and breeder region SAs

Another important parameter which has been compared for the two solutions is the axial neutron flux profile. For the axial direction, the Serpent model was chosen to be the basis for the comparison as it had less many universes compared to the number of nodes established in the PARCS model. Meaning that where one Serpent universe contained more than one PARCS node, the fluxes in the adjacent nodes were averaged in PARCS and compared to the corresponding Serpent universe. Data for three different SAs are plotted in Figures 25-27 to assess the accuracy of corrected and uncorrected SK solutions compared to the reference Monte Carlo solution:

- 1) the inner core SA (Figure 25) is located adjacent to the central SA;
- 2) the outer core SA (Figure 26) is located at the inner-outer core periphery;
- 3) the breeder SA (Figure 27) is situated at the outer core-breeder region periphery.

From Figures 25-27 it is shown that by using the proposed hybrid SK sampling (PARCS Sampling) solution, the calculated flux profile for all 3 presented SAs are closer to the reference Monte Carlo solution, which is especially pronounced at the highest flux nodes of the models.

The static solution results show that the proposed methodology is capable of increasing the accuracy of the default solution of a nodal diffusion solver compared to a reference Monte Carlo simulation (another assessment using this method is given in Appendix C, applied on the China Experimental Fast Reactor (CEFR)). Based on this assessment, the method is going to be used for transient calculations for which its use was originally intended for TRACE-PARCS coupled calculations. The transient solution for a ULOF calculation, based on the same reactor core model, together with transient calculation with a spatially highly non-uniform perturbation, is going to be presented in Chapter 4.

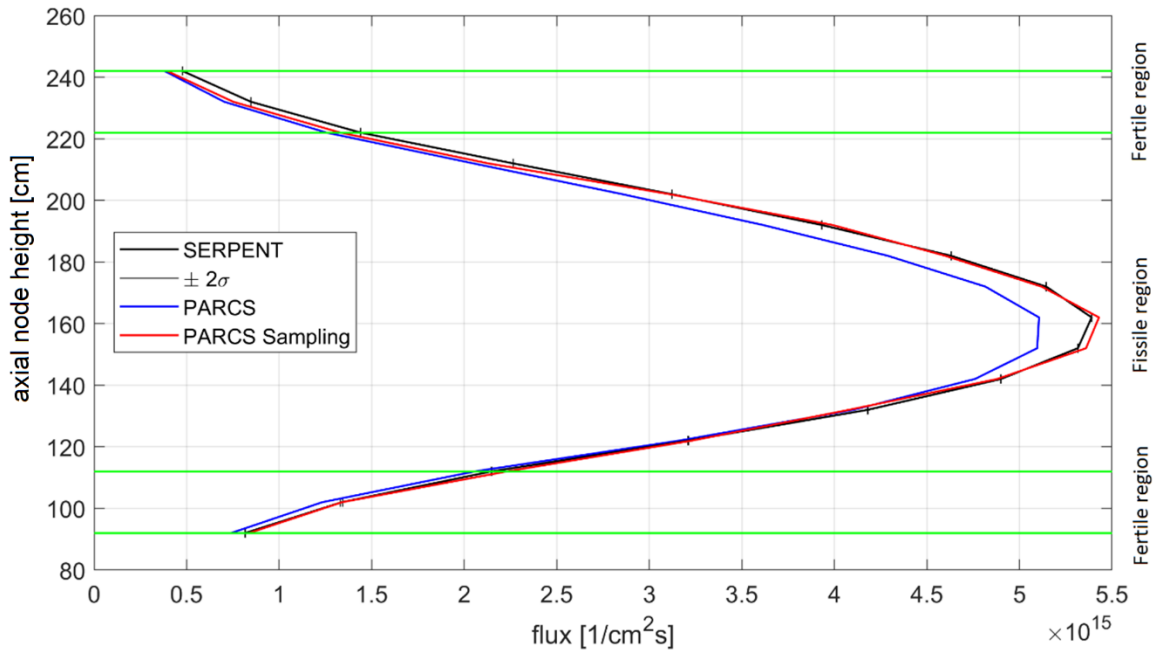


Figure 25. Inner fuel SA axial flux profile comparison between original PARCS and PARCS with sampling method

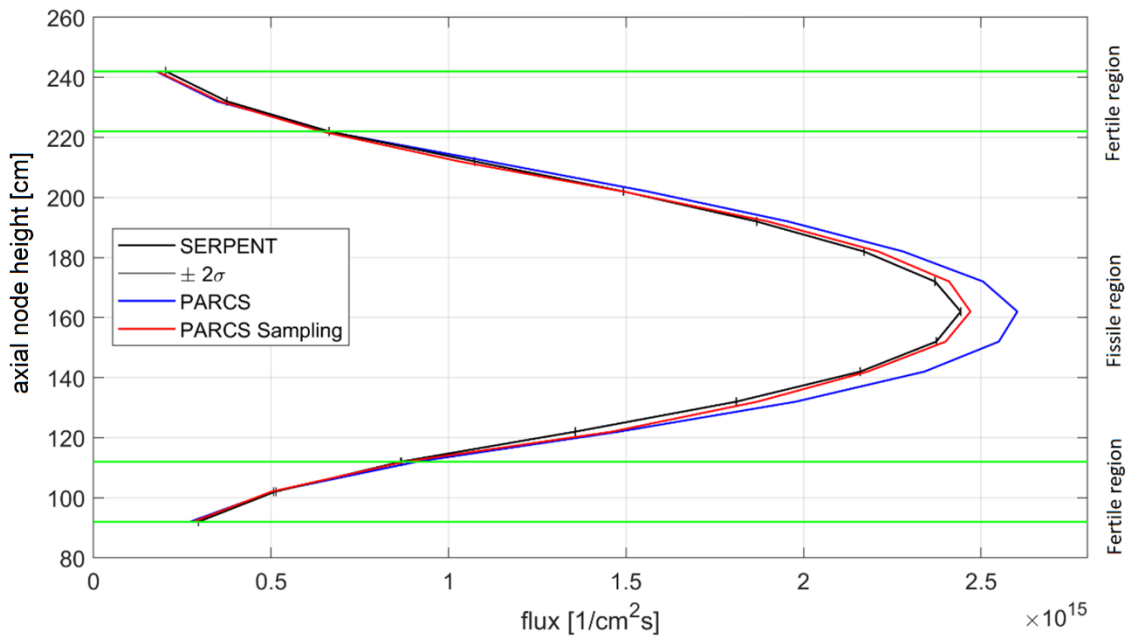


Figure 26. Outer fuel SA axial flux profile comparison between original PARCS and PARCS with sampling method

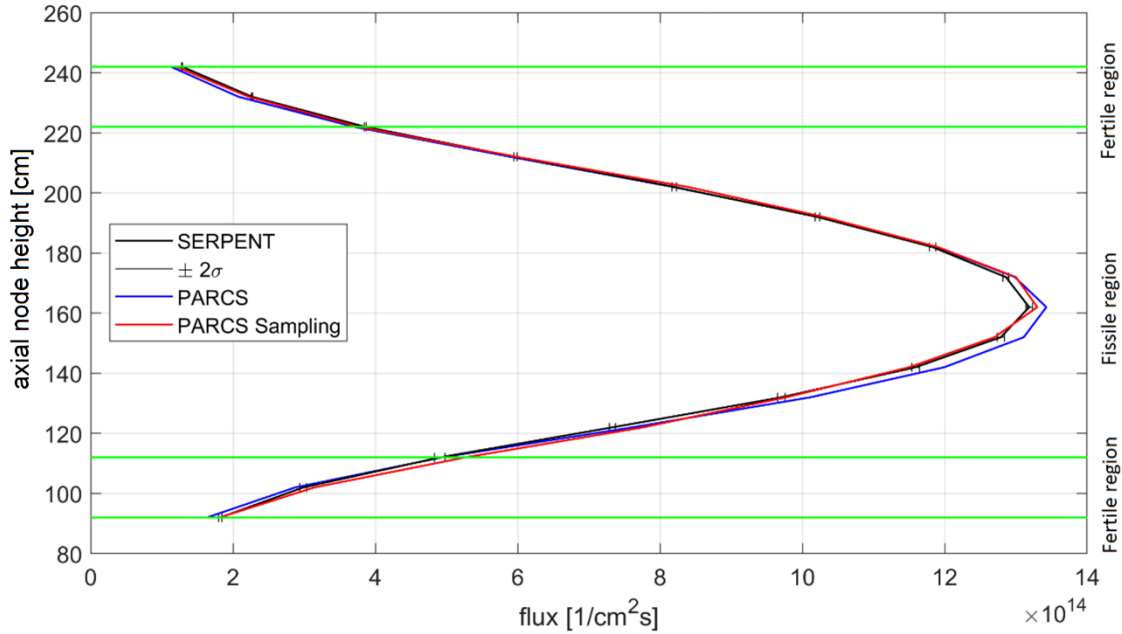


Figure 27. Breeder fuel SA axial flux profile comparison between original PARCS and PARCS with sampling method

2.4. Core mechanic methodology

In the past there have been reactivity incidents initiated by reactor core deformation, as it was described in Chapter 1, thus an improved core mechanical analysis tool is of interest for the calculation of non-uniform core deformation. Therefore, a new method is proposed to provide a tool for the quantification of the reactivity change due to fast transients in the reactor [63]. Within this new methodology the deformed core geometry is calculated with a finite element solver called Nastran, which is then used directly in the Serpent 2 Monte Carlo code to calculate the reactivity effect of the deformation. This approach allows a more realistic calculation of the deformed reactor core, as both radially and axially non-uniformly deformed core states can be simulated, where local perturbation sources are involved.

2.4.1. Methodology overview

The proposed method is based on two main steps to calculate the reactivity effect of any deformation of the reactor core (Figure 28):

- 1) The deformed geometry of the reactor core has to be calculated through a finite element solver (Autodesk Inventor Nastran) [35] with a non-linear transient response calculation option dynamically or statically, assuming different perturbation (load) scenarios;
- 2) After the deformed geometry has been obtained, it is used as input for Serpent 2 Monte Carlo code [60] with which static neutronic calculation is completed.

By repeating the second step for a number of deformations calculated in the first step, the effect of the core geometry change can be converted into a reactivity effect for each configuration. This can be done either 1) by using the obtained k_{eff} values from each static core deformation snapshot to calculate the reactivity effect at various time points or 2) by parametrizing cross sections with respect to the deformation field. Afterwards, the prepared reactivity states can be used by point or spatial kinetics solver to simulate the relevant transient conditions.

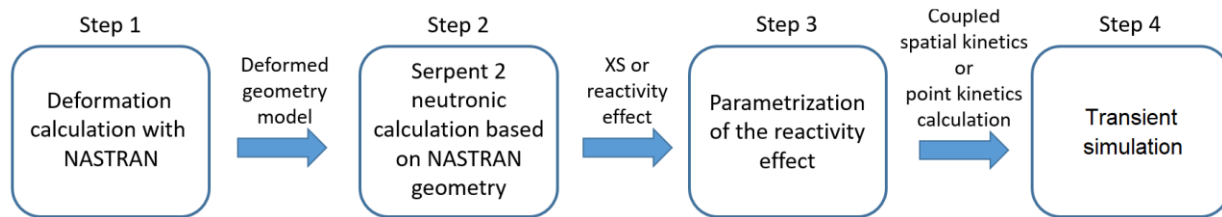


Figure 28. Main steps of core distortion conversion into reactivity effect

This non-uniform deformation approach is important for applications, such as the analysis of the effect of SA movement induced by local temperature gradients present in the reactor core and corresponding thermal stresses or by pressure peaks, e.g. resulting from local sodium evaporation and condensation. In the given methodology description, the static part of the procedure is introduced with specific attention to the sanity checks, verification and validation using the Phenix reactor end-of-life tests as the source of experimental results [64],[65]. The complete four-step procedure for transient calculations is shown in Chapter 4, where the method is applied in an attempt to reproduce an actual reactivity incident observed during the operation of the Phenix reactor.

2.4.2. Sanity check of the coupled methodology

Initially, to evaluate that the geometry, obtained from the finite element solver, is correctly modeled with the built-in interface of the Monte Carlo code, meaning, the unstructured mesh-based geometry is accurately created, a simple test has been performed. A dummy core has been created within the Monte Carlo code in two different ways. 1) The core geometry has been modeled with the traditional text-based input in comparison to 2) the geometry which has been obtained from the finite element solver without applying any load on the model, meaning that the output from the solver is a non-deformed geometry. Within this test, the dummy core consisted of 7 hexagon assemblies with the material composition of mixed oxide fuel (MOX) for the whole length of the SA, utilizing the JEFF-3.1.1 cross section library provided with the Serpent package [60] for the simulations. Figure 29 shows the geometry of the model, where the height of the modeled assemblies was 3500 mm and the face-to-face distance of the hexagons was 150 mm. Regarding the surroundings of the core model, there was a 5500 mm thick sodium reflector around the core to make the system leakage negligible. In the geometry, detectors were introduced to measure the neutron production rate in the core and the neutron absorption rate in the three out-of-core regions: below the core, above the core and at the core level.

As the second half of this evaluation, another comparison was prepared between a uniformly deformed and an equivalently non-uniformly deformed geometry by using the proposed methodology. The uniform deformation was approximated by taking the center of mass position of the non-uniformly deformed

assemblies and moving each SA to this corresponding new position. In this way, the gap between the assemblies is 4 mm for the undeformed option, whereas, for the uniform deformation option, it equals 7.15 mm. As for the non-uniformly deformed case, at the top of the SA the distance is 12.24 mm, while at the bottom, the original 4 mm was kept as the assemblies were fixed there. A schematic representation of the evaluated geometries is shown in Figure 30.

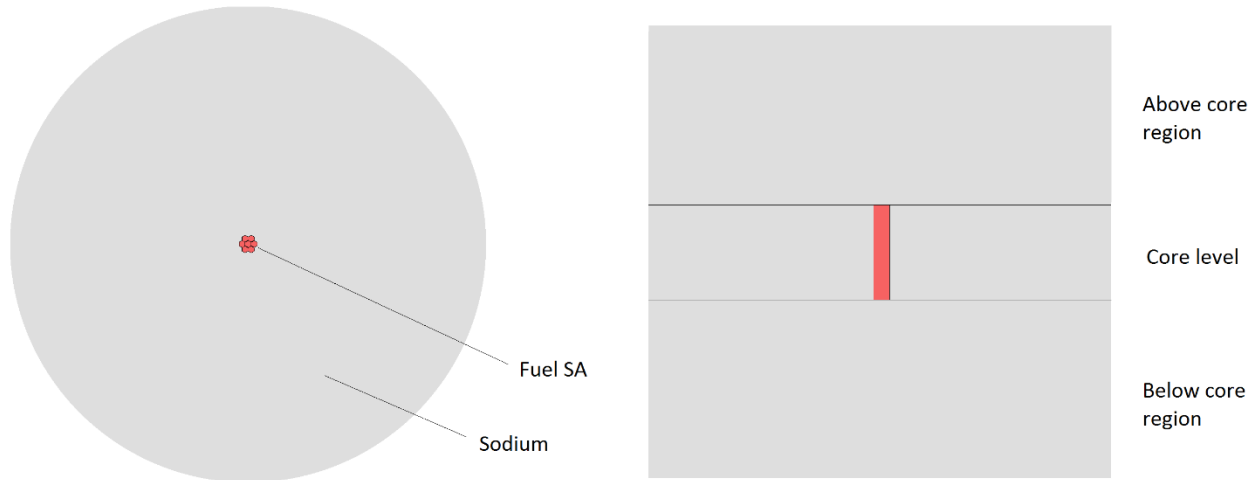


Figure 29. Geometry specification and detector region description of the 7-SA fuel bundle simulation

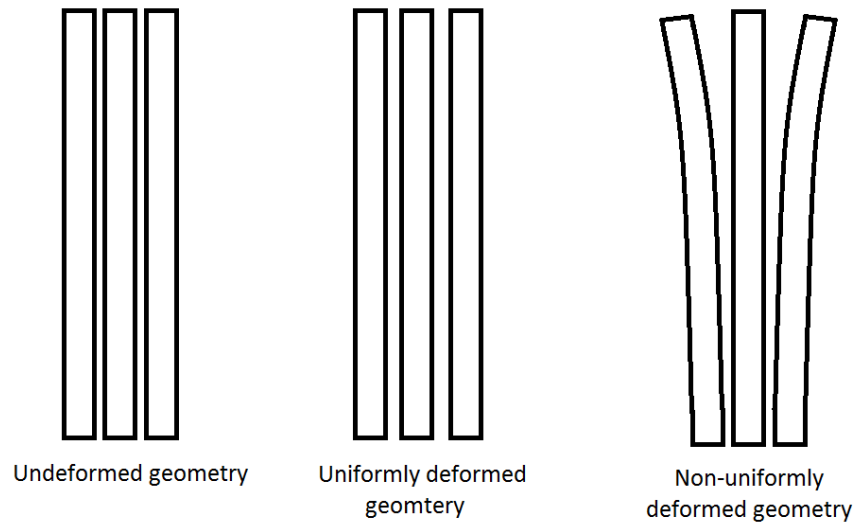


Figure 30. SA geometries for the production rate and absorption rate calculations

In Table 6 the outcomes of the previously mentioned calculations are presented. From the results of the two undeformed cases, it was confirmed that the Nastran model was read well by the Serpent interface as the results are close to equal between the text-based input and the finite element input models. Among two deformed cases, a difference is shown in the Table regarding the absorption rate below and above the core. For the uniformly deformed case, this absorption rate is symmetric, i.e. the absorption rates are equal below and above the assemblies. In contrast, for the non-uniformly deformed case, this symmetry is broken and there is a greater absorption below the reactor core. This can be explained by a change in

the axial neutron flux profile. Figure 31 shows this neutron flux profile shift toward the bottom of the assemblies which indicates that by opening the SA bundle at the top the neutron production drops there.

Set-up	Production	Absorption			
		Outside the core			In the core
		Below core	At core level	Above core	
Undeformed geometry from Nastran	1.40×10^{-3} $\pm 4 \times 10^{-8}$	6.44×10^{-5} $\pm 9 \times 10^{-9}$	3.50×10^{-4} $\pm 1 \times 10^{-8}$	6.44×10^{-5} $\pm 9 \times 10^{-9}$	9.13×10^{-4} $\pm 2 \times 10^{-8}$
Undeformed geometry from text-based input	1.40×10^{-3} $\pm 4 \times 10^{-8}$	6.44×10^{-5} $\pm 8 \times 10^{-9}$	3.50×10^{-4} $\pm 1 \times 10^{-8}$	6.44×10^{-5} $\pm 7 \times 10^{-9}$	9.13×10^{-4} $\pm 2 \times 10^{-8}$
Uniformly deformed geometry	1.37×10^{-3} $\pm 4 \times 10^{-8}$	6.44×10^{-5} $\pm 8 \times 10^{-9}$	3.49×10^{-4} $\pm 1 \times 10^{-8}$	6.44×10^{-5} $\pm 8 \times 10^{-9}$	8.97×10^{-4} $\pm 2 \times 10^{-8}$
Non-uniformly deformed geometry	1.38×10^{-3} $\pm 4 \times 10^{-8}$	7.02×10^{-5} $\pm 9 \times 10^{-9}$	3.49×10^{-4} $\pm 1 \times 10^{-8}$	5.85×10^{-5} $\pm 8 \times 10^{-9}$	9.00×10^{-4} $\pm 2 \times 10^{-8}$

Table 6. Production and absorption rate measurement for different geometry SA bundles calculated with Serpent and normalized to flux

The multiplication factor of the system was calculated and compared to the output value obtained from Serpent directly. To do this, Eq. 9 was used, where k_{eff} is the multiplication factor, P is the neutron production rate and A is the absorption rate (the leakage from the system is assumed negligible).

$$k_{eff} = \frac{P}{\Sigma A} \quad (9)$$

In Table 7, the calculated k_{eff} values are presented in comparison to the k_{eff} obtained directly from the Serpent output. In the analysis, for the calculated k_{eff} value, the neutron production and absorption rates were used for the estimation, obtained through specific detectors in the Monte Carlo code, to reproduce the value given by Serpent, as one number in the output. As the maximum deviation from the k_{eff} values is up to 11 pcm it was concluded that the obtained production and absorption rates consider the most important neutron producing and absorbing interactions. It also shows that as it was anticipated, the leakage rate is negligible as a sufficiently great size sodium volume was modeled surrounding the SA bundle. The k_{eff} calculation revealed an interesting phenomenon, meaning that there is an effect in case of uniformly deformed geometry is about 100 pcm (~17%) stronger than the one for non-uniform case. This can be explained by the fact, that as the neutron flux distribution is shifted closer to the bottom of the SAs, where the overall deformation is lower, the neutron energy spectrum is harder (more compact fuel region). Thus, the rate of neutron production is increased compared to the rate of absorption. Although this difference might be pointing towards the increased accuracy of a non-uniformly deformed geometry model, it has to be underlined that the modeled SA bundle consists only of fissile material composition, which perhaps enhances the reactivity effect of the deformation. It also needs to be mentioned that an SA volume check has been prepared to ensure the consistency of the fissile material mass before and after the deformation by the finite element model. From this measurement, the resulting change is $7 \times 10^{-6} \%$, corresponding to about 0.4 g of mass change in a 5.3 t SA bundle, which can be considered negligible.

Set-up	Serpent calculated k_{eff} (Std: 1.6 pcm)	Calculated k_{eff} (Std: 3.5 pcm)	k_{eff}
Undeformed geometry from Nastran	1.00446	1.00453	0.00007
Undeformed geometry from text-based input	1.00449	1.00456	0.00007
Uniformly deformed geometry	0.99758	0.99769	0.00011
Non-uniformly deformed geometry	0.99853	0.99863	0.00010

Table 7. k_{eff} comparison between direct Serpent output and calculation from neutron production and absorption rate

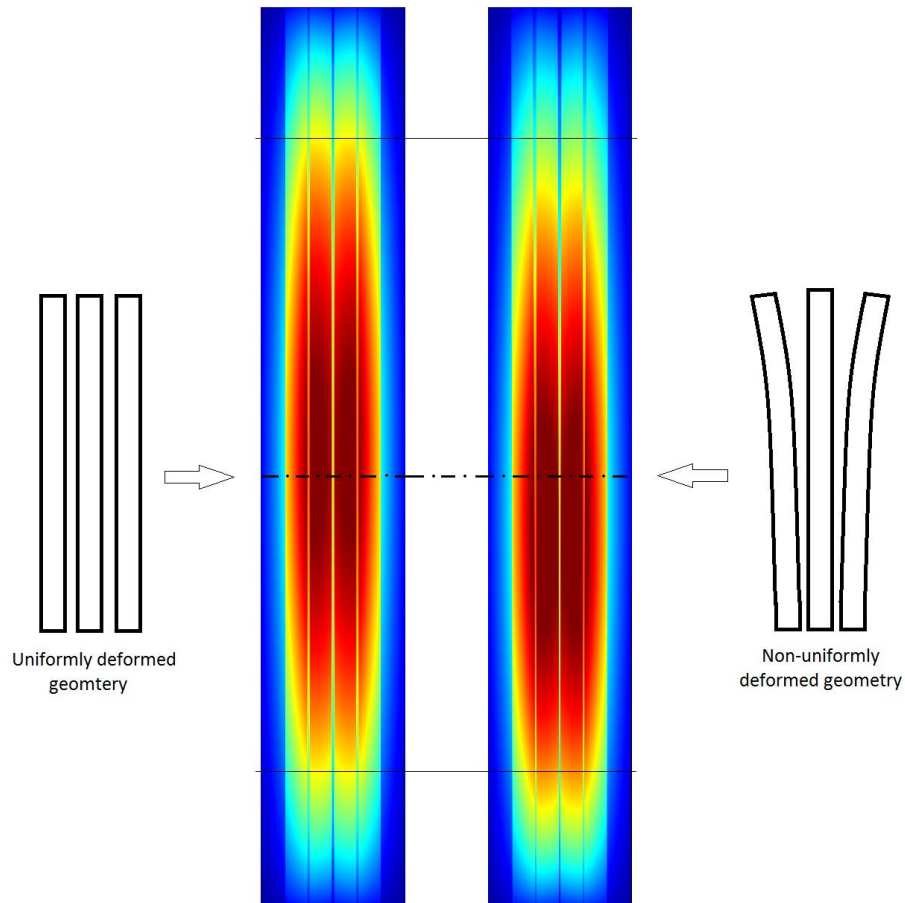


Figure 31. Axial neutron flux profile shift between uniformly and non-uniformly deformed assemblies (hotter color corresponds to higher flux)

2.4.3. Verification of the mechanics part

A verification case has been performed in support of the methodology. This verification consisted of a cantilever beam deformation. This cantilever beam problem refers to a hexagonal beam being fixed with a constraint at the bottom of the beam and a force is applied at the top of the beam, see in Figure 32. By using this problem definition, an analytical solution could be obtained through the following equation (10) [66]:

$$\Delta x = \frac{F}{6EI} (z^3 - 3Lz^2) \quad (10)$$

where F is the force applied on the beam, E is the Young modulus of the beam material, L is the length of the beam, z is the position of the applied force and I is the moment of inertia along the x axis.

For the verification of the model, the above-mentioned analytical solution was compared to the simulation results of the same problem.

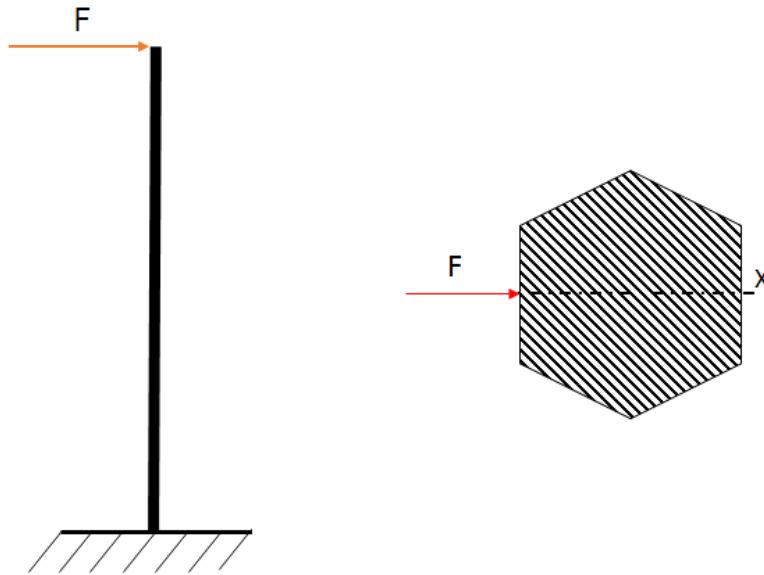


Figure 32. Cantilever beam example, side view (left) and cross-sectional view (right)

The results of the verification case are shown in Table 8. The analytical solution has been calculated for two example cases, where forces of 5000 N and 1000 N have been applied on a hexagonal SA. This hexagonal SA had a face-to-face distance of 150 mm and a height of 3500 mm. These analytical solutions were compared to the solution for the same problem calculated by the finite element solver. Moreover, to check the sensitivity of the method on the mesh size of the finite element model, different meshes have been used for the same calculation. From the results, even by using the coarsest mesh, it provides a good agreement to the analytical solution, having a relative error of around 1%, which drops to around 0.34% for the most refined mesh. Based on this comparison, the finite element solver calculates well the deformation of one SA and for the best computational performance, the mesh size equal to the face-to-face distance of the hexagonal wrapper tube can be used.

Finite element mesh size [mm]	Deformation [mm]		Error relative to analytical solution [%]	
	F=5000 N	F=1000 N	F=5000 N	F=1000 N
150	11.583	2.317	1.03	1.03
50	11.656	2.331	0.41	0.42
25	11.661	2.332	0.36	0.38
5	11.664	2.333	0.34	0.34
Analytical solution	11.704	2.341	-	-

Table 8. Verification results and sensitivity analysis on the mesh size of the finite element simulation

2.4.4. Validation of the coupled methodology

For the validation of the proposed core mechanics methodology, the Phenix end-of-life experimental measurement data was chosen, which has been published in references [64] and [65]. During this experimental test series on the Phenix SFR, a core mechanical study has been performed where the reactor core has been deformed in multiple steps and for each deformation step, the reactivity effect of the deformation has been measured.

The investigated Phenix core was based on the core configuration described in [64] and [66]. The fuel material within the core was MOX fuel with 18% and 23% plutonium content within the inner and outer core respectively. As an end-of-life core was used within the experiments, the fuel composition corresponds to burned fuel with the maximum burnup of 115 GWd/tHM. In the experimental study, 2 different temperatures were used, namely 180°C and 400°C, to conduct the measurements. For the validation of the methodology, the 400°C case was chosen, as it is closer to the operational conditions with the corresponding 0.25 mm gap between the assemblies at the wear pad level. The total height of the assemblies was 4300 mm from which 783 mm was below the diagrid upper plate. In this sense, the modelled geometry consisted only of the part above the diagrid, meaning the height of 3517 mm. The wrapper material of the Phenix reactor was the so-called EM10, ferritic-martensitic steel.

2.4.4.1. Deformation calculation on the PHENIX core model

To increase the speed of the reactor core deformation calculation, only 1/6th of the core has been modeled up to 11 rings of assemblies. This subsection of the core allows accurate modeling of the experimental set-up [64], where load has been applied only to the 6 assemblies adjacent to the center SA, at the SA pad region. In Figure 33, the model with the deformation contour can be seen. The assemblies at the sides have been cut to half to keep the symmetry of the model and frictionless constraints have been applied to them. It is well visible that after the load has been applied, the deformation is greatest at the top of the assemblies next to the center. The center SA stays without deformation as the applied forces on the adjacent SA pads are directed towards the periphery of the core to create the so-called flowering effect.

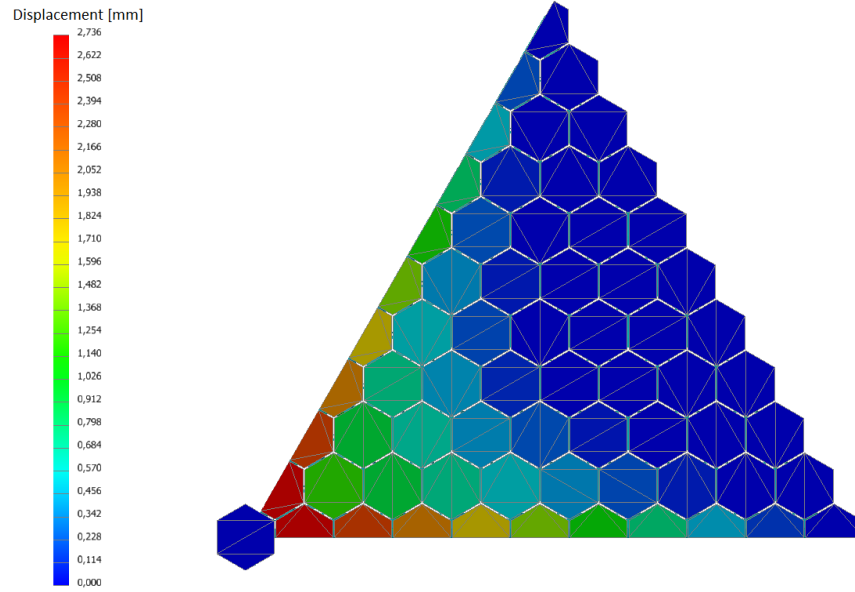


Figure 33. Modeling of the core distortion within the finite element solver for 6th of the full core (upper core view)

The assemblies are modeled as full hexagons, meaning that all the inner structure was smeared together into a homogenous mixture of materials. This approach can be used for fast reactors as the mean free path of the neutrons are around an order of magnitude higher compared to thermal reactors, meaning that the heterogeneity effects are less important within the assemblies. As a demonstration of this fact, a study on the reactivity effect of the radial core expansion has been performed. In Figure 34, a part of the heterogeneous core model is plotted beside the homogenized model, to show the amount of simplification done on the model. It is visible that though the SAs have been homogenized, the inter SA gap was not smeared into it, as the distance between the assemblies are of key importance to model the reactivity effect of the core deformation. In Table 9, the results of the simulation are presented, from which the reactivity effect of the core radial expansion is comparable between the heterogeneous and homogeneous core model. Nevertheless, the mechanical behavior of a full SA is different compared to only a hexagonal wrapper deformation, mainly because of the different moment of inertia, which is geometry dependent. Furthermore, the material properties are influenced by the neutron irradiation and, as the experimental tests were performed at the end of reactor life, it is necessary to take into account some change of the elasticity of the material even if the used EM10 steel is more resilient to irradiation damage than the formerly used austenitic steels [68][69].

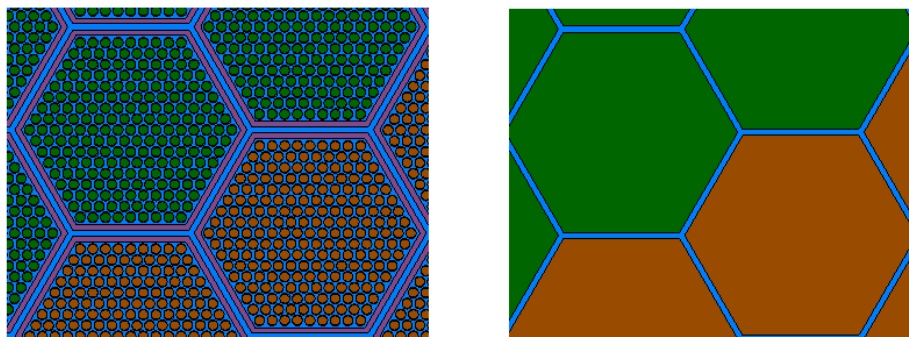


Figure 34. Heterogeneous (left) and homogeneous (right) Serpent model comparison

		k_{eff} (Std:3 pcm)	[pcm]
Heterogeneous model	Reference	1.00655	-
	0.25% radial expansion	1.00509	-144
	0.5% radial expansion	1.00359	-293
	1% radial expansion	1.00070	-581
Homogeneous model	Reference	1.00044	-
	0.25% radial expansion	0.99892	-152
	0.5% radial expansion	0.99736	-309
	1% radial expansion	0.99438	-609

Table 9. Comparison of radial expansion reactivity effects between heterogeneous and homogeneous Serpent models

To consider this difference in geometry between the actual SA and filled hexagons, furthermore, the irradiation hardening effect on the material, a calibration of the Young modulus, the proportionality coefficient between stress and strain, has been performed. The initial Young modulus in the Nastran simulation was corresponding to a general ferritic-martensitic steel of around 200 GPa [70], which was the base material of the hexagonal wrapper of the Phenix reactor. To do this adjustment, the measurement data was utilized, where the displacement of a 5th row SA was measured at the top level of the Phenix core, see Figure 35. Seven separate cases have been modeled, each of them differs in the applied forces on the pad levels of the SA, starting from 1000 N up to 7000 N in increments of 1000 N. These forces were applied to each of the 6 assemblies next to the center SA.

In the experiment, which is described in [64], the central SA has been modified to facilitate the deformation of the reactor core. More precisely, a piston was inserted from the top of the middle SA, which encountered a mechanism that pushed the contact pads of the central SA, towards the adjacent SAs, applying a load on them. In this sense, from the experiment, the vertical piston displacement could be measured directly, which then could be converted into horizontal forces on the contact pads. Following the conversion of the applied forces from the simulation into vertical piston displacement, it was possible to calibrate the Young modulus of the model and to reproduce the experimentally measured deformations of the reactor core. The results of this adjustment and the calculated displacement compared to the experimentally measured ones are plotted in Figure 36. There were two sets of measured data available for this test case, both cases show the same overall tendency regarding the displacement of the 5th row SA top, nevertheless, the spreading of the data is relatively high. Overall, the calculated data fit everywhere to the spreading of the measured data, thus it was concluded that the chosen Young modulus, 130 GPa, gives a reasonable deformation result at the chosen location. Such a significant modification of the Young modulus value is needed mainly to correct the geometry difference between a real hexagonal SFR SA and the simplified completely filled SA used in the models. Nonetheless, by doing this calibration, not only the geometry but also the irradiation hardening effect has been taken into account. To perform this calibration, for the Phenix reactor, measured data was available, in the case of other SFRs for which this data is not present but similar SA geometry is in use, the same Young modulus ratio change could be considered as a reasonable approximation for an end of cycle core.

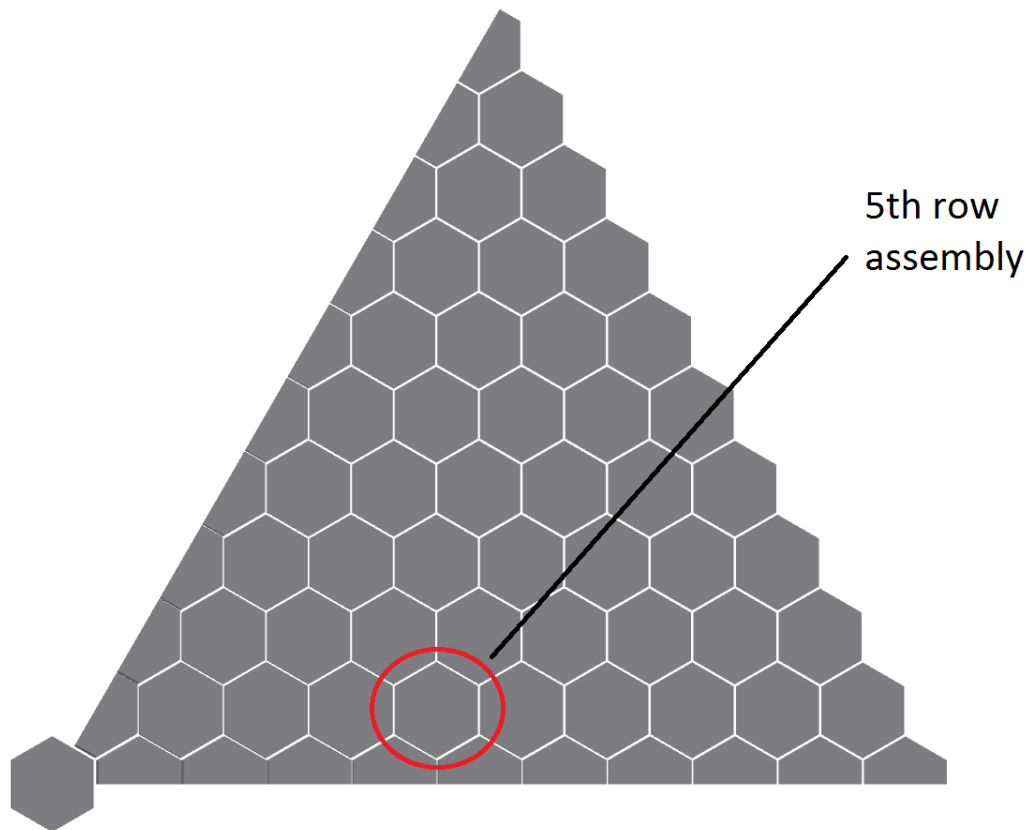


Figure 35. 5th row SA position which was used for the calibration of the young modulus of the SA material

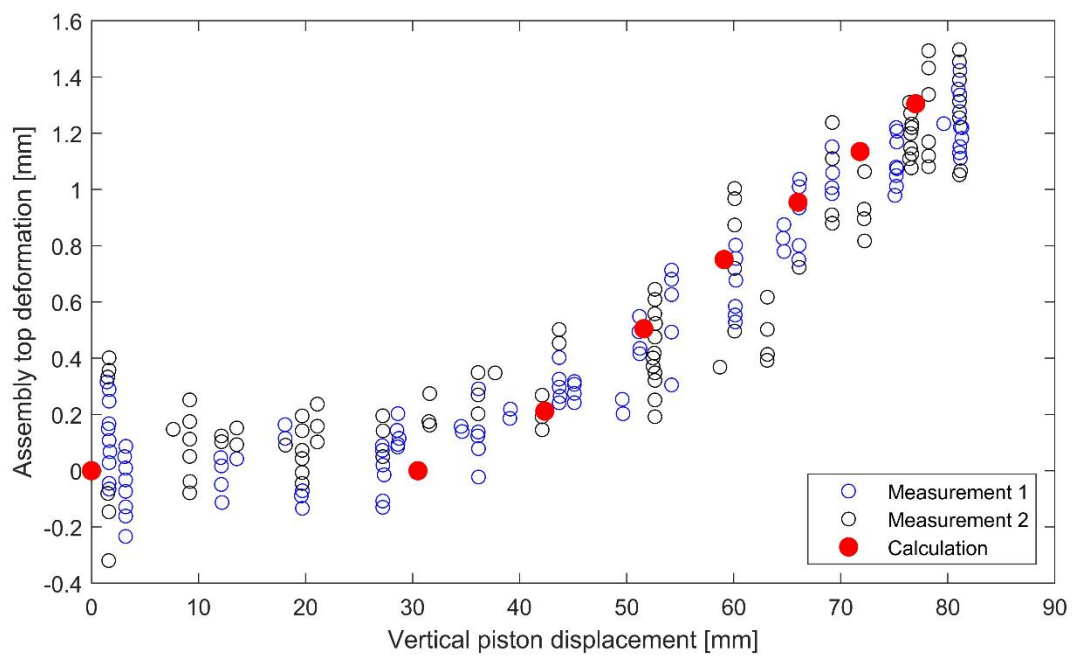


Figure 36. Displacement of the measured 5th row SA in comparison to the experimental results

2.4.4.2. Neutronic calculation based on the deformed PHENIX core model

The second step in the methodology, following the calculation of the deformed geometries of the aforementioned cases, is to implement these core models, shown in Figure 37, in the Serpent 2 Monte Carlo code. To do this, the material densities have been calculated for the different regions of the core, corresponding to a homogenized SA model. The model has been divided axially and radially according to the present material composition, such as inner fuel fertile region, inner fuel fissile region, etc. After the deformed model has been sliced corresponding to the distinct material regions, each of these pieces of the model has been loaded into Serpent with the matching material composition which was followed by a criticality calculation. The Serpent input geometry preparation, following the approach written above, can model any general deformed core shape and it is not restricted to the 60° symmetric deformation to the center used for this validation, which was required to reproduce the experimental conditions. This is provided by the fact that the finite element results are used directly without further geometry simplifications in Serpent allowing any geometry to be simulated.

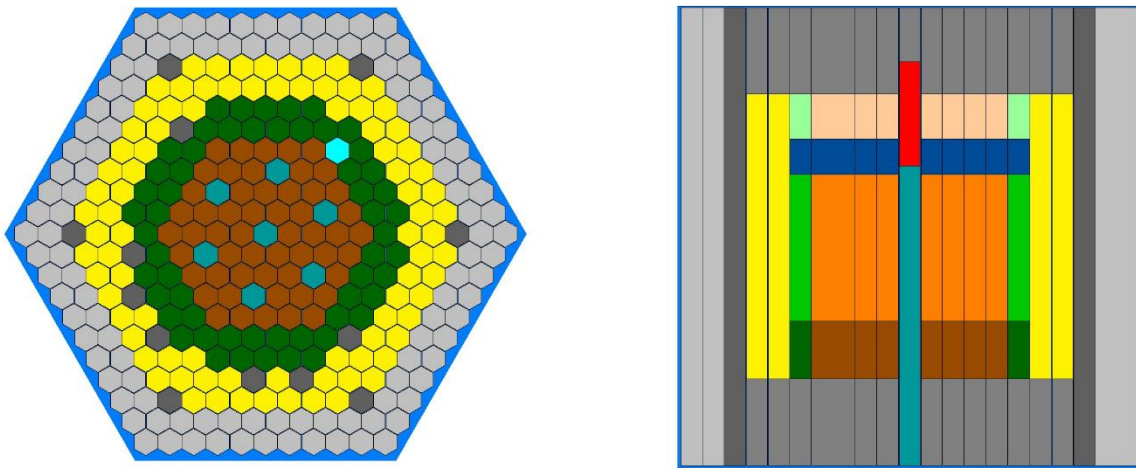


Figure 37. Serpent 2 model based on the deformed geometry of the reactor core, different colors correspond to separate model sections with different material compositions

The criticality calculation run by Serpent on the deformed core gives a direct k_{eff} value of the analyzed core geometry. By running the calculation for the 7 cases, a plot on the reactivity effect of the core deformation could be drawn. Figure 38 shows this reactivity effect versus the vertical piston displacement allowing again a direct comparison to the data which was experimentally measured. The calculated points go well along with the measured data points on the graph, showing that the calculation can give back relatively closely the reactivity effect compared to the experimental set-up.

To compare the result against another set of data of the same experiment, the reactivity effect was plotted versus the experimental device displacement at pad levels. Figure 39 shows this plot, where it is seen that the calculated data points are following well the measured data set until around 2.5 mm displacement at pad levels. From that point on, the data sets start to deviate from each other and the calculation overestimates the reactivity effect. The origin of this deviation can come from different factors. It can be that the irradiated core had different gaps between certain assemblies in some regions and it only showed effect when the deformation was high enough that the cumulative addition of small

errors, on the distance at the pad level between the assemblies, add up to an effect which is quantifiable. Another possible explanation to this is the fact that the Phenix reactor core has a slight dissymmetry and on one side of the core [64], some SAs were not modeled. This symmetry approximation could introduce some error to the calculations, especially at higher deformations.

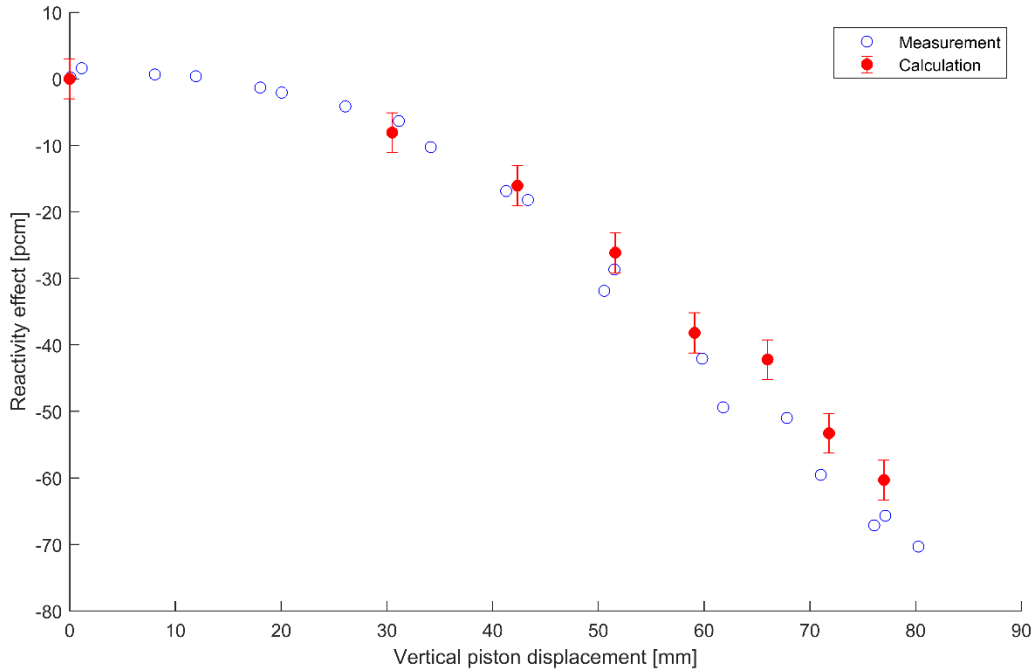


Figure 38. Reactivity effect comparison between the data previously measured [65] and calculated with the proposed method

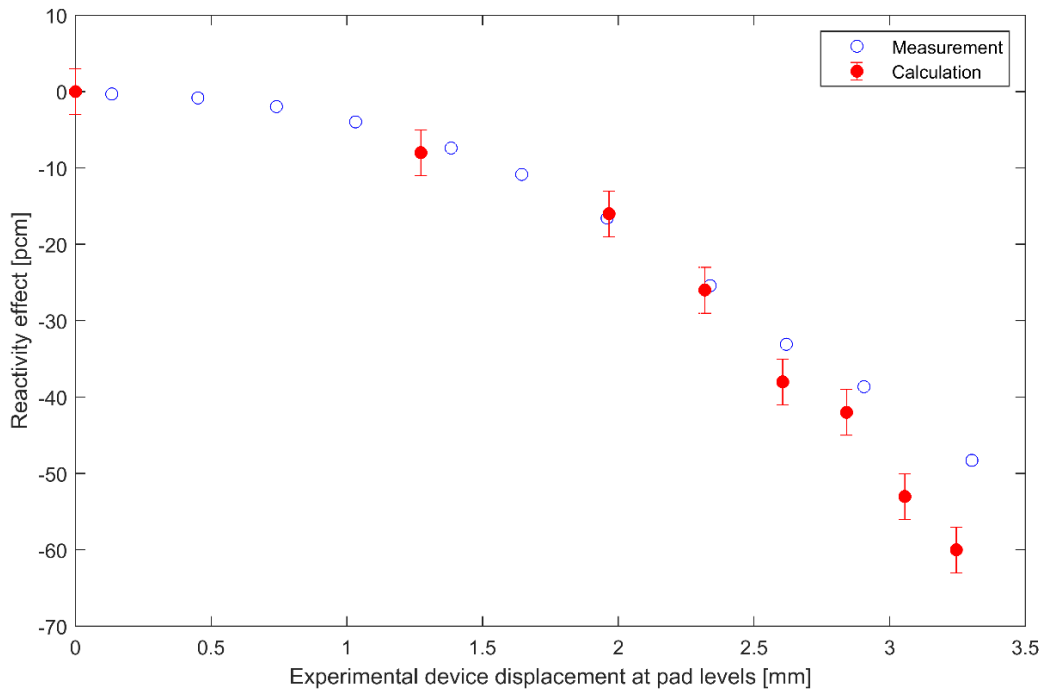


Figure 39. Reactivity effect comparison between measurement data [64] and calculated data point regards to the experimental device displacement at pad levels

2.5. Summary of Chapter 2

In the Chapter, the various main codes and methodologies have been introduced which were used for the safety assessment described in the thesis. To accomplish the research goals, a multiphysics analysis was required utilizing various domains of physics.

1. The conceptual design of the reactor, with all of its main components have been created in a CAD software, creating a 3D model of the whole reactor. This methodology has been the base for all other simulations, as it provided input data in various means for the different code packages used for the assessment. Besides of being a basic tool for the PhD research, the ESFR-SMART project as whole have taken good advantage of the generated models.

2. Another basic tool for the safety study is the TRACE thermal-hydraulic system code. Through the previously applied modifications in the code at PSI, SFR safety studies are now possible with this validated system code, allowing the study related to the reactivity control safety function and heat removal safety functions of the thesis. The whole reactor with primary, secondary and tertiary systems have been modeled and the modeling approach is described in this Chapter. For accidental simulations presented in Chapter 3 (DHRS analysis study) this whole reactor model has been used, whereas for the ULOF studies in Chapter 4, a simplified TRACE model was prepared due to the computational time requirement of the whole model.

3. For the power evolution calculation during the accidental conditions two methods are used in the thesis. 1) The point kinetics method, which is the built-in technic used in TRACE allowing fast power calculation during a transient simulation. 2) A new method is developed using the TRACE-PARCS thermal-hydraulic/spatial kinetics coupled codes with a XS correction technique called sampling. With the spatial kinetics calculation route, certain limitations of the point kinetics method could be overcome, allowing to obtain more accurate results when strong spatially dependent reactivity perturbation is introduced into the reactor core. To assess the accuracy gain of the proposed XS correction technique applied on PARCS, which is the new feature of the method, a static benchmark analysis is performed using the Superphenix reactor core and the results obtain with the reference Monte Carlo calculations. As the aim of the method is not to run static but transient calculations, in Chapter 4, another benchmark analysis is performed using the same Superphenix reactor core, and comparing the ULOF results obtained from TRACE using point kinetics and the new XS correction technique with the coupled TRACE-PARCS.

4. To calculate reactivity effect induced by reactor core deformation, as a results of for example sodium boiling or an earthquake, a new calculation route has been prepared in this work using the 3D core geometry from the CAD model. A commercial finite element analysis tool is used to calculate any general core deformation scenario, obtaining the generic core geometry, being radially and axially non-uniform. Therefore, as the individual SA movement is reproduced accurately, a common simplification has been overcome with the method, compared to more usual core geometry reactivity effect calculations, where radially or axially and radially the core is kept as uniformly deformed. Lastly, the deformation reactivity effect is calculated with Serpent 2 Monte Carlo code, using directly the deformed shape 3D output from the CAD software, creating a simple yet accurate neutronic calculation. In Chapter 4, this method is utilized as the tool for evaluation of static core deformation reactivity effect for the ESFR-SMART core design. Moreover, a transient study is performed on the Phenix reactor core using a hypothetical sodium boiling induced core deformation scenario, assessing its effect on the reactivity evolution.

CHAPTER 3

Safety function: Heat removal

Following the Fukushima nuclear accident, it is important to demonstrate that a reactor design under development can withstand conditions such as those that occurred during the accident. In the current Chapter the behavior of the ESFR during an accidental scenario, called Protected Station Blackout (PSBO) is being assessed. As part of the study, new safety measures are being assessed and selected, ensuring safe operation and shutdown of the reactor in a PSBO like accidental conditions [71].

To guarantee that the residual heat is safely removed from the reactor during an accidental scenario, three different DHRSs have been allocated for this reactor design. These systems are completely independent from each other and can operate separately. The DHRS-1 and DHRS-2 both use secondary sodium for the heat removal, and both of them can operate in a completely passive manner, whereas the DHRS-3 is the pit cooling system and uses forced convection. The main goals of the study presented in the chapter are to assess the operation and performance of these DHRSs in different operating arrangements and provide recommendations for possible further improvements. The calculational tool used for the analysis (TRACE code) was validated using the Phenix End-Of-Life Natural Circulation Test [67].

DHRS-1 design

The system is designed to work in a passive manner using the sodium present in the secondary loop. In Figure 8, the main components of the system are presented. The DHRS-1 circuit is connected to the secondary side of the IHX in parallel to the main secondary system. The cold leg is connected to the bottom of the central downcomer tube having cold secondary sodium in it, whereas the hot leg is connected right above the IHX piping outlet. During operation, the natural convection drives the system with the aid of a thermoelectric (TE) pump¹ [72], thus facilitating the establishment of the desired flowrate and flow direction within the system. The heat removal from the sodium is achieved through a sodium-air heat exchanger situated at the bottom of the DHRS-1 chimney. During normal operation, the air openings are closed. The removed heat is only significant after the latches are opened once the signal is received that the sodium temperature threshold of 600°C at the IHX inlet is exceeded. The target performance to be demonstrated by the DHRS-1 is to ensure safe thermal conditions for the considered accidental scenario even when 1 out of 6 units is unavailable due to maintenance or failure. The geometrical details of the system is provided in Appendix B, Drawing 10.

DHRS-2 design

Being the second main system, the DHRS-2 is integrated in the secondary sodium circuit, having no additional circuits, to ensure the heat removal from the primary system. For the operation, atmospheric air is circulated, which is in contact with the modular SGs' outer surface. This is achieved by having doors at the bottom and the top of the SG casing, as shown in Figure 9. To operate the system, these doors need

¹ Passive pumps based on various technologies will be considered in future to identify the most reliable and economic option

to be opened, facilitating the establishment of natural air convection within the casing. Following the opening of the doors, the system works in a completely passive manner. The secondary sodium flow is assisted by a TE pump, serving to stabilize the flow in the circuit during an accident. The initiation temperature is set to 600°C, similar to the DHRS-1 units, just like the target performance, which should ensure safe thermal conditions under the simulated transient even when 1 unit is not operational from the 6 available ones. More details on the secondary circuit geometry is provided in Appendix B, Drawing 9.

DHRS-3 design

A primary purpose of the system is to ensure cooling of the concrete surrounding the reactor keeping it below 70°C at nominal operation, and to maintain the vessel wall temperature at an acceptable level [8]. The system consists of two main heat removal circuits, an oil circuit attached to the liner of the reactor pit and a water coolant circuit in the concrete, as presented in Figure 10. In the ESFR design, the safety vessel has been replaced by a pit liner [8]. The pit liner is cooled with the oil circuits being welded to the surface of the liner, and these circuits are operated with forced convection, using a centrifugal pump, thus, this system cannot operate passively on the contrary to DHRS-1 and DHRS-2. As for the heat transfer medium for the oil circuit, a high-temperature-resistant oil was chosen, called Diphyl THT, which can operate even above 300°C, and in case of getting into contact with sodium, there is no danger of hydrogen production. Following the liner, an insulation layer protects the concrete from high heat fluxes from the reactor, and finally, the concrete is cooled with incorporated water circuits using centrifugal pumps. Radiative heat transfer is the main mechanism of heat exchange between the vessel wall and the liner as the pit is filled with inert gas, thus, the heat removal capability of the system is limited. Geometrical details of the system is provided in Appendix B, Drawings 6-8.

3.1. PSBO scenarios

The initiating event is a loss of electrical power supply, while the reactor is fully operational and is in its normal operation conditions. As the protected scenario is considered, the control rods' insertion is ensured, thus shutting down the reactor, while the forced convection is lost in all cooling circuits. Following the reactor trip, the primary pumps coast down with the mass flow halving time of 10 s for the reference design. No pony motors are started due to an assumption of loss of diesel generators (no auxiliary power supply is considered). The secondary and tertiary pumps coast down occurs with the mass flow halving time of 3 s.

To obtain a global picture of the reactor behavior during these accidental conditions, three scenarios (cases) have been chosen to be assessed before implementing the proposed DHRS in the design:

- 1) In the first case, after the reactor shutdown, heat removal in the tertiary system is maintained due to the remained feedwater supply of 5% of the nominal value, ensured by an external power source, thus ensuring a stable long-term cooling. No DHRS are assumed in operation and the goal of this exercise is to evaluate transition from forced to natural convection.
- 2) In the second case, the feedwater supply is lost, thus, the heat sink of the tertiary system is not available. This case provides a comparative basis for the DHRS-2 analysis.

3) The third case is the most penalizing scenario, where the loss of heat sink of the primary system is assumed at the start of the accident by setting zero heat exchange rate at IHX. This case draws the basis for DHRS-1 and DHRS-3 studies.

During the analysis, certain limiting temperatures were taken as indicators of the necessary power removal. The main limiting temperatures are the maximum vessel temperature, which is limited to 650°C to avoid high creep rates, and the reactor pit concrete temperature of 70°C. Another limiting temperature could be the maximum fuel temperature. However, as the assessed transients are always protected ones, the fuel temperature drops significantly at the beginning of the transient, and it stays even lower than under nominal conditions. Besides, the efficient heat removal from the fuel by the sodium coolant, which has a high heat conductivity compared to water, ensures that fuel melting is of no concern during the proposed accidents.

3.2. Assessment of ESFR decay heat removal with reference secondary circuit design

3.2.1. TRACE models

The reactor design was simulated through two main models to run the PSBO analysis, a full model and a simplified model. The full model is a very detailed model of all main components of the primary, secondary and tertiary systems, described in Chapter 2, Section 2.2.2. This model was used for the PSBO accident simulations and for the decay heat removal performance analysis, where it was extended with each analyzed DHRS.

In the case of the simplified model, the primary system has been modified, and only one secondary loop with the corresponding tertiary system have been installed for the calculation. This model was used for certain sensitivity cases to reduce the calculation burden, where only one single aspect of the simulation has been assessed, and the results would not benefit from the detailed calculation. The model and its application will be discussed in more detail in Section 3.2.3.1.

3.2.1.1. DHRS-1

The overview of the DHRS-1 model is shown in Figure 40. The sodium piping follows the path of the actual design, and the connection points to the IHX were also kept at the same locations, as they are determined in the design drawings. For the chimney, a boundary condition with constant air flowrate is considered during the operation of DHRS at the pipe corresponding to the square box situated at the bottom of the chimney where the sodium-air heat exchanger is placed. From this pipe, the connection leads to another pipe equivalent to the chimney itself, which ends with an atmospheric pressure boundary condition of 0.1 MPa. The heat exchange happens with the aid of a heat structure connecting the air pipe under the chimney and the part of the sodium piping cooled down with air in accord with the actual design. The heat transfer coefficient under the modeled air flowrate and heat exchanger geometry was estimated, on average on the heat exchanger length, around 11.4 W/m²K.

The reference scenario for DHRS-1 intervention considers the loss of the flow circulation path in the secondary loop, while the secondary side of the IHX is integrated in the DHRS-1 loop. In order to isolate the secondary circuit for the study of DHRS-1 performance, the secondary sodium flow outside of the IHX

was blocked by closing a valve at the start of the accident, and thus, only the heat exchange of primary sodium with the secondary sodium circulating in the DHRS-1 loop was allowed. This approach also allowed to exclude the influence of the secondary flow on the flow conditions in the DHRS-1 loop. In addition, the availability of the secondary circuit would result in a later time point of the air inlet opening of DHRS-1, as it would take longer to reach 600°C at IHX primary side inlet due to the higher secondary sodium heat capacity.

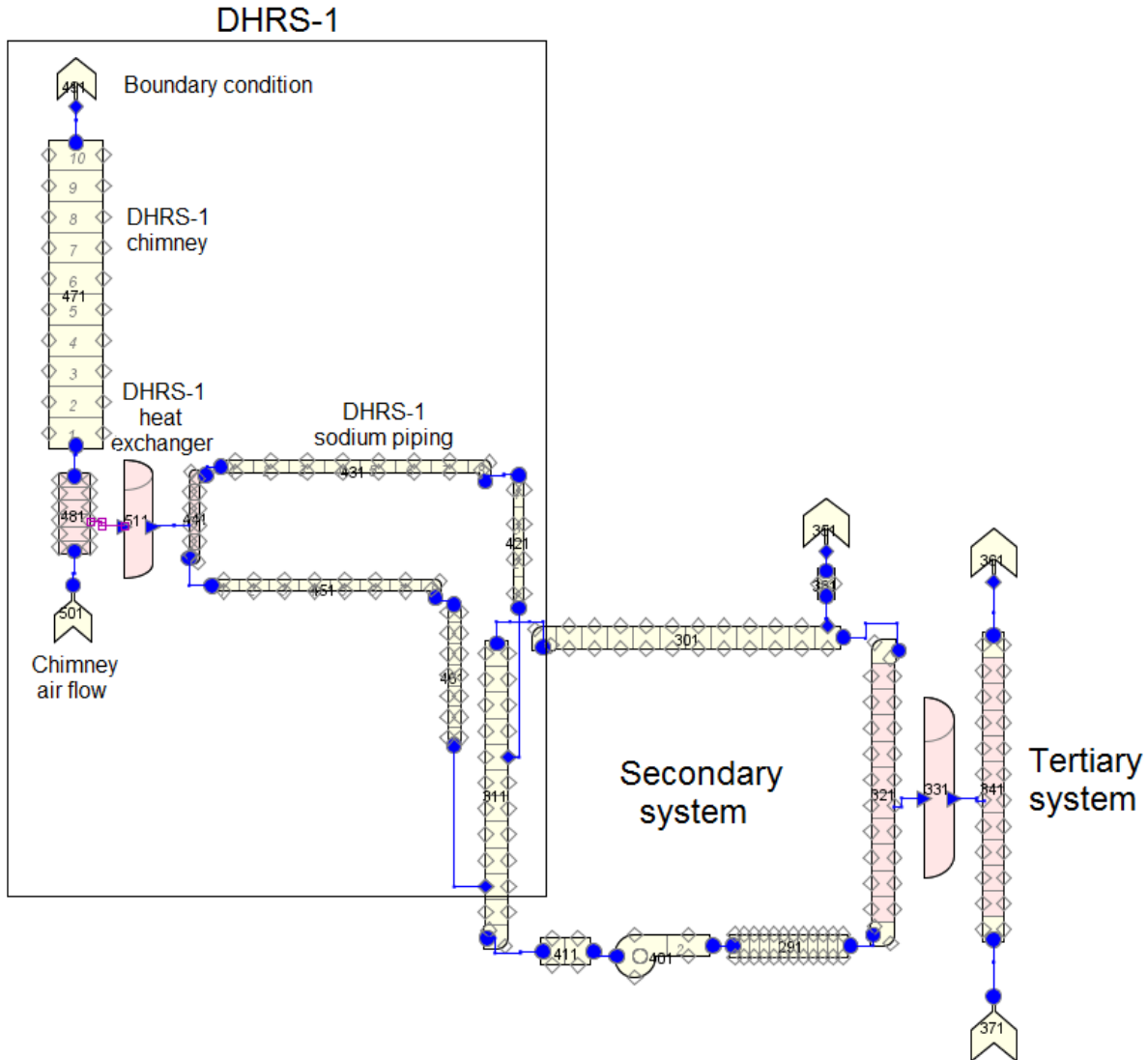
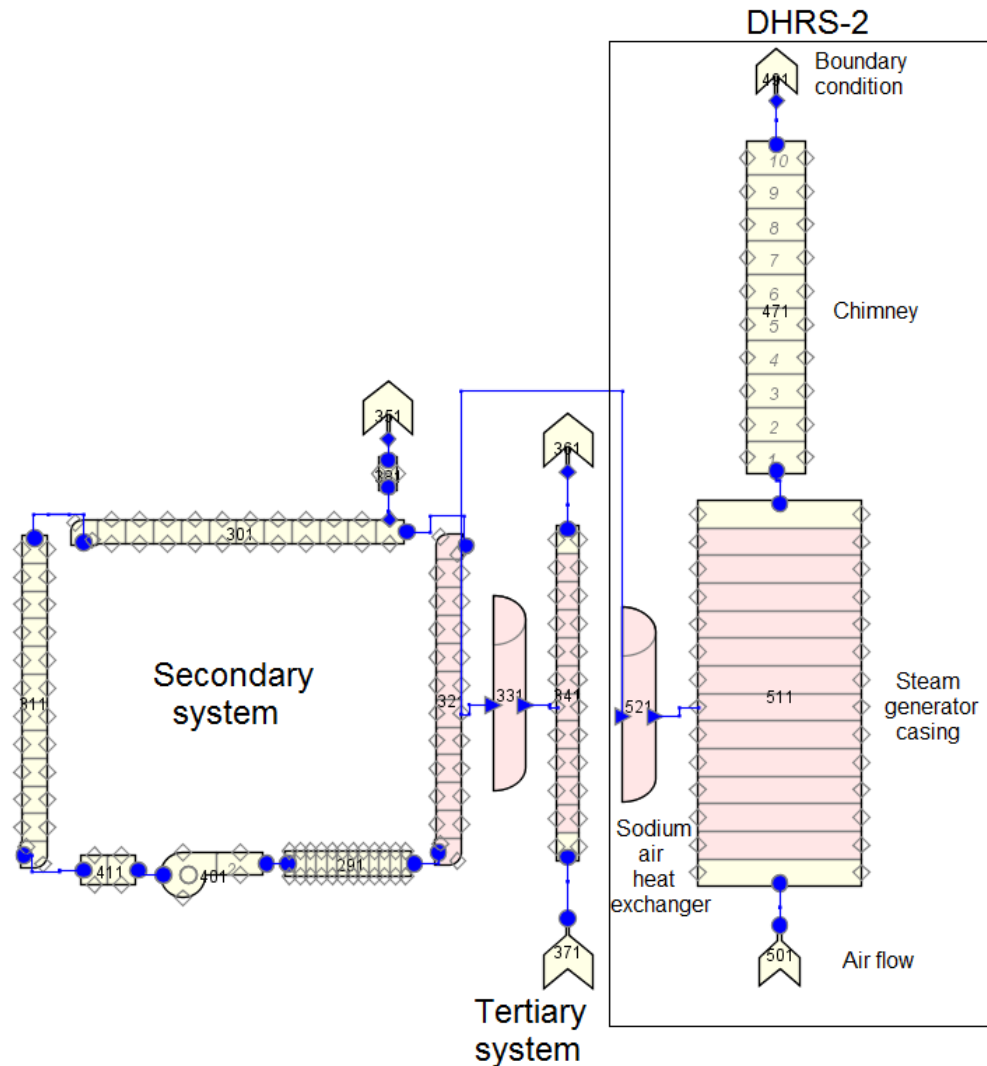


Figure 40. Schematic view of the DHRS-1 system in the TRACE model, connected to the secondary sodium loop (Figure nodalization for visualization purposes only)

3.2.1.2. DHRS-2

DHRS-2 serves as the main DHRS by the availability of the secondary loops. The system itself is relatively simple as the heat is removed from the outer surface of the SGs by natural air circulation within the SG casing. To model DHRS-2 in TRACE, a boundary condition with a predefined constant air flowrate estimated to be 23 kg/s [73] has been used in connection to a pipe, representing the SG casing geometry. This pipe is connected to subsequent piping, which embodies the chimney above the SG casing. On top

of the chimney, an atmospheric pressure boundary condition of 0.1 MPa has been set. DHRS-2 is connected to the secondary sodium circuit through a heat structure that allows heat exchange between the SG outer periphery and the air in the casing, as presented in Figure 41. The corresponding base PSBO case for this simulation was the “no feedwater” simulation option, i.e., the feedwater supply was completely lost at the beginning of the accident. The heat transfer coefficient under the previously described air flowrate and heat exchanger geometry was estimated, on average on the heat exchanger length, around 11.3 W/m²K.



start, similarly to the study of DHRS-1, has been considered by setting the heat exchange rate in the IHX to zero.

The modeling followed the design of the actual system, shown in Figure 42. It has two main cooling circuits: 1) an oil cooling circuit situated between the pit liner and the insulation and 2) a water cooling circuit immersed into the surrounding concrete. At the inlet of both circuits, a boundary condition with a constant flow velocity of 1 m/s is provided, representing the centrifugal pumps, whereas, at the outlet, there is a pressure boundary condition of 0.1 MPa. The heat exchange between the reactor and the different cooling circuits is provided by multi-layer heat structure elements. The first heat structure represents the reactor vessel wall, gas gap, liner, and oil circuit pipe wall. The second heat structure represents the layers between the oil and water circuits, i.e., oil pipe wall, insulation, concrete, and water pipe wall. The third and last element creates the connection between the water tube wall and the environment using layers of a water pipe wall and concrete, having a constant temperature of 40°C at its outer periphery.

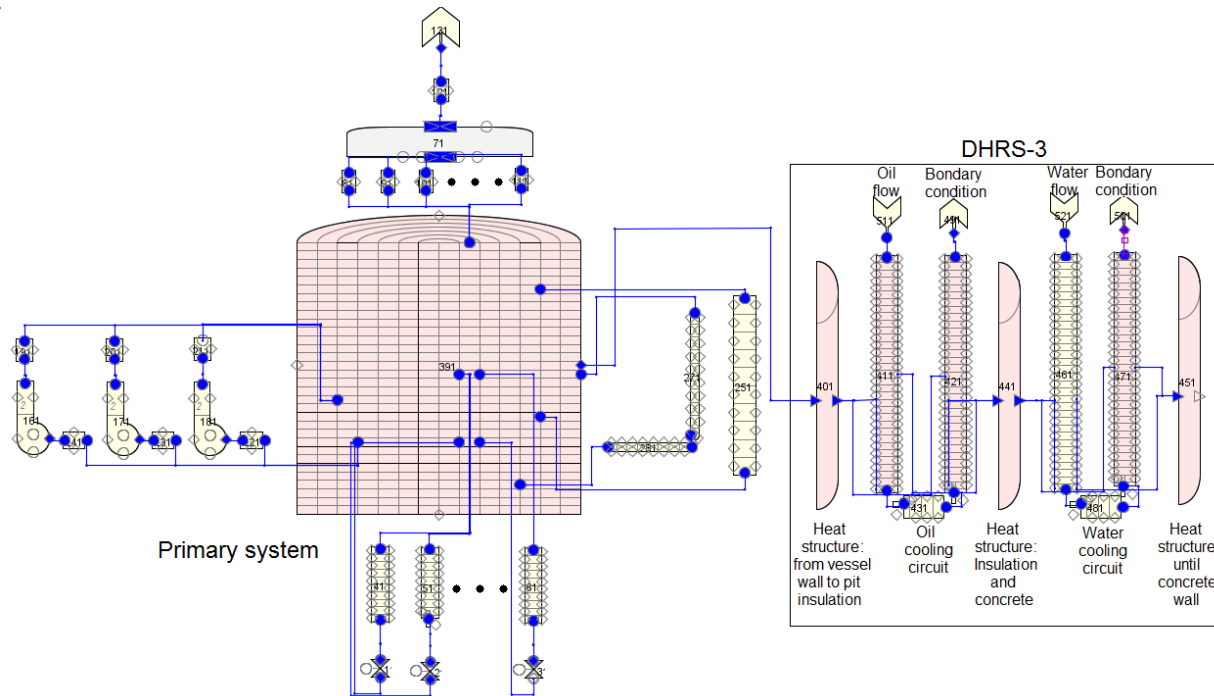


Figure 42. Schematic view of the DHRS-3 model and its connection to the primary system in TRACE
(Figure nodalization for visualization purposes only)

3.2.2. Simulation results for PSBO scenarios with no DHRS activated

In the following simulations, the applied model includes the primary, secondary, and tertiary systems without any DHRS implemented. As discussed in Section 3.1, these calculations serve as a comparative basis where the reactor behavior can be evaluated with and without any auxiliary heat removal to see the available grace period of the reactor and the extent of the system behavior change due to the DHRS implementation in the subsequent models. In the first model, the heat removal is ensured by a 5% residual feedwater supply. For the second case, the feedwater supply is stopped, and the reactor is kept

within thermal safety margins for a considerable period of time due to its great thermal capacity, originating from the large amount of primary and secondary sodium, as it absorbs a big amount of the reactor power, thus damping any possible prompt temperature spike (“no feedwater” case in Figures). This heat capacity is reduced for the third case, where the secondary sodium is not available as a heat sink (“loss of secondary circuit” case in Figures) after the start of the accident.

According to the PSBO description, when the accident begins, the control rods are inserted into the reactor core, thus, the reactor is shutdown, and the power rapidly decreases determined by radioactive decay, as shown in Figure 43. Furthermore, the primary and secondary pumps are stopped with the mass flow halving times of 10 s and 3 s, respectively. The pump’s coast down results in decreasing flowrates in the systems until the establishment of the natural circulation, driven by the buoyancy effect originating from the residual heat produced by the reactor core.

In Figure 43, an oscillating behavior can be observed for the primary and secondary flow of the case where the 5% feedwater supply was kept. These oscillations originate from a strongly non-uniform temperature distribution along the secondary loop established after the rapid flowrate decrease in the primary and secondary circuits, shown in Figure 44. It results in a strong variation of the heat up at the secondary side of the IHX and in corresponding oscillations in the natural circulation head and mass flow of the secondary loop. The flow oscillations cause the IHX primary side outlet temperature to oscillate also, affecting the SA outlet temperatures as well, as can be observed in Figure 45, where the primary sodium temperatures at different locations are presented for all three PSBO cases. Due to a large amount of sodium in the hot pool, the IHX inlet temperature, in contrast, changes very smoothly, decreasing in accord with the power generation. For every cyclic rise of the secondary flow, the primary flow is also accelerated due to enhanced heat exchange in the IHX, which results in a corresponding decrease of the IHX outlet temperature on the primary side.

In the “no feedwater” case, the secondary flow exhibits fluctuations with reversal in multiple time points. The reason for this is that no stable natural circulation in the secondary loop can be established due to the absence of the heat removal on the tertiary side, thus the extra natural circulation pressure head is not available, unlike the case of 5% feedwater. Furthermore, the fluctuations are governed by the non-uniform sodium temperature distribution, similar to the 5% feedwater case, along the secondary loop. Due to the reduced secondary mass flow and limited heat exchange between the secondary loop and the IHX, the primary flow oscillations are only weakly present in the results. Finally, the primary flow of the “loss of secondary circuit” case displays a stable natural circulation flow pattern at nearly the same level as for the “no feedwater” case.

The evolution of the plotted primary circuit temperatures exposes the major differences in Figure 45 between the three presented cases. For the simulation with 5% feedwater flow, following the sudden temperature drop, due to the control rod insertion and fuel temperature decrease, the temperatures at different locations are constantly decreasing, thus, the reactor is safely shutdown by using the residual feedwater supply for the decay heat removal.

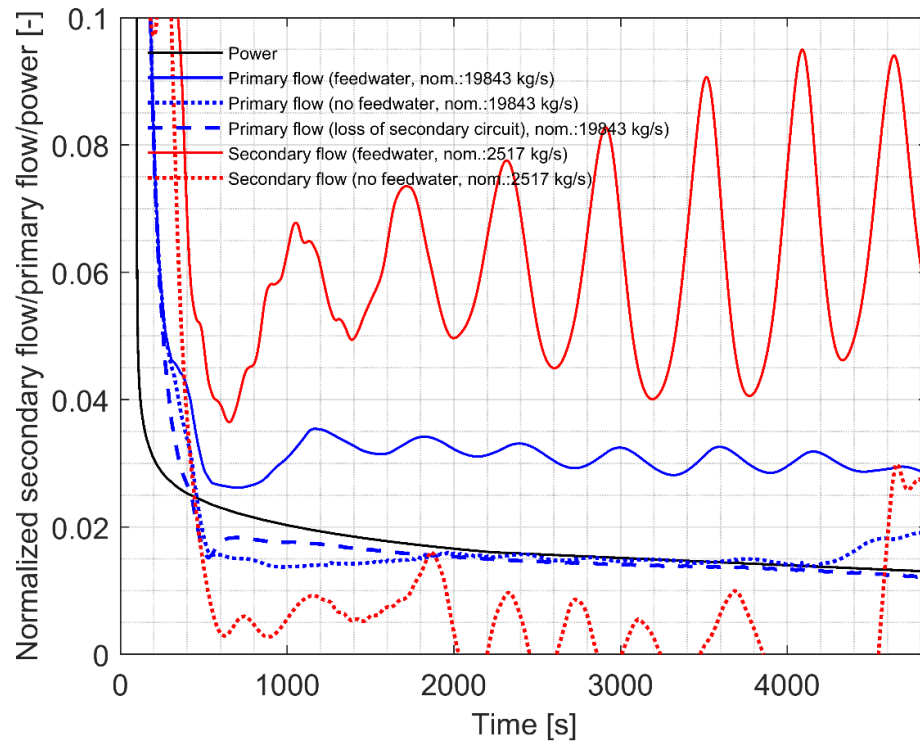


Figure 43. Evolution of reactor power, primary and secondary mass flow for different PSBO scenarios without activation of DHRS (air inlets are closed)

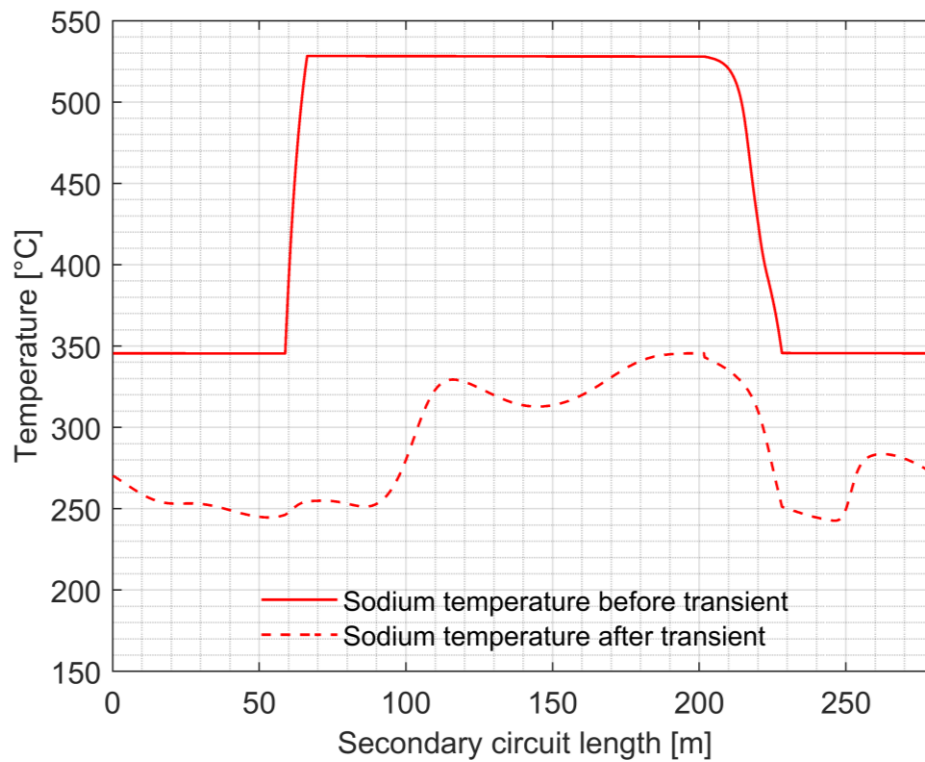


Figure 44. Temperature profile over the length of the secondary circuit before transient initiation and 1500 s after for the "feedwater" calculation case

For the other two cases, a similar initial drop of the SA outlet temperature is visible right after the reactor shutdown, as the fuel temperature drops quicker compared to the more gradual flowrate reduction due to the existing pump run out. Due to a lack of heat removal in the primary circuit, cold and hot pool temperatures gradually increase, as can be observed following the plotted temperatures at the SA outlet, IHX inlet, and outlet. The conditions without intervention of a DHRS ultimately lead to exceeding safety margins for temperatures of primary sodium and structural components, although this heating up is slow due to a high thermal capacity of the primary system. In the most penalizing “loss of secondary circuit” case, higher temperatures are reached as compared to the other two simulations. For this scenario, the predefined DHRS initiation (DHRS-1) temperature of 600°C at the IHX primary side inlet is reached after about 3000 s of the accident, while the availability of the secondary circuit as a heat sink in “no feedwater” case results in an additional grace time of about 2000 s (the trigger temperature was not reached during the simulated 5000 s), prior to the initiation of DHRS (DHRS-2). This fact also shows that for the DHRS-2 simulation, longer than 5000 s calculation time will be required.

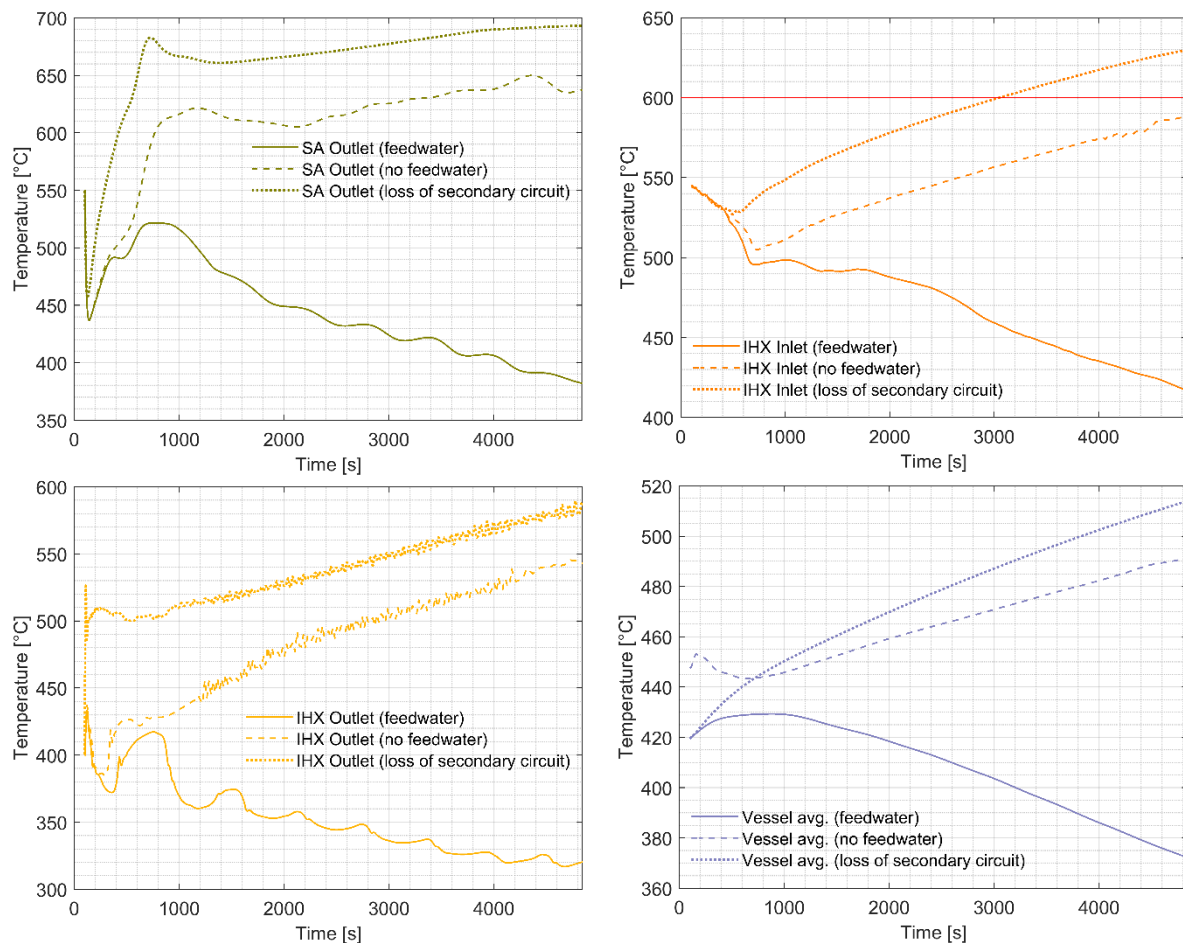


Figure 45. Evolution of selected primary system temperature parameters during the PSBO accident without activation of DHRS (SA outlet-top left, IHX inlet-top right, IHX outlet-bottom left, Vessel average-bottom right)

3.2.3. Individual DHRS simulation results

3.2.3.1. Evaluation of heat removal capabilities with DHRS depending on air flowrate conditions

The efficiency of the main DHRSs rely on the air flow conditions in the chimneys. Natural circulation is considered by the design, while a forced air flow using electric blowers also can be applied to intensify heat exchange in the chimneys. A study has been performed to evaluate the DHRS-1 air flowrate, from a potentially achievable set of flows, in the chimney for which the pre-determined heat removal capacity can be achieved. In order to conduct such a study, a simplified model has been developed in TRACE, shown in Figure 46, where the primary circuit has been modified by removing the vessel component, thus using plenums for the cold and hot sodium pools instead. A further simplification was that only 1/6th of the primary cooling circuit has been simulated, corresponding to only one IHX, a primary pump with reduced flowrate, and 1/6th of the fuel assemblies. The secondary and tertiary systems have not been modified, they have been kept identical to the full reactor model. In the simplified model both DHRS-1 and DHRS-2 have been included and operated simultaneously. In this way, even though the DHRS-1 chimney air flowrate is the analyzed quantity, DHRS-2 is also removing heat from the core. Nevertheless, this fact does not significantly influence the assessment, as DHRS-1 is expected to remove considerably greater amount of heat than DHRS-2, thus it can serve as an initial air flowrate determination study. The air flow in DHRS-2 has not been varied as it was predefined in a previous study [73].

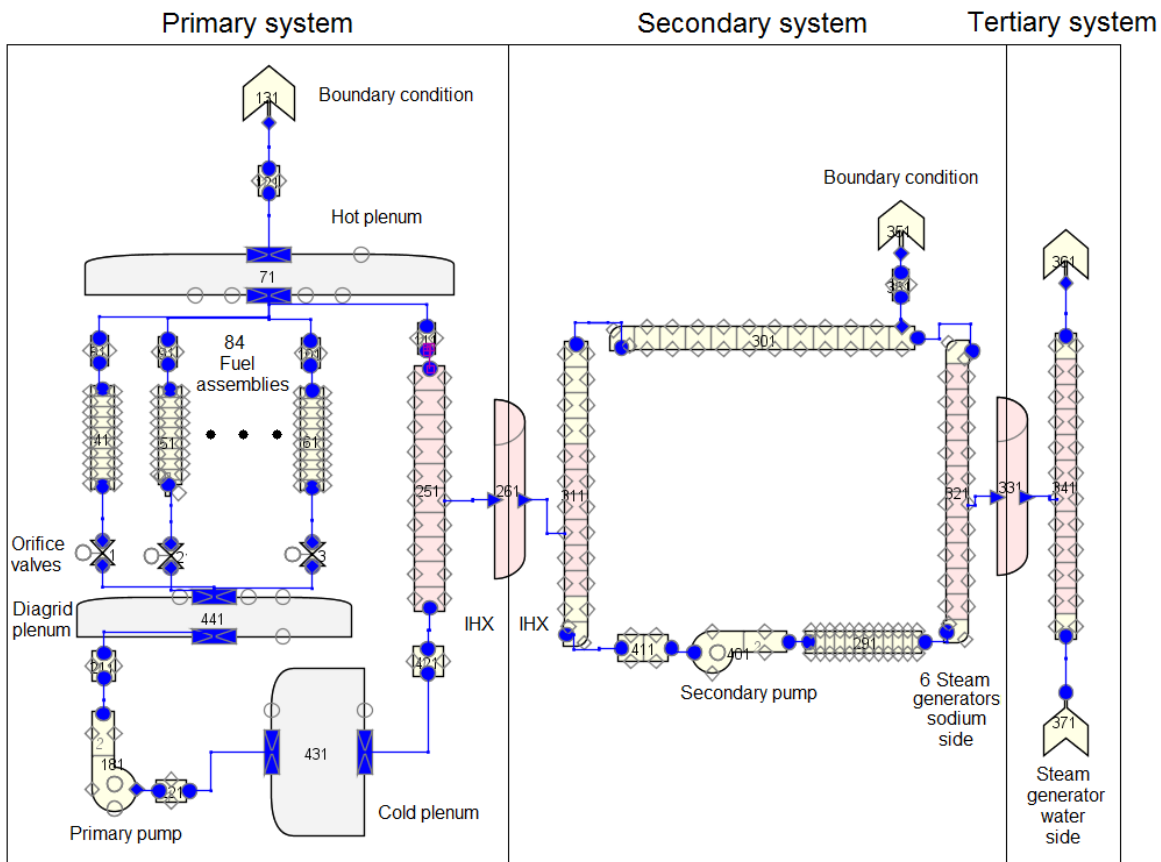


Figure 46. The simplified TRACE model of ESRF for sensitivity analysis (Figure nodalization for visualization purposes only)

The simplification was performed to reduce the required time to obtain results from transient simulations, which allowed to run a sensitivity study and to determine the minimum required air flowrate in the DHRS-1 chimney. In Figure 47, the results from this study are plotted, where the crossing of the power ratio of 1, shown by the red line of the Figure, describes the point where the removed heat by DHRS is greater than the produced by the reactor core. Based on this, by using DHRS-1 and DHRS-2 together, it is possible to remove all produced power from the reactor in less than 4500 s following the initiation of the transient even by using an air flowrate of 30 kg/s. By using as low air flowrate as possible, the calculations can be considered as being conservative, and it is more ensured that the required air can be supplied through natural convection. Equation 11 is used to calculate the approximate natural air flowrate in the chimney above the DHRS-1 sodium-air heat exchanger, originating from the so called stack effect of the chimney [74].

$$Q = C_d A \rho \sqrt{2gh \frac{T_i - T_0}{T_i}} \quad (11)$$

where: Q is the natural air flowrate arising from stack effect, C_d is the discharge coefficient taken as 0.65, A is the flow area, ρ is the average air density inside the chimney, g is the gravitational acceleration constant, h is the distance between the air opening at the bottom and outlet of the chimney, T_i is the average temperature inside the chimney, whereas T_0 is the ambient air temperature. Using the above equation for the DHRS-1 chimney design assuming 28 m height and 2.8 m diameter, expecting 313 K (40°C) ambient temperature, the achievable air flowrate is 44 kg/s. This approach gives an approximate flow value, as the obstruction of air by the heat exchanger piping in the bottom of the chimney is not precisely accounted for, nor the air moisture level is defined. Nevertheless, it gives a basis to accept 30 kg/s flowrate as a reasonable value for the calculation, especially considering that the same order of magnitude has been used for DHRS-2 analysis, which was based on the evaluation given in [73].

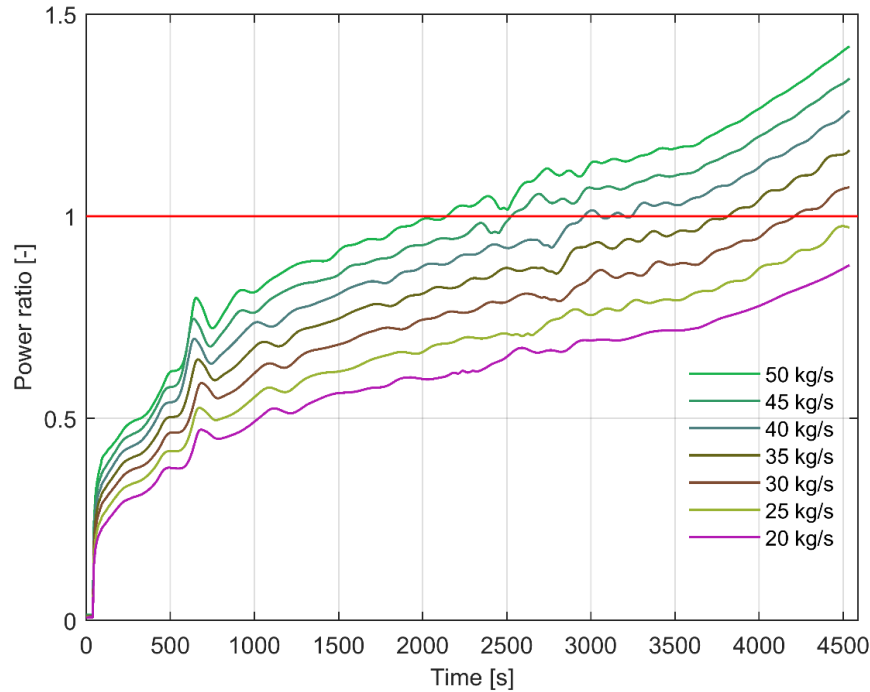


Figure 47. Sensitivity study on the DHRS-1 heat removal versus the applied air flowrate in the DHRS-1 chimney with the removed power by the DHRS vs decay power produced by the core (Power ratio)

3.2.3.2. DHRS-1 system simulations

3.2.3.2.1. Application of auxiliary pump on DHRS-1 loop

A preliminary study on DHRS-1 has revealed that the direction of the sodium flow in the system during normal operation is opposite to that of what is envisaged in the design specifications caused by the pressure distribution in the system. Due to this phenomenon, the cold sodium is sucked into DHRS-1, at the bottom of the central IHX column, flows through the system, and is ejected to the hot sodium part of the IHX, close to the top of the heat exchanging tube bundle. This flow reversal ends up slightly decreasing the total reactor efficiency in nominal conditions, as a small part of the secondary cold sodium is directly injected into the hot sodium side, thus lowering the maximum sodium temperature flowing towards the SGs. In order to fix the flow direction in the system and to help the establishment of natural convection within DHRS-1, the application of an auxiliary pump in the DHRS-1 loop was considered. Two options were assessed: electromagnetic (EM) and TE pumps.

EM pumps are often used in liquid metal loops. In case of application of this pump, the pump head will be lost immediately (with no run out) following accident start, as the result of the loss of power supply. The TE pump is a passively operating pump, where the Seeback effect is used to generate a pressure head in the liquid metal coolant [72]. With both options, it is possible to generate enough pumping power to counteract the unfavorable pressure difference at the ends of DHRS-1, thus changing the flow direction within the loop.

A sensitivity study was performed on the simplified loop to estimate the pump head that needs to be generated by the TE pump. Using the results, a MATLAB script was developed at PSI, allowing to determine the required TE pump length to generate the additional pressure head. The calculations show that, based on the geometry and pump materials predefined in the project [8], the equation derived to show the relationship between the TE pump length and the produced pump head is:

$$\Delta H = 182.9L \cdot B \cdot \Delta T \quad (12)$$

where: ΔH is the produced pressure head, L is the length of the TE pump, B is the magnetic field strength, and ΔT is the temperature difference between the hot and cold parts of the thermocouples. The resultant required head pressure to be supplied to reverse the flow in the DHRS-1 loop is ~41 kPa, based on the study. Using equation 12 to determine the necessary pump length, using 80°C as ambient temperature, ~500°C as sodium average temperature in the loop, and 0.1 T magnetic field strength, the required pump length is about 5.4 m.

In Figure 48, the result of the designed TE and EM pump head can be seen for different operational options in terms of flowrate in the DHRS-1 loop. Three different options are indicated in the Figure: 1) The first one (pump stop, delayed air inlet opening) is emulating an option of EM pump, being stopped at the start of the transient. The jump in the flowrate at 3300 s corresponds to the air inlet opening of DHRS-1, resulting in an increased flowrate and establishment of natural circulation in the loop; 2) The second option uses the same set-up, but this time, the DHRS-1 air inlet opening follows the transient initiation directly, thus, the flowrate stays on a constant, elevated level; 3) The third case represents the TE pump usage, thus, the pump is not stopped during accidental conditions, while DHRS-1 is also activated immediately after the start of the transient. Not surprisingly, the third option gives the highest flowrate in the system for the accidental conditions. For normal reactor operation, as shown in the Figure, the flow

direction is ensured with a relatively small flowrate, thus creating favorable conditions for no interaction between flows in the DHRS-1 loop and secondary loop, potentially increasing the flow stability and transition to accidental operation of DHRS-1. The application of TE pump allows increasing by about three times the flowrate in the DHRS-1 loop compared to purely natural convection case, however the power evacuated by the system is poorly dependent on the flowrate in the loop, thus increasing by ~10% for the case where the TE pump facilitates the flow. In further study of DHRS-1, the conservative option with EM pump is considered.

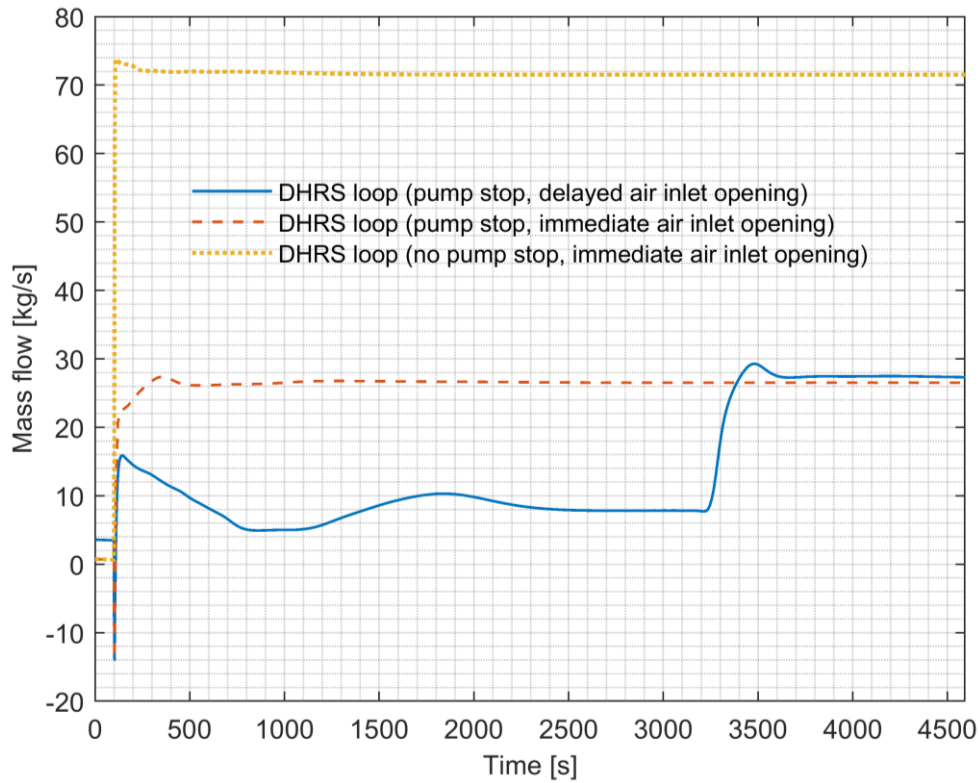


Figure 48. Different pump operation options with the induced flow in the DHRS-1 loop

3.2.3.2.2. DHRS-1 simulation results

In this Section, an assessment of the behavior of the power plant is discussed during PSBO with the intervention of DHRS-1 following the basic “loss of secondary circuit” scenario described in Section 3.2. According to the design, this system is expected to remove the greatest amount of heat from the reactor during an accident, thus being presumably the most effective DHRS of the reactor.

The system is activated, by opening the air inlets at the chimney bottom, at about 3000 s of the accident with the signal on exceeding the IHX primary side inlet sodium temperature of 600°C. With the predefined 30 kg/s air flowrate at the chimney, the removed heat by all 6 DHRS-1 loops stabilizes around 42 MW, as shown in Figure 49. The TRACE model included the components related to DHRS-3 (gas gap, insulation, etc.), to take into account the vessel’s thermal inertia and demonstrate that its maximum temperature does not exceed safety margins (stays below 650°C), but without imposing forced convection in its cooling circuits. Another reason for this is that in the actual design, though there is no forced convection, the heat capacity of the surrounding concrete would play a role in heat dissipation. In this sense, the modeled

scenario does include the reactor pit, which can absorb ~ 4 MW heat during the accident that is added on top of the DHRS-1 heat evacuation, shown by the “Total heat removal” line in Figure 49. Under these conditions, the total power removed from the reactor reaches the produced decay power in about 2000 s after the initiation of DHRS-1 and in 5000 s after the start of the accident.

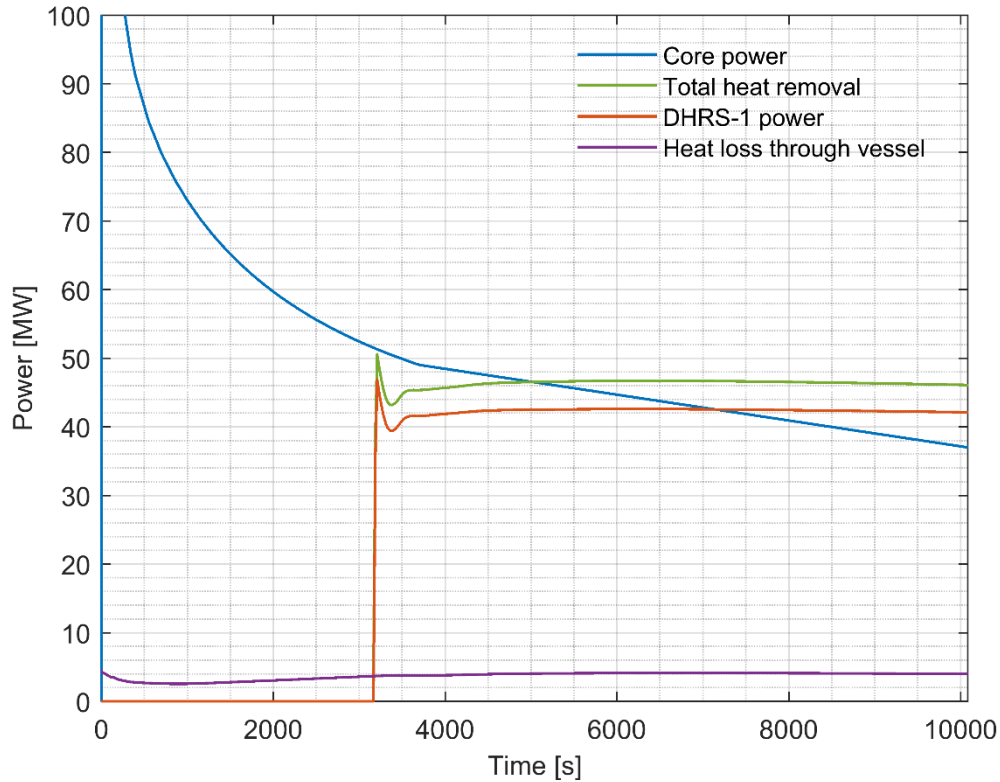


Figure 49. DHRS-1 heat removal capability used as an individual heat removal

The selected primary system temperatures are plotted in Figure 50. The core heating up undergoes the same scenario as one of “loss of secondary circuit” before the air inlet opening of DHRS-1. The open air inlets of this system results in cooling down of the cold leg sodium, followed by the establishment of the natural circulation in the DHRS-1 loop, facilitating the heat transfer in the IHX as the cold sodium from the loop enters the secondary side of the IHX. The corresponding decrease of the IHX primary side outlet temperature at stabilized natural circulation flow conditions in the primary system results in a decrease of SA outlet temperature. Afterward, a gradual cooling down of the primary system is observed, as the core power continues to decrease, while the evacuated power stays nearly constant. The decrease of temperatures is observed further for the rest of the simulated time, thus indicating a safe shutdown of the reactor. The vessel average temperature does not exceed the level of 500°C (maximum vessel temperature stays below $\sim 620^{\circ}\text{C}$), thus the reactor is kept within the envisaged safety margins.

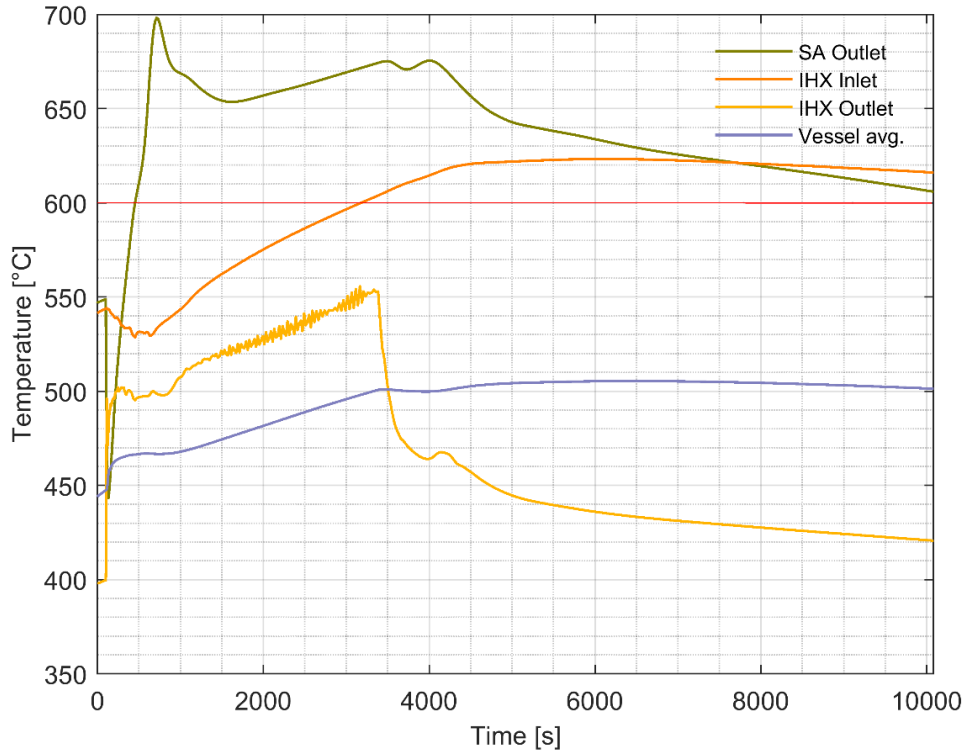


Figure 50. Primary sodium temperatures evolution during the accident using only DHRS-1

3.2.3.3. DHRS-2 system simulations

3.2.3.3.1. DHRS-2 simulation results

For the study of DHRS-2, the same scenario sequence as in “no feedwater” one was considered up to the moment of activation of air flow in the SG casing, which is done by opening the bottom and top doors of the casing. The same way as in the study of DHRS-1, the reactor pit was included in the model, allowing heat dissipation to the surrounding structures. Taking this into account, the results on evaluated power are plotted in Figure 51. Using the DHRS-2, the IHX inlet temperature reaches 600°C, which is the set limit for the SG casing air way opening, around 5500 s after accident start, considerably later in time as compared to the DHRS-1 scenario discussed above. It is clearly observed that the total heat evacuated by the 6 secondary circuits, available in the model, is significantly lower than it is for DHRS-1. It shows that DHRS-2 itself is capable, under the current conditions, to remove ~13 MW of heat, which is only about a third of the generated power in the reactor core even after 10000 s. This result indicates that in the current design and simulated accidental scenario, using only DHRS-2 in natural air convection may become not sufficient to safely evacuate enough decay heat following the reactor shutdown during the analyzed event without exceeding thermal safety margins.

In order to get a more detailed picture of the primary system conditions, the sodium temperatures at different locations have been plotted (see Figure 52). The temperature evolution is less smooth compared to the DHRS-1 case, and the overall tendency is that the reactor is gradually heating up, which corresponds to the results shown in Figure 51, where the generated power exceeds the total heat removal. Thus, the thermal conditions of the primary system are not stabilized. The vessel average temperature exceeded ~500°C at the end of the simulation time, and it was continuing to increase. The evacuated power is

expected to match the generated power at somewhat about 45000 s after reactor shutdown in accord with the evaluations performed in [73]. Up to this moment, a further core heating up may result in exceeding the safety margin for the vessel wall maximum temperature.

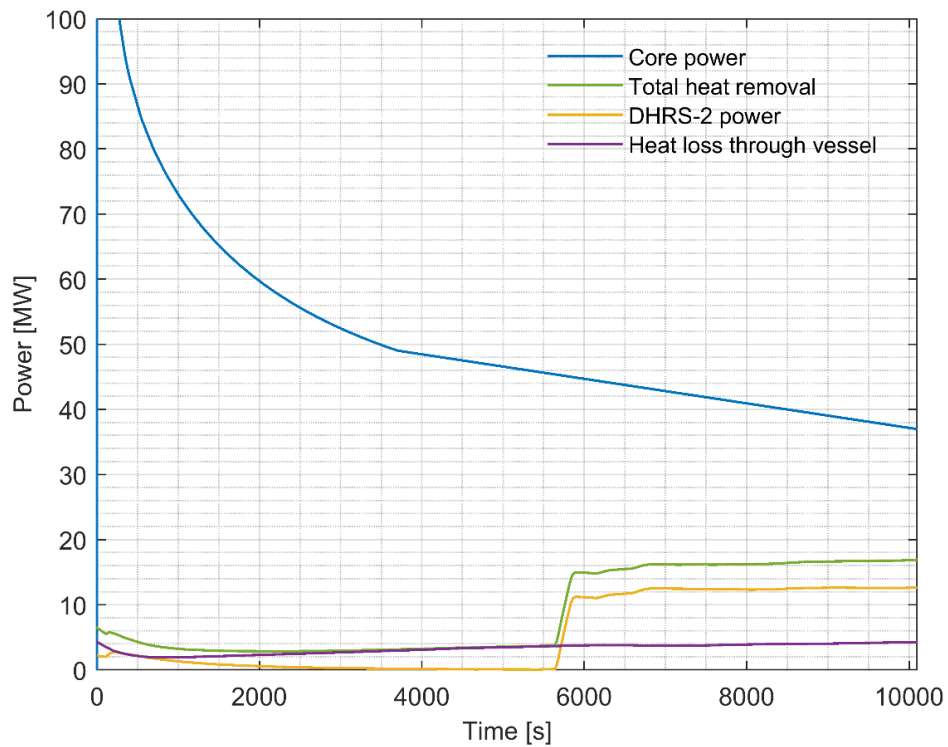


Figure 51. DHRS-2 heat removal capability used as an individual heat removal means

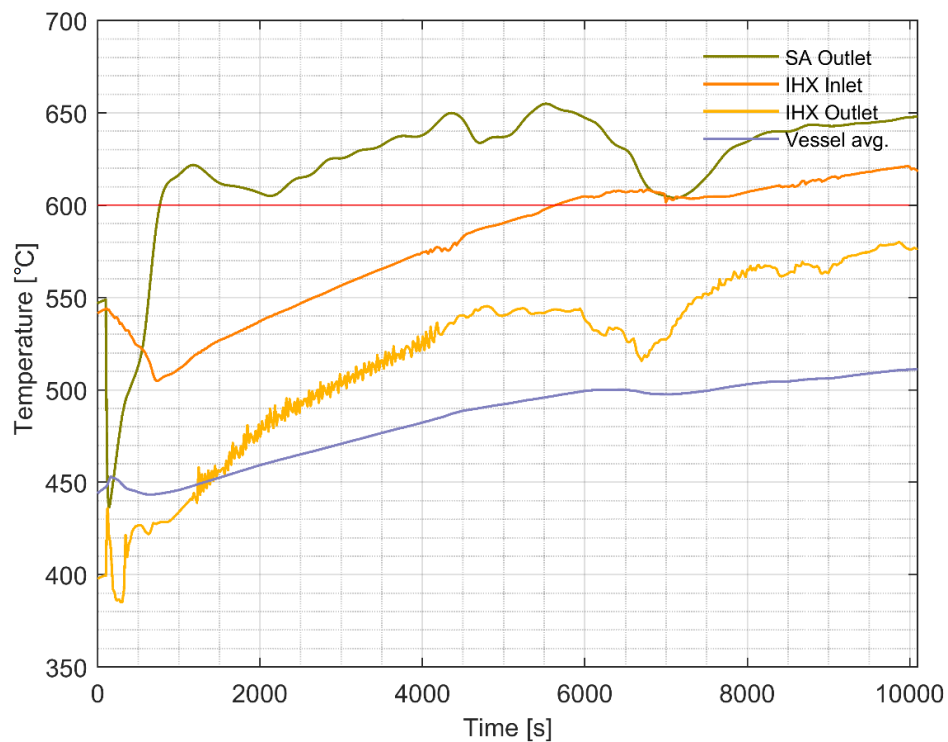


Figure 52. Primary sodium temperature evolution during the accident using only DHRS-2

To further investigate the reason for the less smooth temperature evolution, the sodium flowrate in the secondary circuit has been visualized in Figure 53. This Figure reveals that there is a fluctuating behavior of the flow direction in the circuit prior to the air inlet opening of DHRS-2, also observed in the “no feedwater” case simulation without DHRS. These instabilities are not eliminated after air inlets of DHRS-2 are open, due to a relatively weak natural circulation head in the system and a strongly non-uniform sodium temperature profile along the loop. To reduce this instability in the flow, the implementation of a TE pump has been proposed, similar to the one used for DHRS-1.

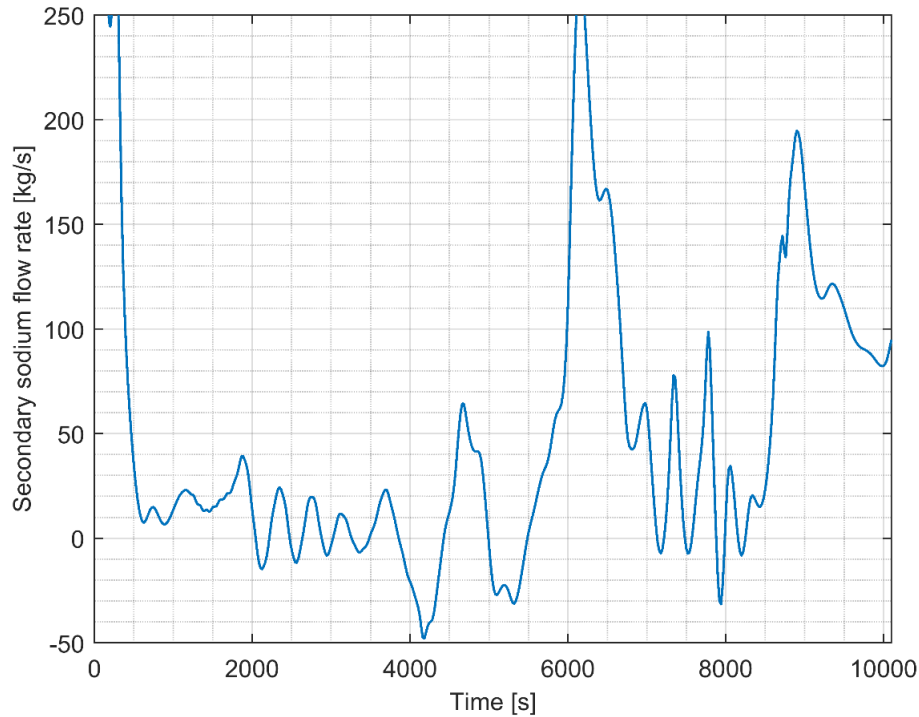


Figure 53. Temporal evolution of the secondary system sodium flowrate

3.2.3.3.2. DHRS-2 sensitivity study

To assess the required pressure head produced by the TE pump for the stabilization of the flow in the secondary circuit during the accident and potential improvement of the DHRS-2 heat removal capabilities, a sensitivity study has been performed. In this study, the TE pump was simulated as a centrifugal pump, established with a constant 5% and 7% of the nominal pump rotation speed in the circuit following the initial pump run out. The corresponding pressure head increase in the circuit is ~ 0.8 kPa and ~ 1.35 kPa for the 5% and 7% pump rotation speed supply, respectively. Using a centrifugal pump for the sensitivity calculations can be justified, as the hot leg temperature in the secondary circuit is relatively stable at $\sim 600^\circ\text{C}$ (being close to the IHX primary side inlet temperature), which would drive the TE pump and, therefore, would ensure a stable pump performance. Furthermore, the study is performed mainly to assess at which flowrate can a stable secondary flow be achieved, which may serve as input data for the required TE pump geometry calculation. The resulting temporal evolutions of the DHRS-2 evacuated power, temperatures at different locations, and mass flowrate in the secondary circuit are presented in Figure 54.

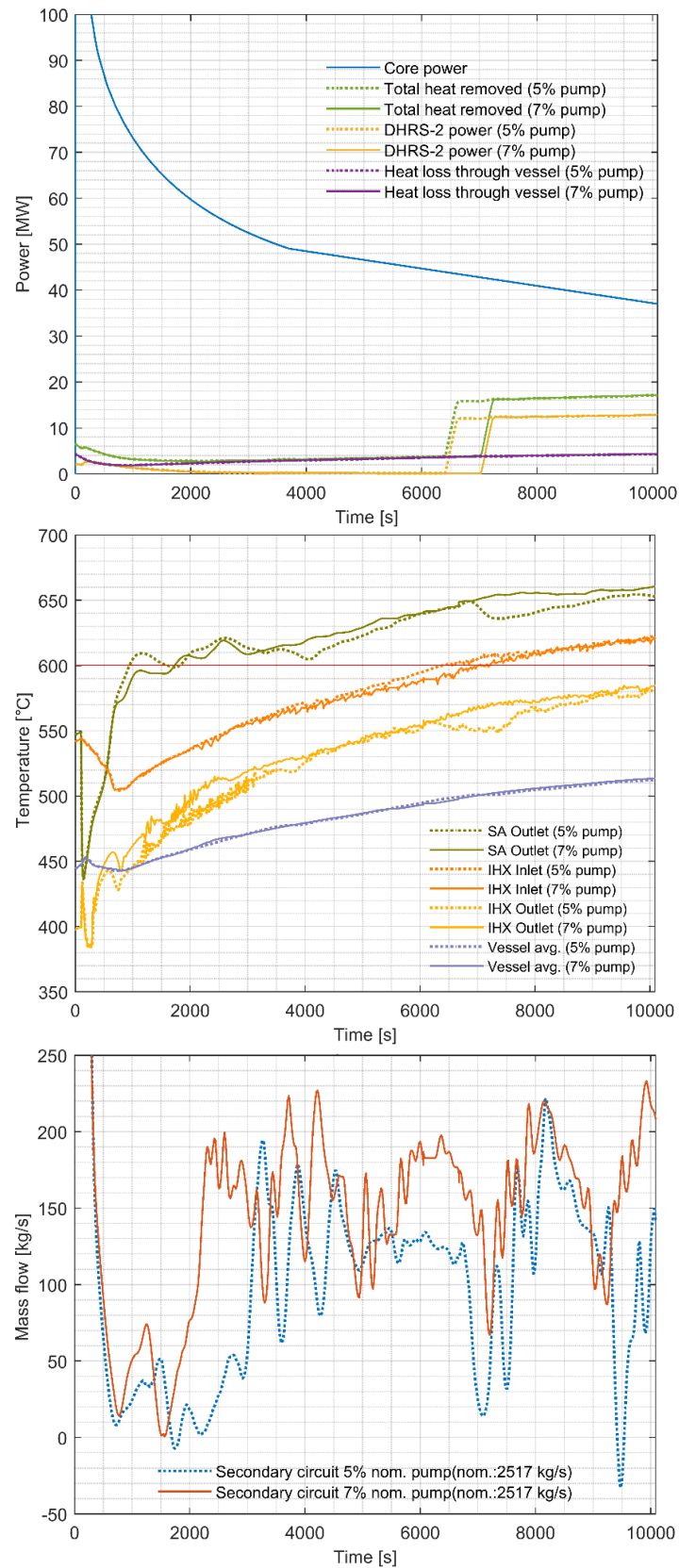


Figure 54. DHRS-2 power (top), primary sodium temperature (middle), and secondary flowrate (bottom) evaluation by using 5% versus 7% nominal pump rotation speed

The flow is more stable when a pump is used on the circuit, but to completely eliminate the flow reversal, at least 7% of the nominal pump rotation speed is required to be supplied by the TE pump. When the evacuated power is compared between 5% and 7% cases in Figure 54, no noticeable difference can be realized. Whereas for the temperature evolution, the more stabilized flow has a clear effect on the smoothness of the curve as a result of the more uniform heating up of the secondary sodium along the loop. Correspondingly, the activation of the DHRS-2 air flow is delayed by about 1000 s and 1500 s for 5% and 7% cases, respectively, as compared to the reference case. The temperature increase is more linear, which corresponds well to the flow Figure (Figure 54, bottom plot), where it is shown that the flow fluctuation is decreased and the flow reversal is eliminated with the 7% pump rotation speed supply.

Another study has been performed, which was aimed to assess the possibility of the increase of the DHRS-2 heat evacuation capability. Two different scenarios have been investigated: 1) For the first one, the sensitivity of the air flowrate on heat removal has been assessed by increasing the flowrate from 23 to 50 kg/s assuming an ultimate upper boundary achieved for the air natural circulation flow in the chimney; 2) In the second case, the previously introduced 50 kg/s flow was kept, but the DHRS-2 initiation temperature was decreased from 600°C to 550°C. Both cases were modeled by using a TE pump, thus providing a conservative value of 5% of the nominal pump rotation speed (corresponding to the study above).

In the previous study [73], it has been shown that there is a strong correlation between an increase of air flowrate in the SG casing and the removed heat by the system. Based on this, it was expected to see that by simply increasing the air flowrate to 50 kg/s, the removed heat would be closer to the total produced power in the reactor core. On the contrary, as it is shown in Figure 55, the power removed stayed at 14 MW giving nearly the same result as in the reference case. This phenomenon can be explained by considering that the increase of the air flow from 23 kg/s to 50 kg/s results in the correspondingly almost two-fold decrease of the air heat-up and a minor increase of the power removed because of the very low heat exchange efficiency on the airside determined by both low heat exchange coefficient and low heat exchange surface area. In line with this outcome, the temperature evaluation in the reactor stayed unchanged as well.

In the second case, where the initiation temperature was lowered by 50°C, as expected, the removed amount of power remained the same as in the first case. Nevertheless, the respective temperatures have been decreased at the same time points since the system started to remove power from the reactor around 4000 s earlier.

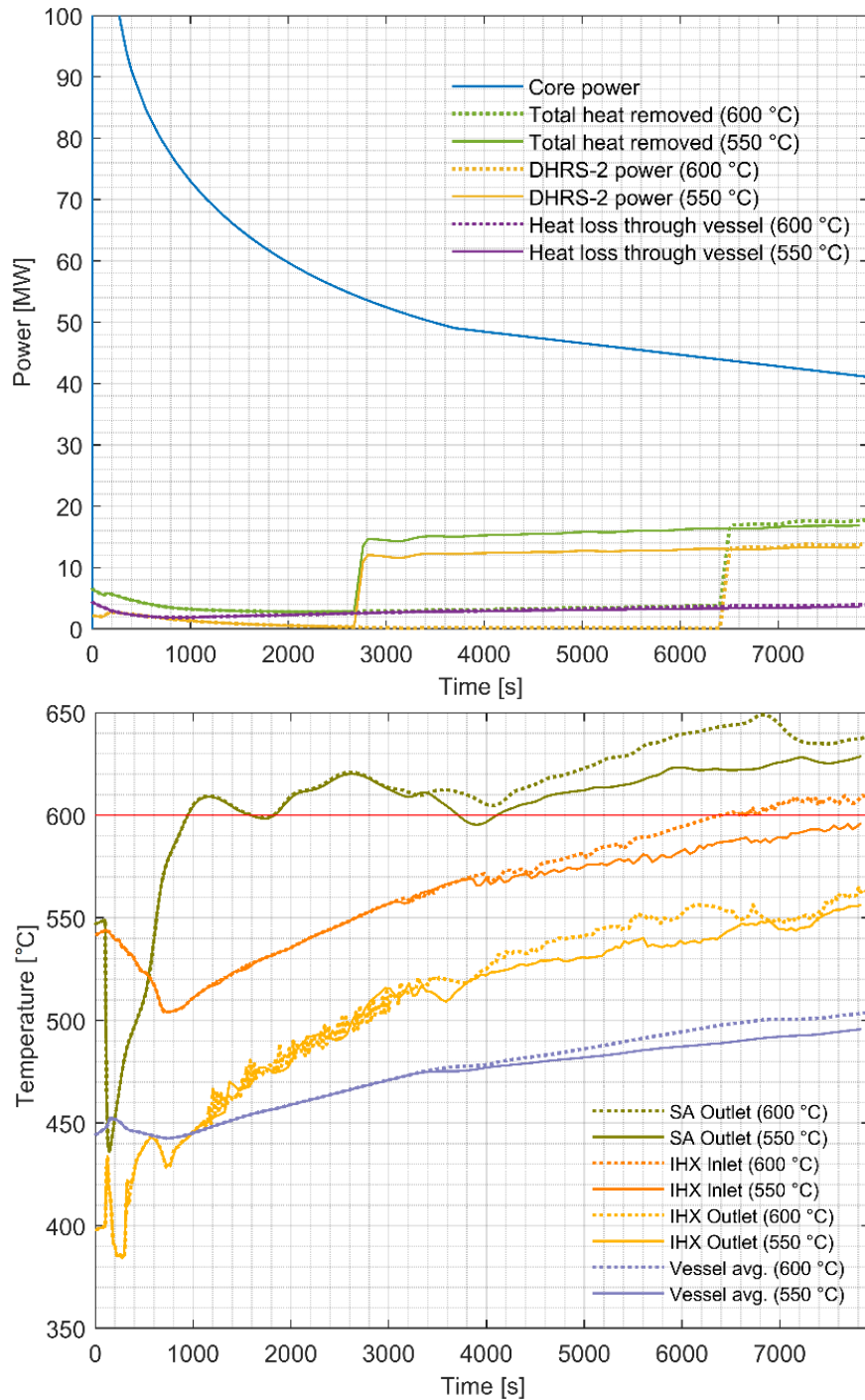


Figure 55. DHRS-2 power (top) and primary sodium temperature (bottom) evaluation by using 50 kg/s air flow at 600°C and 550°C temperatures limits as signal for the air inlet opening

3.2.3.4. DHRS-3 simulation results

Looking at the DHRS-3 removed power over the time of the accident, as shown in Figure 56, it is clear that it is indeed not possible to safely remove enough decay heat from the reactor after its shutdown using only this type of decay heat removal route. The overall behavior of the system is very similar to the “loss

of secondary circuit” case discussed in Section 3.2, as the evacuated power by DHRS-3 is much smaller compared to other DHRS. As the primary system is heating up and the temperature of the vessel wall is increasing, the removed heat by the DHRS-3 is increasing as well. The simulation, due to time constraints, was limited to 10000 s, and by the end, it removes around 1/4th of the total decay heat produced in the reactor. In this way, though alone it is not sufficient to remove the whole residual power, it is shown that it can be of significant support to any of the other two DHRS.

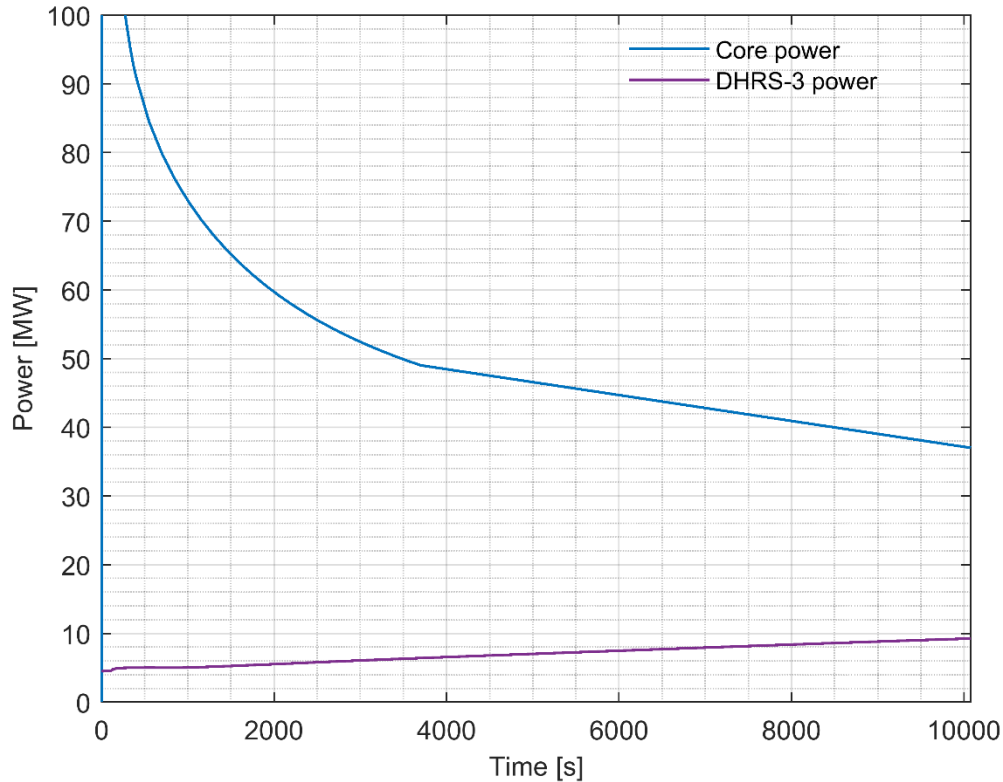


Figure 56. DHRS-3 heat removal capability used as an individual heat removal option

No oscillations of the temperatures in the primary system are observed in case of DHRS-3 operation, which can be explained by the fact that the heat removal does not depend on the flow in the secondary or primary circuit. In this sense, the temperature at every point of the reactor’s primary system is gradually increasing. The observed temperature values in Figure 57 indicate that the reactor is still far away from any serious damage as there are still great margins for both cladding and structural elements, not to mention the fuel, which, by using the control rods, are at a lower temperature value compared to nominal conditions. Nevertheless, further investigation revealed that though the average vessel temperature is still acceptable being at ~550°C, the maximum vessel temperature is approaching the predefined temperature safety limit of 650°C at the end of the simulation. The criterion of maximum vessel temperature would not allow the use of DHRS-3 as the only DHRS of the reactor, although its performance is increasing with time, due to reaching the temperature limit at the top of the vessel around the hot pool. From the Figure, it is also clear that the temperature of the concrete is of no concern for the simulated period of time as, due to the high volume and insulation between the vessel wall and the concrete, the maximum temperature is nearly not affected (increased by less than 1°C), and thus the 70°C limit is still far away.

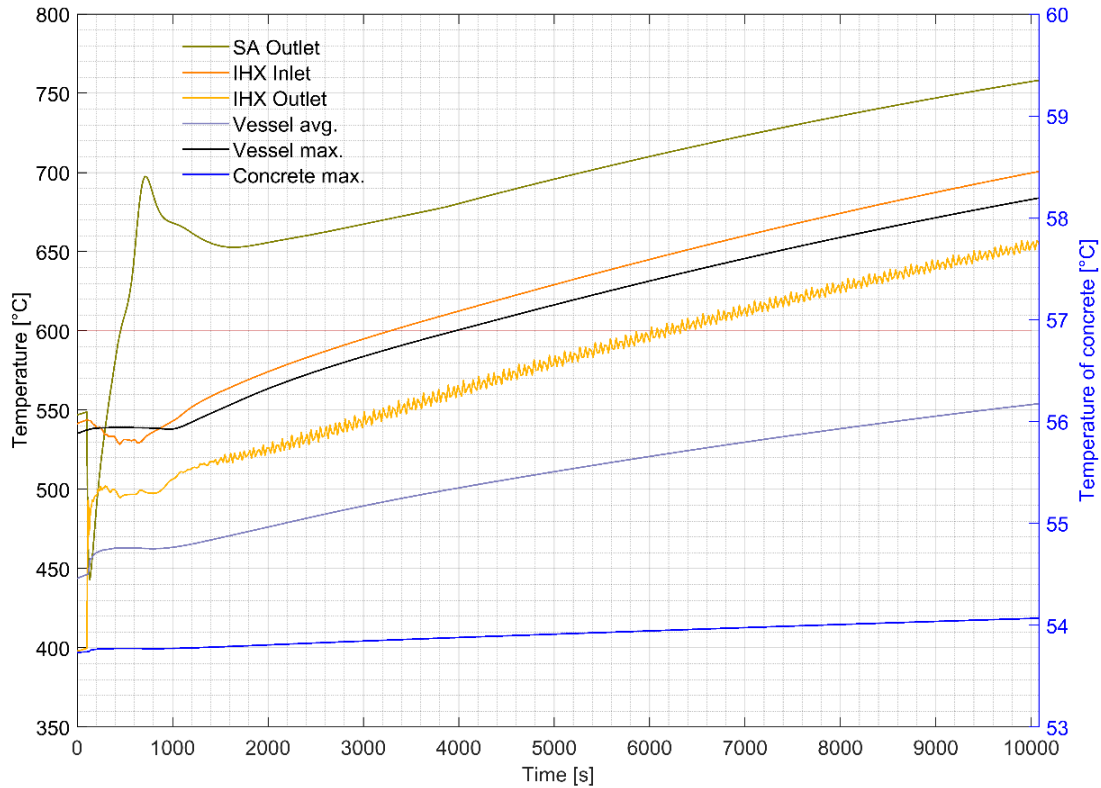


Figure 57. Primary sodium temperature evolution during the accident using only DHRS-3

3.2.4. Multiple DHRS cases

A sensitivity study has been performed to assess the DHRS behavior when they are operated not separately but according to the design specification – using at least two systems in parallel. These scenarios correspond rather to normal reactor shutdown when the DHRS are used routinely to evacuate the decay heat. As the overall DHRS behavior follows the same pattern for the multiple systems as it is for the individual ones, the Section is focused on the difference in grace time given by the reactor for the various DHRS arrangements.

3.2.4.1. DHRS-1 and DHRS-3

The first set-up discussed hereafter is the case where DHRS-1 and DHRS-3 are used in parallel. As the previous studies have revealed, it seems that DHRS-1 is most efficient to keep the reactor stable and safely remove the decay heat. In this sense, this set-up has the greatest potential to be used as the main line of defense in case of an accidental scenario. In Figure 58, the power removal is plotted for the two different DHRS arrangements. The Total heat removal term in the Figure refers to the case where the heat dissipation through the reactor pit is added to the DHRS-1 heat removal or when both DHRS-1 and DHRS-3 are used, then their heat removal is added together. The DHRS power lines describe the heat removal of each DHRS separately, same as in the previous plots, and following their names, in parenthesis, the specific arrangement is given, either DHRS-1 used alone, or DHRS-1+DHRS-3 used together. From this

plot, it can be seen that by having the two DHRS implemented, the grace time of the reactor increases by ~200 s compared to the single DHRS-1 heat removal option.

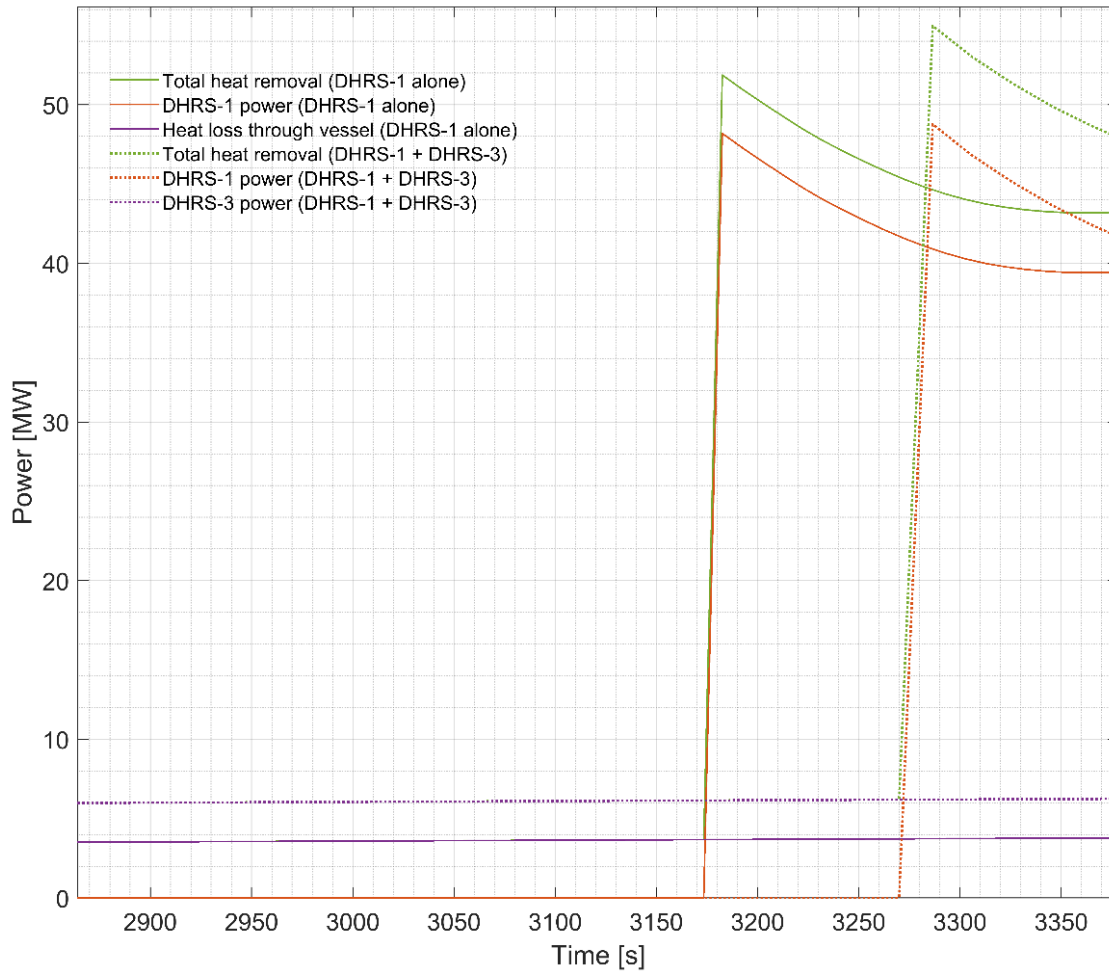


Figure 58. DHRS-1 initiation time comparison by DHRS-1 alone versus DHRS-1 and 3 together

3.2.4.2. DHRS-2 and DHRS-3

To complete the evaluation of the possible scenarios, a calculation has been performed when DHRS-2 and DHRS-3 are being operated simultaneously. Figure 59 shows the results of these simulations with identical plot naming logic to the DHRS-1 + DHRS-3 case. Similarly also to this previous case, the grace period increase was quantified by using the two DHRSs together in comparison to the individual DHRS-2 operation. The plot shows the grace time increase of 500 s until the DHRS-2 power removal begins, thus providing some extra safety margin to the reactor design.

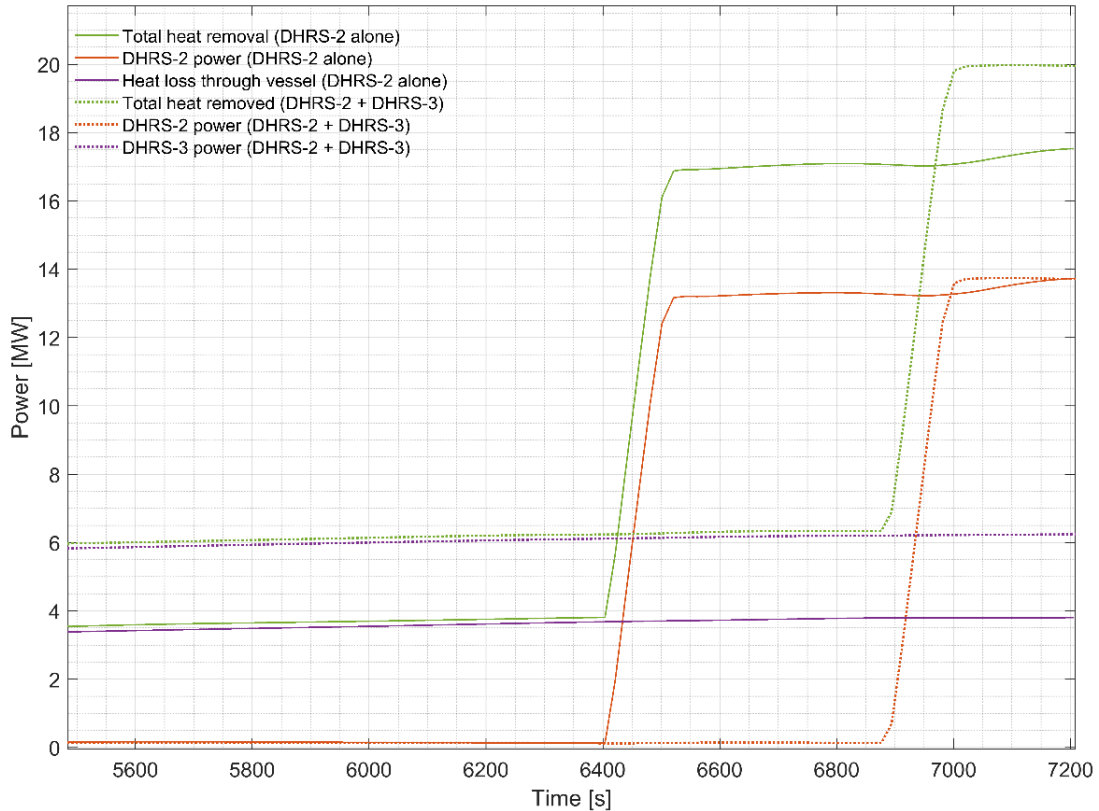


Figure 59. DHRS-2 initiation time comparison by DHRS-2 alone versus DHRS-2 and 3 together

3.3. Assessment of ESFR decay heat removal with updated secondary circuit design

3.3.1. Modified secondary circuit design

Within the thesis work, an optimization study of the secondary loops has been performed. In this study the previously applied design with long bends on the piping, to account for the thermal expansion, has been revised and instead the design features applied on the BN-1200 project have been proposed [33], [34]. The modification was intended to achieve various safety and cost related benefits, such as:

- 1) shorter pipe lengths,
- 2) decreased sodium volume in the loop,
- 3) reduced overall size of the secondary system building,
- 4) more efficient pipe supports against earthquakes,
- 5) reduced probability for sodium leaks due to fewer welding as a results of the simpler circuit layout,
- 6) common chimney for DHRS-1 and DHRS-2 allowed by the closer location to each other.

Furthermore, the current assessment is performed to analyze the effect on the DHRs system behavior, especially in relation to the previously observed undesired behavior during establishment of the natural circulation conditions in the secondary circuits, described in Section 3.2.3.3. With the shorter pipe lengths, it is assumed that the optimized design would increase the efficiency of the natural convection within the loop due to the decreased pressure drop. Moreover, the height difference between the IHX (lowest point) and SG (highest point) has been increased ~5 m, to facilitate the straight pipe design, which also supports the better natural convection establishment.

The modified circuit includes certain new components, called bellows, which have a wave like surface in order to accommodate the thermal expansion of the connected pipes. This component have been successfully implemented in the Phenix and Superphenix reactor designs [10], though not on the secondary circuit but as part of separate components, such as the Superphenix heat exchanger. Using this element, it is possible to use straight tubes in-between connecting components, such as the IHX, the secondary pump and the SGs. In Figure 60, the proposed optimized design is shown, displaying the simplicity of the piping structure. To reduce the secondary system building size even further, the DHRS-1 and DHRS-2 have been moved closer to each other, so that one common chimney could be used for both systems.

The straight pipe design, allowing the SGs to be moved closer to the IHX, carries significant pipe length reduction possibility, shown in Table 10. The 850 mm diameter main pipe length could be reduced by 66%, whereas the 350 mm diameter pipe length, which connects the individual SGs to the main pipe, has been reduced by 92%. Similar improvement has been achieved on the available sodium volume in the circuit, 68% and the required land area for the primary and secondary system buildings have been reduced by 66%. These improvements highlight the potential cost reductions related to the secondary system building of the reactor.

Modified component	Reference secondary loop	Modified secondary loop
850 mm diameter tube length	195 m	67 m
350 mm diameter tube length	150 m	12 m
Sodium volume	116 m ³	37 m ³
Primary and secondary system building area	6537 m ²	2881 m ²

Table 10. Comparison of pipe lengths, sodium volume and building surface area between the reference and modified secondary loops

Figure 61 shows the optimized secondary circuit layout around the reactor pit. Using a common chimney for the DHRS-1 and DHRS-2 allows moving the SG units close to the primary circuit, in a circular radial arrangement, with which further pipe length reduction could be achieved. In Figure 62, the potential secondary system building size reduction is shown, with the new circular arrangement, for the comparison of the required building surface of the reference and the optimized arrangements, the actual values are given in Table 10.

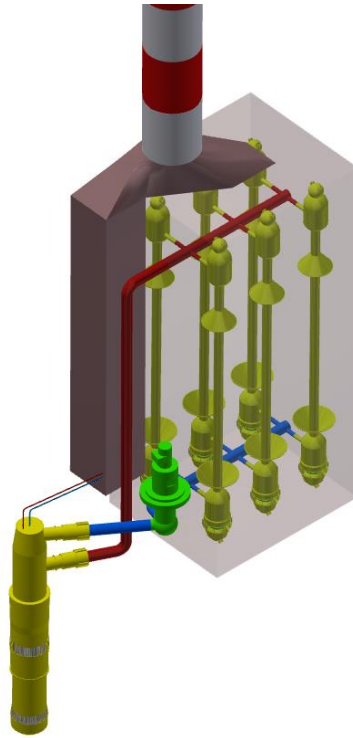


Figure 60. Modified secondary circuit design with DHRS-1 and DHRS-2 with the common chimney for both systems [34]

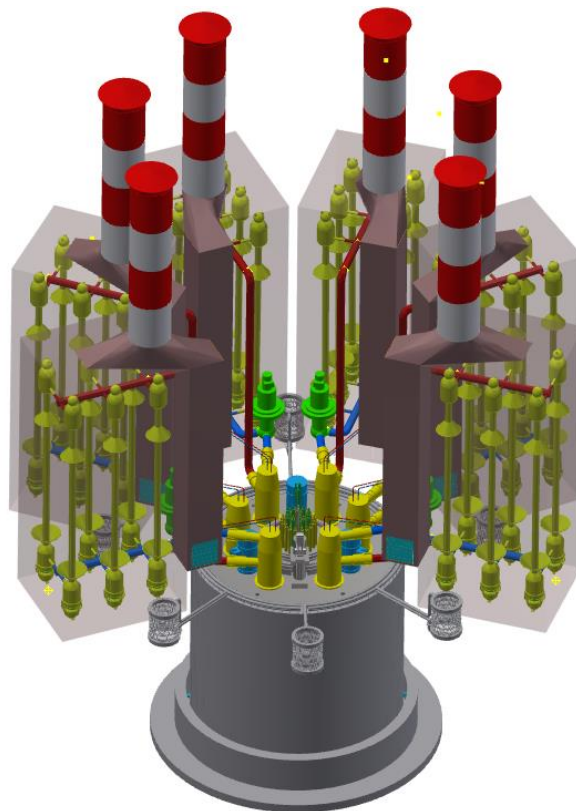


Figure 61. Optimized layout of the secondary circuits having a circular distribution around the primary system [34]

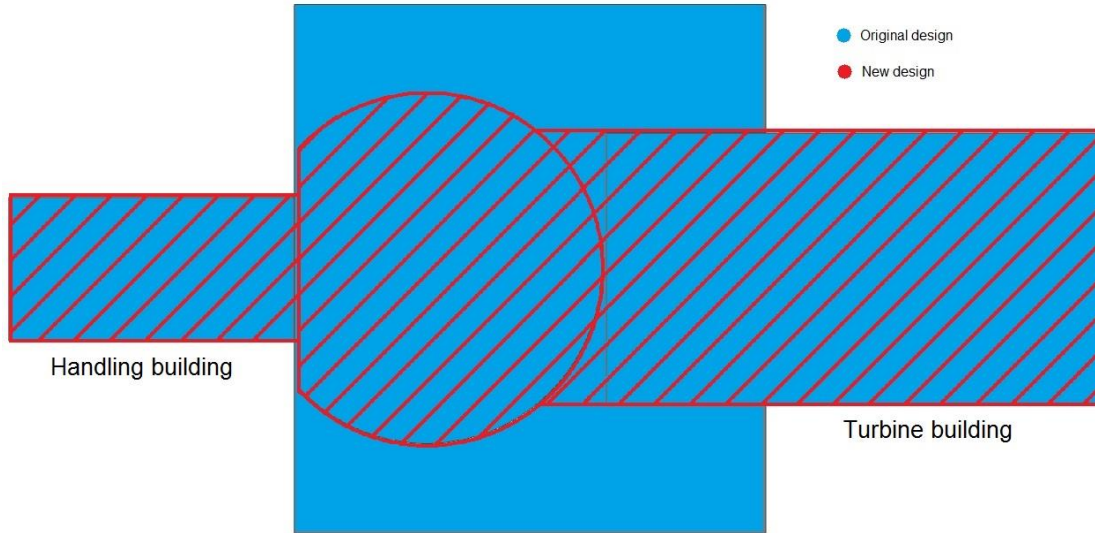


Figure 62. Layout comparison of the optimized circular secondary circuit and the reference system arrangement [34]

3.3.2. Simulation results for PSBO scenarios with no DHRS activated

Similarly to the assessment of reference design, the calculations were made to assess the reactor behavior for the modified design of the secondary system under PSBO scenario without any DHRS implemented in the model. The feedwater and the no feedwater cases have been analyzed, shown in Figure 63, as the loss of secondary circuit would lead to the identical results as before, as no modifications on the primary system were considered.

When the results are compared to the feedwater case, where 5% of the feedwater supply is retained as heat sink, the secondary flow shows a different behavior than before (Figure 43). It starts with a high frequency fluctuating behavior, which gradually decreases into a steady flow at around ~ 3500 s following the transient initiation time. This is in contrast of the reference design where the fluctuation has a lower frequency and within the simulated timeframe, the fluctuation height seems to rather increase in magnitude (Figure 43). The origin of this fluctuation is concluded to be the same for both results, meaning a temperature variation within the secondary sodium along the pipes. The higher frequency fluctuation for the modified design can be attributed to the shorter circuit, therefore the time required for the different temperature sodium plug to make a full cycle is decreased by a factor of 3 and the temperature deviation can be smoothened faster than in the reference design. In this way, it is possible to see the smooth flow behavior faster, already within the 5000 s simulated time period.

The assessment of the no feedwater case shows, overall comparable behavior within both the reference and the modified circuits. Differences which can be seen, is the stronger reduction in secondary flow soon after the initiation of the transient, which can be attributed to the lower sodium volume and thus smaller inertia within the system. This initial difference decreases the primary flow also into a lower level than

before but it quickly recovers. Following the initial decrease of flow, the secondary flow starts a high frequency oscillatory behavior until it recovers and displays a net flow after ~2000 s. This is the strongest deviation between the reference and the modified design, as with the reference there is no flow recovery but it keeps on oscillating around 0 kg/s flow throughout the simulated time period.

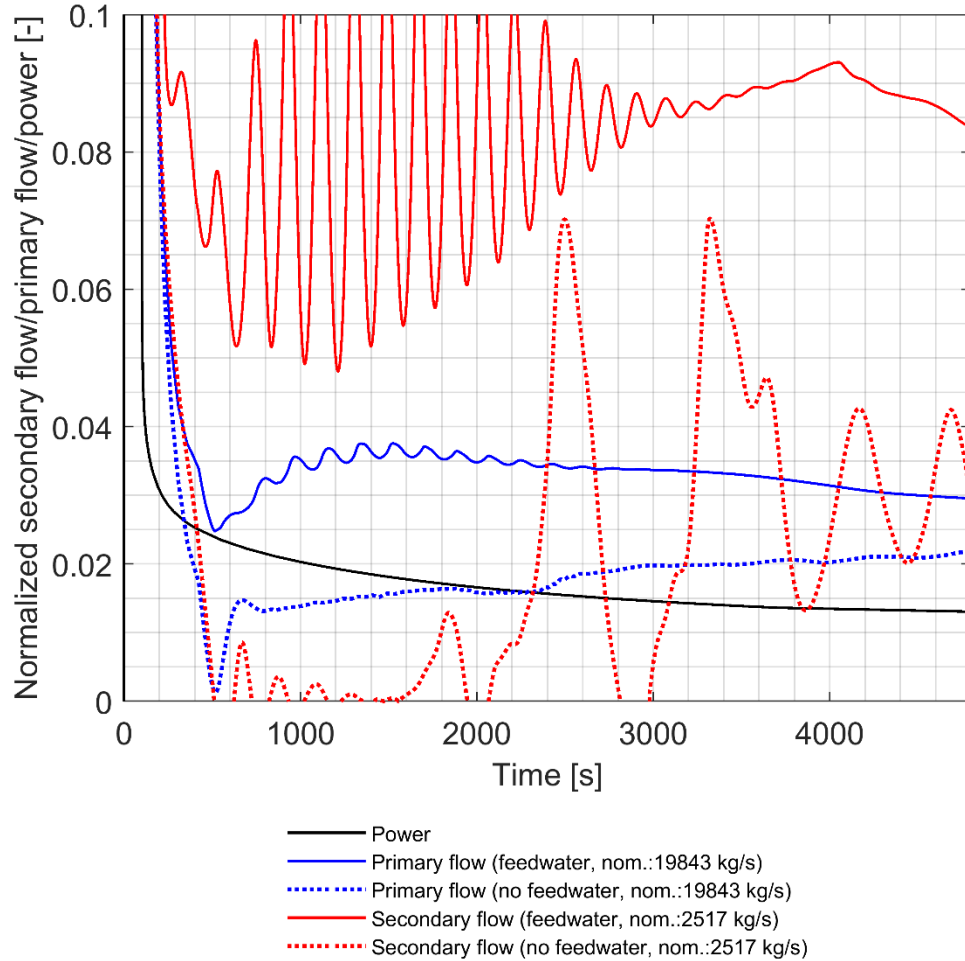
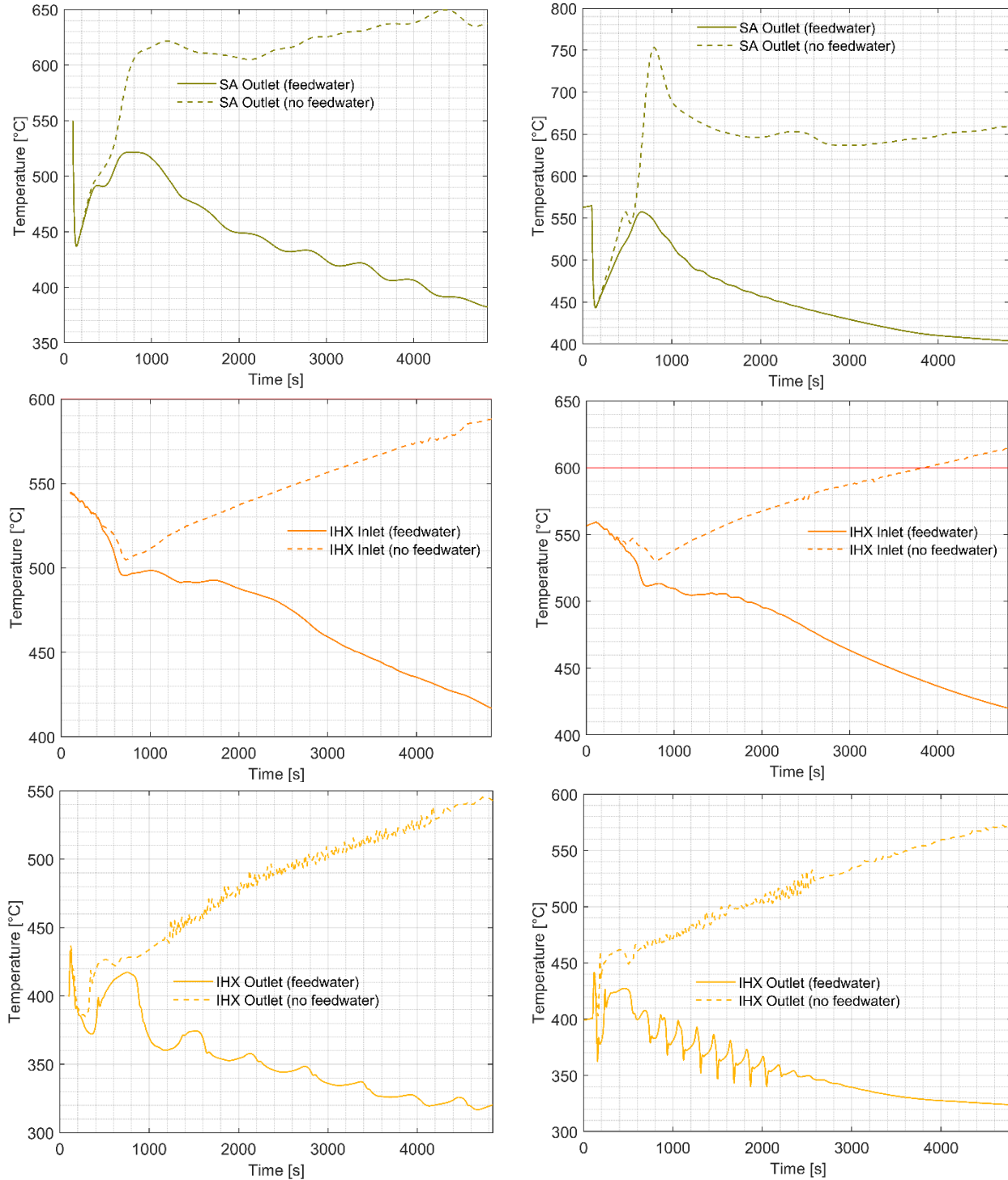


Figure 63. PSBO reactor behavior assessment without the use of DHRs using the feedwater and no feedwater cases

The temperature evolution comparison at different locations of the primary system is shown in Figure 64. Again only the feedwater and no feedwater cases are presented as of interest. The overall temperature evolution in the curves are comparable. For the feedwater case, the obtained temperature level is nearly identical by the end of the simulation but the higher frequency fluctuation, compared to the reference design results, is also visible in these plots, especially in the IHX inlet Figure. As Figure 63 displays the smoothening of the secondary flow level, it has a direct effect on the primary temperature evolution also, as after ~3500 s, the temperature variation smoothenes.

The assessment of the no feedwater results reveals a generally higher primary circuit temperature level throughout all presented locations. It is especially visible at the SA outlet location where the initial temperature increase is ~130 °C higher for the modified secondary circuit. This general temperature

increase can be understood when the primary flow drop is assessed in Figure 63, ~500 s following the transient initiation. This shows that the flow nearly stops in the primary system, causing a high temperature increase, potentially reaching close to the sodium boiling level at certain higher power SAs.



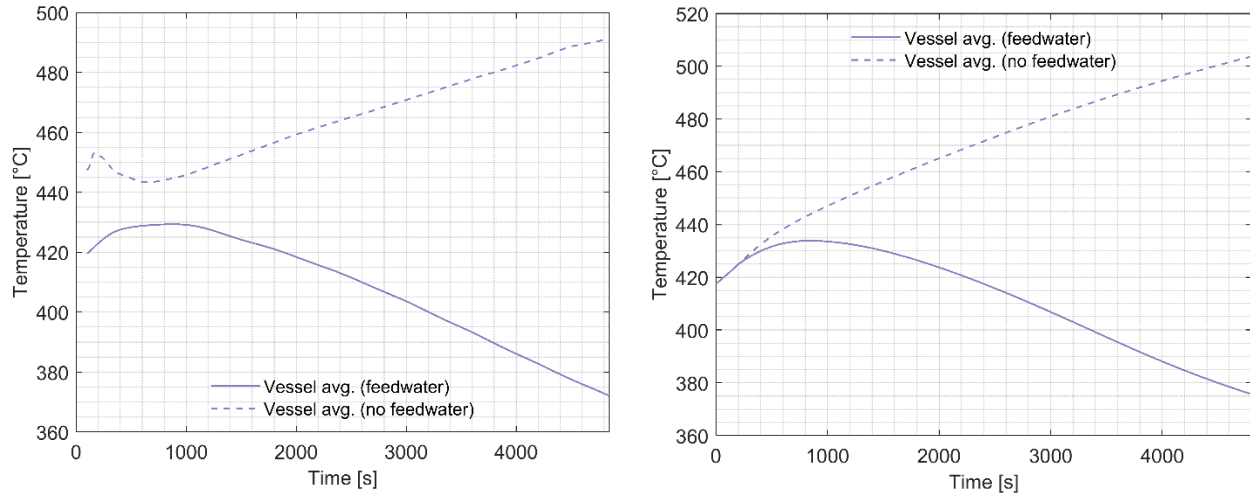


Figure 64. Primary sodium temperature comparison between reference (left) and modified (right) secondary loop design for SA outlet, IHX inlet, IHX outlet and vessel average temperatures

3.3.3. DHRS-1 simulation results

It is an important safety assessment that the operation of the main DHRS systems are not altered negatively with the introduction of a new secondary circuit design. Therefore, the power removal capability and the primary circuit temperatures have been assessed for the DHRS-1 and DHRS-2 operation.

In Figure 65 the DHRS-1 power removal capability is presented when it is the only operating DHRS. The Figure displays that the operation of DHRS-1 has not changed significantly, which is according to expectations, as the main difference compared to the reference DHRS-1 solution is the reduced secondary sodium heat capacity due to reduced volume. The overall removed power is comparable to the case when the reference secondary circuit design is used. The two main differences are the ~100s earlier initiation time and the ~1 MW power removal increase. This difference mainly comes from the fact that there is a higher DHRS-1 loop flowrate in the system for the modified design, ~38 kg/s, compared to the reference design, where it is ~27 kg/s, shown in Figure 66. With the higher flowrate the average temperature difference in the sodium-air heat exchanger is higher for the modified case, thus with the same airflow rate, there is an increase in the total removed power.

In Figure 67, the temperature values show close similarity again for both simulations. The SA outlet temperature initially goes ~30 °C higher than for the reference case but within ~400 s it recovers to the same value. This is due to a lower initial primary flowrate as it was observed for the no DHRS cases also. The IHX inlet temperature, as it was for the SA outlet also starts with a higher temperature value of ~5 °C until it reaches the DHRS-1 initiation temperature of 600 °C, which results in an earlier DHRS initiation time point. Following this point, it gradually decreases under the temperature value observed for the reference case, due to the higher DHRS-1 heat removal capacity. The average vessel temperature follows the same evolution for both simulated cases, the only difference is that for the modified design it is ~5 °C lower, due to the lower average primary system temperature. The greatest deviation between the temperatures is seen on the IHX outlet temperature, where for the modified design the temperature

value is $\sim 25^\circ\text{C}$ higher. This can be attributed to a higher sodium flowrate in the primary system, $\sim 15\%$, shown in Figure 66, and therefore the temperature decrease is reduced. The increase in primary system flowrate is assumed to come from the increased heat removal capacity with DHRS-1.

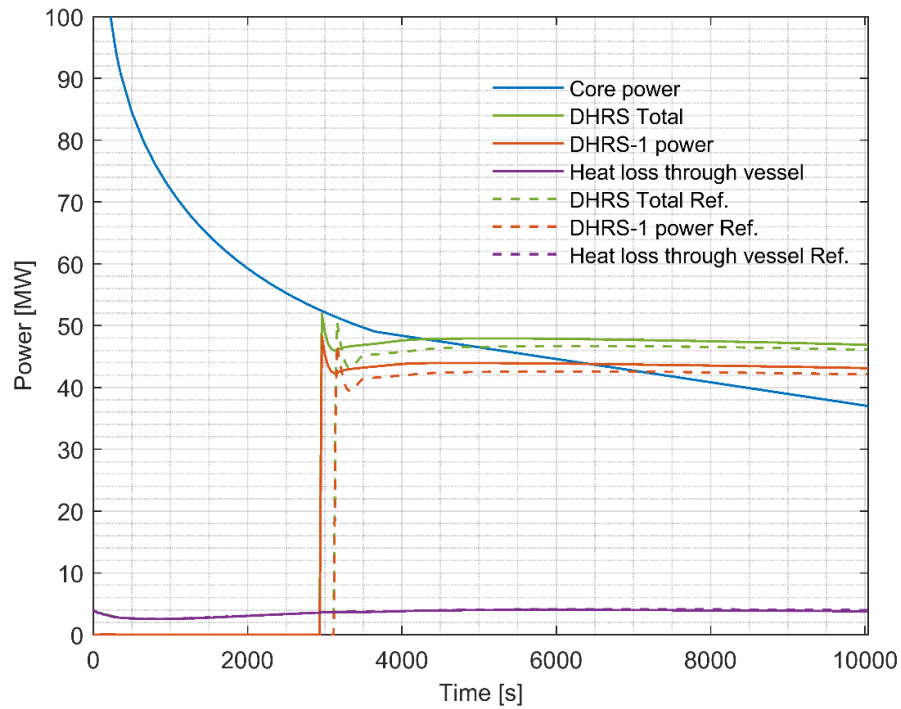


Figure 65. DHRS-1 heat removal capability comparison between modified and reference secondary circuit design used as an individual heat removal means

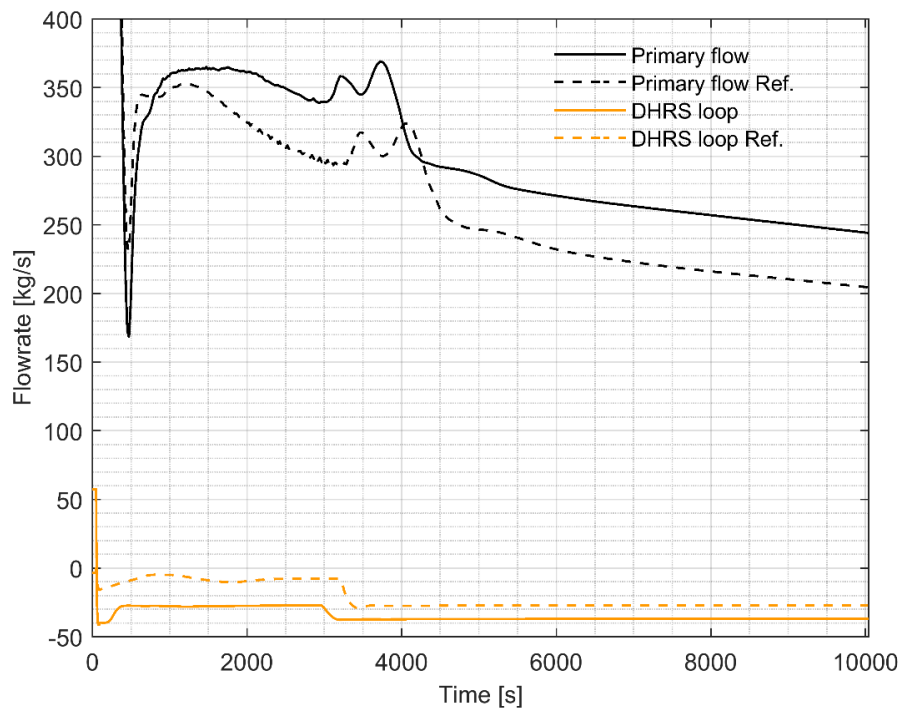


Figure 66. Primary and DHRS-1 flowrate comparison between reference and modified secondary loop designs

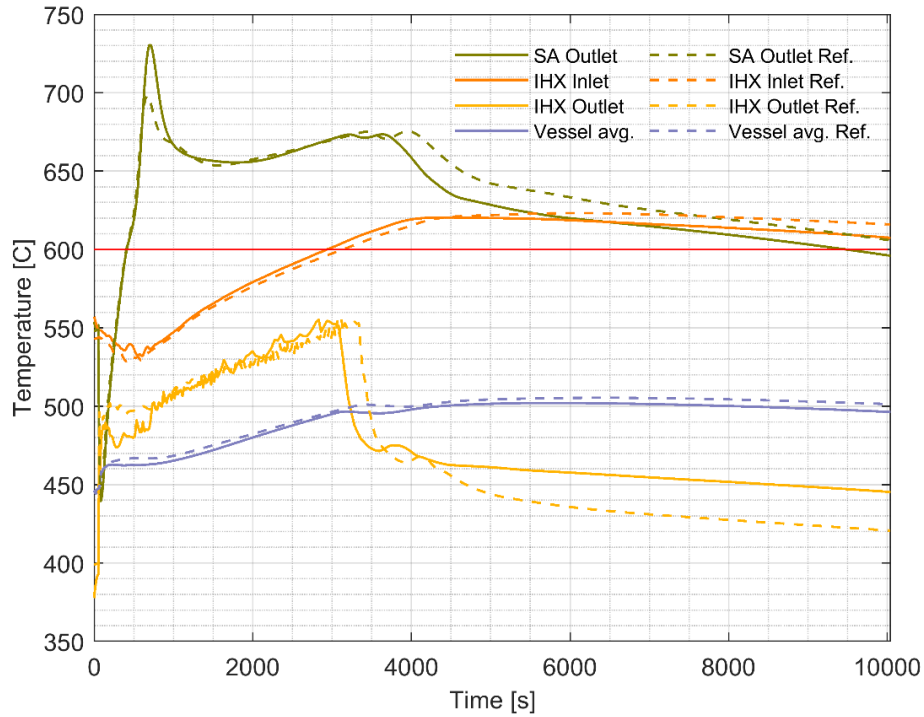


Figure 67. Primary sodium temperature evolution comparison between modified and reference secondary circuit design using only DHRS-1 heat removal

3.3.4. DHRS-2 simulation results

In the evaluation of the DHRS-2 system, it was expected that the difference, introduced by the new secondary circuit design, should be higher than it was for the DHRS-1, owing to the fact that to remove the heat from the SG, the whole circuit with new design is used. In this sense, Figure 68 shows ~2 MW power removal increase compared to the reference design case, which is ~13% efficiency increase. This increment comes from two sources, on the one hand the DHRS-2 unit removes more heat due to a general increase in the primary system temperature, shown in Figure 69 and the available tough fluctuating net secondary sodium flow, shown in Figure 70. On the other hand heat loss through the vessel is also increased due to the higher average vessel temperature ~20 °C. These two sources add up to the overall ~13% power removal increment. Nevertheless, even with this heat removal increment, the DHRS-2 units alone are still not capable of removing sufficient heat to keep the reactor under the predefined limiting temperatures. Throughout the simulated timeframe the temperatures are rising and the produced power in the core is still significantly higher than the removed heat.

The overall higher temperatures shown in Figure 69 come from the same source as it was for the no DHRS case, namely the greater initial primary sodium flow decrease with the new secondary loop design, described in Section 3.3.2.

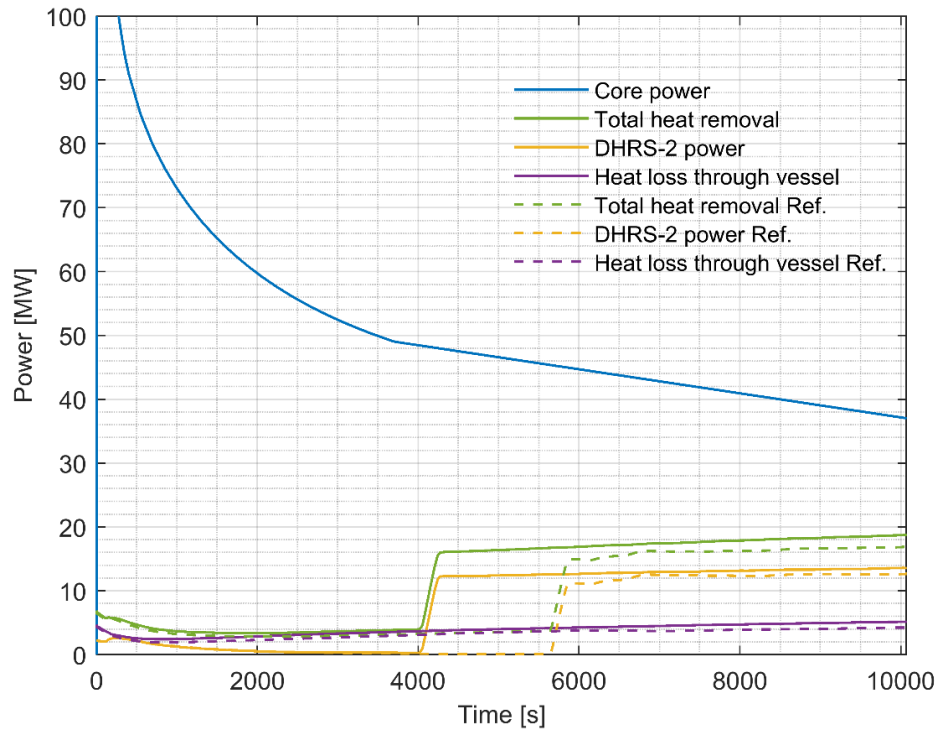


Figure 68. DHRs-2 heat removal capability comparison between modified and reference secondary circuit design used as an individual heat removal means

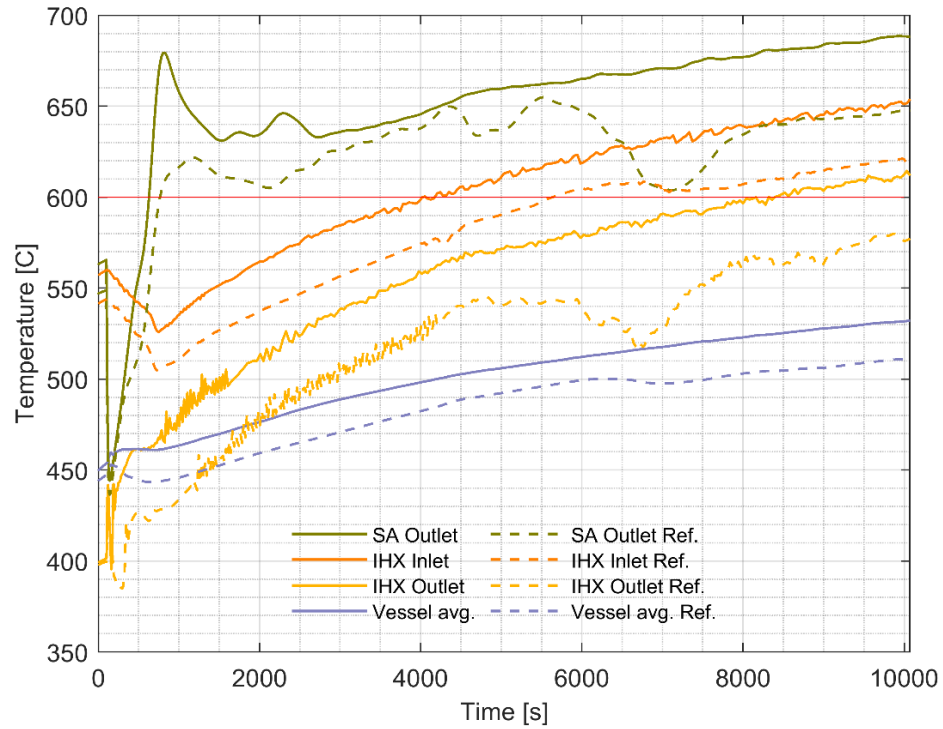


Figure 69. Primary sodium temperature evolution comparison between modified and reference secondary circuit design using only DHRs-2 heat removal

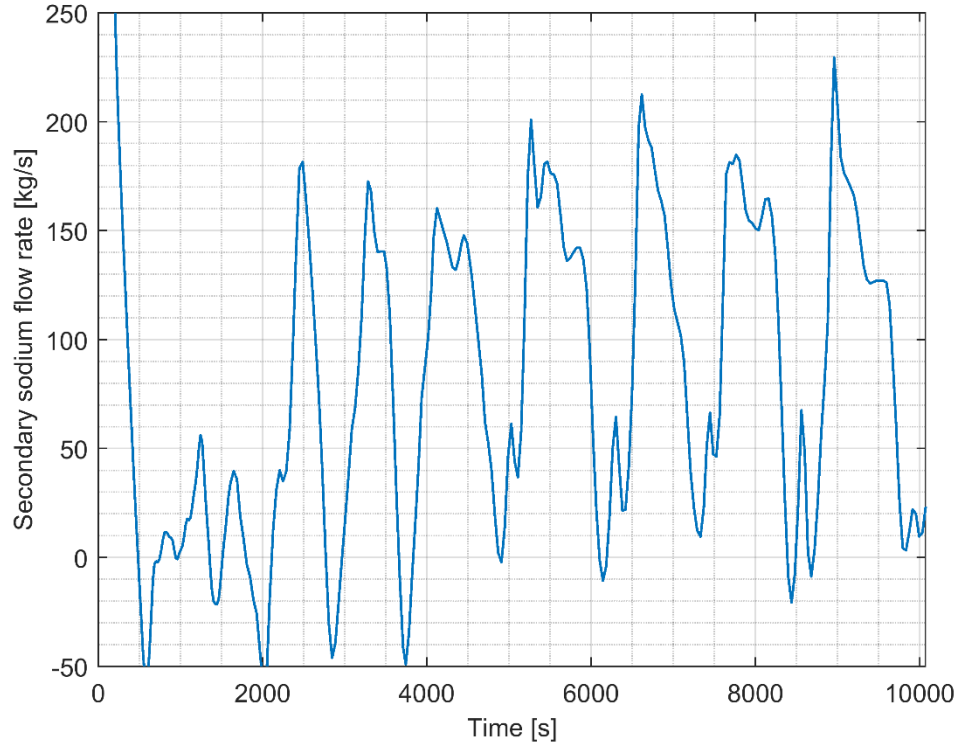


Figure 70. Temporal evolution of the secondary system sodium flowrate within the modified secondary circuit

3.4. Conclusions of Chapter 3

In the Chapter, the ESFR behavior under PSBO transient conditions has been investigated using multiple DHRS arrangements and base cases where no DHRS have been used. The assessment has been performed for the reference secondary circuit design and for a modified design using shorter straight pipe layout with bellows to compensate for thermal expansion. A full reactor model, with its secondary and tertiary circuits, has been developed in the TRACE thermal-hydraulic code and individual DHRS models and their performance have been described and analyzed.

The PSBO cases, where no DHRS has been used, showed the reactor behavior in three different settings, serving as the base models for the various DHRS implementations. As for the various DHRS assessment, the results can be summarized as follows.:

- DHRS-1 alone (6 units), in the case of the simulated transient scenario, is removing ~ 42 MW, which is higher than the produced decay power in the reactor core after about 7000 s following the accident, with a rather stable heat removal characteristic. Thus, after air inlet opening of DHRS-1, ESFR can be safely cooled down using only this DHRS. Besides, through the auxiliary pump study, it was shown that the initial reversed flow in the circuit could be counteracted to obtain the designed flow direction.
- The DHRS-1 assessment with the modified secondary circuit reveals only marginal differences compared to the reference design. In this sense, there is a 1 MW increase in heat removal, as a result of

the higher primary system temperatures due to the lower heat capacity of the reduced secondary sodium. Caused by the quicker temperature increase, the DHRS initiation time occurs earlier for the modified case by ~200 s.

- DHRS-2 alone, in the case of the simulated transient scenario, is removing ~13 MW following the air inlet opening, with the tendency to slightly increase heat removal with time. However, the DHRS-2 only does not assure that ESFR can be safely cooled down during the simulated PSBO transient because all primary cooling circuit temperatures continue increasing, thus approaching the upper temperature limit (650°C) for the reactor vessel. Furthermore, to stabilize the sodium flow in the loop following the pump trip, an auxiliary pump could be implemented in the circuit, providing an extra pressure head, supporting the natural convection in the system.
- The DHRS-2 assessment with the modified secondary circuit, as was for the DHRS-1 case, removes more heat from the system, ~13% higher than with the reference design. This improvement originates from two factors: 1) The overall primary system temperature is increased, just as for DHRS-1 and 2) the natural convection provides an overall positive net flow in the circuit. With the new system, the auxiliary pumps could be potentially removed but the heat removal capability of the system is still not sufficient in itself to keep the reactor long term under the limiting temperatures.
- DHRS-3 alone, in case of the simulated transient scenario, is removing 4.6 MW at the start of the accident and 9.3 MW at time $t=10000$ s into the accident. The generated decay heat at time $t=10000$ s is several times higher than the power removed by DHRS-3. Thus, DHRS-3 alone is not capable to safely cool down the reactor during the simulated transient.
- Having DHRS-3 in operation and after the air inlet of the DHRS-1 are open, the reactor can be safely cooled down during the simulated PSBO transient.
- Having DHRS-3 in operation and after the air inlets of the DHRS-2 are open, the reactor still cannot be safely cooled down during the simulated PSBO transient because all primary cooling circuit temperatures continue increasing in time, thus approaching the upper temperature limit (650°C) for the reactor vessel.

Based on the results, it can be concluded that not all DHRS arrangement can safely cool down a reactor during an accidental condition. When DHRS-1 is in operation with or without the use of DHRS-3, the reactor can be safely shutdown and the long term cooling can be achieved at the desirable level. On the contrary, the heat removal capability of the DHRS-2 is lower than it was previously foreseen, besides the natural convection establishment is not satisfactory with the current design, without the usage of auxiliary pump. In this sense, to have 2 reliable DHRS means for the total decay power removal, further research is required to improve the heat removal capability of the DHRS-2 unit.

The study of the modified secondary circuit design shows substantial reduction in material need for the secondary circuit and therefore being more cost effective and resulting even in safety related improvements. The DHRS assessment shows, that the overall functionality is retained with the new design, having improvement in the natural circulation establishment for secondary circuit sodium, improving the coolant circulation for DHRS-2. A potential disadvantage of the new system is related to the reduced thermal inertia available in the secondary circuit, which results in an overall more rapid increase of the primary system temperatures, reducing the available safety margin for the sodium boiling.

Nevertheless, according to the simulations, DHRS-1 is capable of avoiding such scenario. Overall, the modified design is suitable to serve as the reference design for future studies but the previously mentioned DHRS-2 heat removal capability improvement is still required.

CHAPTER 4

Safety function: Reactivity control

Performance of the safety function of reactivity control for different SFR designs are assessed in this study for two cases: 1) coupled neutronic and thermal-hydraulic behavior of ESFR (Section 4.1) and SPX (Section 4.2) in Unprotected Loss of Flow accident and 2) coupled neutronic and thermal-mechanical behavior of ESFR and Phenix cores in an accident induced by a core geometry distortion (Section 4.3). In both cases the reactivity change is mainly caused by a perturbation of the fuel-to-sodium volume fraction ratio. In the first case this perturbation is caused by the sodium density change due to heating up and boiling, while in the second case – by the core geometry change. Some increase of the core dimensions in the second case also has an impact on the reactivity via neutron leakage.

4.1. Assessment of ESFR under ULOF conditions

As part of the ESFR-SMART project, different accidental conditions are assessed to evaluate the behavior of the reactor under critical circumstances [75]. One of these accidental conditions is the Unprotected Loss Of Flow (ULOF) accident, which is described in this Section. This accidental scenario is the most severe accident evaluated within the research project, providing an insight into what happens with the reactor in a beyond design basis accident, where the integrity of the reactor cannot be guaranteed by specifically designed safety features.

Although there is no specific safety feature ensuring the safe reactor shutdown under ULOF conditions, a state-of-the-art low void effect core is implemented [76], which is anticipated to stabilize the reactor behavior during the accident. This low void effect core has been considered in recent studies [77][78], where a so-called sodium plenum is incorporated at the top of the fuel instead of the traditionally used fertile material region. This feature is meant to decrease the positive reactivity effect of the core voiding, due to sodium boiling, by increasing the neutron leakage from the core. This is achieved by the voiding of the plenum region, as a result of sodium boiling propagation upward from the fuel region of the SA, and a corresponding decrease of neutron reflection towards the fissile fuel region. It has been previously demonstrated that such a design can result in a stabilized sodium boiling process, and subsequent power excursion can be evaded [20][79]. The capability of this core design to keep the reactor stable during an unprotected accidental scenario is to be assessed in this study.

4.1.1. ULOF accidental scenario

The initiating event of the accident is the loss of forced primary flow due to pump failure or loss of power supply followed by a hypothetical failure of any safety system to shut down the reactor, thus the control and safety rods are not inserted into the reactor core. Under these conditions, the primary pumps of the reactor trip and coast down with the primary mass flow halving time of 10 s. As the reactor shutdown systems fail, there is no sudden power drop in the system, but instead, the power evolution is governed

by the inherent core reactivity feedback effects. This series of events could be initiated in principle by, for example, a loss of offsite power incident and though its probability of occurring is very low, in the range of 10^{-8} per reactor year [49], its implications are assessed as it is one of the most dangerous accident in regards of endangering the structural integrity of the reactor.

As the forced convection is gradually decreasing according to the pump coast down characteristics, the natural convection takes over the main flow driving force in the system. This driving force is governed by the balance between the buoyancy effect and the friction forces within the primary system [49].

In these circumstances the core thermal conditions are defined to certain extent by the ratio of power to mass flow. Considerable increase of this ratio, and, correspondingly, increase of the sodium heat-up may result in sodium boiling onset, with subsequent pin cladding dry-out, melting and further progression of the core disruption accident. This is due to the fact that with the onset of sodium boiling, the appearing vapor phase will interact with both the liquid and structural elements of the SA, thus increasing the friction forces affecting the balance between buoyancy and friction drag. This effect decreases or potentially even stop the flow in the boiling SAs, further deteriorating the heat removal from the fuel pins.

Thus for the new core designs, it appears of a high importance to ensure a reasonable variation of the core power level during the accident, through the optimization of the core inherent features, i.e. minimization of the global sodium void effect, to avoid any power excursion, in particular, driven by a positive sodium void effect. Even though such measure is not able to prevent clad melting, it could at least increase the grace time period before cladding melting would occur.

4.1.2. ULOF modeling

The ULOF modeling is organized into three main parts.

- 1) A so-called reference case is used to model the accidental scenario to obtain results of the reactor behavior. This model corresponds to the description of the ESFR-SMART core design, presented in Chapter 2, using a simplified 42 channel TRACE model.
- 2) A new feature in the SA design has been introduced within the second model, described in [24] and [25]. The modification consists of a 4 cm diameter window on each side of the hexagonal wrapper in 42nd axial node in the model, corresponding to the axial level just below the initial boiling region, which is top of the fuel region. The diameter of the wrapper window was selected as a reasonable compromise between providing a large enough path for the sodium flow but without severely affecting the mechanical integrity of the SAs. In accord with [24], the wrapper window aims to provide an accessible path for the coolant flow even if the sodium vapor production blocks the top of the channel. Hence, the cooling of the fuel region of the SA can be maintained, as schematically shown in Figure 7, which is envisioned to improve the reactor behavior following the boiling onset.
- 3) Lastly, a number of sensitivity cases are presented, making changes in various core related parameters, to assess their influence on the core behavior during the accident.

The simulation is composed of two phases: 1) Up until 1000 s, a steady-state calculation is performed through which an equilibrium reactor state is to be reached, with nominal operational settings. 2) At 1000

s, the transient phase starts, initiated by inlet sodium mass flowrate decrease in accordance with the primary mass flow halving time, and the power evolution is calculated by the point kinetics solver.

4.1.2.1. ESRF core description

As a general description of the core, the fuel region can be divided into inner core (IC) and outer core (OC) sections with 216 and 288 SAs, respectively, shown in Figure 71. The core was designed with a 6 batch fuel reloading pattern to smoothen the reactivity variations and the power peaking between the batches. The reactivity control is ensured by the 24 control and shutdown devices (CSD) and 12 diverse shutdown devices (DSD) present in the reactor core. An innovative safety measure of the new ESRF core is the corium guide tubes, which provide a clear path for the melted corium downwards to the core catcher, where long-term cooling can be maintained, should the core meltdown not be avoided. The primary vessel and internals are protected by several layers of shielding and reflector SAs at the periphery of the reactor core.

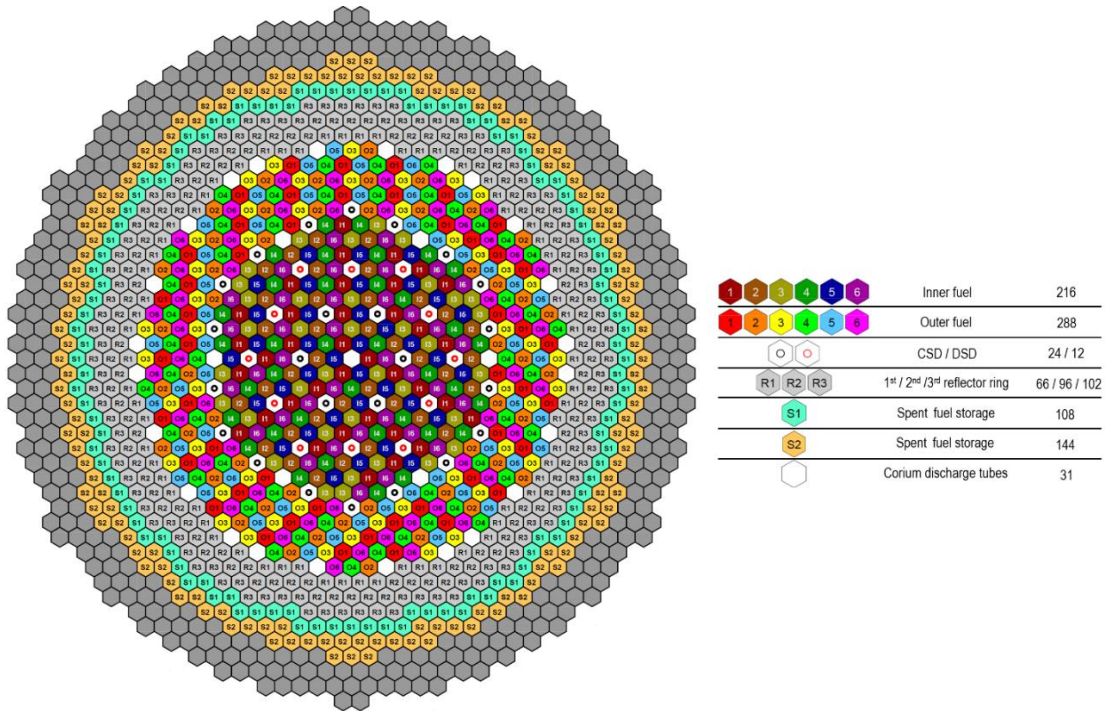


Figure 71. ESRF-SMART core radial layout with the different batches and SA types

The inner and outer core SAs were divided into different cooling groups (CG), shown in Figure 15, in line with their power output. Each CG has a different orifice scheme at the inlet of the SA to achieve even sodium heat up in all regions of the core. The resultant coolant flowrates within CG1 to CG5, in nominal conditions, and the number of SAs within each CG is presented in Table 11.

Cooling groups	# of SA in CG	Sodium flowrate [kg/s]
CG1	216	8802
CG2	111	4894
CG3	69	2558
CG4	60	1693
CG5	48	981

Table 11. Cooling groups with the corresponding SA numbers and sodium flowrates within each group

Axial composition of SA of inner and outer cores are shown in Figure 72. Apart from the fuel height difference and the orifice in the foot, all SAs are identical.

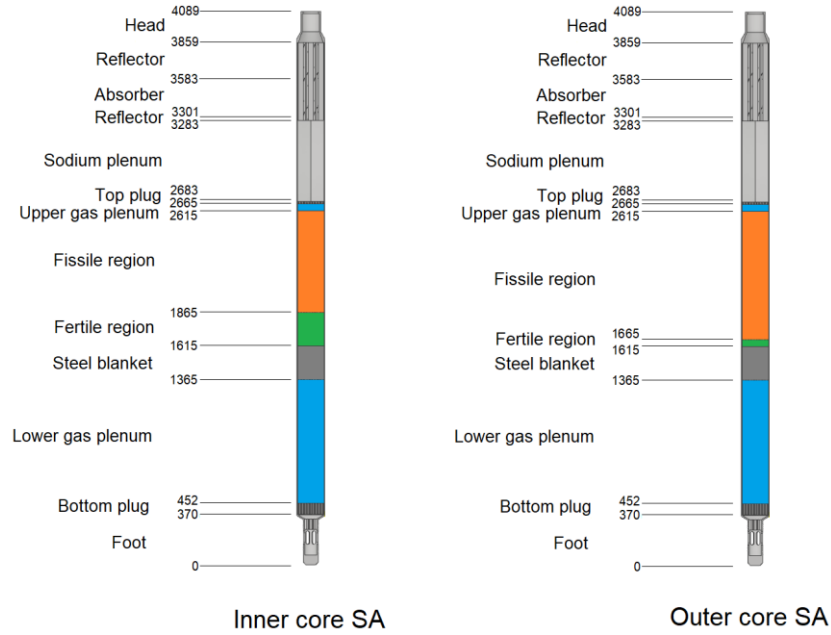


Figure 72. Inner core and outer core SA axial region and heights

4.1.2.2. Point kinetics model

The reactivity and power evolution during transient are calculated using the built-in point kinetics model of TRACE, utilizing the pre-calculated feedback coefficients [23]. The reactivity feedback effects considered in the modeling are the Doppler, axial fuel expansion, control rod driveline (CRDL) expansion, sodium density, and void effect were calculated by Serpent Monte Carlo code (Table 13). The definitions and specific implementation of these feedback coefficients have been described in Section 2.2.

Reactivity effect	Value
Doppler IC Fertile	-61.4 pcm
Doppler IC Fissile	-344.6 pcm
Doppler OC Fertile	-13.6 pcm
Doppler OC Fissile	-385.7 pcm
Fuel expansion	-10.6 pcm/mm
CRDL expansion	-0.334 pcm/°C
Sodium void fuel	1422 pcm
Sodium void plenum	-1035 pcm
Sodium density fuel	48 pcm/%density
Sodium density plenum	-13 pcm/%density

Table 12. Modeled reactivity effects and their values

The power distribution used in the model is obtained from [47], having separate axial power distribution for the IC and OC fuel regions, with individual radial power peaking for each SA. As for the kinetic parameters, the data was obtained from the study presented in [47] as well.

4.1.2.3. TRACE model for ULOF study

The modeling of the ESFR-SMART core, to conduct the current analysis, was performed by utilizing a 42 one-dimensional channel model, shown in Figure 73, which is a simplification compared to the previously used full reactor model for other accidental conditions [71]. This simplification was necessary due to the required resources to perform the simulation of the whole reactor model. Each of the 42 channels corresponds to a SA of the actual core, giving a 1/12th representation of the entire core, allowed by the symmetry of the design, modeling 18 IC and 24 OC SAs. Axially the IC and OC SA nodalizations were identical, using 74 nodes of 0.05 m in length. The only alteration between the regions is the 5 fertile nodes and 15 fissile nodes for the IC channels and the 1 fertile node and 19 fissile nodes of the OC channels, shown in Table 13 and Figure 72.

SA region	number of nodes in IC SA	number of nodes on OC SA
head section	4	4
reflector zone	6	6
shielding zone	6	6
sodium plenum	12	12
upper fission gas plenum	1	1
fissile zone	15	19
fertile blanket	5	1
steel blanket	5	5
lower fission gas plenum	20	20

Table 13. Modeled IC and OC SA regions in TRACE with corresponding node numbers

The inlet flow supply is connected to an inlet plenum, representing the diagrid under the SAs. The inlet sodium flowrate is set as a boundary condition within the model, providing equivalent flowrate evolution to what was observed in the full reactor model [71], where the flowrate was supplied by modeling the actual pump with their cost down curves. This simplification was considered to be reasonable, for the given inlet core pressure, the primary system pressure drop and overall mild boiling pattern in the low-void core, no strong boiling-induced primary flowrate oscillations were expected in the ULOF conditions. This assumption is supported by [19], where it was shown that the inlet flowrate oscillation is only a small fraction of the gradually reducing primary mass flow rate, especially considering that only the first ~100 s of the ULOF transient is simulated. Furthermore, as all SAs are modelled individually and a large number of SAs are not involved in boiling for the simulated period of time, the breakdown of the residual forced flow (which stays above 10% of the nominal flowrate for the simulated period of time) is not expected. Thus, the total inlet flowrate is not affected noticeably by boiling, and strong local fluctuations of the flowrate is observed in boiling channels only. Each SA is connected to the inlet plenum through a valve component, establishing the right orifice of the SA to account for the different cooling groups of the core and to set up the right flowrate within each SA. At the top of the channel, another plenum component is situated, representing the hot pool of the reactor, which is connected to a pressure boundary condition of 0.2 MPa.

The sodium between the SAs (in the so-called inter-SA gap) is modeled using a 4 radial ring vessel component, where the first 2 rings correspond to the IC region and the outer 2 rings to the OC region. The inlet and outlet of the vessel are connected to the inlet and outlet plenums, respectively. By using

this modeling approach, the radial pressure difference between the rings can be represented. In the first axial node of the vessel, the friction factor has been increased to model the high pressure drop present in the actual reactor between lower and upper plena, originating from the labyrinth seal at the foot of each SAs, through which the sodium enters the inter-SA gap, in order to achieve a reasonable mass flowrate through the inter-SA gap. The heat exchange between the inter-SA sodium in the vessel component and the sodium in the SAs is achieved through heat structure elements at each axial node simulating the stainless steel SA wrapper. Through this heat structure, the sodium, which is heated by the fuel elements can conduct its heat to the sodium flowing in the vessel component, representing the inter-SA gaps.

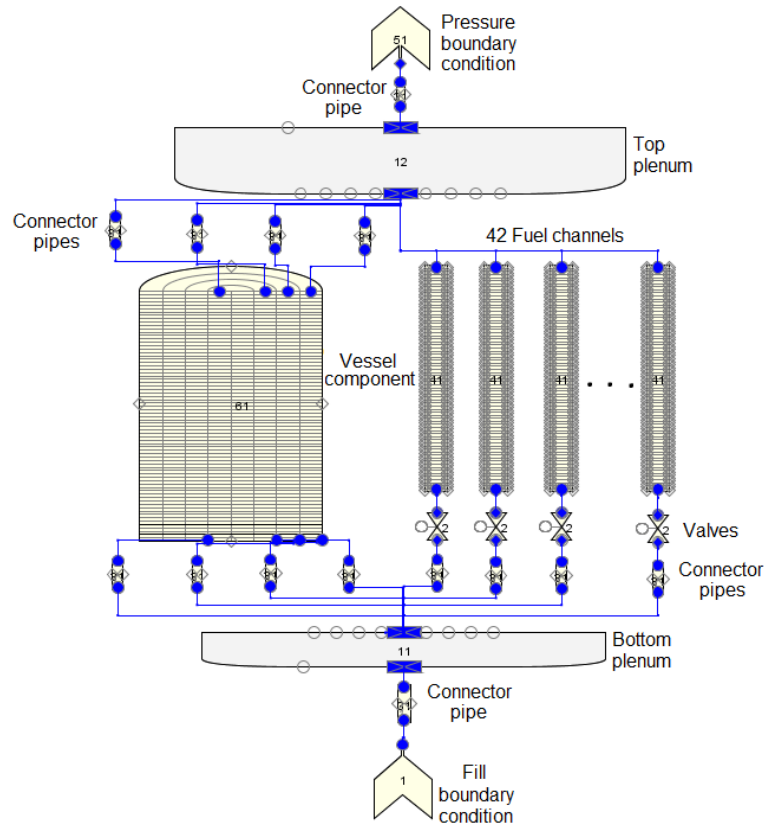


Figure 73. TRACE nodalization diagram of the ULOF 42 channel model

4.1.3. Reference calculation results

In Figure 74, the power and mass flowrate normalized to their initial values are shown starting from the initiation of the transient phase. Therefore, from time 0 s, the substantial flowrate reduction is prominent since the forced convection of the primary system is lost. The blue curve indicates the power evolution, which exhibits a smooth reduction of the reactor power until ~50 s, from where the power starts to fluctuate with higher frequency resonances. These resonances, as it will be shown later, are related to the boiling of the sodium and subsequent quick condensation of the sodium bubbles. The simulation ends at 110 s, where the local clad melting temperature is being approached but still not reached (shown in

Figure 78), avoiding the simulation to abort and providing a consistent timeframe for the different simulation cases to be compared.

The right plot, in Figure 74, with the given normalized power to flow ratio, is more representative for demonstrating the power removal capability and the thermal conditions in the core. Naturally, as the power to flow ratio increases, the reactor is approaching the limiting temperatures as the heat is not removed as readily as it is when higher coolant flow is present within the reactor core. In this sense, it is crucial to keep the power to flow ratio as stable and low as possible, increasing the grace time for any safety mechanism to be applied to keep the reactor under control.

In the current simulation, until boiling of the sodium is reached, there is a steady but slow increase in the ratio, which halts at ~ 50 s, which is the point of boiling onset in the peak power SA. Starting from this moment, the transient is essentially driven by the balance of positive (spectral hardening) and negative (increased leakage) contributions of sodium density effect. Initially, the power decreases due to an insertion of additional negative sodium voiding reactivity contributions at the sodium plenum and at the top of the SA just below the sodium plenum. The voiding of the sodium plenum increases the neutron leakage out of the reactor core, which in return results in decrease of neutron multiplication in the core. Further transient progression is characterized by an intensive sodium vapor generation and boiling front propagation downwards towards the mid-height of the fuel region of the SAs, which has an opposite effect on the reactivity of the core compared to the plenum voiding. This is mainly because the neutron spectrum is hardening with the lower amount of sodium, which in a fast reactor increases the reactivity. When the vapor propagates downwards in multiple SAs, a considerable positive reactivity is introduced, resulting in increased power generation, as it happens from ~ 90 s in the calculation. Following the power increase, at ~ 100 s, the reactor power drops again, resulting from the boiling onset of an increasing number of SA due to this sudden power peak, initially introducing negative reactivity in the core. From this point onwards, it is expected that the sodium vapor gradually propagate downwards and the positive reactivity contribution would dominate within these newly boiling SAs, creating an even larger power increase than it was observed at 90 s.

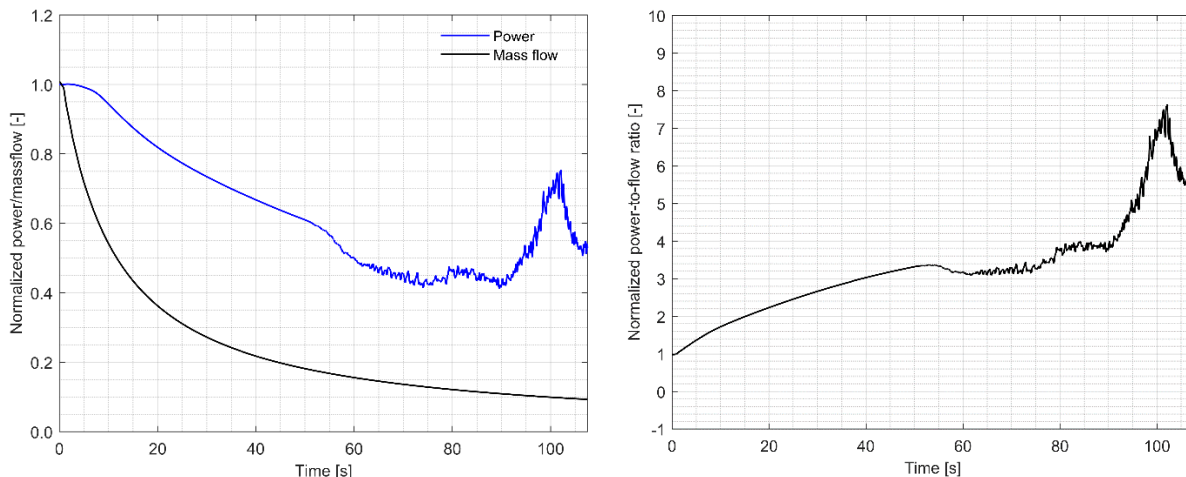


Figure 74. Temporal evolution of the normalized power and mass flowrate (on the left) and normalized power to flow ratio (on the right) following the initiation of the transient

The vapor propagation phenomenon described previously is visualized in Figure 75 for the peak power SA located in the OC. The void fraction is plotted using grades of blue along the SA, demonstrating the vapor

propagation along the axial height of the channel. The horizontal axis shows the elapsed time, starting from ~50 s corresponding to the boiling onset in the SA. The white color represents the liquid sodium in the channel, whereas the blue shows the sodium vapor. The bottom horizontal black line indicates the bottom of the fuel region, the middle line indicates the top of the fuel region, and the top line – the top of the sodium plenum region. The initial vapor volume mainly occupies the top of the SA region, including the plenum, but with the passing of time, the vapor enters deeper into the fuel region until it is nearly entirely voided. Although the plot shows only the peak power SA, the same phenomenon happens increasingly for the other SAs, which eventually causes the power to increase rapidly.

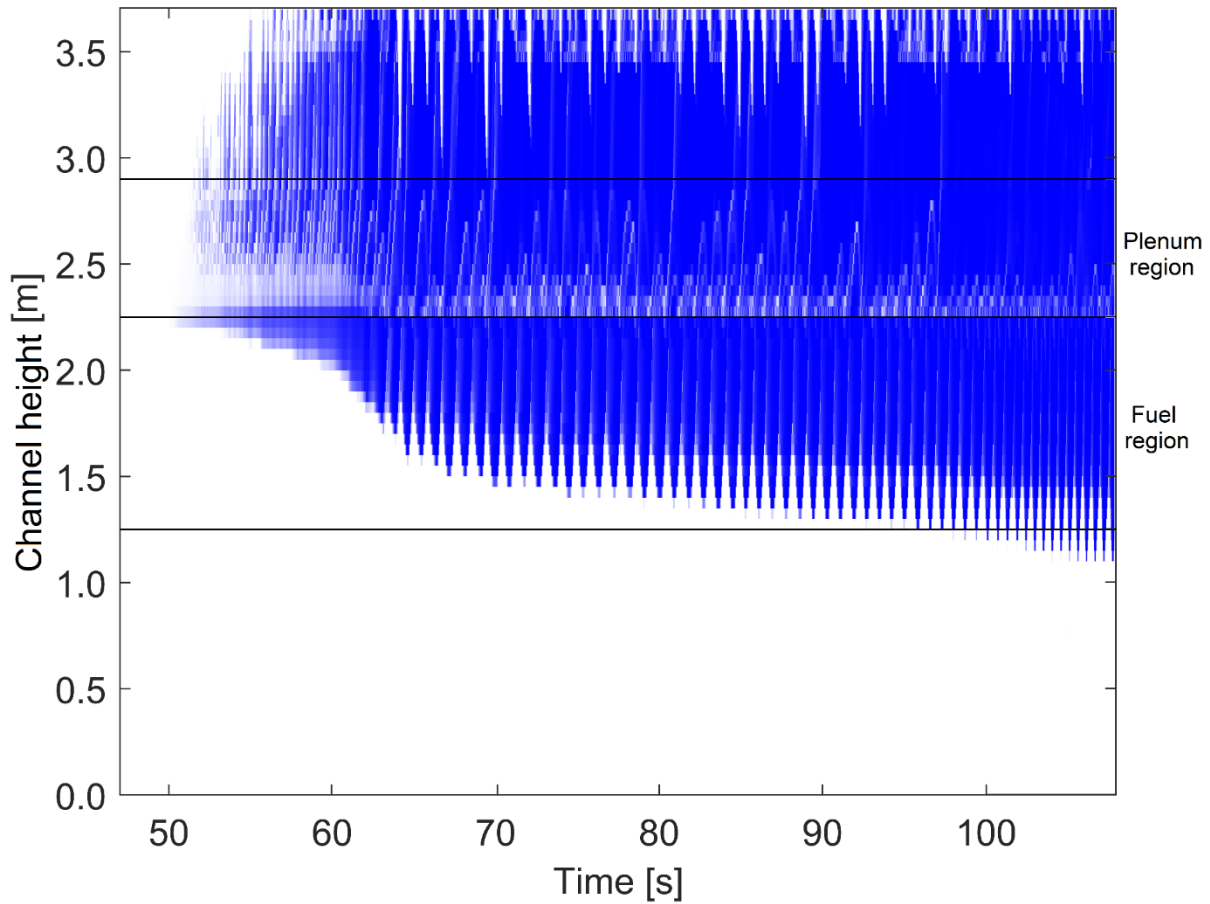


Figure 75. Peak power assembly void fraction distribution axially versus time plotted from the boiling onset

Figure 76 provides information about the reactivity evolution and its decomposition. The most prominent reactivity components after the boiling onset are related to the sodium effect. This effect was separated into the fuel and plenum regions, contributing with large positive and negative effects, respectively, while the blue line indicates the overall sodium effect in the core. At the transient initiation point, the effect is positive, as the decrease of sodium density in the fuel region has a stronger impact than the increased leakage due to density reduction in the plenum region. When the boiling starts, the overall positive sodium effect is mitigated as more vapor appears in the plenum regions. Nevertheless, in later stages, the positive effect starts to increase again as the fuel region is increasingly filled with vapor.

As for the Doppler effect, when the core power decreases, the temperature of the fuel pellets is also decreasing, resulting in a positive feedback. This positive reactivity component decreases only when the sharp power peak occurs, resulting in an increase of fuel temperature from ~95 s. The control rod driveline (CRDL) reactivity is determined by the outlet sodium temperature evolution. The sodium temperature in the core and correspondingly the core outlet temperature are increasing, explained by the higher power to flow ratio shown in Figure 74. This temperature increase results in a negative CRDL reactivity feedback as the control rods are inserted more into the core due to thermal expansion of their drivelines. The fuel expansion effect, driven by the increasing clad temperature, has a comparatively small effect on the generated power, decreasing the net reactivity.

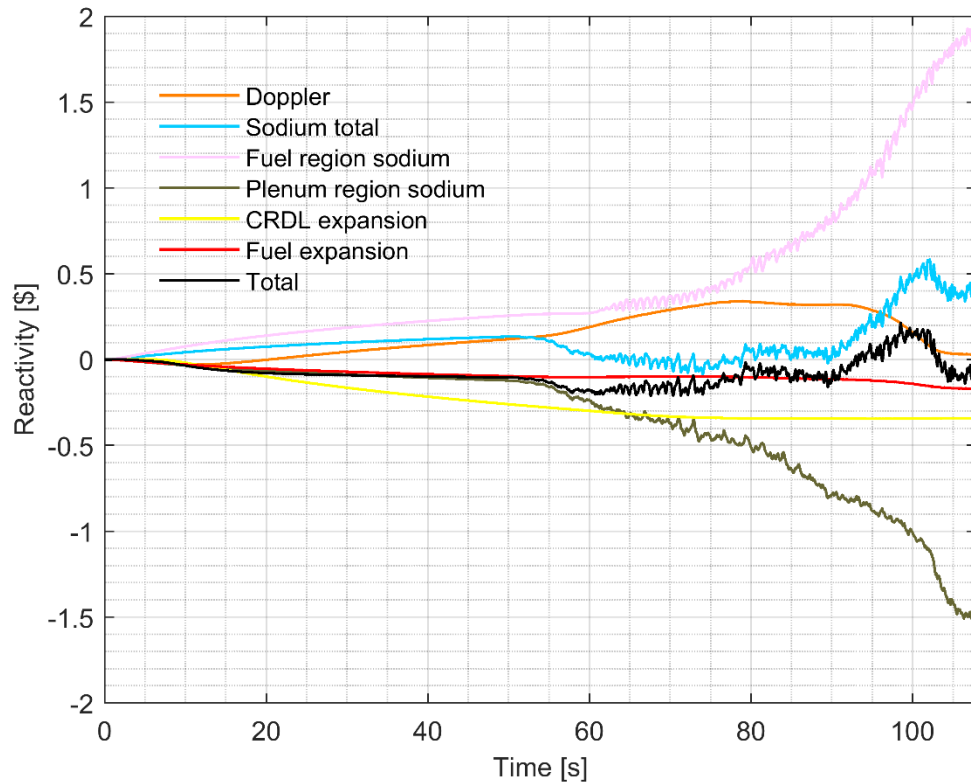


Figure 76. Reactivity components used in the point kinetics model vs. time

In the following plot, in Figure 77, a more detailed decomposition of the sodium effect is given as now the reactivity components are separated not only to plenum and core regions but also according to the different CGs of the reactor core. The summed total of the core and plenum region lines are identical to the corresponding reactivity components shown in Figure 76.

The Figure shows that CG2 has the fastest increase, first with the plenum sodium effect and then with the fuel region sodium effect. This is not surprising considering the fact that the highest power SAs are located within this group. Following the transient progression, the next group with the significant impact on the total core reactivity is the CG1, corresponding to the SAs in the IC region with high power outputs, which consists of nearly half of all SAs. Close to the end of the simulation, the previously observed sudden decrease of core power can be understood by looking at the sharp decline of the CG2 plenum reactivity component, driving down the reactor power. This phenomenon comes from the fact that the previous

increase in power initiated sodium boiling in SAs, which did not boil previously. As it was shown before, the initial boiling phase is more pronounced in the plenum region until the vapor propagates down to the fuel region of the SA. Thus nearly simultaneous involvement in boiling of a large group of SAs results in the introduction of the negative reactivity first. Later on, it can be expected that as the fuel region is also voided, the power will experience an even more significant increase than it was previously seen. The other cooling groups CG3, CG4, CG5, which are in the periphery of the core, are just starting to boil, and their effect is less pronounced, as well as less important in general as the number of SAs in CG at the core-periphery is smaller and both positive and negative contributions are weaker.

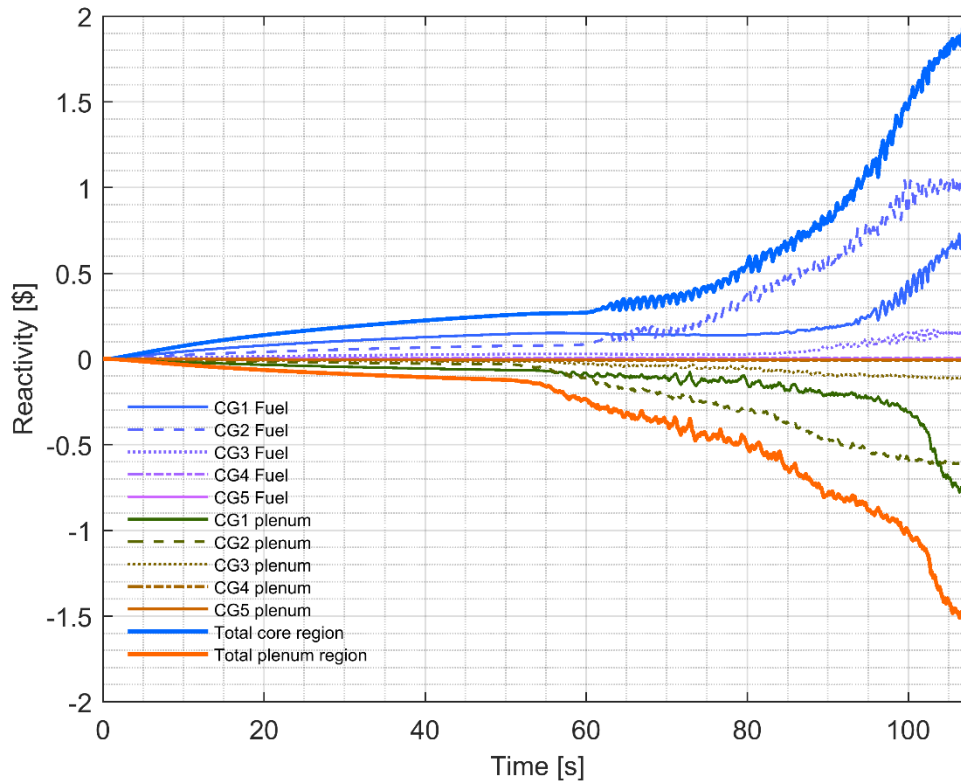


Figure 77. Decomposition of sodium reactivity evolution with respect to CGs and axial regions (fuel and plenum) vs time

To observe the limiting temperature evolution within the peak power SA, Figure 78 is plotted. The two most important temperatures, limiting the accidental scenario, are the fuel and cladding temperatures, of which the inner surface values are plotted. Axially, the fuel node number 10 was chosen to be displayed as it is at the middle of the fissile fuel region having the highest power production. The sodium temperature is of little interest as it is already at the saturation point. Moreover, as it is a fast transient, the structural materials are not included either in the limiting temperature values as a more extended time period would be required for significant material creep.

The Figure shows that the fuel temperature initially decreases, governed by the power reduction. This decreasing temperature phase ends soon after the boiling onset because the vapor produced in the peak power SA channel obstructs the sodium inflow, and therefore the cooling capability is declining. The vapor continues to fill the channel and propagates downwards, thus because of the positive void effect power production increases in the core, causing a jump in the fuel temperature by the end of the simulation. As

for the cladding inner surface, the temperature evolution follows well the power to flow ratio growth up until the point of boiling onset, at which there is a jump in surface temperature followed by a high-frequency oscillating temperature phase. The sudden jump in the cladding temperature at ~60 s corresponds to the vapor propagation into the fuel region, reaching the middle fissile section, which reduces the heat transfer in the channel drastically. Finally, the further temperature increase at the end of the simulation is due to the substantial power increase similarly to the fuel temperature jump.

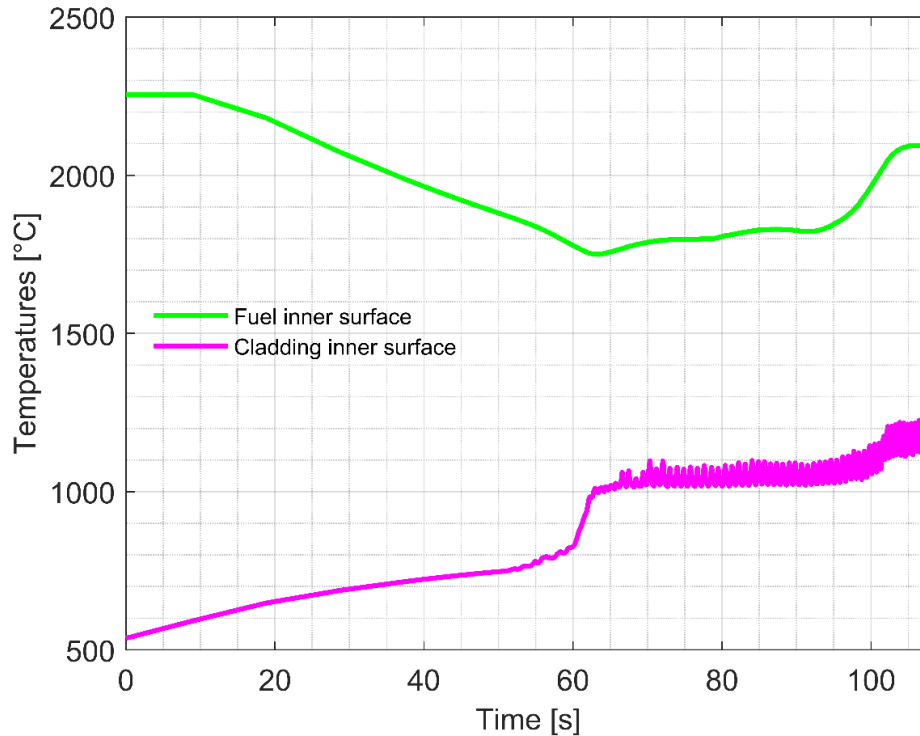


Figure 78. Fuel inner surface and cladding inner surface temperature evolution in the peak power channel at the fissile fuel middle-height node vs time

4.1.4. Results for modified wrapper case

Based on the aforementioned results and the unfavorable behavior of the reactor after sodium boiling, displaying power increase by the end of the simulation that potentially leads to loss of the pin and SA structure integrity and further severe accident progression, a new simulation has been performed, where the SA wrapper design has been modified, as described in Section 1.3.1.1.

The evolution of the core parameters and conditions are discussed hereafter for the improved SA design, as compared to those presented already for the reference case. First, the normalized power and mass flowrate are depicted in the left plot of Figure 79. The mass flowrate is identical as it is a boundary condition of both simulations. On the other hand, the power evolution shows significant differences. Although, until the boiling onset, the power evolves the equivalent way for both reference and modified design cases, at ~60 s following a quick power decrease, there is a recovery and then a stable, slow reduction until the end of the simulation. The normalized power to flow ratio, shown in the right plot of the Figure, also reveals a promising tendency, as following the boiling onset, the value stays stable, not

exceeding 4. Similar to the power evolution line, a decrease and a quick recovery at ~60 s are noticeable in this plot also.

To understand more the mechanism causing the dip and recovery of the power, Figure 80 is plotted. The general structure of the Figure is the same as it was for the reference case, but here there is an extra horizontal red line, which corresponds to the elevation where the windows on the wrapper surface have been implemented. From the Figure, it is clear that at ~60 s after the start of the transient, there is a quick vapor generation within the peak power SA, where the vapor starts to propagate towards the fuel region. This vapor propagation quickly recovers, and as the bubbles are collapsing, the amount of vapor also reduces in the plenum region, which corresponds to the power increase in the reactor. This is followed by a more stable boiling pattern, which can be characterized as chugging boiling regime [80], creating the possibility of a stable decrease of the core power as the sodium vapor is retained only in the SA top region, including the plenum.

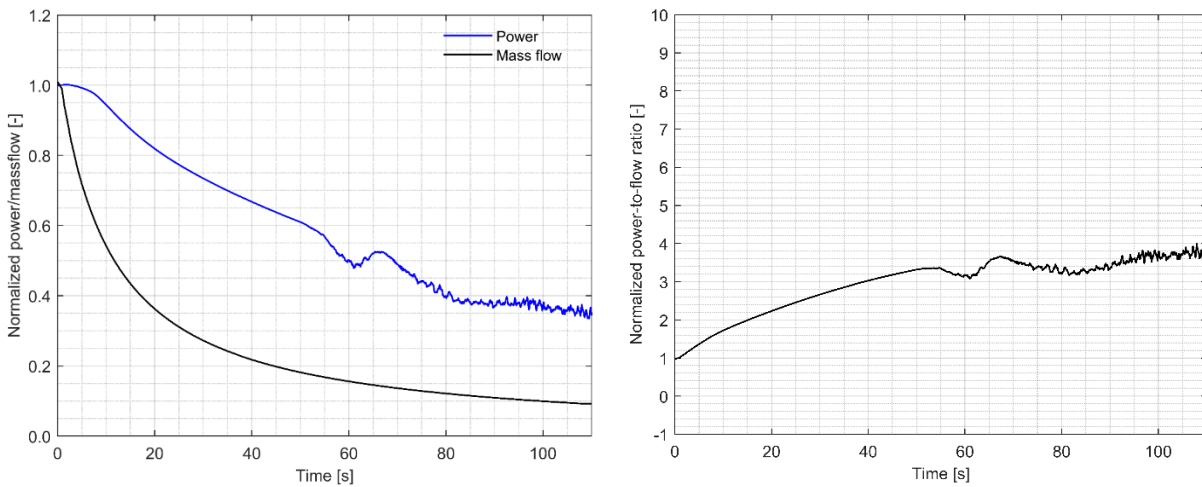


Figure 79. Normalized power/mass flowrate (on the left) and normalized power to flow ratio (on the right) vs. time following the initiation of the transient

The reactivity decomposition, shown in Figure 81, visualizes essential differences of the sodium reactivity effect evolution compared to the reference case. Soon after the boiling onset, the plenum contribution effectively counterbalances the fuel region boiling due to the applied design modifications. Therefore, the calculation shows close to zero overall sodium reactivity effect, which is an important safety accomplishment. As for the rest of the reactivity effects, both qualitatively and quantitatively comparable to the reference solution, except the Doppler effect, which does not include the decrease at the end of the simulation as the fuel temperature stays stable during the course of the calculation.

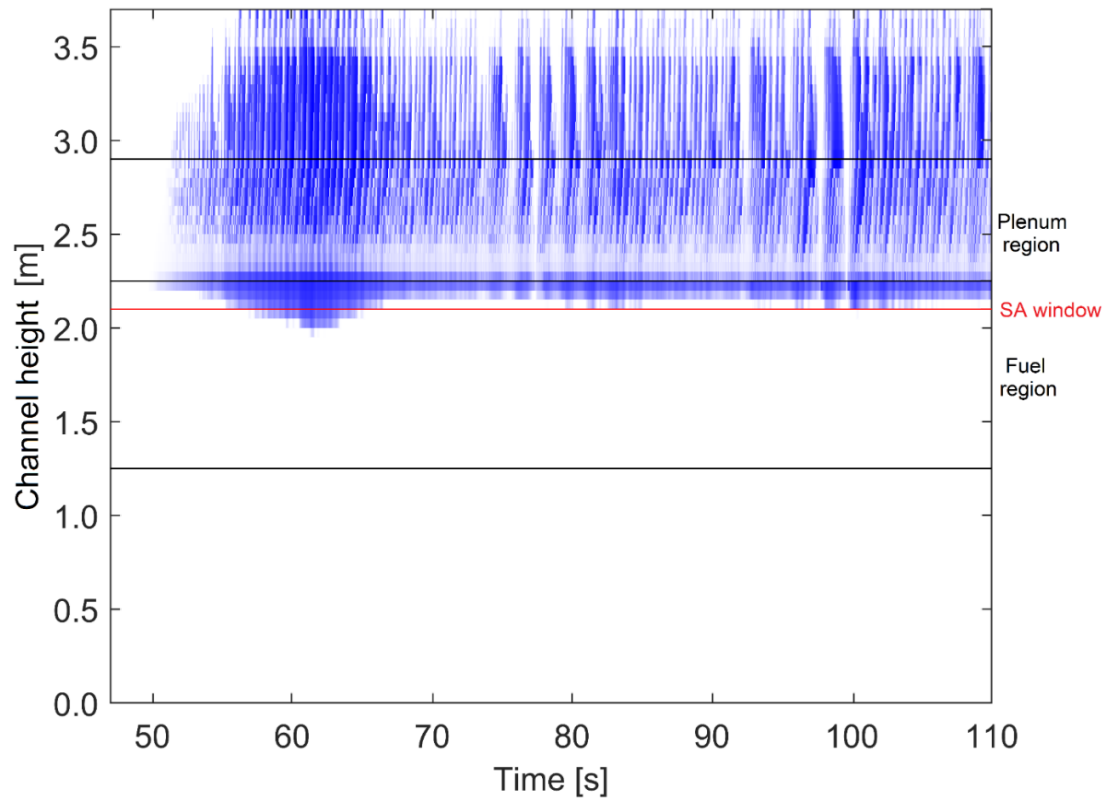


Figure 80. Peak power assembly void fraction distribution axially versus time plotted from the boiling onset

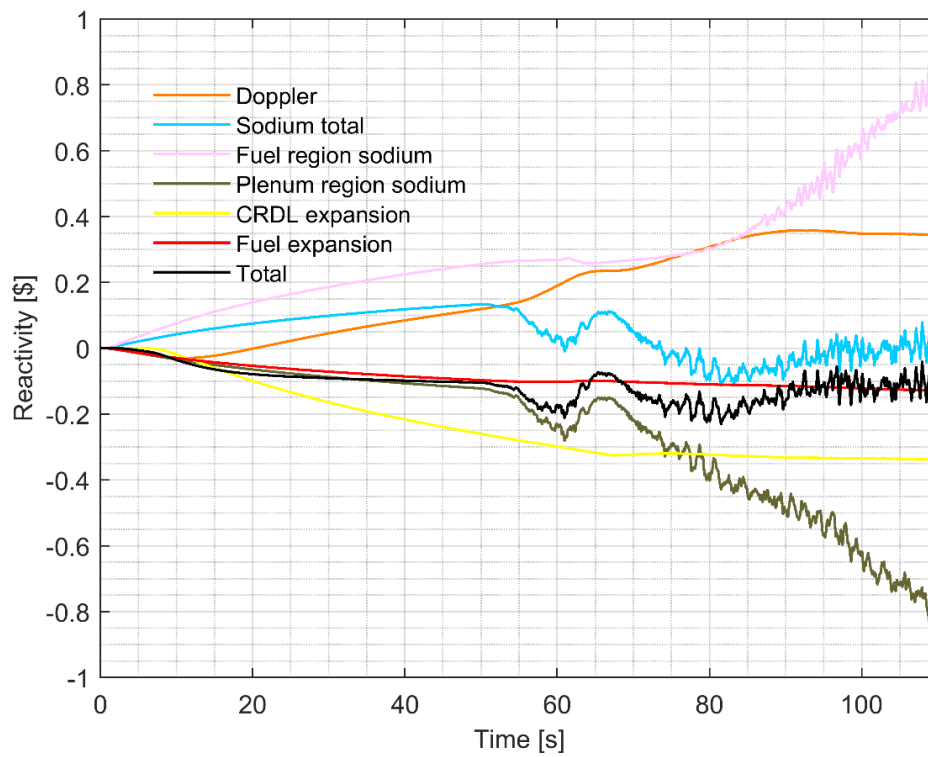


Figure 81. Evolution of the reactivity components used in the point kinetics model vs. time

The distribution of the sodium effect between different CGs and axial regions is shown in Figure 82. In this Figure, significant variation can be recognized compared to the reference case, which shows different boiling progress within the core. Initially, similarly to the reference Figure, the peak power SA starts to boil in the CG2 region. This is followed by the bubble collapse and the stabilization of the boiling, reducing to a relatively low level of reactivity contribution from this CG. Simultaneously, within the CG1 region, both plenum and fuel sodium effects rapidly increase, dominating the overall sodium reactivity evolution. Overall, the plenum and fuel region contributions stay well balanced, having a close to zero total effect on the core. This shows that an increasing number of SAs reach the boiling onset, but the vapor propagation towards the fuel region is kept under control with the help of the windows in the SA wrappers. The changed flow pattern in the SAs gives greater importance to the CG1 SA units at least until the end of the simulated time period. Furthermore, the vapor generation in CG2 and CG3 are greatly reduced compared to the reference case, and they affect only marginally the sodium reactivity feedback effect. Should this stabilized boiling continues to spread radially towards the periphery region of the reactor, a further decrease in the reactivity could be foreseen because the leakage contribution is more significant in the periphery region SAs.

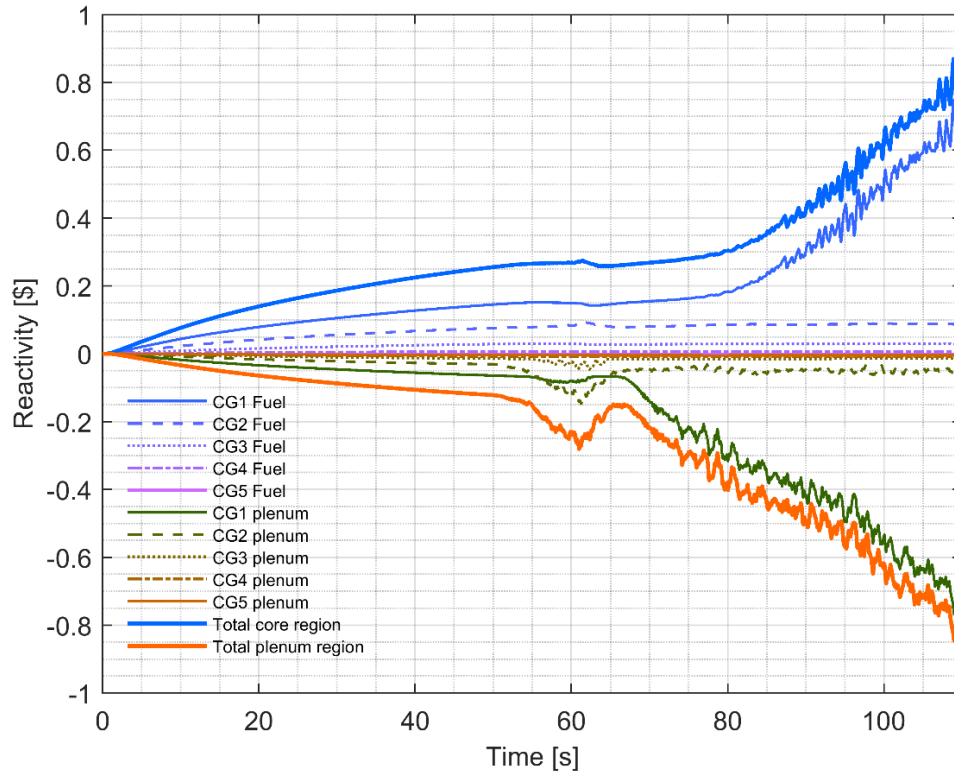


Figure 82. Sodium reactivity effect evolution in time distributed amongst the different cooling groups and fuel/plenum regions vs time

In Figure 83, the improvement in the limiting temperatures is shown. The parameters in the same SA and axial node are depicted as in the reference case analysis. When the fuel inner surface temperature is evaluated, there is a continuous decrease throughout the duration of the whole simulation, which is a definitive improvement on the reactor thermal state. Although the fuel temperature is improved, it has not been the primary concern but rather the melting point of the cladding, which was only around $\sim 100^{\circ}\text{C}$

away. With the improved design, following a slow increase of temperature and a peak at ~ 60 s, it stabilizes at a nearly constant level. As the vapor does not propagate downwards towards the fuel, as it is blocked at the level of wrapper windows by the upward liquid sodium flow, a sufficient heat transfer from the fuel pins to the liquid sodium is ensured, and a sudden temperature increase, observed in the reference simulation, is avoided. (The fuel and cladding temperature stay stable even above the modeled windows, thus being in the stagnant two-phase region, as the power density at the top of the fuel is sufficiently low.) This confirms the potential safety improvements which can be achieved by implementing the proposed design modifications.

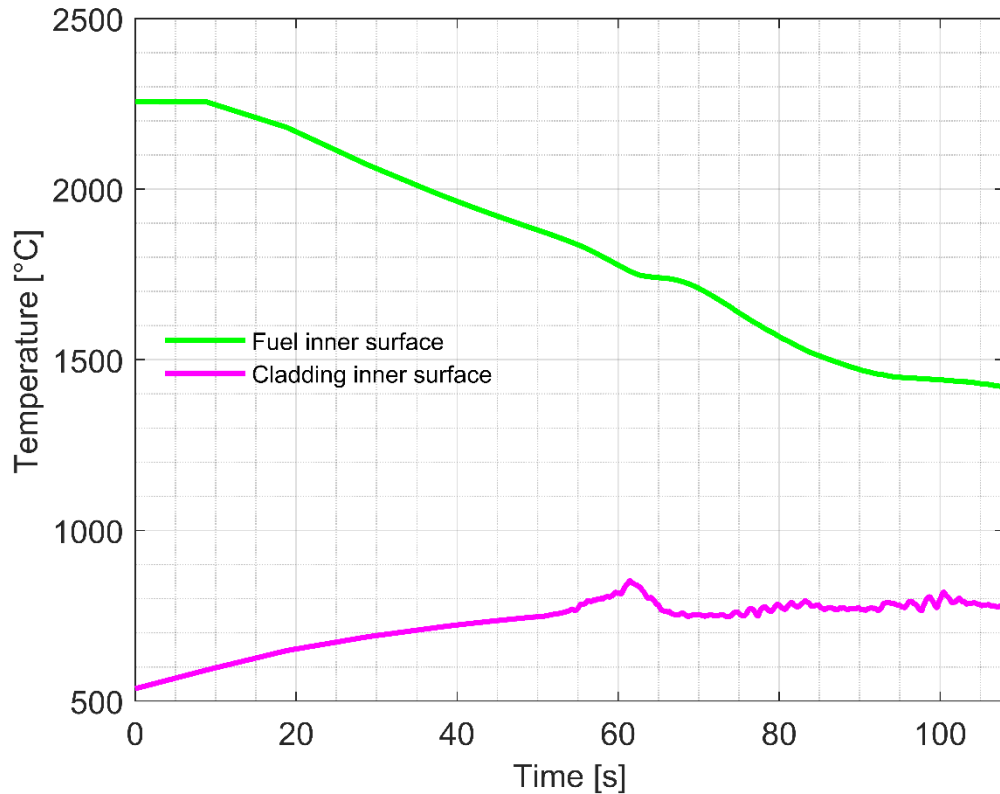


Figure 83. Fuel inner surface and cladding inner surface temperature evolution in the peak power channel at the fissile fuel middle node height vs time

4.1.5. Comparisons and discussion

To better understand the phenomenon behind the improved reactivity feedback effect evolution and more efficient power decrease during the accident progression in the core with the modified wrapper design, Figures 84-86 have been plotted.

The expectation from the wrapper window was that it creates a path for the liquid sodium to flow through the major part of the fissile region even if the top of the SA is blocked by vapor as a result of the coolant boiling. In Figure 84, the channel inlet and outlet liquid sodium velocities are depicted. On the left plot, which relates to the reference case, there is a fluctuating inlet flow velocity around 0 m/s during a few seconds time period at the end of the simulation, meaning that there is no real coolant flow into the SA.

Periodically, the liquid sodium enters the channel when the condensation of a bubble occurs, and it is ejected from the channel when the evaporation increases. This inevitably leads, over time, to an increase of void fraction within the channel as the power generation continues. On the contrary, for the channel flow velocity on the right for the modified design, the liquid inlet flow velocity stays positive for the whole time period shown in the Figure, meaning the sodium inflow is maintained into the boiling channel. When, in the same plot, the liquid velocity at the channel outlet is assessed, it displays similar overall behavior as it was for the reference case, namely that the liquid is ejected and sucked into the channel as the sodium bubbles are increasing in size or being collapsed. This suggests that the sodium entering the channel can pass through the wrapper windows.

In Figure 85, the sodium pressure evolution is plotted at four axial locations within the peak power SA for the reference case and the modified design case. The pressure plot reassures the chugging boiling pattern for both calculation cases and the bubble formation-driven flow velocity at the channel inlet for the reference case when the pressure peaks are compared to the inlet flow peaks in Figure 84. Nevertheless, the size of the pressure peaks is about a factor of three times greater for the modified design case, suggesting a complete collapse of the sodium bubbles, in contrast to the partial decrease for the reference case. Therefore, by implementing the windows on the wrapper, the extra amount of cooling of the fuel, provided by the continuous coolant flow, allows complete bubble collapse, which is also visible in Figure 80 in contrast to Figure 75.

The state of the core can be characterized by the average void fraction in the plenum and fuel region over all channels, shown in Figure 86, as the sodium reactivity feedback effect evolution is mainly governed by these two parameters. The left plot in the Figure presents the void fractions for the reference core design, exhibiting a step increase in void fraction both in the fuel and in the plenum regions. As more SAs reach the boiling onset condition, there is a continuous increase in the plenum voiding, but soon after the plenum boils, the sodium vapor propagates downwards into the fuel region, causing an exponential void increase in that region for the considered simulation time. When the image at the right is compared, which is the modified design case, to the reference condition, a stark difference to realize is the factor of two decrease in sodium void fractions. Besides, the void propagation throughout the core also differs significantly. At ~60 s, following a rapid increase in both the plenum and fuel void, it decreases close to zero, which relates to the initial power peaking SA boiling onset and the subsequent recovery and stabilization of the boiling process. Overall, the void propagation in the plenum is significantly stronger than it is in the fuel region, indicating a potentially safer and more stable boiling regime for the reactor. This leads to the conclusion that the boiling pattern improvement seen in the power peaking channel is valid for the other channels of the reactor core also.

In this study, the specific sodium boiling modeling aspects included in TRACE by PSI have not been evaluated but rather emphasis was given to analyze the specific behavior of the ESFR-SMART core design. This is because such study has been performed in [46], based on the validation exercise of TRACE with a ULOF sodium boiling experiment.

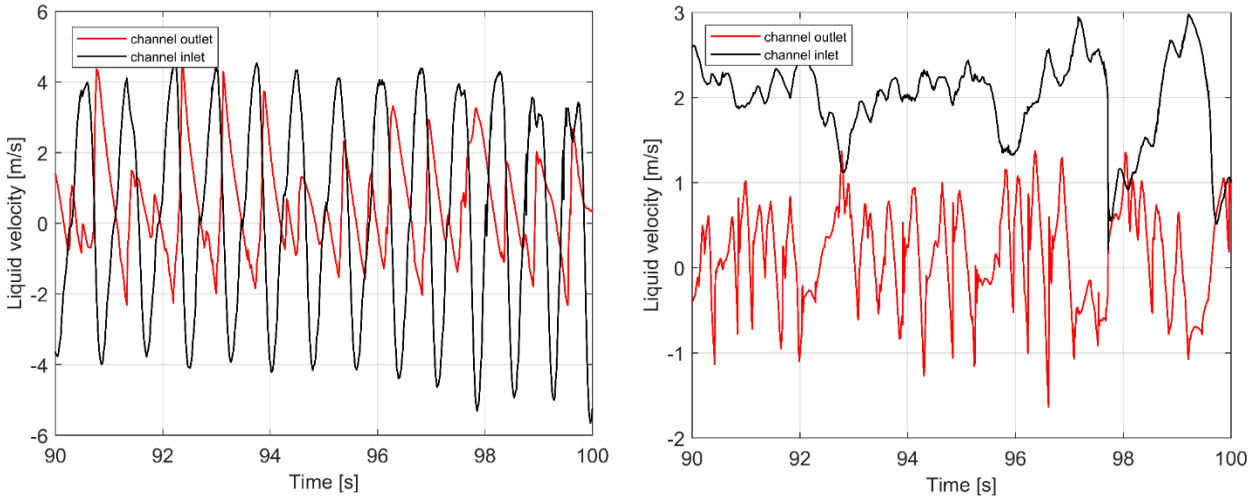


Figure 84. Liquid sodium velocity at the channel inlet and outlet for the reference case (left) and the modified design case with windows (right) within the peak power SA vs time

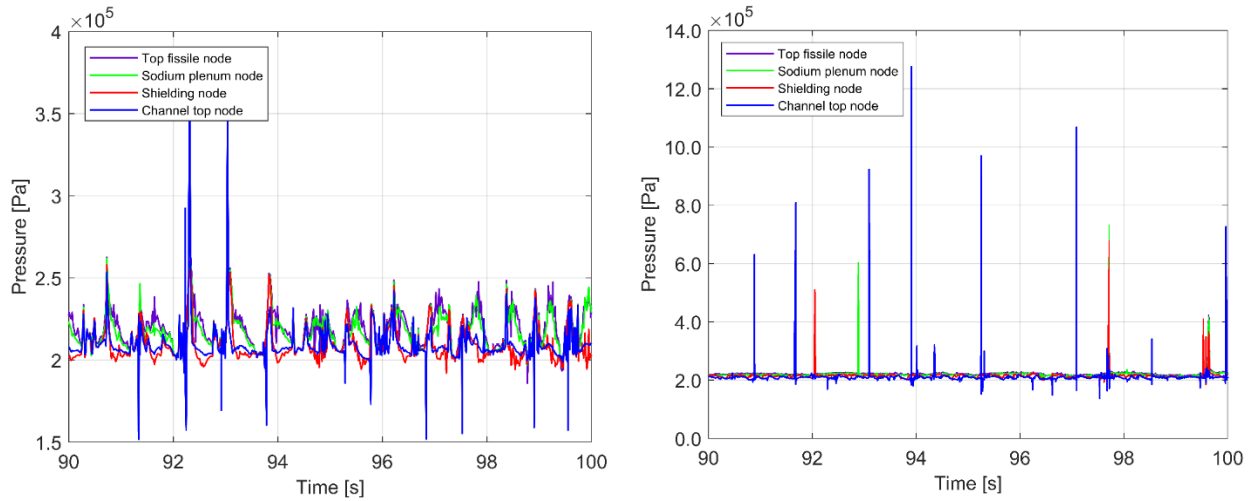


Figure 85. Pressure evolution at the fissile top, sodium plenum, shielding, and channel top axial nodes for the reference case (left) and the modified design case with windows (right) within the peak power SA vs time

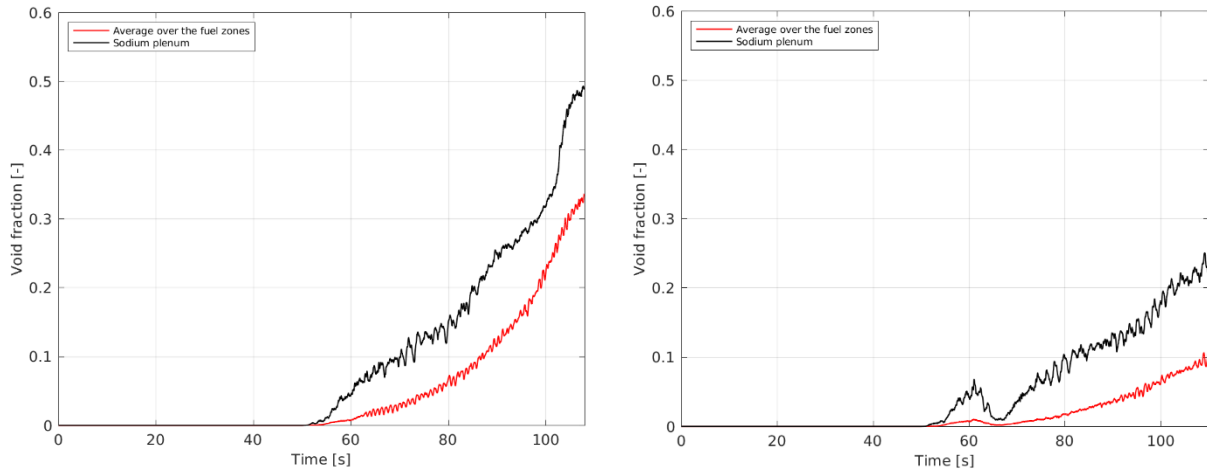


Figure 86. Average void fraction along the fuel and plenum regions over all the modelled channels for the reference case (left) and the modified design case with windows (right) vs time

4.1.6. Sensitivity study of various core parameters

A sensitivity study has been performed in the research to evaluate the boiling behavior evolution with the modification of a few key design parameters. Two separate groups of parameters can be distinguished: 1) Design modifications of the SAs, affecting the void propagation and 2) reactivity effect related parameters. For the current sodium boiling analysis the two most important reactivity effects are the Doppler effect and the sodium density reactivity effect. According to this, the chosen parameters have either direct effect on the reactivity evolution, such as plenum sodium void reactivity coefficient change or indirect effect, introduced by fuel gap conductance alteration, affecting the Doppler effect. The sensitivity cases are presented in Table 14.

Sensitivity case	Change magnitude
Inter SA gap heat exchange modification	The inter SA gap heat exchange was removed from the modeling completely
SA outlet design modification	The pin bundle geometry of shielding and reflector was changed into a sleeve geometry [10]
SA flow gagging scheme modification	3% of the CG1 sodium flow was redirected to the higher power CG2 zone
Fuel gap conductance modification	10% increase
Plenum sodium void reactivity coefficient modification	20% increase

Table 14. Applied sensitivity cases with change description

For the analysis of the sensitivity cases only the power, power to flow, separate reactivity effects, detailed sodium reactivity and peak power SA fuel and cladding temperature evolution have been assessed. Moreover, to see the effect of the sensitivity cases on the available grace time of the reactor, being an important parameter, a new no inter SA gap heat exchange model is used as for the comparison of the modifications. In this way the cladding melting could be reached within the simulated timeframe, allowing the required computational time to be kept relatively low. Consequently, in Section 4.1.6.1., the effect of the new no SA gap heat exchange is assessed on the results, whereas for the later sensitivity cases, this calculation was used as the reference simulation.

4.1.6.1. Reference case without inter SA gap heat exchange

For the first sensitivity case, the effect of the inter SA gap heat exchange is examined. In previous studies [25][81] this heat exchange was often neglected, resulting in a conservative approach. To characterize this effect, a sensitivity case was performed, where the heat exchange towards the inter SA sodium flow was switched off, in contrast to the previously described assessment, where it was included in the model. By doing so, the heat removal is decreased from the hot primary sodium flowing through the SA, by not having an extra sodium flow around the SA hexcans.

In Figure 87 the difference between the reference (Figure 74) and the current case can be immediately seen. Until the boiling onset, the power evolution is comparable for both calculations. Following that point at ~50 s, for the case without inter SA gap, the power starts to increase within a few seconds, having a sharper peak at ~80 s, leading to cladding meltdown and to thus to the end of the simulation. The normalized power to flow ratio shows similar trend, as the flowrate is equal for both simulation and

therefore the difference is based on the power evolution discrepancy. Although the power to flow ratio does not reach the level which was observed for the reference case (7.5 normalized power to flow), but stay under 6, the overall steady power increase leads to the melting temperature in the cladding, which was previously not observed. This comes from the fact that available coolant inventory has been decreased, by ~15%, therefore the lower amount of sodium has a more rapid temperature increase and boiling progression in the peak power SA, causing dryout and subsequent clad melting in the channel.

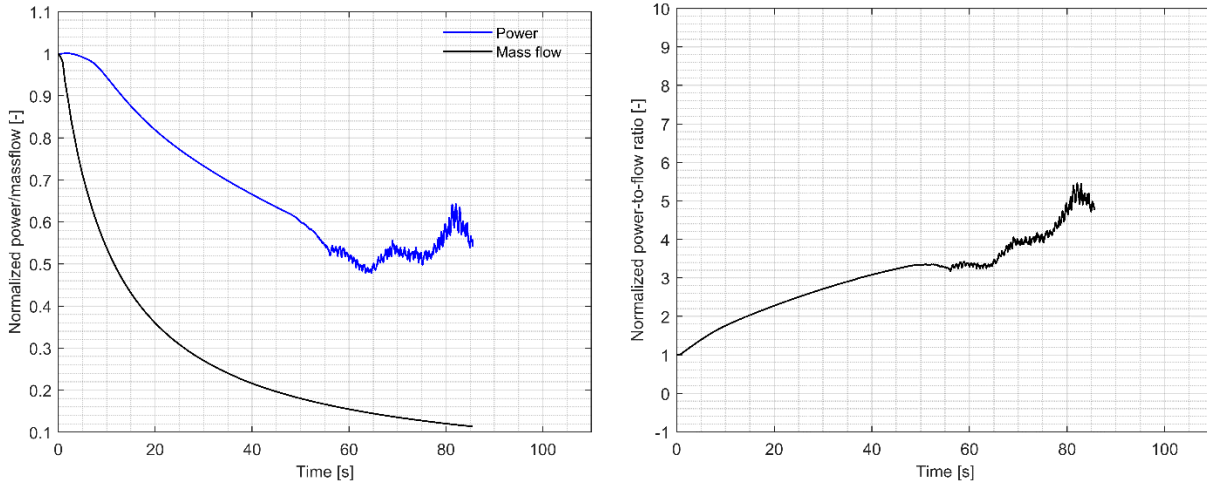


Figure 87. Normalized power/mass flowrate (on the left) and normalized power to flow ratio (on the right) vs. time following the initiation of the transient

When Figure 88 is evaluated, plotting the evolution of the various reactivity effects, the overall progression is comparable to the reference case, though lower absolute values are reached due to the earlier simulation end. The main difference, which points to a more rapid boiling progression, is the higher peak in the total sodium effect curve, pushing the total reactivity above 0. The plot on the right, reinforces this idea, as it shows that there is a strong increase in the CG2 fuel axial region sodium reactivity effect, compared to the reference solution (Figure 77), representing a fast void propagation downwards, towards the fuel region.

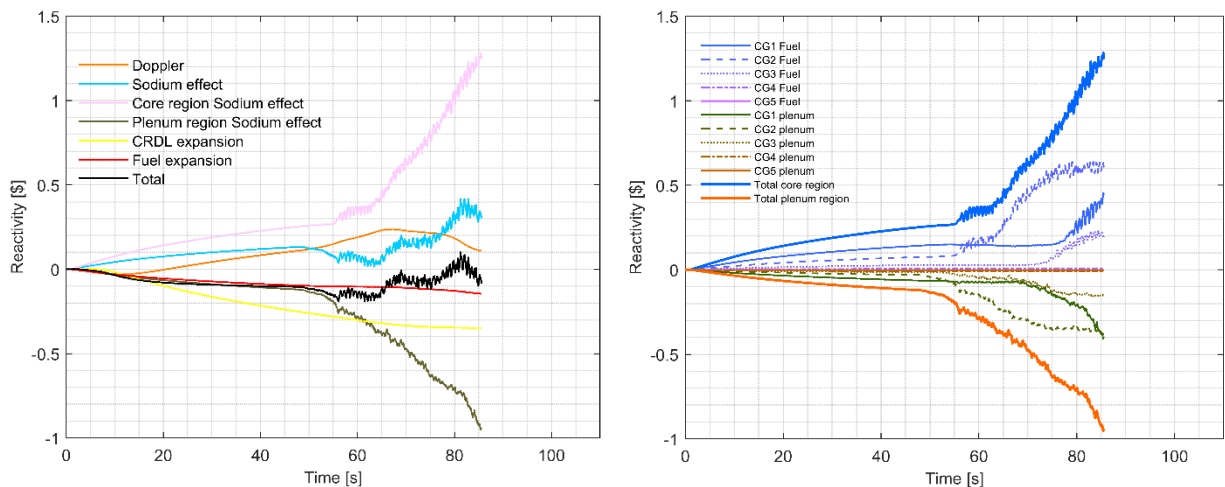


Figure 88. Evolution of the reactivity components used in the point kinetics (left) and sodium reactivity effect evolution, distributed between the different CGs for fuel and plenum axial regions (right) vs time

In Figure 89, the cladding melting temperature is reached at the presented 65 cm axial fissile height node, which caused the termination of the simulation. Following the boiling onset, the cladding experiences a rapid temperature increase, observed also in the reference case, which is followed by a slower and fluctuating temperature increase, due to partial bubble collapse during boiling, until the melting point is reached. The fuel temperature is still far from melting, but even here a steady temperature increase is shown, soon after the boiling onset.

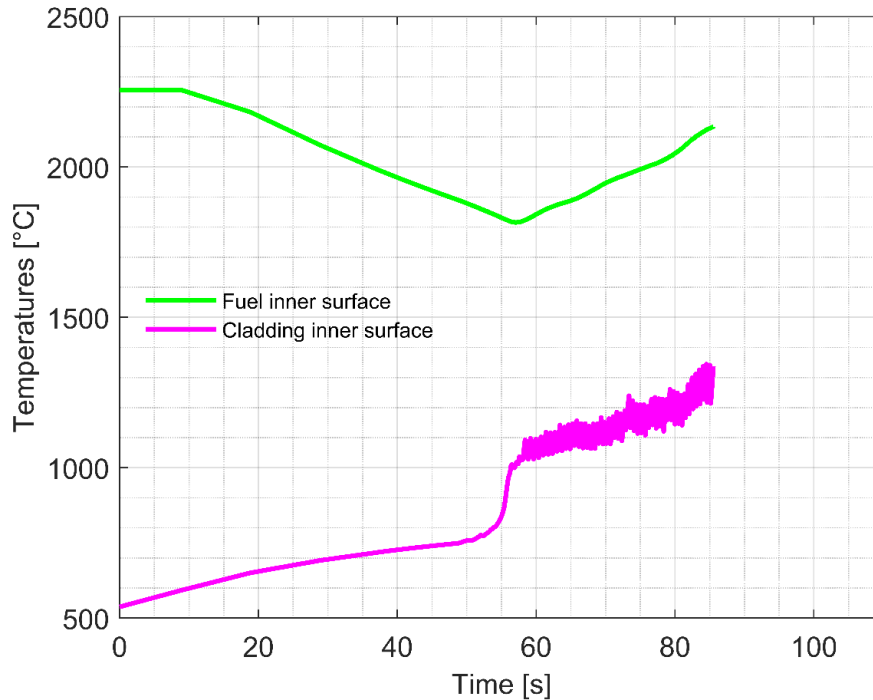


Figure 89. Fuel inner surface and cladding inner surface temperature evolution in the peak power channel at the fissile fuel middle node height vs time

4.1.6.2. Influence of the SA shielding and reflector design modification

The first geometry related sensitivity study is the modifications of the SA shielding and reflector design. The original design uses pin bundle upper shielding and reflector set-up, which was modified to a sleeve design used in the Superphenix reactor [10], with the keeping of the overall shielding and reflector material volume unchanged. With this modification, the hydraulic diameter is increased and the pressure drop at the SA top is reduced. As it was mentioned in Section 4.1.6, the current and the later presented sensitivity cases are compared to the results of the case without the inter SA gap heat exchange, described in Section 4.1.6.1, being the reference solution for the sensitivity study.

Figure 90 shows the effect of the modified SA outlet geometry on the evolution of the power following the boiling onset, which starts at the same time as it did in the reference design, at ~50 s. At ~70 s there is a power increase, but it starts later and recovers to a lower value, moreover, the immediate further sharp power increase is not present. The other obvious difference is the achieved longer simulated time until the cladding melting temperature is reached, providing an increased grace period of ~10 s. Similarly, the power to flow ratio, though exhibits a bump in the curve, the overall progression of the boiling seems to be more gradual, and the simulation does not end with a sudden power increase.

The reactivity components assessment is consistent with the reference case, only small discrepancies can be seen, which is true to the rest of the sensitivity cases also. In this sense, the Figures are provided in Appendix D for the interested reader.

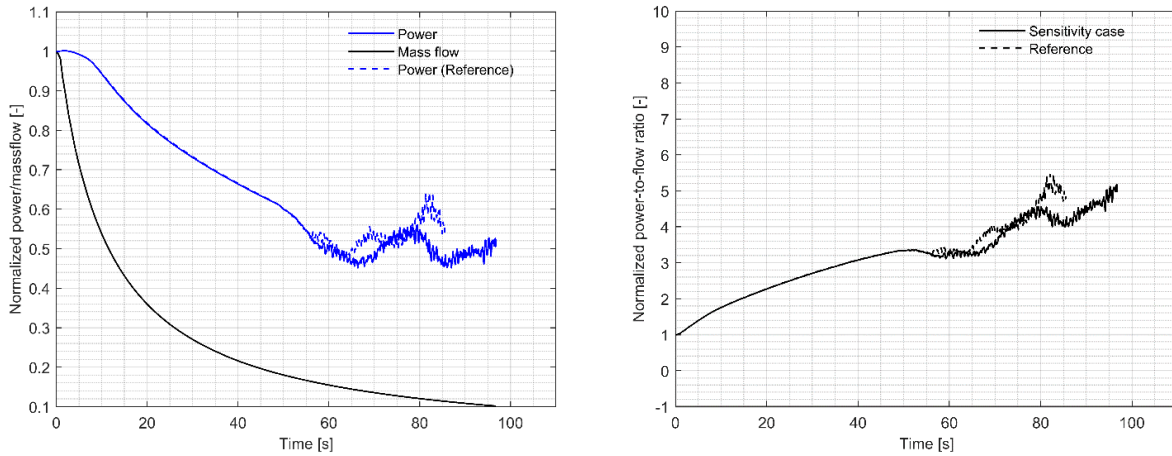


Figure 90. Normalized power/mass flowrate (on the left) and normalized power to flow ratio (on the right) vs. time following the initiation of the transient for SA outlet geometry sensitivity case

In Figure 91, the cladding inner surface and fuel inner surface temperature evolution is compared to the reference case. The cladding temperature increase is in general more gradual and following the boiling onset, it stays under the reference temperature value. For this case, the melting point is not reached in the node corresponding to 65 cm axial fissile height but in the node above that, at 70 cm, as it takes longer time for the vapor to propagate downwards. The fuel temperature increase also starts later in the sleeve outlet design, providing higher safety margin.

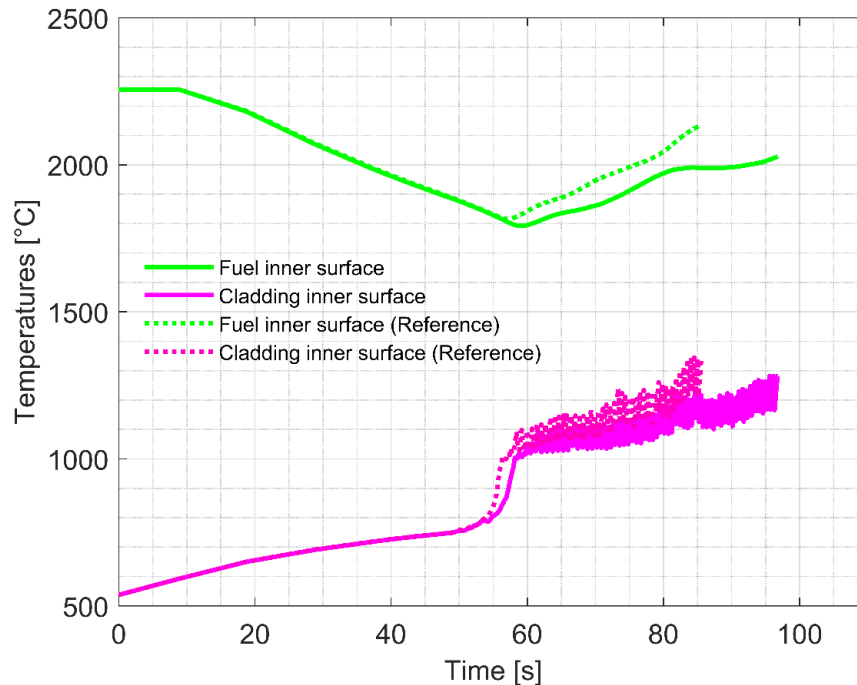


Figure 91. Fuel inner surface and cladding inner surface temperature evolution in the peak power channel at the fissile fuel middle node height vs time for SA outlet geometry sensitivity case

4.1.6.3. Influence of the cooling group flow distribution modification

The final geometry modification related study is the cooling group flow distribution modification. As it was seen earlier, the first SAs to boil are in the CG2, thus for this sensitivity case, a small fraction (3%) of the CG1 flowrate is redistributed to the CG2 SAs, by changing the orificing at the SA bottom. The case is only performed as a hypothetical scenario to assess the change due to potential flow re-distribution, as such change would affect the nominal operating conditions of the reactor on an undesirable manner, without core neutronic optimization.

The overall effect of the change in the sodium flow through CG1 and CG2 is comparable to the SA outlet design modification. The power and power to flow ratio in Figure 92, shows an increase at ~75 s with a sharper increase at the end of the simulation. The gain in grace time for the reactor during the simulated accidental scenario is ~10 s more before cladding meltdown occurs.

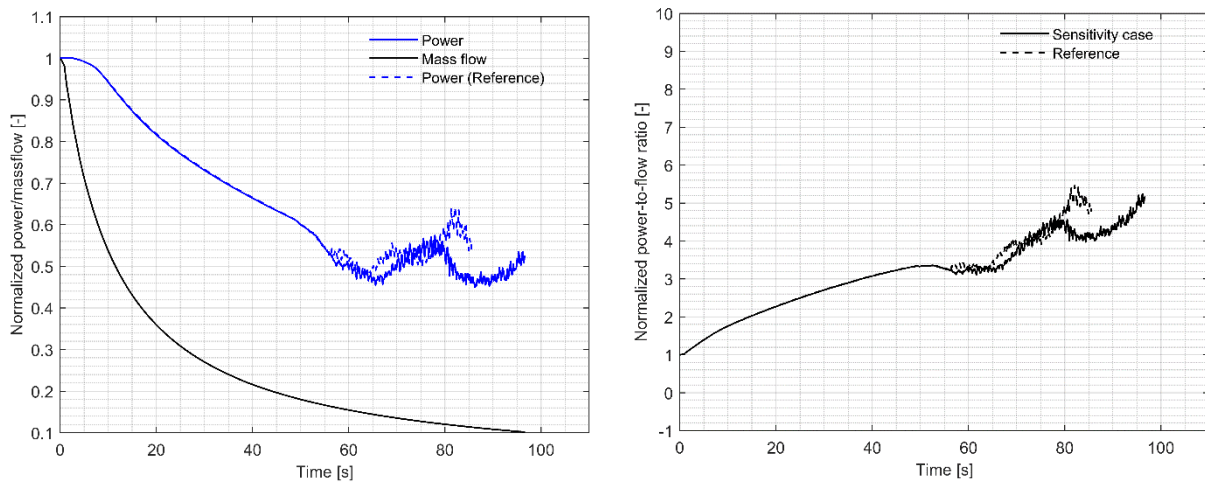


Figure 92. Normalized power/mass flowrate (on the left) and normalized power to flow ratio (on the right) vs. time following the initiation of the transient

As the previous Figures showed comparable results to the sleeve geometry modification case, the fuel inner surface and cladding inner surface temperature evolution also shows the same effect in Figure 93. Meaning, the clad melting occurs in a higher node compared to the reference case, with a general more gradual cladding temperature increase.

The observed difference can be explained by the reduced hydraulic resistance, similarly to Section 4.1.6.2., for the peak power SAs in CG2, originating from the different SA orificing at the bottom of the SA.

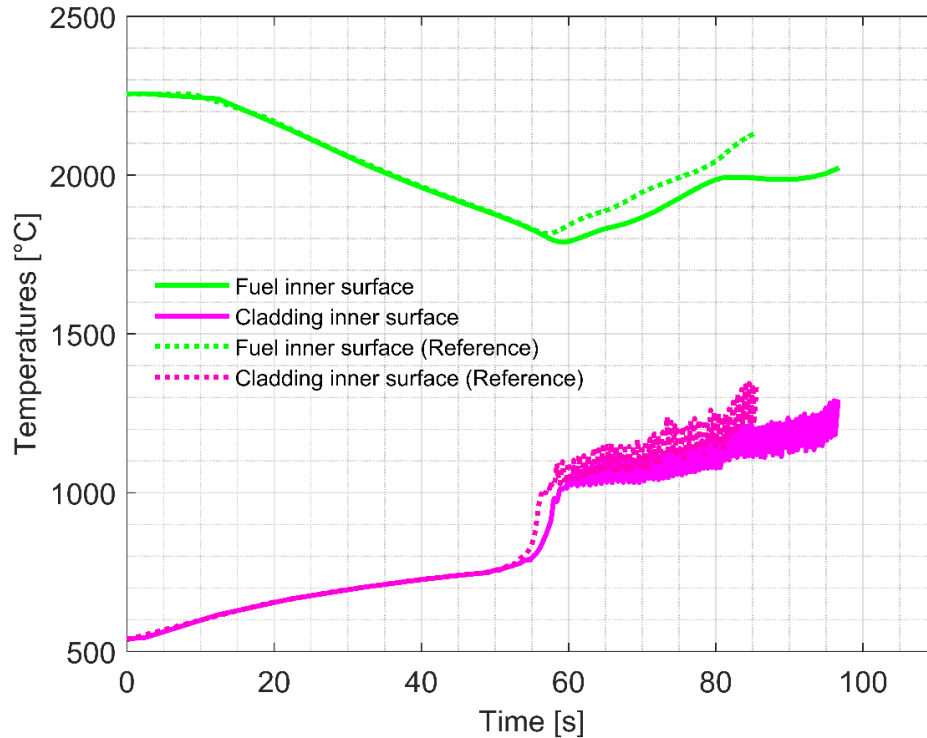


Figure 93. Fuel inner surface and cladding inner surface temperature evolution in the peak power channel at the fissile fuel middle node height vs time for CG flow distribution sensitivity case

4.1.6.4. Influence of the fuel gap conductance modification

In the next two sensitivity cases two non-geometry related parameters have been changed: first, the gap conductance has been increased by 10% for every SA in the model. It was assumed that by applying a higher gap conductance for the transient calculation, the average temperature of the fuel could be decreased, affecting the Doppler reactivity effect, and due to the different temperature profile, the overall reactor behavior.

In Figure 94, the plotted power evolution shows a very close behavior to the one which was observed for the sensitivity cases with geometry modification, especially the one with the modified CG flow distribution. The main difference between these two cases is the even further increased available grace time period of about 16 s.

The fuel and cladding inner surface temperature evolution, shown in Figure 95, is close to identical to the CG flow distribution modification study.

The presented Figures show that the overall effect of gap conductance modification affects the fuel temperature and boiling evolution related reactivity effects, shown in Appendix D, Figure A-D-5, comparably to the previous sensitivity cases with geometry modification.

In addition to impacting the Doppler effect, the gap conductance modification slightly changes the original energy deposition in fuel as well as the fuel-to-clad heat exchange rate during the transient.

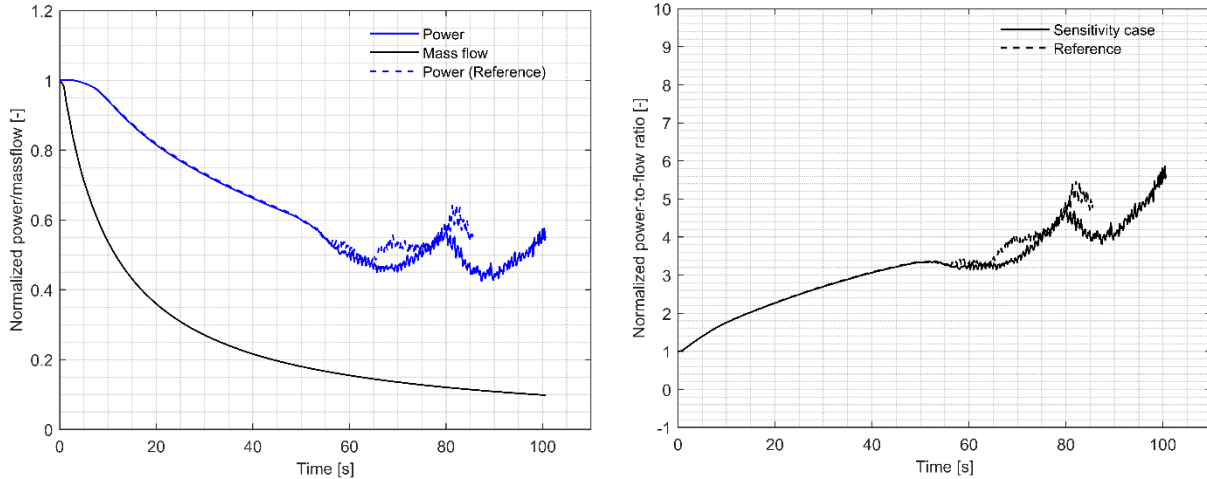


Figure 94. Normalized power/mass flowrate (on the left) and normalized power to flow ratio (on the right) vs. time following the initiation of the transient for the fuel gap conductance sensitivity case

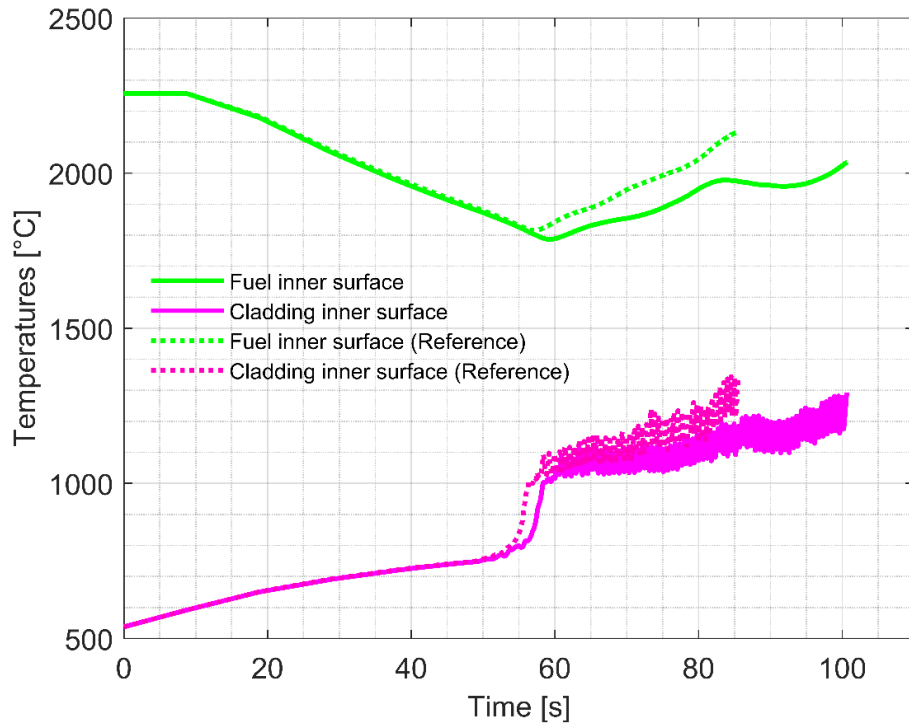


Figure 95. Fuel inner surface and cladding inner surface temperature evolution in the peak power channel at the fissile fuel middle node height vs time for the fuel gap conductance sensitivity case

4.1.6.5. Influence of the sodium plenum reactivity worth modification

For the last sensitivity case, the sodium plenum reactivity coefficient has been increased by 20% in the model. In reality, similar effect could be achieved by increasing the length of the plenum, affecting the neutron leakage out of the core in case of sodium boiling in that region.

In Figure 96, the effect of the change is clearly visible, as the normalized power curve shows the smallest reactivity increase at ~80 s, compared to the previous sensitivity cases, displaying less than 10% power

increase. Furthermore, from ~90 s, the power stays at ~40% of the nominal power, starting to increase only at the end of the simulation. Even though the power is closed to stable, the power to flow ratio keeps on increasing, due to the continuous reduction in core flow. Therefore, it results in the melting of the cladding and the termination of the simulation at ~105 s, providing 20 s extra grace time compared to the reference case.

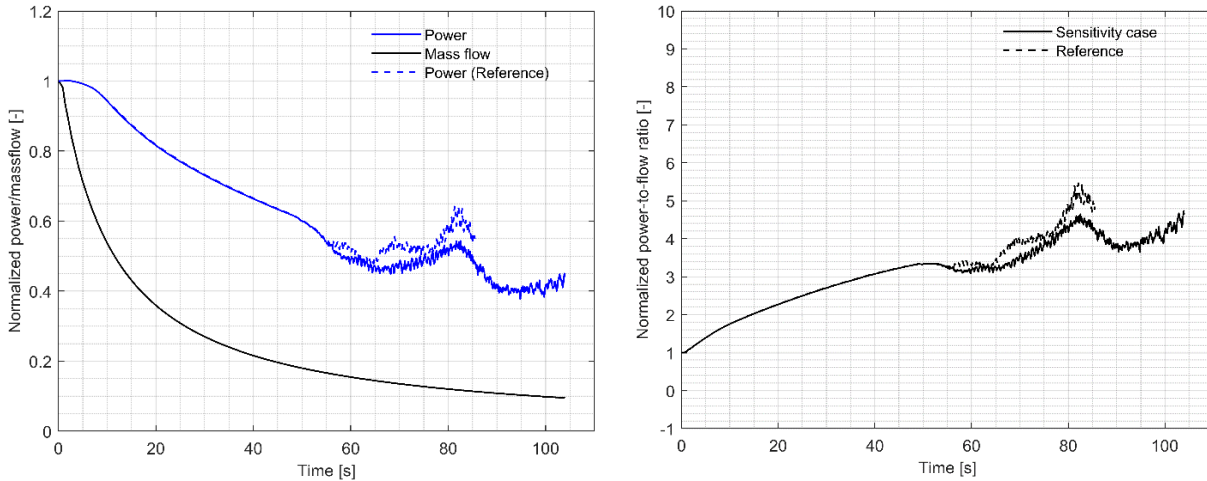


Figure 96. Normalized power/mass flowrate (on the left) and normalized power to flow ratio (on the right) vs. time following the initiation of the transient for the sodium plenum sensitivity case

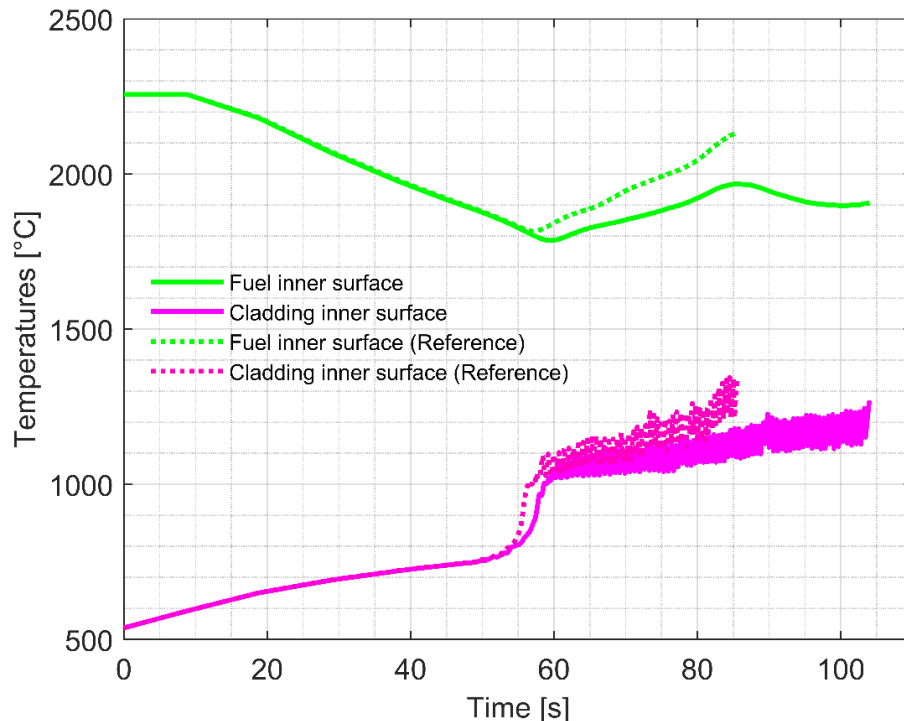


Figure 97. Fuel inner surface and cladding inner surface temperature evolution in the peak power channel at the fissile fuel middle node height vs time for the sodium plenum sensitivity case

The fuel and cladding temperature assessment, in Figure 97, shows also the benefit of the increased plenum effect, as they have the lowest gradient within the sensitivity study, resulting in the highest safety

margin increase. As it has been written in Section 4.1.6.2, and has been the case for most sensitivity simulations, the cladding melting temperature is reached in an axially higher node than in the reference calculation, showing that longer time was required for the vapor to propagate downwards in the SA.

4.1.7. Conclusions of Section 4.1

In this Section, the ESFR-SMART core behavior under ULOF accidental conditions has been investigated with the TRACE system code, using a low void effect core design. In the analysis, special attention has been given to the sodium boiling reactivity effect and the coolant flow pattern evolution throughout the accident. The full reactor model in TRACE was simplified into a 42 channel reactor core model, accounting for 1/12th of the full core, exploiting the symmetry of the reactor. A ULOF accident simulation starting from an initial steady-state at nominal operating conditions is studied for the time period of 110 s. The simulations are performed for the reference design case and for the one with the modified SA wrapper design with the aim of increasing the stability of the reactor behavior during sodium boiling. Beside these two main calculations, calculations for few sensitivity cases have been also performed, assessing the effect of various SA design and core parameters on the core behavior under ULOF. The following conclusions are made based on the analysis results:

- For the reference SA design, the reactor power stays stable for ~40 s following the boiling onset, providing a large available grace time period. Later on, it starts to show instability and fluctuation. The sodium vapor initially fills the plenum above the fuel within the SA, counterbalancing the otherwise positive sodium reactivity effect. The anticipated stable chugging boiling is not reached with the originally proposed design as the vapor does not collapse entirely when vapor bubbles leave the channel and liquid sodium re-enters the channel, but starts to propagate downwards to the fuel region, providing positive reactivity insertion into the core. Although stable boiling condition was not reached, no power runaway has been observed throughout the accident for the simulated period of time, which can potentially provide enough grace for other safety measures, such as a passive magnetic control rod release device, to shut down the reactor safely [8].
- As a modified case, a change has been implemented on the SA design. Namely, SA wrapper windows have been introduced in the model towards the inter-SA gap providing a flow path for the liquid sodium even when at the top of the SA the path is blocked by sodium vapor. Using this design, stable chugging boiling regime was achieved starting from boiling onset, and the reactor behavior stays stable throughout the simulated timeframe. In this sense, the applied design modification could potentially help to reach the desired safety level for the reactor during a hypothetical ULOF accidental scenario, being a potential reference design option for future SFR designs. This recommendation, however, should be supported by experimental demonstration.
- The various assessed sensitivity cases for the reference design revealed the potential effect of certain changes in the SA geometry, fuel gap conductance or reactivity coefficients on the sodium boiling evolution. Although the cladding melting onset was not possible to avoid with any of the simulated sensitivity options, the available grace time could be increased, providing more time for the reactor operators to act or the passively activating safety mechanism to be initiated in order to avoid the reactor damage.

4.2. Assessment of SPX under ULOF conditions with new methodology

In Section 2.4.2, a hybrid spatial kinetics (SK) methodology based on sampling of transport cross sections has been proposed for the calculation of the reactor power coupled with TRACE thermal hydraulic system code. The development of the proposed methodology was originally intended to perform transient simulations, where quick neutronic calculations are required. In this Section a ULOF in the Superphenix reactor core was simulated with this new methodology until the sodium boiling onset. No experimental data are available to compare the simulation results with and, since a point kinetics (PK) model of Superphenix was validated using the start-up tests [82], it has been used for comparison with the new methodology.

4.2.1. ULOF simulation description

Before the different calculation methods were run, a steady-state calculation was performed to provide the identical nominal starting conditions for both neutronic methods (hybrid SK sampling (later just SK) and PK). From this starting point, both calculation schemes were applied on the core, first, by keeping the nominal operating condition to provide enough time for the stabilization of the simulation following the restart process from the nominal state. After this point, following the initiation of the simulation, the ULOF transient starts (time=0 point in the Figures), with gradually decreasing inlet flowrate, corresponding to the primary pump coast down with halving the pump rotational speed at every 10 s [82]. As it has been in the previously presented ULOF calculation in Section 4.1, the control rods are kept in the nominal operating condition level, failing to reduce the core power to the shutdown level. With decreasing inlet flowrate and without utilizing the control rods, the reactor behavior is governed by the various feedback effects. In the current analysis, these effects are limited to the sodium density effect and Doppler effect, for both point and spatial kinetics, corresponding to the effects also analyzed in the static stage of the assessment. These feedbacks can be strongly spatially dependent, especially when sodium boiling is reached or when strong local perturbation is applied on the core, such as a control rod ejection, therefore their use is crucial for the comparison with the point kinetics method.

4.2.2. Model description

For the aforementioned SK ULOF analysis, the PARCS code coupled with the TRACE thermal-hydraulic system code was used. In the coupling, each SA modelled in PARCS was connected to a separate thermal hydraulic channel. In TRACE, only the primary circuit has been modeled [82], thus at the bottom of the channels, a sodium flow with constant temperature of 673 K was specified, corresponding to the nominal operating conditions. At the top of the SAs, an outlet pressure boundary condition has been used, shown in Figure 98.

The XSs used within PARCS have been prepared already in the previous static analysis part, described in Section 2.3.2, where the modeled core geometry was also presented. The kinetic parameters were obtained from the Serpent 2 Monte Carlo calculations for the same core model. In this sense, 8 group of delayed neutron precursors were considered in the model, using the effective delayed neutron fractions.

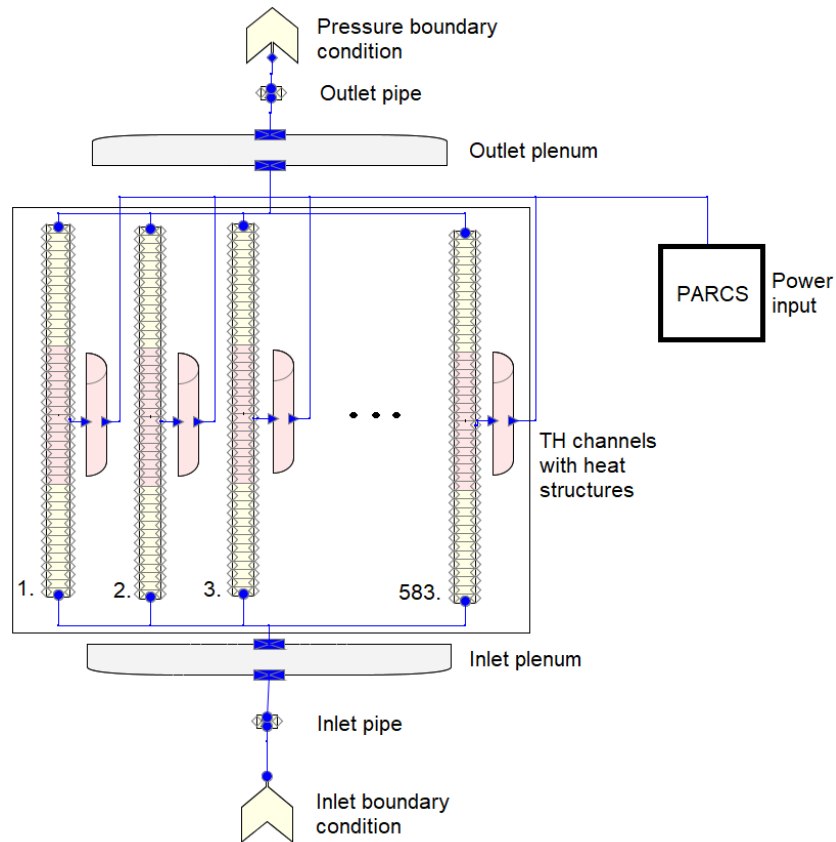


Figure 98. Superphenix model of the coupled TRACE/PARCS codes for the ULOF analysis

4.2.3. Transient results with sodium and Doppler feedbacks

To compare the two methods, the first parameter which was assessed is the reactor power temporal evolution. In Figure 99, the reactor power normalized to the nominal power is plotted. Both methods give close results to each other, having ~1% higher power for the PK method at ~30 s of the calculation. The behavior of the reactor shows qualitatively identical progression, meaning that in the first seconds of the calculation there is a small increase in reactor power, which is followed by a sharp power decrease until the end of the simulation, reaching sodium boiling onset, due to the dominating effect of the fuel heat-up.

In Figure 100, the fissile average fuel and core average sodium temperature are shown, which define core reactivity feedback. Both temperatures are gradually increasing, which creates a competing effect, as the increasing sodium temperature (thus lower density) would increase the reactivity of the core due to harder neutron spectrum. On the contrary, the increasing fuel temperature would decrease the core reactivity, due to the higher neutron absorption. Overall, the curves for both methods reveal the same tendency, having only a few kelvin of discrepancy between.

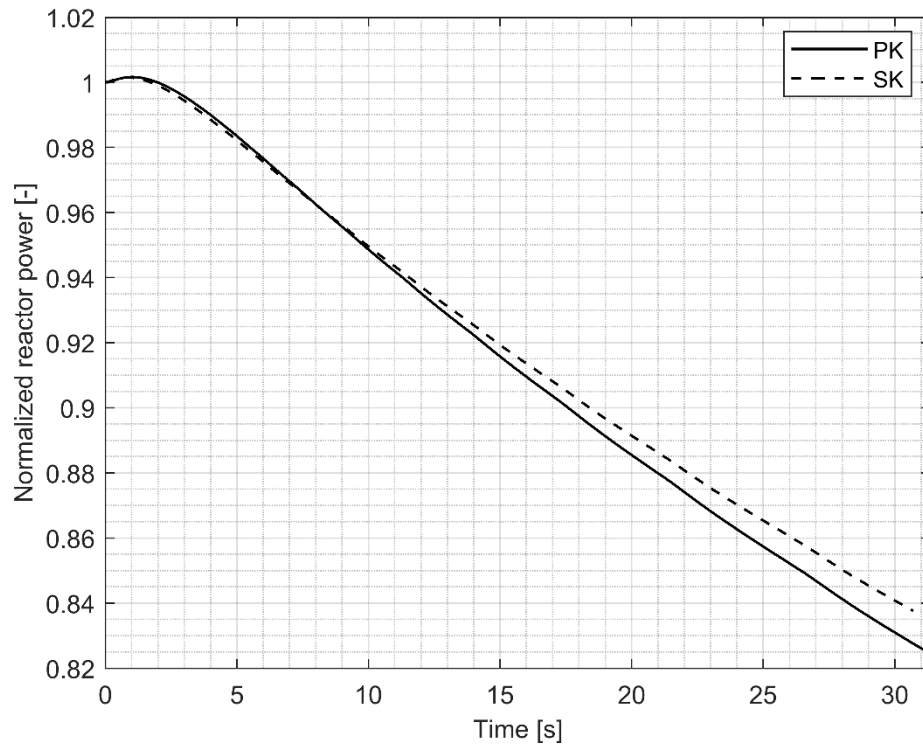


Figure 99. Temporal evolution of the normalized reactor power for PK and SK methods

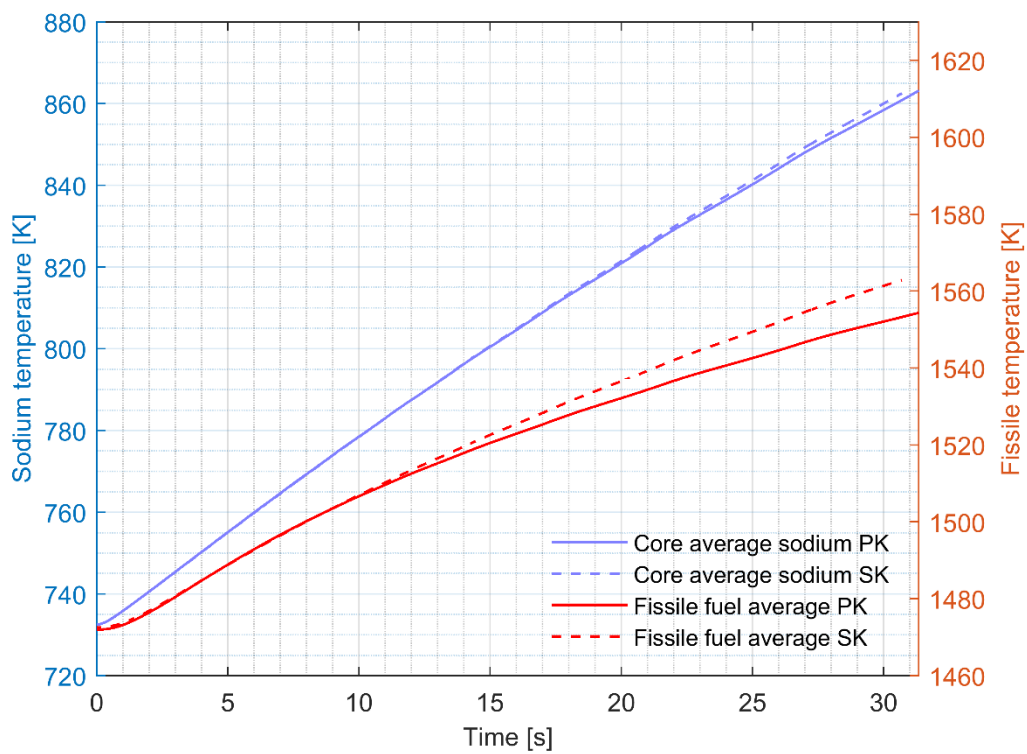


Figure 100. Temporal evolution of the average fissile and core average sodium temperature for the PK and SK simulations

Figure 101 shows the evolution of the reactivity feedback in the reactor core. The Figure emphasizes the small initial reactivity increase, which was also observed on the power evolution plot. This is due to the fact that the initial increase of sodium temperature is more rapid than the subsequent increase in fuel temperature. Therefore, in the first ~ 2 s following ULOF initiation, the sodium density feedback dominates but then it is quickly superseded by the contribution from the Doppler effect, resulting with the overall negative reactivity insertion. Both, neutronic methods agree well qualitatively, providing comparable overall behavior during the course of the simulation. Nevertheless, $\sim 12\%$ discrepancy can be observed by ~ 30 s of the simulation, as the PK method gives higher negative reactivity insertion value.

It is not possible to obtain a reactivity decompositions to have a more detailed Figure of this discrepancy due to the method used in PARCS, as it creates a XS change based on the combined effect of the applied feedbacks. Therefore, two separate simulations have been conducted, applying the sodium and Doppler feedback effects separately using the same model. The power evolution plots are presented for all these calculations in Figure 102. Overall, the power evolution agree qualitatively between the 2 methods for all feedbacks, but certain deviation can be observed, especially for the sodium reactivity feedback case. Due to the sodium feedback coefficient difference, the predicted reactivity increase is greater within the PK simulation, which further increases the sodium heat-up, resulting in $\sim 4.3\%$ power difference at ~ 30 s of the simulation when cladding meltdown occurs. As for the Doppler feedback only, the difference is smaller, resulting in $\sim 2.5\%$ power difference by the end of the simulation. The two feedback differences balance each other out when both of them are applied in the mode, resulting in an overall $\sim 1.7\%$ power deviation.

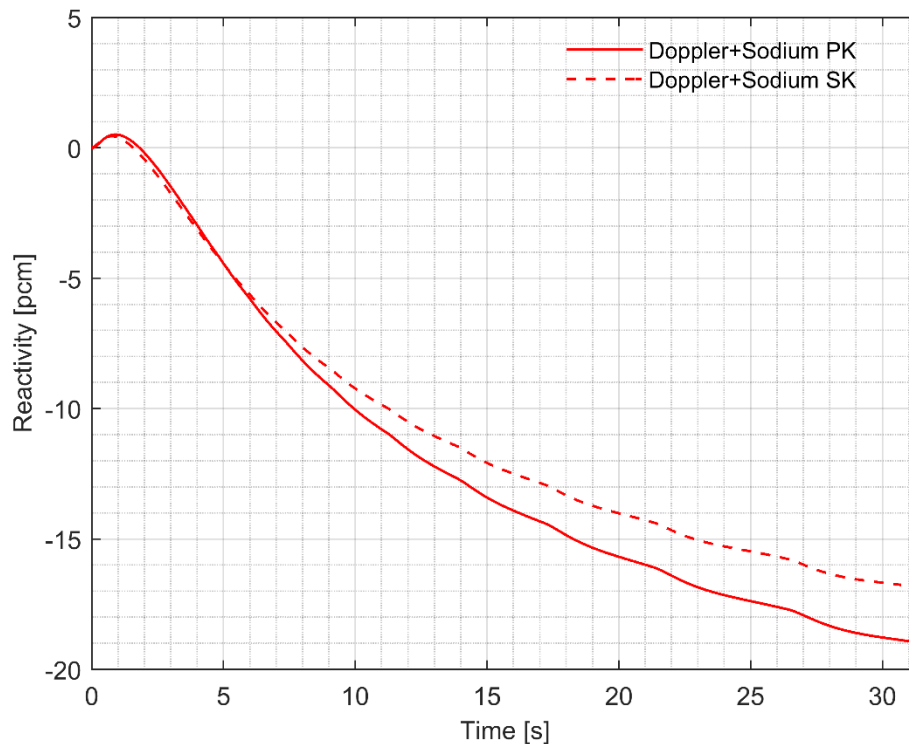


Figure 101. Reactivity insertion comparison between PK and SK methods measured from the ULOF initiation point

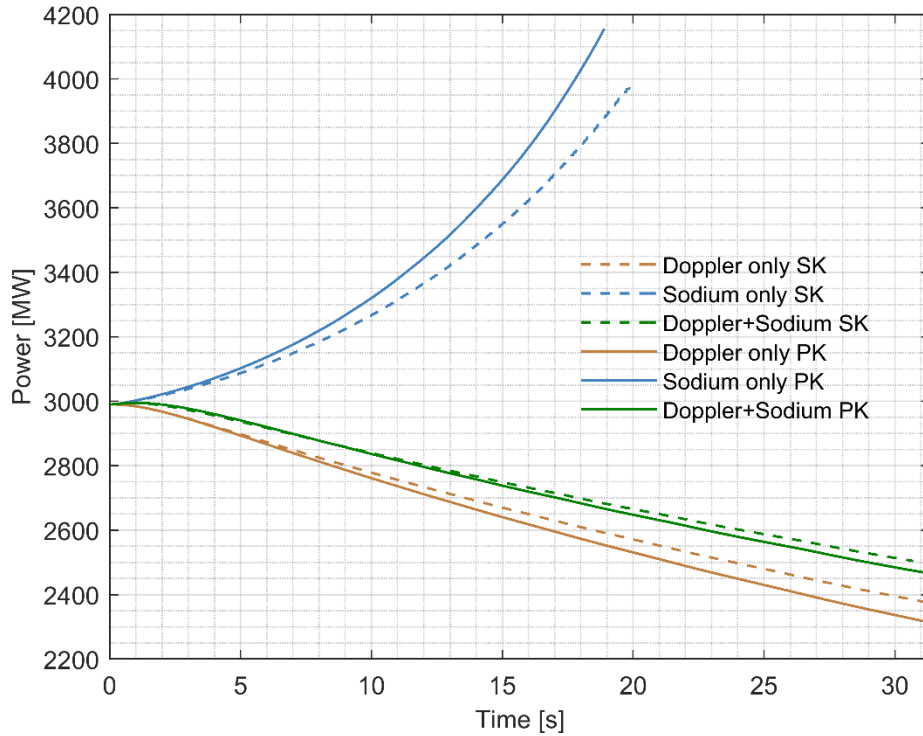


Figure 102. Comparison of the temporal evolution of the power between PK and SK methods with reactivity feedback decomposition

In Figure 103, the radial map of the relative SA power difference between PK and SK is presented for the Doppler plus sodium density feedback model, showing the core state at the end of the transient simulation, just before boiling onset. As in the beginning of the transient both PK and SK have identical power distribution and the power peaking does not change for PK throughout the simulation, the Figure can be understood as showing the SA power deviation due to the implemented spatial dependence on fuel temperature and sodium density. The overall power difference is low, peaking $\sim 0.2\%$ at the middle of the reactor core, which shows that due to the spatial dependence, the SK method predicts a higher power at the core center region, whereas around the periphery of the fissile core it predicts lower powers by a maximum of $\sim -0.1\%$. This change shows a steeper radial power using SK compared to PK. This effect can be explained by a higher relative Doppler contribution at the peak power SA regions, close to the periphery the inner core, shown in Figure 20. For the highest power SAs, due to greater fuel heat-up, the Doppler reactivity contribution is increased compared to the center of the reactor core. Thus, the relative power change is decreased more at inner core periphery than it is at the core center [49]. Furthermore, the more positive reactivity contribution of sodium density change at the center of the core can also play a role in the power shape deviation, due to the lower neutron leakage compared to the more periphery SAs. In the breeder region at the core periphery, the difference can be up to -0.3% but as the produced power is orders of magnitudes lower than it is in the fissile region, this difference is generally negligible.

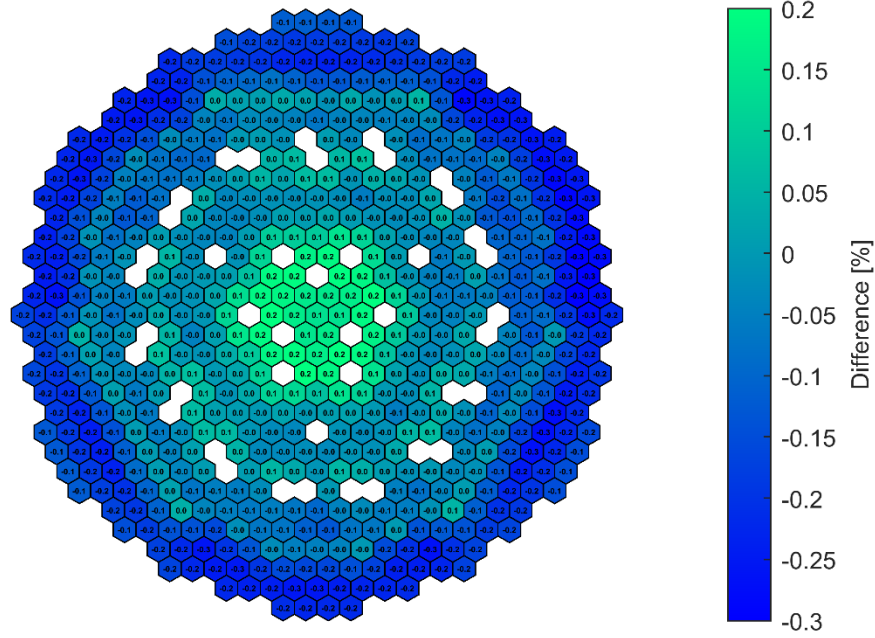


Figure 103. Relative power difference comparison between SK and PK

4.2.4. Control rod shift simulations

Previously it was demonstrated that for the ULOF calculation until the sodium boiling onset, both SK and PK neutronic methods gave reasonably close results of power evolution. To demonstrate the importance of the proposed new hybrid SK sampling method, another case was assessed, where strong local neutronic perturbation has been included in the model, by means of the insertion and withdrawal of specific control rods. The rods, which were moved in the model are shown in Figure 104. The pattern follows the way it was described for the Phenix control rod withdrawal test, performed as part of the end of life experiments [83]. In this sense, the model consist of a nominal condition calculation, during which the reactor reaches its nominal temperature distribution. Following this, the transient starts with the insertion of one control rod into the reactor by 10 cm within 0.5 s, this is followed by a 50 s of stable operation, through which the reactor power reaches its new level. To increase the flux disparity, after this 50 s stable operation period, another control rod is moved, withdrawing it by 10 cm from the core within 0.5 s. This state of the core stays until the end of the total 100 s simulated transient time.

For the proposed simulation, the control rod worth was required for both the 10 cm rod insertion and the 10 cm rod withdrawal. For the PK method, the reactivity effect was obtained from the Monte Carlo simulation, showing the reactivity effect of -49 pcm for the control rod insertion and 53 pcm for the rod withdrawal. These values were simply implemented in a table format within TRACE. As for the SK method, no specific calculation was performed to process new XS set but rather the available control rod XS data was used, simply adjusting the axial region height according to the control rod movement. Therefore, small differences in the reactivity effect between the two calculations is possible.

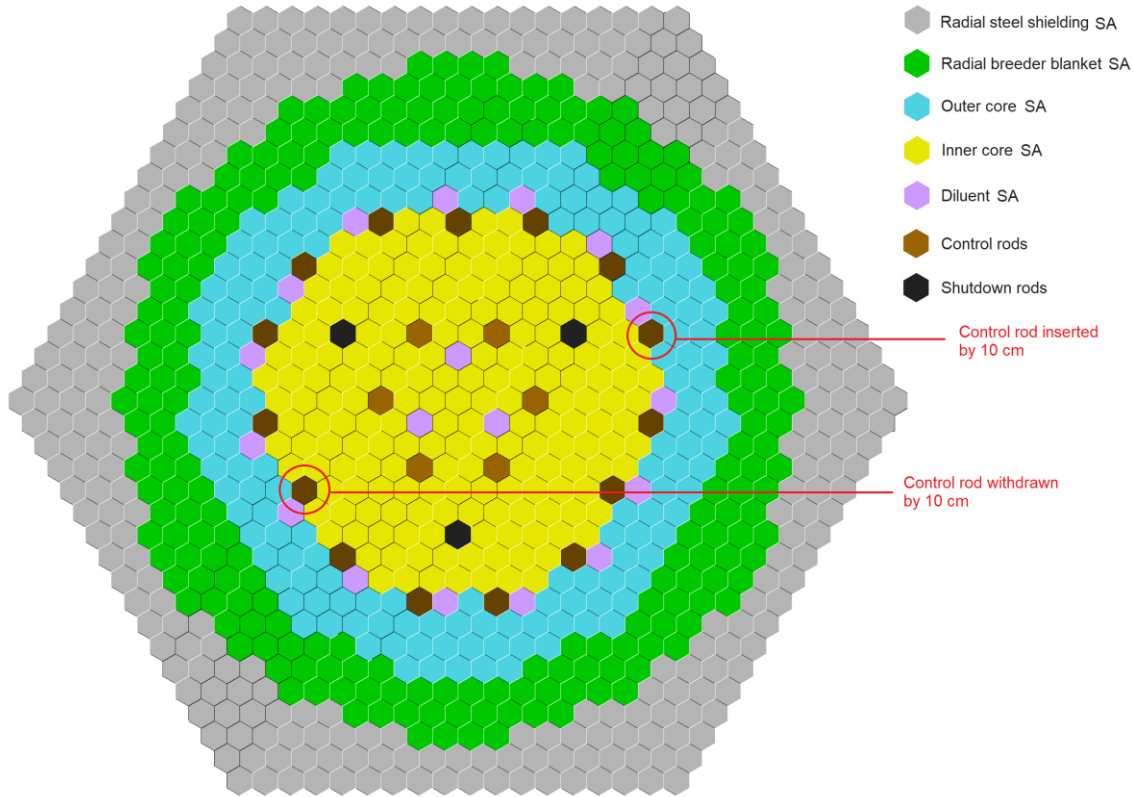


Figure 104. Superphenix reactor core radial structure with the adjusted control rods highlighted

In Figures 105-107, the temporal evolution of specific core parameters are plotted. In the Figures, the time starts 10 s before the initiation of the transient, namely the moving of the control rods. Therefore, from between 0 and 10 s, the nominal conditions are depicted.

Figure 105 shows the power evolution for both PK and SK calculations, showing a higher power decrease at 10 s and power increase at 60 s, corresponding to the control rod insertion and withdrawal, due to the difference in rod worth between the methods. Although, the initial power change difference is ~4% at the control rod insertion and ~10% at the control rod withdrawal, the stabilized power level, due to the reactivity feedback, stays close for both calculation schemes at ~1% and 2% for control rod insertion and withdrawal, respectively.

In Figure 106, the reactivity effect introduced by the control rod movement is plotted. As the control rod movement happens in short time, 0.5 s, there is a sudden reactivity change, equal to the control rod worth inserted or withdrawn by 10 cm. Following the sharp reactivity change, the Doppler and sodium density feedback effects quickly counter balances the control rod movement and the reactor is approaching again 0 reactivity by the end of the 50 s stabilizing time. Overall, the temporal evolution of the reactivity is close to identical in both methods, showing again that the feedback effects are well implemented in the proposed new hybrid SK sampling method.

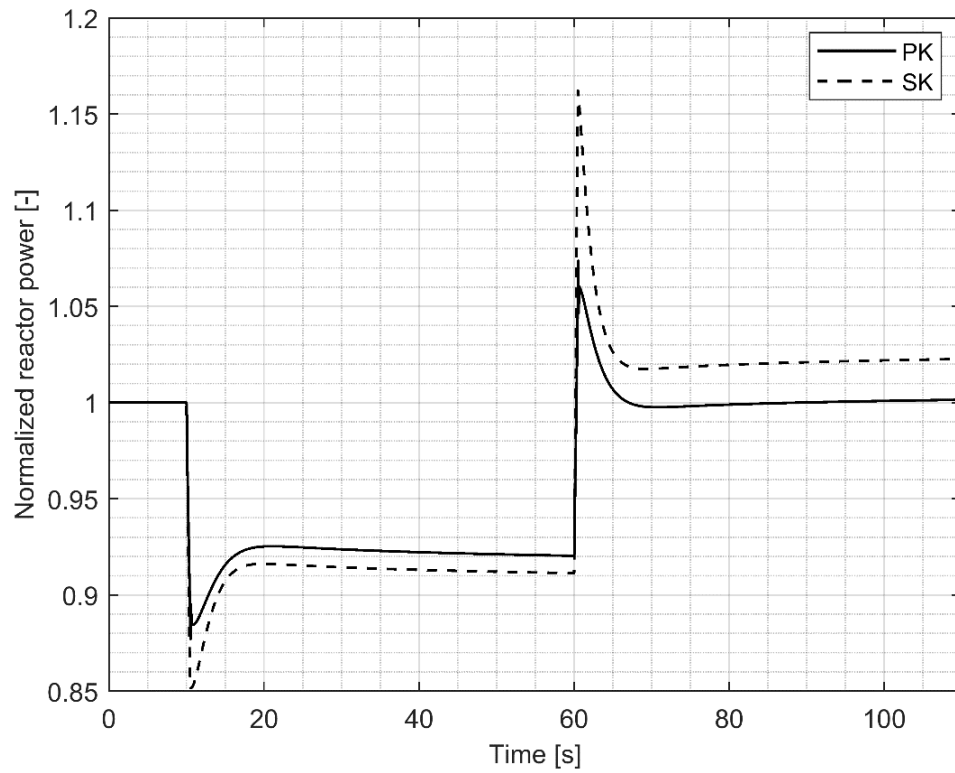


Figure 105. Temporal power evolution of PK and SK during the transient, which starts at 10 s

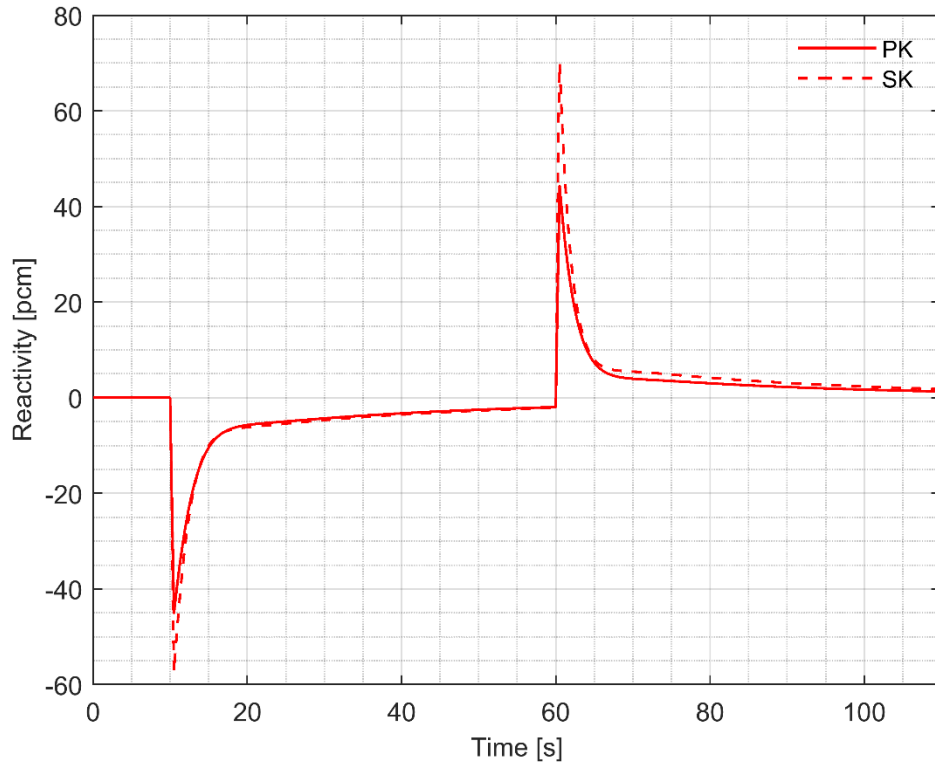


Figure 106. Temporal reactivity evolution of PK and SK during the transient, which starts at 10 s

Figure 107 presents the evolution of the fissile core average temperature and the core average sodium temperature. The evolution of these temperature fields determine the magnitude of the Doppler and sodium density feedback effects for the different calculation methods. As the temperature evolution is dependent on the reactor core power and the coolant flow rate, which was kept equal for both methods, it is not surprising that the SK reactor core temperature is lower for the control rod insertion stage and higher for the withdrawn stage than it is for PK. The $\sim 1\%$ lower power translates into about ~ 10 K lower core average temperature, whereas in the second stage the $\sim 2\%$ higher core power results in ~ 20 K higher average fissile temperature. Consequently, this change impacts the Doppler feedback effect, counteracting the difference in the control rod reactivity effects. As for the core average sodium temperature, a maximum of ~ 1.2 K difference can be observed, which results into a marginal density change and, therefore, into a small reactivity effect difference.

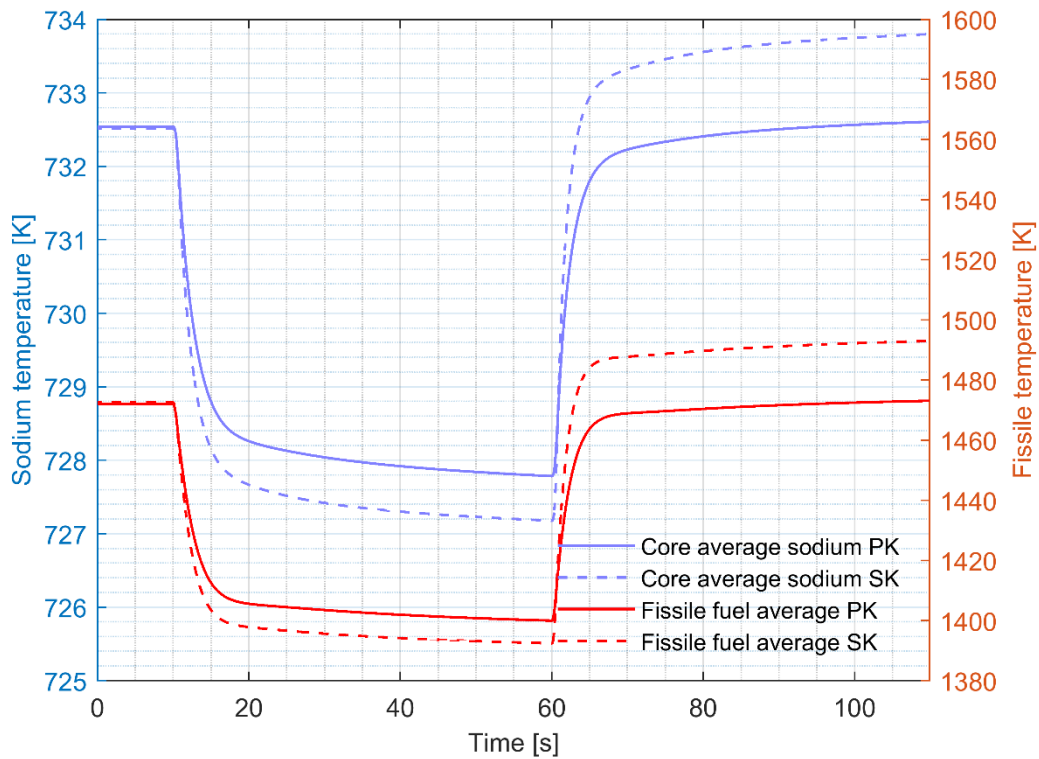


Figure 107. Temporal evolution of the inner and outer core average and core average sodium temperature of PK and SK during the transient, which starts at 10 s

Figure 108-109, shows the advantage of the proposed hybrid SK sampling method as it allows the more accurate resolution of a local perturbation, in contrast to PK, where it is only the amplitude of the flux which is perturbed but the overall shape is not affected.

In this sense, Figure 108 presents the SA wise power difference between PK and SK and as it was mentioned above, significant deviation can be observed. This deviation is especially emphasized around the control rods, which were moved within the simulation, reaching -16.2% around the control rod inserted by 10 cm and 15.9% , where the control rod was withdrawn.

Similar trend is shown in Figure 109 also, where the maximum fuel temperature difference is presented, having a maximum difference of -182.6 K and 266.7 K, in accordance with the power difference.

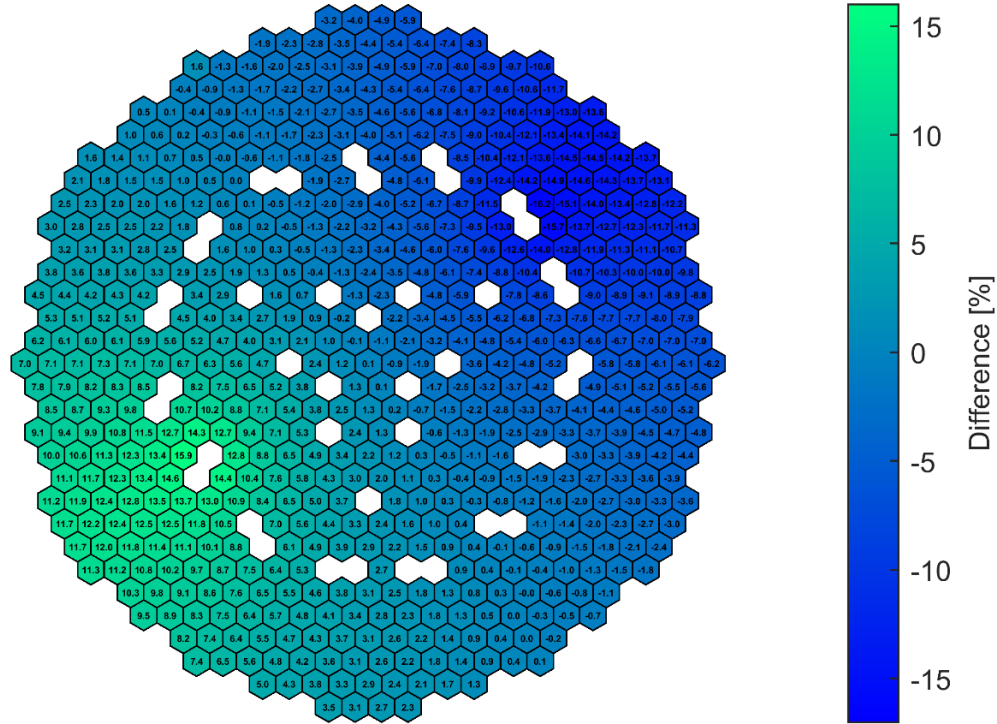


Figure 108. Relative power difference of the different SAs in the core for SK and PK

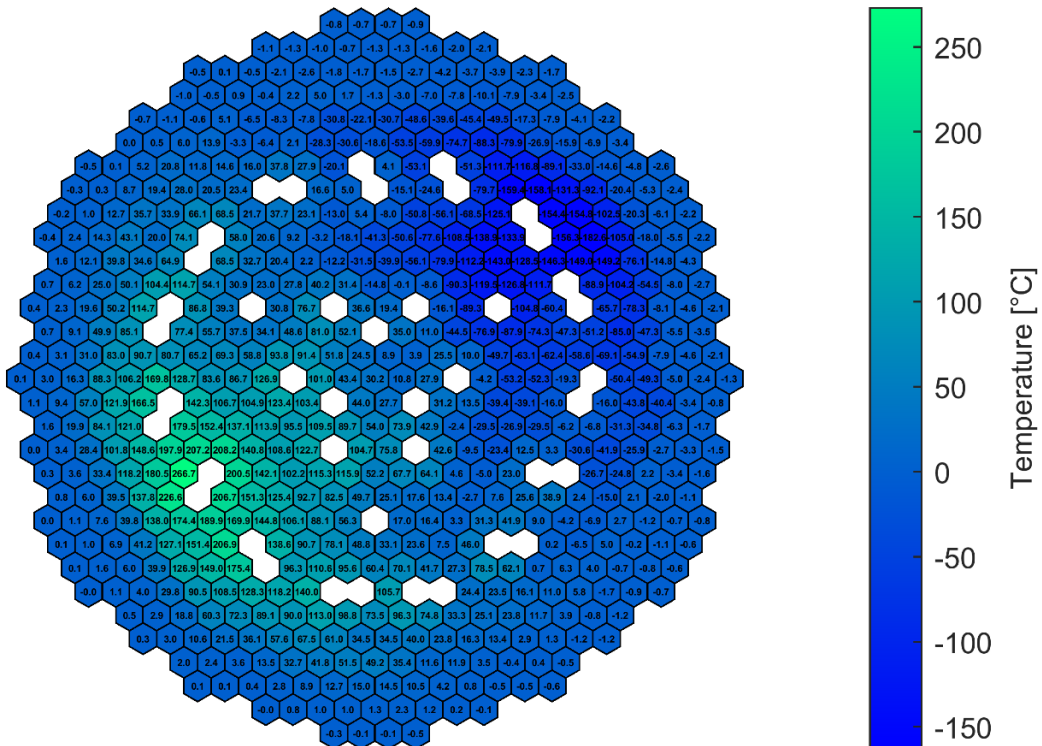


Figure 109. Maximum fuel temperature difference of the different SAs in the core for SK and PK

4.2.5. Conclusion of Section 4.2

In the analysis, two different transient simulation scenarios have been modeled and assessed using the Superphenix reactor core model, described in Section 2.3.2. In this Section, the proposed hybrid spatial kinetics sampling method has been compared with the well-established point kinetics method, serving as a transient benchmark. In the first case, a ULOF simulation was performed, up until the point of sodium boiling onset, using only the Doppler and sodium density reactivity feedback effects, presented in the static part of the analysis. In general good agreement was achieved between the two calculation routes. Qualitatively all results agree, which reinforces that the developed methodology can be utilized for transient calculations, although proper validation work is still required using actual plant data.

In the second transient scenario, a strong local perturbation has been applied on the reactor core by moving 2 of the control rods opposite to each other, one inserted by 10 cm and the other withdrawn by 10 cm. By doing so, the strong difference was seen in the SA wise radial power and maximum fuel temperature map. This final calculation shows the need for a 3D method, such as the proposed nodal diffusion method, where the strong local perturbation can affect the conclusions of a safety analysis.

4.3. Assessment of core geometry distortion effect

The assessment of core geometry distortion effect is divided into two separate studies in the thesis. 1) In the first part of the study, the static core deformation assessment methodology is applied on the ESFR-SMART core design, which was also applied on the Phenix study and EOL experiments in Section 2.4. By doing so, the core flowering reactivity effect can be compared to the effect observed on the Phenix reactor. 2) Within the second part of the study, a transient core deformation is simulated for the Phenix reactor design described in Section 2.4. The reactivity evolution throughout the transient is assessed at various time points, covering the course of the deformation calculation. The core geometry distortion scenario was set-up to simulate the likeness of a sodium boiling induced core deformation, from which the core deformation induced power evolution was calculated. As the overall deformation is similar to the dynamic of a core flowering effect, the power evolution was compared to the Phenix reactor power during the AURN negative reactivity event, for which the currently prevailing explanation is reactor core flowering as the origin of the reactivity variation in the incident.

4.3.1. ESFR-SMART static core flowering calculations

4.3.1.1. Core modeling and simulated scenarios

The static core geometry distortion scenario for the ESFR-SMART core design was set-up to replicate the study performed in Section 2.4. Therefore, the modeled reactor core, shown in Figure 110, was loaded with forces placed on the first ring SAs, adjacent to the center SA, at the wear pad level, displayed by the red arrows in the Figure. The total length of the SAs in the model were 3719 mm, corresponding to the ESFR-SMART SA height above the diagrid, whereas the wear pads are located at 2082 mm height, 163 mm below the fissile core top (an inner core SA geometry is given in Appendix B, drawing 2).

Within the study, 7 deformation cases have been simulated, with increasing loads on the pads. The first simulation was corresponding to the unloaded core condition, creating the non-deformed reference case for the reactivity effect calculations. Following this, forces were applied on the pads up to 30 kN with steps of 5 kN. This set of forces are greater than the ones applied on the Phenix SAs, by a factor of 5, due to the reason that the SA face-to-face (F2F) distance is significantly larger for ESFR.

In ESFR, the SA F2F distance is 205.35 mm compared to the Phenix F2F distance of 123.7 mm, coupled with the fact that the wrapper thickness of the ESFR SAs are also greater, 4.5 mm compared to the 3.5 mm in Phenix, with resulting moment of inertia for the ESFR wrapper is being ~6 time greater. As a significant portion of the SA rigidity comes from the internal structure, using only the wrapper moment of inertia difference, might not be completely representative, but gives a simplified view on the SA deformation difference between ESFR-SMART and Phenix cores.

In this sense, based on the similarity of the internal structure of the two SFR cores, the same Young modulus was used as it was obtained from the Phenix deformation study. In this way, the deformation differences reduces to the differences between the SA F2F difference, which results in the ~5 greater load requirement to obtain deformation magnitudes corresponding to the Phenix flowering study.

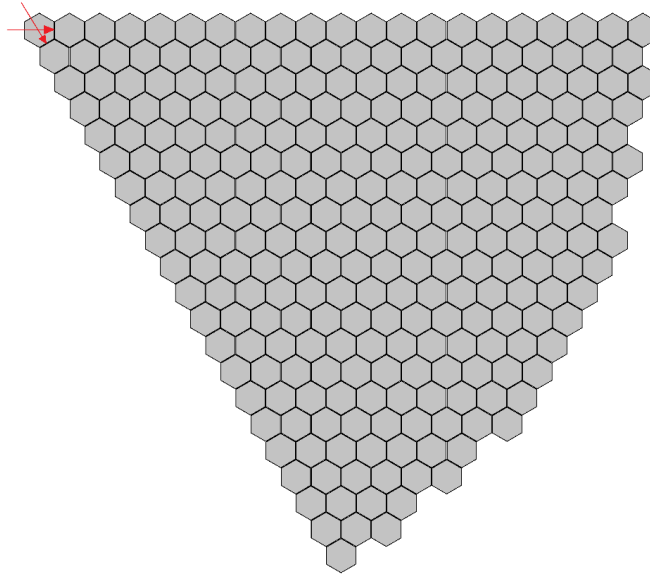


Figure 110. ESFR-SMART core loading for the flowering deformation simulation

4.3.1.2. Neutronic calculations of the deformed ESFR geometries

Following the deformation calculation, the resulting deformed geometry was used in Serpent 2, shown in Figure 111, to calculate the reactivity effect of the core deformation. The results from this calculation are given in Table 15. The obtained maximum deformation is lower than the maximum observed in Phenix, where it was just above 5 mm, compared to the 4.22 mm seen here. One of the reason for this is that in Phenix there was 1 more performed calculation, although based on the trend of the ESFR results the deformation would have stayed under still 5 mm. Besides, the applied 5 times greater forces were marginally underestimated. Nevertheless, the overall deformation magnitude is comparable between the 2 studies.

When the resulting K_{eff} values are assessed, all values appear to be equal within 2 sigma error range, as shown in the Table. This shows that with the applied deformation magnitude, there is no observable reactivity effect, which is a significant difference compared to the Phenix results. In Section 2.4, the reactivity effect versus pad level deformation was plotted in Figure 39. For comparison, the maximum pad level deformation of ESFR is ~2.4 mm, from the Figure, the reactivity effect of the Phenix core at 2.4 mm pad level deformation is ~-25 pcm. There are three main reason, why this strong difference can exist between the two core designs:

1. The ESFR F2F distance is significantly greater than it is for the Phenix core. As a result, the fuel volume ratio to the sodium coolant is significantly increased, as the inter SA gap in the models are kept equal for both cores. Thus, the change in fuel volume/sodium volume ratio is reduced, resulting in a decreased reactivity effect. Qualitatively, a 1 mm increase of the sodium inter SA gap around the Phenix SA, creates a 1.64% decrease in the fuel to sodium amount, using the SA wrapper outer F2F distance to calculate the fuel surface area, whereas, a 1 mm increase in the SA gap around the ESFR SA results in a less than 1% change in fuel to sodium ratio.

2. The active core (inner and outer core region) radius is significantly larger for ESFR. There are 13 rings of SAs in the inner and outer core for ESFR, whereas in the Phenix design there are only 6 SA rings in these regions. This means, that whereas the total active core is deformed with such loads as were applied on the core for the Phenix reactor, this was not achieved for ESFR. Therefore, in the Phenix active core region there was a global net sodium volume increase, as the SAs even at the outer core periphery bowed outwardly, whereas in the ESFR core, there was no overall increase of sodium volume, only local changes.
3. The ESFR-SMART SAs are ~200 mm higher in the model, by not taking the SA foot into account, than the Phenix SAs. Whereas, the top of the fuel is only ~100 mm lower in Phenix than it is at ESFR. Thus, as there is an overall 100 mm difference between the SA top and fuel top between ESFR and Phenix core models, being farther from the top for ESFR, the resulting overall fuel region deformation is lower, as the deformation magnitude decreases with the increasing distance from the SA top.

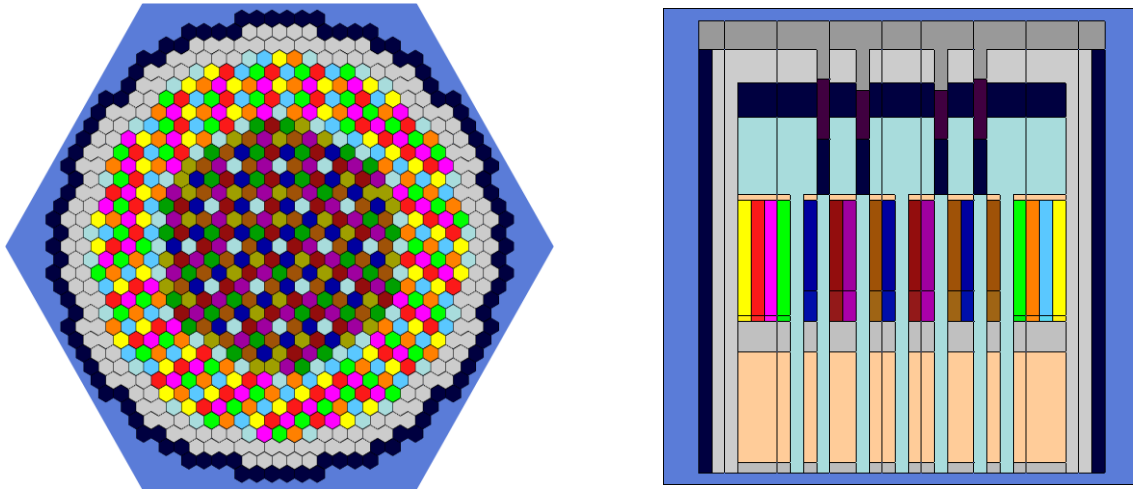


Figure 111. Model of the deformed ESFR core in Serpent 2 Monte Carlo code

Force applied [N]	Deformation [mm]	K_{eff} (std:1pcm)
0	0	0.99288
5000	1.87	0.99289
10000	2.54	0.99289
15000	3.08	0.99287
20000	3.49	0.99286
25000	3.88	0.99287
30000	4.22	0.99288

Table 15. ESFR-SMART core flowering core deformation and K_{eff} values as a function of applied force

4.3.2. Transient core deformation simulation using the Phenix core design

4.3.2.1. Transient modeling

In an attempt to simulate a sodium boiling induced core deformation reactivity effect, a study on the Phenix reactor core was performed. The Phenix core was preferred over the ESFR core due to two main reasons:

1) The ESFR core deformation related reactivity effect seems to be considerably lower, using comparable deformation magnitudes, therefore, to increase the effect, greater deformation would have been needed to be used, increasing the computational efforts using the ESFR model.

2) Besides, the ESFR SAs are more resilient against deformations, as a result of the change in geometry compared to the Phenix SAs, meaning that the pressure spikes resulting from the sodium boiling, and used for this study, obtained from Figure 85 of the ULOF study, might not create high enough deformations to have any observable reactivity effect.

In this sense, the Phenix NASTRAN model can be seen in Figure 112. With red color, the SA surface is highlighted where the load from the bubble collapse pressure spike is applied. The geometry of the model was identical to the one which was used in Section 2.4. In the first ring of SAs, adjacent to the center, the 1 MPa observed pressure spike is used, whereas for the second ring SA, in-between these two first ring SAs, a dumped pressure is applied, equal to 0.15 MPa. For the rest of the SAs, the pressure was assumed to be dumped enough to not to apply any load on them, as a simplification of the model. Axially the surface where the load was applied stretched from the fuel top region, ending below the SA top. The total simulated time period was ~210 millisecond, due to the speed of the event. The pressure on the SAs was applied in three steps:

1. Linearly increasing the load from 0 to 100% between time 0 s and 10 millisecond.
2. The 100% load was kept on the SA surfaces between 10 millisecond and 20 millisecond.
3. The load was removed, decreasing linearly to 0% from 20 millisecond to 30 millisecond of the simulated time frame.

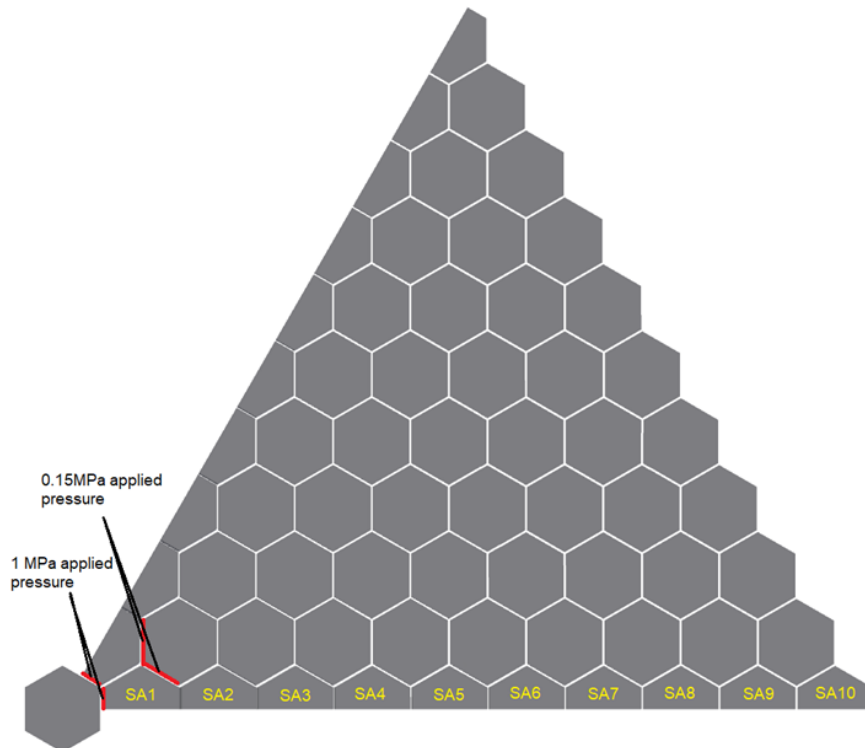


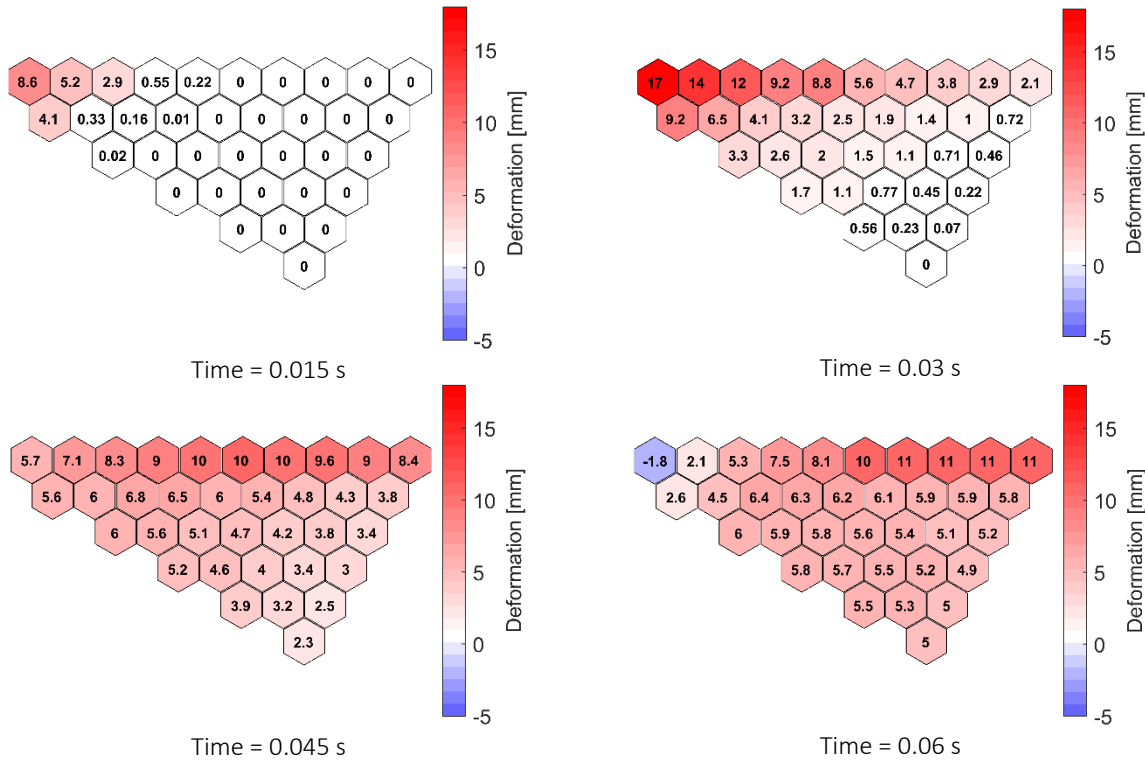
Figure 112. Phenix reactor core model used with the applied pressure loads on the SAs with the diagonal SA numbering for the SA movement characterization

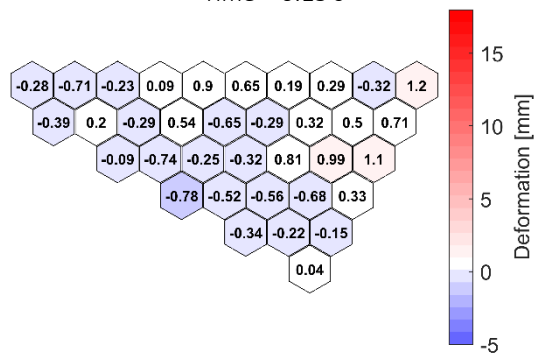
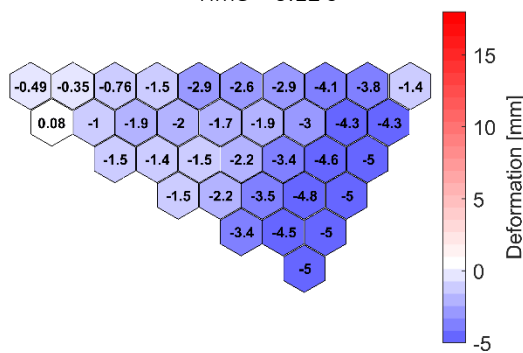
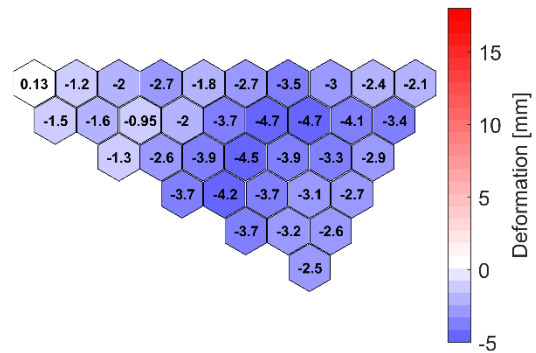
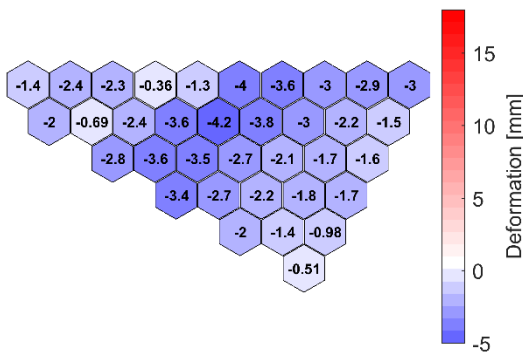
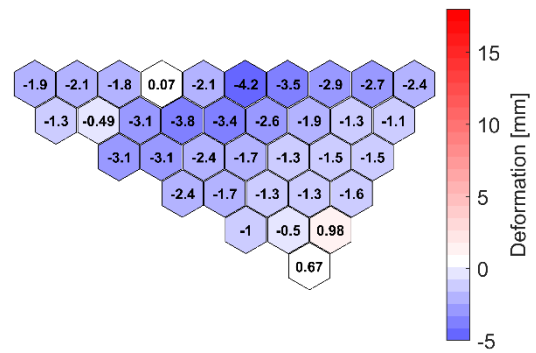
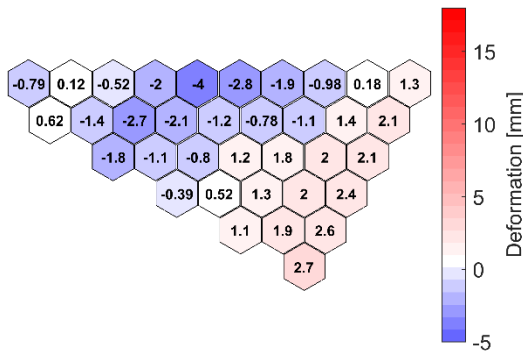
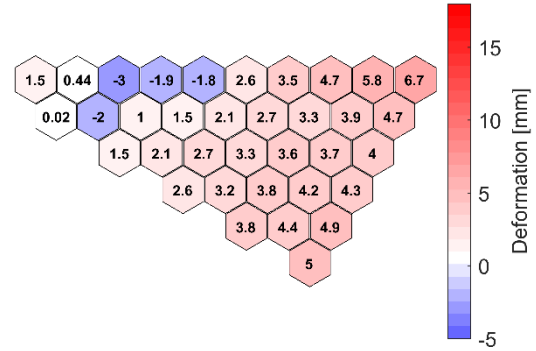
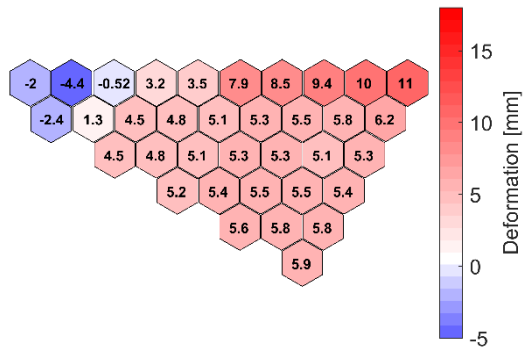
This shape of the pressure load correlates with a typical pressure spike in Figure 85.

Following the mechanical calculation with NASTRAN, the obtained deformed core geometries were used as input in Serpent Monte Carlo code to calculate the K_{eff} for each of the core states. Afterwards, the reactivity effect, corresponding to each deformed core states were obtained from the resultant K_{eff} values.

4.3.2.2. Transient deformation results

For the assessment of deformation dynamics and the resultant reactivity feedback effect, 13 time points were chosen to be analyzed, in the total simulated ~210 millisecond, shown in Figure 113. As the pressure pulse distorts the first row SA, there is an initial strong distortion which gradually moves towards the periphery of the core, red colored SAs in the Figure. The maximum deformation is obtained at ~30 millisecond, where the first ring SA top reaches 17 mm deformation towards the core periphery. The applied structural damping of the SA dissipates the initial energy originating from the pressure pulse, therefore, the outer ring SAs reach a lower maximum deformation, in the range of 11 mm. From the flowering, the SAs bounce back and create a core compaction, blue colored SAs in the Figure, which can be dangerous for an SFR, as it has a positive reactivity effect [26].





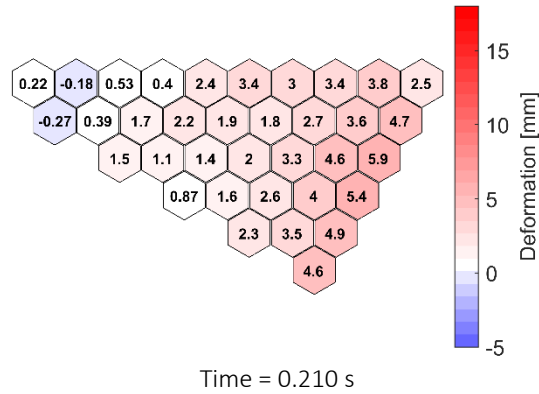


Figure 113. Deformation magnitude of the SAs for 1/12th of the reactor core at the assessed time points

In Figure 114, the diagonal row SAs dynamic is shown, together with the resulting reactivity effect, calculated at every time step. The Figure shows, that although the greatest deformation corresponds to the first time steps with the initial deformation of the first few rings, the reactivity effect is more influenced by the resulting global total deformation, which is significantly influenced by the periphery ring SAs. This is due to the fact, that although on a few inner SA higher deformation is attained, the total deformation from the outer core rings are larger as more SAs are located in those regions. This idea is reinforced when the maximum reactivity effect time location, ~ 0.05 s, is compared with the overall deformations shown in Figure 113, where the global deformation peaks between the time 0.03 s and 0.06 s, closer to 0.06 s.

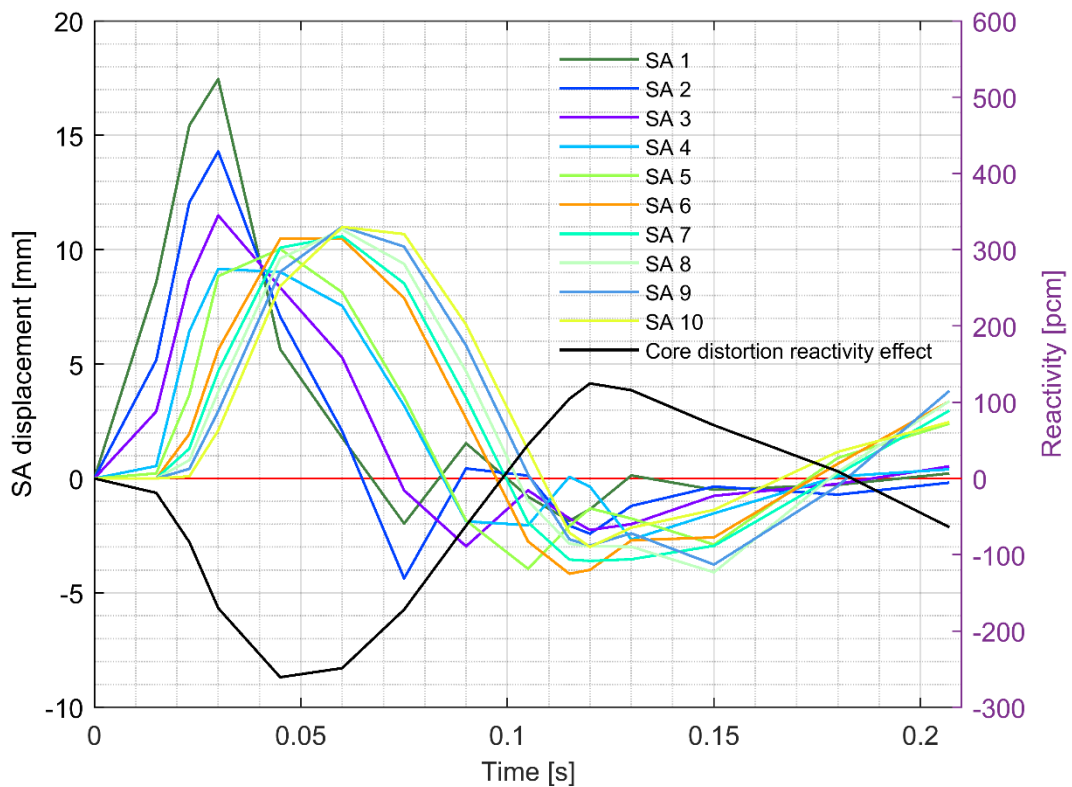


Figure 114. Diagonal row SA deformation (SA numbering shown in Figure 112) together with the core distortion reactivity effect evolution throughout the simulated time frame

Based on the attained deformation dynamic, which in the beginning shows similarities to a core flowering effect, the calculation was compared to a measured event happened in the Phenix reactor, the so called AURN negative reactivity event [28]. During this event, the reactor core power went through a sinusoidal change, decreasing in the beginning, followed by a power recovery close to the nominal value, then another decrease with a subsequent power increase over the nominal value in the end. At the last power increase the reactor safety system became operational and shutdown the reactor safely. In this sense, the obtained reactivities from the calculation was used in TRACE as a table data, with the point kinetics method without using any other feedback effect, to calculate the reactor power evolution. This power evolution was then compared to the measured AURN event, for which the hypothesis is that the initiation event was related to core flowering.

The comparison is presented in Figure 115, showing a very comparable power decrease in the first core expansion stage of the simulation, where all SAs are bowing outwardly. After ~ 0.1 s, the calculated power reaches significantly higher values and the overall power evolution is different compared to the measured data.

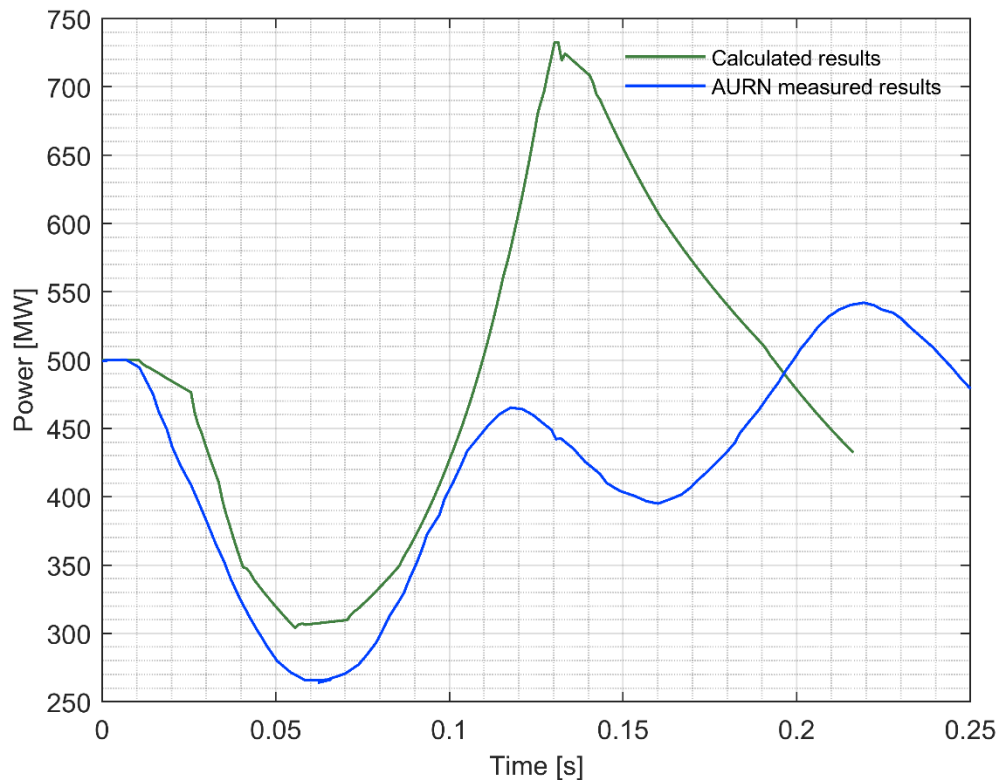


Figure 115. Power evolution during the measured AURN event aligned with the calculated Phenix core - deformation due to sodium boiling

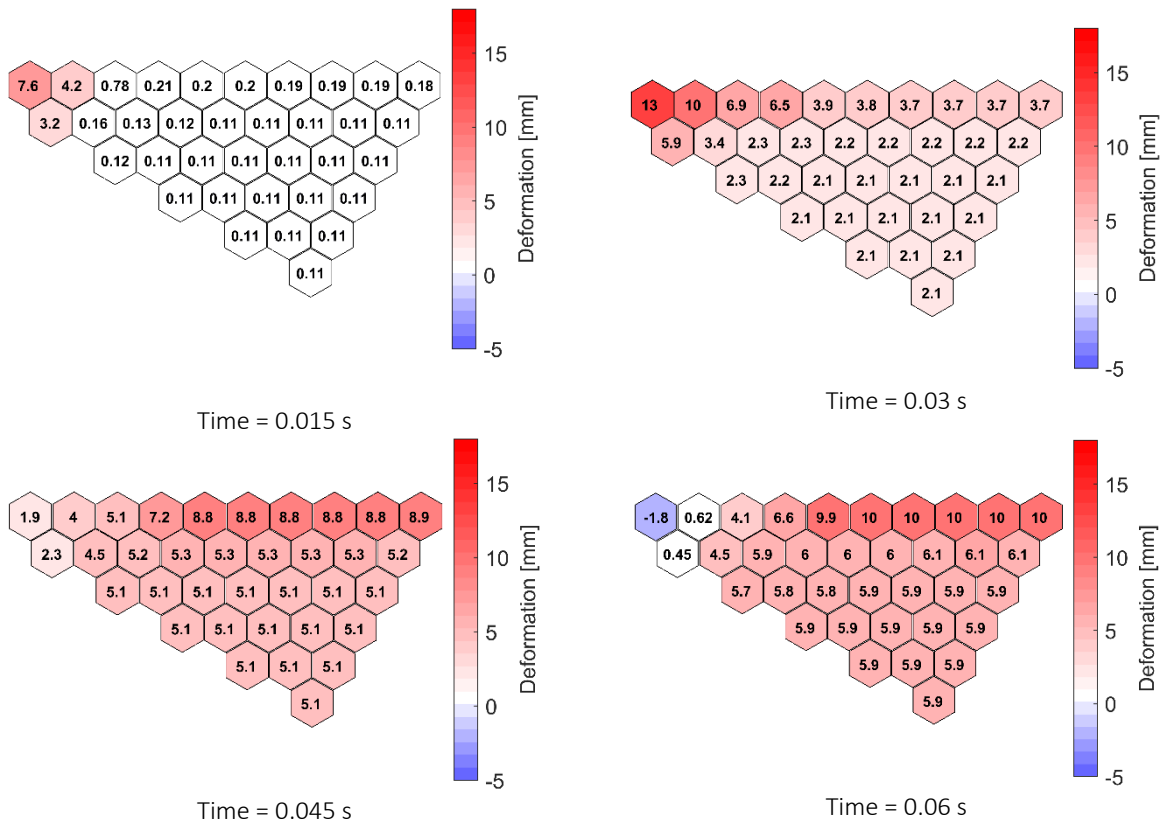
Although, the actual cause and dynamics of the core flowering during the accident are not known, the initial similarity between the two curves are surprisingly close. Therefore, to further analyze such flowering event and study the influence of core condition on results, the sensitivity case with modified pads distance (SA contact surface distance) was conducted. The pad distance was decreased to zero (pads in contact), compared to the previously available 0.25 mm, specified in the Phenix End-Of-Life tests [64].

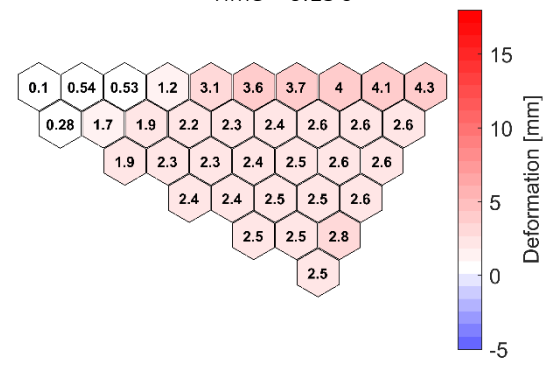
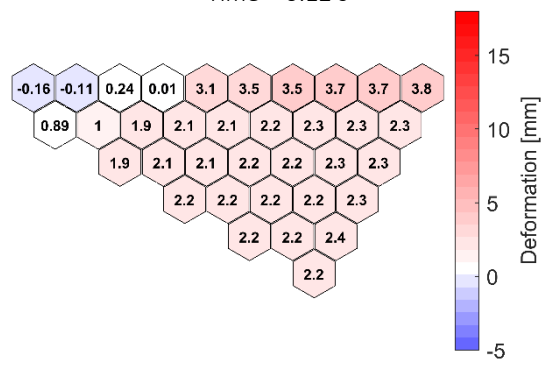
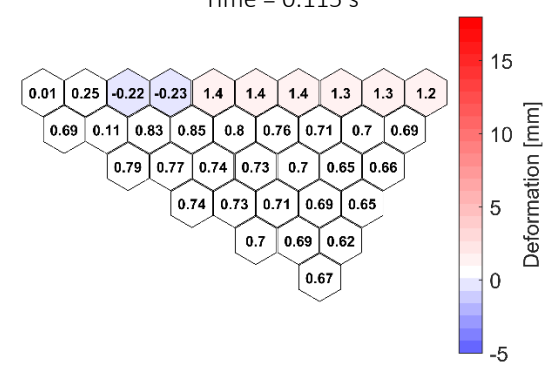
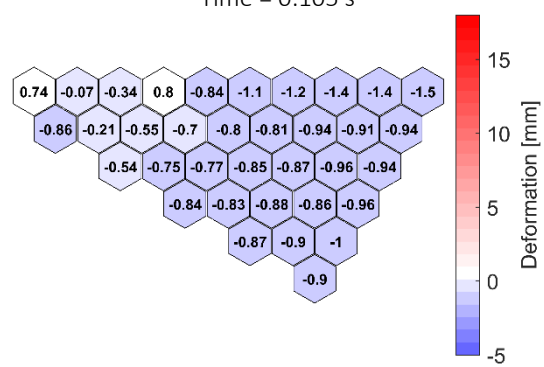
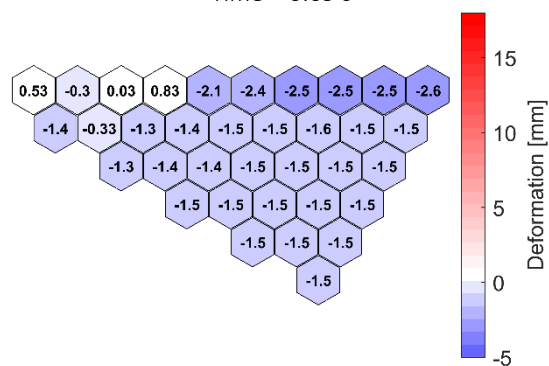
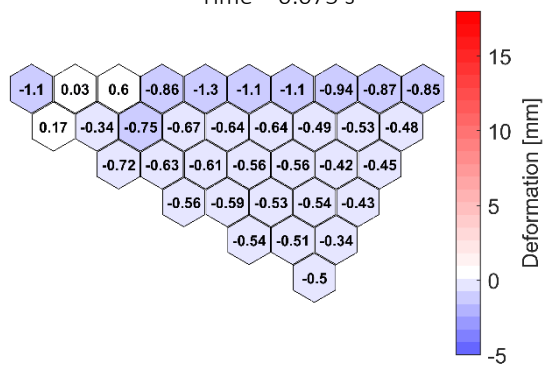
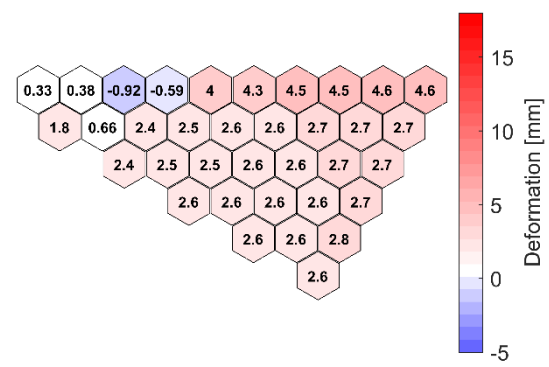
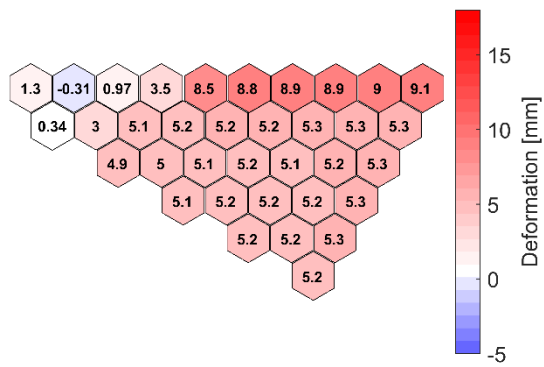
Potentially it can change the character of the deformation progression, while this change is justified, as in normal operation the SAs have an axial temperature profile, with increased temperature at the top and lowest at the bottom, whereas the experiment was performed with a uniform temperature profile axially, having a small gap between the SAs. In this sense, during operation the SAs are touching each other at the pad level, which can potentially limit the core compaction and the resulting positive reactivity effect, when the SAs are bouncing back from expansion state.

4.3.3. Phenix dynamic core deformation sensitivity study

As it was mentioned in the previous Section, a sensitivity case has been performed for the Phenix dynamic deformation assessment, using more realistic SA gap distances. For the deformation calculations, the exact same model was used, with the only deviation of setting the distance between the gaps to 0 mm. After running the analysis, the corresponding time points have been modeled in Serpent to calculate the reactivity effect and finally to compare the power evolution to the measured values during the AURN event, with this more realistic model.

A clear difference in the core deformation of the model having no gaps between the SA wear pads was observed, as shown in Figure 116. The overall deformation is more uniform, with the outer 7 SA rings essentially moving together, rather than in a more detached manner as previously. At this part of the core, the SA movement is not characterized by the initial pressure pulse induced fast oscillations, as it is for the first 3 rings of SA.





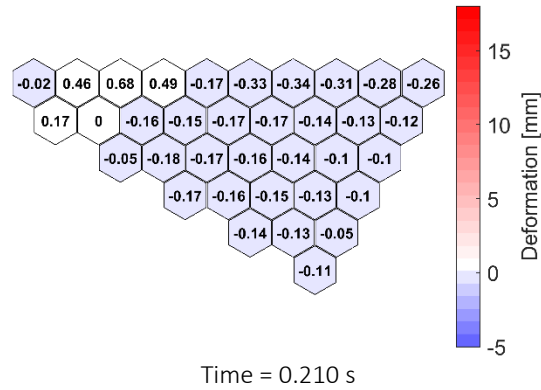


Figure 116. Deformation magnitude of the SAs for 1/12th of the reactor core at the assessed time points for the sensitivity case with pads in contact

This effect is even more emphasized in Figure 117, where the reactivity effect is also included in the plot. As it was mentioned for the reference simulation, it is even clearer here that the total reactivity effect is mainly governed by the deformation of the outer periphery SAs, showing nearly a mirror image of the core deformation of those regions. The reactivity evolution in the core closer resembles a wave like shape than for the reference, having a smaller positive reactivity effect peak than before, due to reduced core compaction.

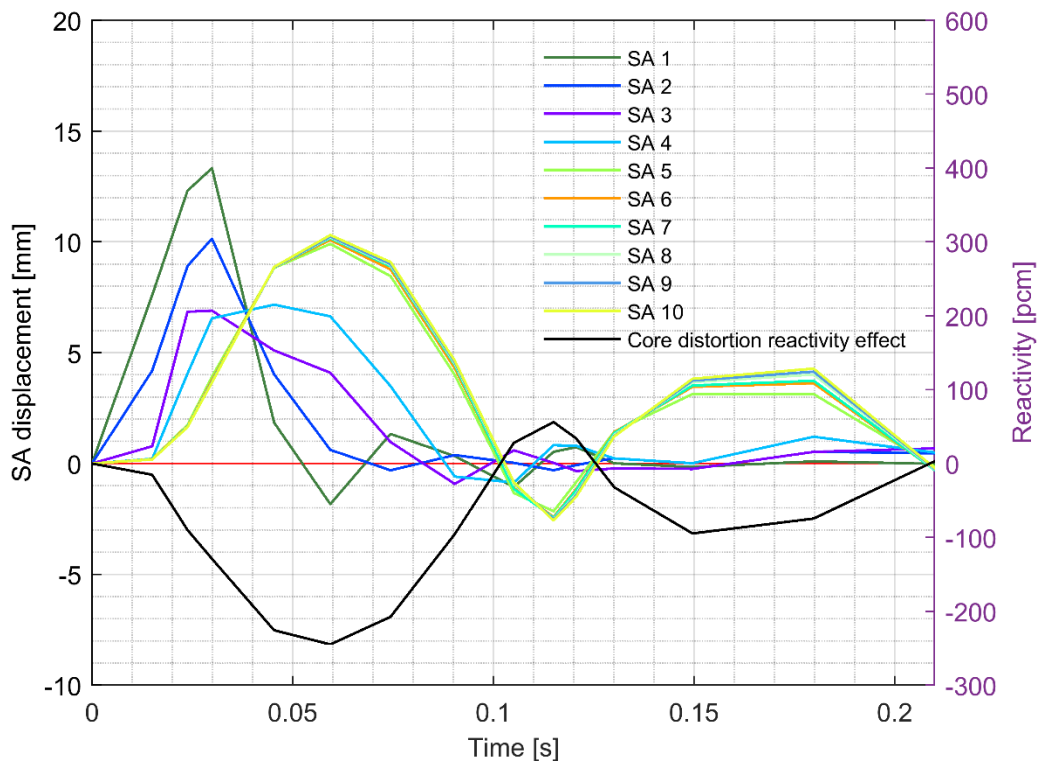


Figure 117. Diagonal row SA deformation (SA numbering shown in Figure 112) together with the core distortion reactivity effect evolution throughout the simulated time frame for the sensitivity case

The power evolution, shown in Figure 118, shows a similar power decrease as was also plotted in Figure 115, with marginally lower maximum decrease, as the lower reactivity change has suggested from Figure 117. The power increase, corresponding to the core compaction, is closer to the measured values from Phenix, and in general the power evolution shape is comparable to the one observed during the AURN event. This observation seems to reinforce the theory, that the origin of the event could be related to a flowering like core deformation.

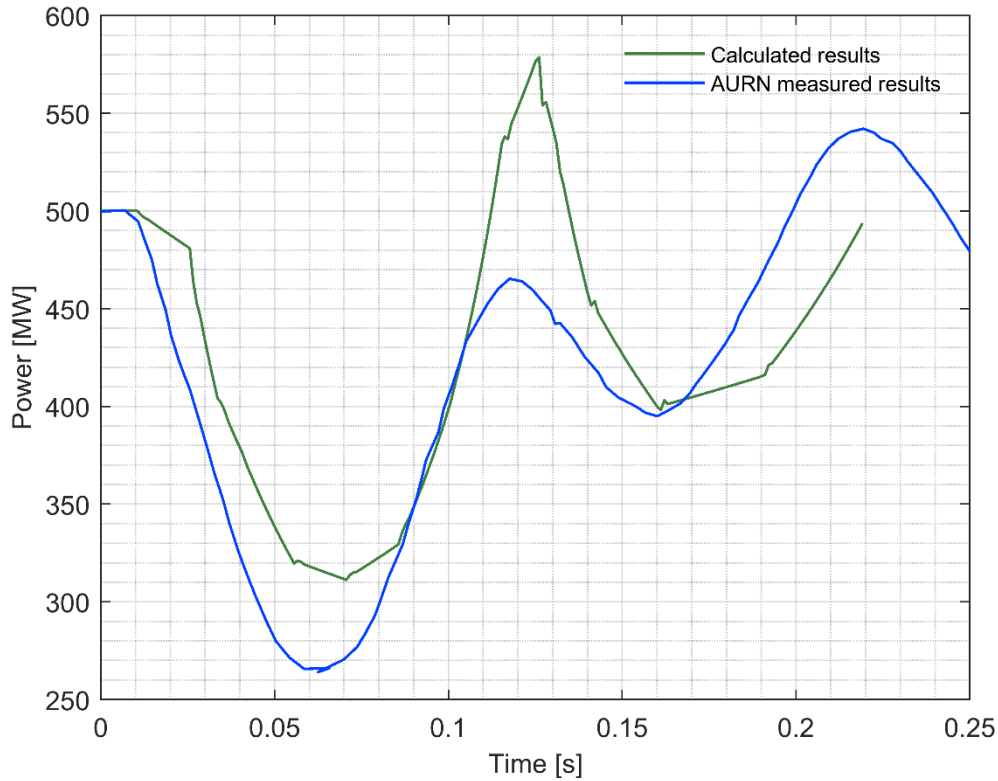


Figure 118. Power evolution during the measured AURN event aligned with the calculated Phenix core deformation due to sodium boiling for the sensitivity case

4.3.4. Conclusions of Section 4.3

In this section, the developed and validated core mechanics methodology (see Section 2.4) has been applied 1) on the ESFR-SMART core design, completing a static core flowering analysis, to obtain the reactivity effect due to this type of core deformation. 2) A dynamic simulation has been performed using the Phenix reactor core model from Section 2.4, to analyze the effect of the potential core deformation induced by a pressure spike, similar to the ones observed during the sodium boiling study in Section 4.1.5. Lastly, a sensitivity case has been performed, by eliminating the gaps between the SA pads, thus creating a more realistic analysis of the nominal reactor conditions for the Phenix core. The results can be concluded as follows:

- Within the static analysis the forces were increased by factor of 5, to obtain comparable deformation at the top of SA of the ESFR core than it was in Section 2.4 with the Phenix model. This difference comes

from the ~65% increased SA hexcan width, resulting in more resilient SAs. The reactivity analysis of the ESFR-SMART core shows negligible effect of the core flowering deformation, compared to the ~25 pcm reactivity observed for the Phenix core with comparable deformation. This difference is attributed to the greater fuel volume to sodium ratio for the ESFR core, together with the greater core radius, meaning that not the whole active core has been deformed, in contrast to the case with Phenix. Lastly, a marginal effect is also contributed from the greater distance between the SA top and fuel top in ESFR, reducing the fuel region deformation marginally.

- The simulation on the Phenix core transient, induced by a pressure spike similar to the ones predicted in the ULOF due to the fast vapor condensation, shows a relatively strong overall core deformation, peaking with ~17 mm. The reactor core is first expands outwardly, showing similarity to the core flowering deformation. Then, the SAs rebound, and core compaction is observed. The general dynamic of the SAs throughout the simulation shows a complex pattern, with the different ring SA having different frequencies. The obtained reactivity effect was used to calculate the power variation, which was compared to the power observed during the AURN negative reactivity event of Phenix reactor, as the prevailing explanation of this event is the core flowering. The comparison shows, that indeed a similar power evolution can be observed using the pressure spike as a driving event, while the power evolution is remarkably close between the performed simulation results and the measurements for the first half of the calculation. Later, when the core compaction occurs, the power evolution deviates significantly.
- In the sensitivity case, with the eliminated gaps between the SA wear pads, potentially reflecting a more realistic core state, the previously observed strong positive reactivity effect due to core compaction was reduced. For the power evolution, the overall similarity with AURN event increased and the power evolution curves show a strong alignment. Although the exact nature of the real event is not known, a dynamic core flowering could have shown similar behavior, to the one observed in the sodium boiling simulation, thus having observed comparable power evolution.

Through these assessed deformation cases, the capabilities of the developed core mechanics methodology has been presented, displaying a valuable tool for safety assessment or general core design optimization purposes.

CHAPTER 5

Conclusions and recommendations for future work

The goal of the present doctoral work can be divided into two main areas. 1) To improve and develop the computational methods facilitating the safety research of SFRs and ESFR in particular. 2) Assess the new safety measures of the ESFR, as well as specific data from the Phenix and Superphenix reactors, related to various safety functions.

For the first goal, the specific tools developed within the work relate to the coupled 3D neutronic/thermal-hydraulic simulations with an increased accuracy-to-speed ratio. In this context, the developed hybrid spatial kinetics sampling method has been established and benchmarked against conventional tools. Furthermore, in the topic of tool development, a core mechanics analysis methodology have been verified and validated as part of the work.

Regarding the safety measures assessment, the various DHRS and low void effect core of ESFR have been specifically targeted with assessment, concerning the heat removal and reactivity control safety functions, respectively. Besides, the developed new simulation methods have been used to assess 1) the ULOF accident in Superphenix, using the hybrid spatial kinetics sampling methodology to determine the reactor core behavior and 2) the reactivity effect due to the core deformation induced by e.g. a sodium bubble collapse in the Phenix reactor core. In this study, only certain accidental conditions are assessed, which either challenge the proposed new safety measures, showing their capability to keep the reactor safe or possess the highest risk to damage the reactor core integrity. Nevertheless, in a later stage, moving away from the conceptual design phase, more complete safety assessment should be performed in a future work.

The concluding Chapter starts with a chapter-wise summary in Section 5.1, which is followed by the description of the main achievements of the work in Section 5.2. The recommendations for future work are presented in Section 5.3, and finally, in Section 5.4 concluding remarks of the research are made.

5.1. Chapter-wise summary

Chapter 1 introduces the research topic of the thesis. It opens with a general description of nuclear power production worldwide, followed by the description of advanced, Generation IV reactors, introducing the concept of SFRs through their working principles. After the general SFR technology description, the ESFR has been described with more details, providing the main subject of the safety assessment performed in the thesis. To introduce the motivation for the safety assessments performed in the thesis, a comprehensive description have been given of the various safety measures analyzed in the thesis, belonging to reactivity control, heat removal and containment safety functions. Thereafter, objectives of the work are formulated, as well as the structure of the doctoral thesis is presented.

Chapter 2 describes the main methodologies of the research. Initially, the description of the Computer-Aided Design tool is given with specific examples of the use of such method throughout the whole research. Following that, the TRACE thermal-hydraulic model of the ESFR is introduced in a detailed

manner, describing the primary, secondary and tertiary system modeling approach for the later safety assessment. Thereafter, the applied reactor kinetics methods, intended to calculate the reactor power evolution, have been described. First, the point kinetics model with the modeled reactivity feedback effects has been presented, followed by the description of the spatial kinetics methodology presenting the main working principles. As this method has been under development in the thesis, a static benchmark analysis is also provided in the chapter to show the agreement with reference solutions using the Superphenix core model. Lastly, the proposed core mechanics methodology has been described, providing verification and validation studies, using the Phenix experimental data for the validation exercise.

Chapter 3 is devoted to the analysis of the heat removal safety function. First the ESFR reactor behavior is assessed under the PSBO accidental condition without employing any of the specific safety measures included in the design. Applying different modeling assumptions for the availability of the secondary circuit of the reactor, the system behavior and its available grace time before reaching any of the limiting temperature constraints is assessed. This was followed by the DHRS 1, 2 and 3 assessment, studying the operation of the various heat removal means and the general reactor behavior during transition from forced to natural convection. The heat removal performances of the DHRSs have been assessed, presenting their capability to provide long term cooling for the system in case of an unforeseen reactor shutdown, avoiding any reactor damage. In the second part of the chapter, the reactor behavior and DHRS performance were assessed using an optimized, compact secondary circuit design, thus revealing potential consequence of the new secondary circuit layout in terms of the plant safety.

Chapter 4 presents the safety study related to the reactivity control safety function. The chapter starts with the assessment of the ESFR low void effect core performance under the ULOF accidental conditions. The main aim of this study was to assess the sodium boiling temporal progression as part of a beyond design basis accident, within the ESFR core design, and capability to avoid reactor power runaway. Various SA design modifications were also assessed in the study, evaluating their influence in the sodium boiling progression and core power evolution, during the accident. Thereafter, the new spatial kinetics method has been benchmarked against a well established point kinetics calculation scheme, using the Superphenix core design. Similarly to the ESFR core, here also a ULOF simulation was chosen as the base transient comparison, together with a supplementary control rod movement study, where there is a stronger local perturbation of the neutron flux. Finally, the core mechanics methodology has been applied to the ESFR core, using static core flowering simulation, and on the Phenix core, simulating a transient deformation case, induced by the pressure spike simulating potential sodium bubble collapse, as predicted in the ULOF simulation. The obtained reactivity evolution due to core deformation was translated to reactor power evolution using the TRACE point kinetics method.

Chapter 5 summaries the thesis work with overview and conclusions. It includes the main achievement of the research study and some recommendations to future work based on the research outcome.

5.2. Main achievements

Within this Section the main findings and achievements of the thesis is presented, according to the objectives described in Chapter 1.

1. Development of a coupled neutronics and thermal-hydraulic method using a hybrid spatial kinetics sampling method.
2. Development, verification and validation of a core mechanics methodology to assess the reactivity change due to the core geometry distortion.
3. Assessment of the decay heat removal systems within the framework of heat removal safety function.
4. Assessment of the low void effect core design of ESRF within the framework of reactivity control safety function

Development of coupled neutronics and thermal-hydraulic method using a hybrid spatial kinetics sampling method

To improve the reactor core power calculation in terms of accuracy-to-speed ratio during the simulation of a transient accidental condition, a hybrid stochastic-deterministic 3D nodal diffusion calculation method was presented, using PARCS nodal diffusion solver with a transport XS correction technique, called sampling (hybrid SK sampling). Using the Superphenix reactor core, static and transient benchmarks have been assessed. The development of such methodology was initiated by the fact that certain accidental conditions where strong local perturbations exist in the reactor core, the point kinetic calculation option, otherwise used within the thesis, introduces limiting assumptions. In Chapter 2, the static benchmark calculations were presented, showing very good agreement with the reference Monte Carlo neutronic calculations, reducing the power deviation from ~5% to 1.5%, and the k_{eff} from 416 pcm to 6 pcm, compared between the reference Monte Carlo solution and PARCS, without and with the applied sampling correction method. Thus, in a static calculation, it was shown that the reactor power calculated with a nodal diffusion solver can be comparable to reference Monte Carlo calculations. As Monte Carlo method is a high fidelity calculation tool, comparable solution with a fast running nodal diffusion solver is expected to provide increased accuracy transient simulation results, where Monte Carlo simulations are still not feasible most of the times.

As the methodology was intended to be used in a transient calculation, a benchmark analysis has been performed in Chapter 4, using two different transient simulation scenarios on the Superphenix reactor core model, which was also the model for the static simulation benchmark in Chapter 2. In this assessment, the proposed sampling corrected method was compared with point kinetics technique, serving as the reference method in the benchmark as its accuracy has been previously assessed in other studies, validating the tool with experimental results. Firstly, a ULOF simulation was performed, until the point of sodium boiling onset, using only the Doppler and sodium density reactivity feedback effects, presented in the static part of the analysis. In the study, the spatial kinetics technique provided good agreement with the reference results, displaying that with the applied feedback effects the methodology can be used for transient calculation, and the adjusted XSs provide qualitatively good results.

In the second part of the study, two control rods were moved, located opposite to each other in the core, withdrawing one by 10 cm and inserting the other by 10 cm. Applying this scenario, strong local flux perturbation was introduced into the core, for which 3D core calculation is required to obtain accurate results. Therefore, strong differences were observed between the reference and the 3D spatial kinetics calculation, predicting different power for SAs close to the perturbation by up to ~16% with the maximum fuel temperature deviation of ~270 K. As in this particular case the assumptions applied in the point

kinetics calculation are emphasized, the requirement for 3D spatial kinetics calculation is shown for certain accidental conditions with strong local flux changes. It was also observed in the assessment that the control rod worth differs between point kinetics and spatial kinetics calculations by ~20%, which shows that specific XS data should be produced with inserted or withdrawn control rods for the spatial kinetics method, as simply moving the control rod without new XS set can lead to an error in that range. The obtained core power difference shows only ~2% power deviation, due to the available Doppler and sodium feedback effects, however, it requires special attention.

Overall, the static calculations and transient ULOF benchmark show that the methodology is ready to perform SFR safety assessment and shows that the sampling method operates as it was intended. Nevertheless, further validation work is still required for the methodology to increase the confidence in performance, i.e. in the improved accuracy. Such validation has been performed in the work presented in Appendix C using only static calculation, thus for transient case it is still required. This is especially needed for a case where strong local perturbation is involved, as the benchmark showed the difference against a point kinetics method which is not capable of assessing such situation accurately anyway, thus for the assessment experimental data should be used.

Development, verification and validation of a core mechanics methodology to assess the reactivity change due to core geometry distortion

A core mechanics methodology has been introduced in Chapter 2, which allows the simulation of general loads on the reactor core subassemblies, producing the core states with deformed shapes, which are subsequently used for the evaluation of the reactivity effect induced by the core deformation. In the chapter, the verification and validation work have been presented, for which the experimental results of the Phenix reactor End-Of-Life tests were used. The comparison of various static deformation points presented good agreement with the experimental data, providing the basis for future transient calculation of SFR core deformations for either safety assessment or general design optimization purposes.

In Chapter 4, the developed core mechanics methodology has been applied 1) on the ESFR-SMART core design, completing a static core flowering analysis, to obtain the reactivity effect due to this type of core deformation. 2) A dynamic simulation has been performed using the Phenix reactor core model from Section 2.4, to analyze the effect of a core deformation potentially induced by the pressure spikes, similar to the ones observed during the sodium boiling study in Section 4.1.5.1. Lastly, a sensitivity case has been performed, by eliminating the gaps between the SA pads, which reflected a more realistic core nominal operating conditions of the Phenix reactor.

The two main outcome from this study are as follows:

Through the ESFR static assessment, using identical deformation approach as it has been performed on the Phenix reactor, it was shown that the resulting reactivity effect is negligible for the deformation magnitude close to the one observed on Phenix. This shows that the different width SA design and increased active core radius reduces strongly the effect of such scenario. This can be explained by the increased fuel volume to sodium volume ratio, with smaller change in the fraction when SA deformation occurs. Furthermore, the fact that the overall core deformation does not reach the periphery SAs for ESFR

in contrast to Phenix, due to the higher number of fuel SA rings, has a strong influence and the net sodium volume within the core stays unchanged under such magnitude of deformation. Thus, the ESFR core appears to be more resilient against deformation induced reactivity change, compared to the Phenix reactor.

The second main outcome is the ability of performing a simulation of general transient dynamic deformation with evaluation of the corresponding core reactivity evolution, which is a new addition to the simulation capabilities of SFRs at PSI. To test this capability, a hypothetical accidental scenario was tested where the sodium boiling induced pressure spike is simulated in the core, generating net deformation. Although the simulation includes certain assumptions on the pressure load on the SA surfaces and the applied structural damping of the SAs based on engineering judgement, the capabilities are well demonstrated through the transient calculation. The calculation included initial core flowering, followed by core compaction, thus, a complicated scenario with a sequence of various deformed core states was obtained, representing the dynamic mechanical response of the core to the initial perturbation, and the resulting reactivity evolution was calculated. Due to similarity of the deformation to the core flowering deformation suspected in a Phenix accident, A.U.R.N. negative reactivity event, the calculated power evolution was compared with measured power during this event. This comparison showed a strong coherency in the initial flowering phase of the calculation, thus a further sensitivity case was analyzed, where a more accurate core state was modeled, by eliminating the distance between the SA wear pads.

In the aforementioned sensitivity case with the modified wear pad distance and the identical initial pressure load, a different dynamic core deformation pattern was observed and the transient simulation results on power evolution exhibited even more coherent behavior with respect to the measured data. This provides a hint that currently prevailing hypothesis that core flowering was the initiator of the core deformation seems to be supported with the results.

Assessment of the decay heat removal systems as part of the heat removal safety function

The second main objective of the current doctoral thesis was the assessment of the ESFR safety measures according to the various safety functions, having emphasis on the heat removal and reactivity control safety functions. Specifically, in Chapter 3, the fulfillment of the heat removal safety function has been assessed through the study of the various DHRS, using TRACE thermal hydraulic system code. The PSBO accidental scenario was used to perform the assessment, allowing the characterization of the DHRS regarding the available decay heat removal performance and the overall robustness of the system moving from forced to natural convection. Two models have been utilized for the study, a reference model, for which the detailed description has been provided in Chapter 2, and a model with modified secondary circuit design, using a more innovative arrangement with shorter and simpler secondary piping.

In the study, initially a few base cases have been modeled, without applying any of the DHRSs, available in the design. These options revealed the favorable reactor behavior and its significant grace time period available before any limiting temperature would be reached, due to the high amount of primary sodium and thus the available large heat capacity. Moreover, within the primary circuit stable transition from forced to natural convection was demonstrated, whereas within the secondary circuit the natural convection establishment requires auxiliary systems for stable operation.

Following this, the various DHRS operational options have been modeled, obtaining results for individual and combined multiple DHRS operation.

The evaluation reveals the favorable performance of the DHRS-1 units. The DHRS-1 operates, using the secondary sodium for the heat removal from the primary system but capable of operating even if the secondary sodium is drained from the loop, utilizing the available sodium reservoir in the IHX. The heat is removed by sodium-air heat-exchanger, which also operates in air natural convection regime. The natural circulation sodium flow in the unit is quickly established, following the pump trips, and removes the predicted ~ 7 MW heat per unit. This allows the decay heat removal exclusively by using the DHRS-1 after ~ 30 minutes following the opening of the air windows in the DHRS chimneys. That being said, one negative aspect was also revealed by the study, showing that the sodium circulation in the units during normal operation is established against the main sodium loop circulation, which introduces a small amount of hot sodium at the cold part, decreasing marginally the efficiency of the reactor during normal operation. This phenomenon can be counteracted by a small auxiliary pump on the DHRS-1 unit, which creates an opposite direction flow circulation, which was also assessed in the Chapter.

The DHRS-2 assessment shows that though it was purposed as one of the main decay heat removal mean, with its current design it is not capable of keeping the reactor temperatures under the limiting values during long term cooling. Thus, the unit cannot be used exclusively, as the sole heat removal option but in the current state could only be used together with the DHRS-1 units, or at least a few of them should operate also. There was indicated that the natural circulation in the secondary sodium loop is not sufficiently established, containing a noticeable sodium temperature variation along the loop, causing flowrate fluctuations which are unintended and not anticipated. Thus, an auxiliary pump is also required to be in operation during the heat removal. To overcome the observed low heat removal performance, sensitivity cases have been analyzed, varying the air flowrate and the sodium flowrate of the system. All these changes brought only marginal increase in heat removal, thus it is concluded that to achieve the desired performance, a modified design would need to be adapted in future projects. In particular, improvement is foreseen by increasing the available heat removal surface area by using advanced SG design such as the printed circuit option.

The results of DHRS-3 analysis show that though it is possible to keep the temperature of the concrete under the set temperature limit in long term, the system is not capable of removing the produced decay heat. As the DHRS-3 was not designed to do so but rather to support the operation of the other two main DHRSs and keep the concrete within designed thermal conditions, it can be stated that the performance of the system meets the expectations.

As was mentioned, the described assessment has been performed by using an optimized secondary circuit design also. The reduced length design has various advantages in costs and certain safety related aspects as well. Thus, the DHRS assessment was conducted aiming to see if there is any impact on the operation of the units, especially in the natural convection establishment within the secondary circuit. Overall, the new design exhibited a comparable behavior of the system with certain differences, such as the available net flowrate in the secondary system following pump trip, although flow fluctuations are still present in the loop. As the circuit is significantly shorter, it takes less time to make a full circle for the sodium flow thus the temperature related fluctuation is more rapid and takes less much time to even out. Lastly, as the heat capacity of the sodium has been reduced in the secondary circuit, the overall primary circuit

heat-up is generally increased, which has two fold implications. On the one hand, due to the temperature increase, the various DRHS units has an increased heat removal capability, though not substantial. On the other hand, the safety margin to reach the limiting temperature values are reduced for the primary circuit.

With this assessment one of the main new safety measures of ESFR has been studied. It was shown that the DHRS-1 and DHRS-3 units overall fulfill their desired heat removal capability, whereas for the DHRS-2 a modified system design or different SG types are required to achieve safe shutdown of the reactor using it exclusively. Thus recommendations have been provided for future research projects in this area. The study with the modified secondary circuit design, show that it can be potentially used as a reference design option in future projects, studying specifically the available safety margin due to the observed higher temperatures.

Assessment of the low void effect core design of ESFR within the reactivity control safety function

The inherent safety potential of the low void effect core design of ESFR has been assessed in Chapter 4. For the assessment, the ULOF accidental scenario was used, which was foreseen to initiate sodium boiling in the reactor core. The effect of the sodium boiling on the core behavior was then studied, under such conditions. A specific reactor core model has been used for this analysis, using 1/12th of the full core with 42 SAs, exploiting the symmetry of the reactor. This simplification was required due to the high computational demand of the full reactor model.

The main feature of the reactor core which has the highest impact on the sodium boiling reactivity effect is the applied sodium plenum in the core design, creating the low void effect core. From previous studies, it was shown that the ESFR full core voiding has a positive overall void effect, but a strong spatial dependency of the effect is observed, i.e. along the SA height and along the core cross-section. Thus, an analysis with the actual void progression in the SA was performed. The study reveals, that initially, when the void is occupying only the plenum and fuel top regions, the negative reactivity effect is dominating. Nevertheless, with time the void propagates downwards deeper into the fuel region, where the void effect is positive. This void or bubble propagation into the fuel region happens due to the reduced sodium flowrate within the boiling SA and considerable power release, thus there is an increasing mismatch between power generation and heat removal capability in the channel. Eventually, the whole of the fuel axial region is occupied with sodium vapor, resulting in cladding meltdown. Although meltdown still occurs with the low void effect core, no power runaway was observed, in contrast to former conventional high-void cores, and there can be potentially enough time for the passive safety shutdown system to reach operation.

Beside the previously mention reference case, a modified SA design was proposed and assessed, by using SA wrapper openings close to the fuel top height. This modified SA wrapper was meant to provide a sodium path towards the inter SA gap, maintaining the positive net sodium flow in the SAs, even when there is sodium boiling at their top. With this design modification, the propagation of sodium vapor towards the fuel region was eliminated in the simulated time frame, thus the sodium vapor mainly occupies the fuel top and plenum regions. Therefore, the overall sodium reactivity effect was negative for this case, and the cladding meltdown was avoided, showing more favorable reactor behavior.

Lastly, a few sensitivity cases have been performed, modifying various core parameters, including geometry modifications, fuel gap conductance and reactivity coefficients. All modifications were applied without the use of the previously discussed SA wrapper opening. Each of them providing a small increase in the available grace time but without exhibiting major change in the core behavior.

As a results of this examination, it is concluded that in order to avoid cladding melting in the SA, an updated core design would be required, with different plenum design and/or with a different axial fuel region layout. Based on the analysis it is also recommended to use the SA wrapper openings as the reference design option, due to the presented void propagation improvements.

5.3. Recommendations for future work

The conducted research contributed to the methodology development and general safety assessment of SFRs, with special attention to ESFR. In this regards, certain recommendation for future work are provided as follows:

1. Continued development for the hybrid spatial kinetics sampling method
2. Further studies to improve the accuracy of the core mechanical analysis method
3. Assessment of the printed circuit SGs as part of the DHRS-2
4. Assessment of the SA wrapper opening influence on the nominal operation of ESFR

Continued development for the hybrid spatial kinetics sampling method

In the current analysis for the modeling and simulation with the spatial kinetics method, only Doppler and sodium density feedback effects have been used, being the main effects until sodium boiling onset. In order to perform a validation on the method, further feedback effects would be required to be accounted for in the modeling, such as the fuel axial expansion, core radial expansion and control rod driveline expansion. Moreover, to increase the scope of the analysis, sodium void effect should also be included so that ULOF analysis could include the boiling phase, essentially if the stable behavior of the core at these conditions is of a high importance.

A further aspect, which could be considered for the continuous development of the spatial kinetics method is the modification of the currently applied sampling statistical XS correction technique, and replace it with a suitable machine learning algorithm. Thus, deeper correlation could be revealed about the applied transport XS change in the way it affects the PARCS results and the already good agreement between the reference Monte Carlo and the PARCS nodal diffusion results could be further improved.

Further studies to improve the accuracy of the core mechanical analysis method

In the presented core mechanical analysis, the Phenix reactor core was used as the base to assess the Young modulus, serving as the correction factor, accounting for the fact that filled hexagons were used for the calculations instead of the actual SA structure, with all the fuel pins included in it. Therefore, this correction factor provides good agreement for the Phenix SA deformations but for other SFR reactor cores, this correction factor was assumed to be equal due to the similarity between ESFR and Phenix SA structure. To validate this assumption, various SFR SA mock-ups should be analyzed to assess the exact

magnitude of the deformation similarity. Furthermore, using the same SA structure, various SA width could be also assessed, characterizing the exact effect of the increased size SAs. From these studies a correlation could be obtained, specifying the Young modulus based on the number of pins and radial width of the SAs.

Besides the Young modulus, another factor which would require further studies for the core mechanical method, is the more accurate structural damping value representation. In this sense, fluid structure interaction assessment for the calculated core design should be studied and the results of such study should be reflected in the applied structural damping value. Consequently, the accuracy of the prediction related to the SA deformation frequencies could be improved through such work.

Finally, additional core deformation scenarios should be included in future studies, where more general, asymmetric core deformations are assessed. In this way, another sensitivity case could be used to further assess the Phenix transient calculation, presented in Section 4.3.3., where the origin of the core deformation load is not at the center but closer to the core periphery regions.

Assessment of the printed circuit SGs as part of the DHRS-2

The DRHSs have been assessed and their performance was discussed in the research. In the discussion it was shown that the DHRS-2, with the current design is not capable to achieve the desired efficiency, even with the presented sensitivity cases. Thus, the DHRS-2 design should be modified in a future project, using SGs, which has a higher heat exchange surface area, from where the heat could be removed by the surrounding air flow. Such, SG type could be the relatively recent printed circuit heat exchangers, which could be considered within a future study. As the natural circulation establishment was of concern already in the current design, and the suggestion was to use auxiliary pumps, the reduced natural circulation character of a printed circuit design would not be of great influence.

Assessment of the SA wrapper opening influence on the nominal operation of ESFR

As part of the low void effect core design analysis with the ULOF simulation, recommendation was made that in future projects, the reference SA design should include the wrapper opening to reduce the sodium vapor downward propagation. Although it showed significant improvement on the core behavior during sodium boiling, the effect of such modification has not been assessed under nominal operating conditions. Thus, while no substantial effect is foreseen by the author, to make a final recommendation, this study should also be completed through an experimental assessment.

5.4. Concluding remarks

The present doctoral research has successfully demonstrated favorable ESFR reactor behavior under various accidental conditions, assessing a variety of the proposed new safety measures. Through various options of the proposed decay heat removal system, it could be avoided to reach the limiting temperatures, shutting the reactor down safely under the assessed accidental condition.

The low void effect core design, though cladding melting could not be avoided without the intervention of a specific safety system, power runaway was not observed and the provided grace time by the reactor could be enough for intervention. Recommendations were made for potential improvements for both the DRHS systems and for the reference SA wrapper design, to improve operational safety.

As part of the research, the simulation capabilities for assessment of neutronic, thermal hydraulic and mechanic SFR behavior have been improved at PSI through the development of the hybrid spatial kinetics sampling and core mechanics methodologies, presented in the work. Verification and validation work has been performed for the core mechanics methodology, while benchmark analysis has been done for the hybrid spatial kinetics technique.

In conclusion, the current doctoral thesis included assessment and optimization of some of new ESRF safety measures, included in the most recent conceptual design, with special attention to the heat removal and reactivity control safety functions. Furthermore, recommendations for design modifications and for future research have been made.

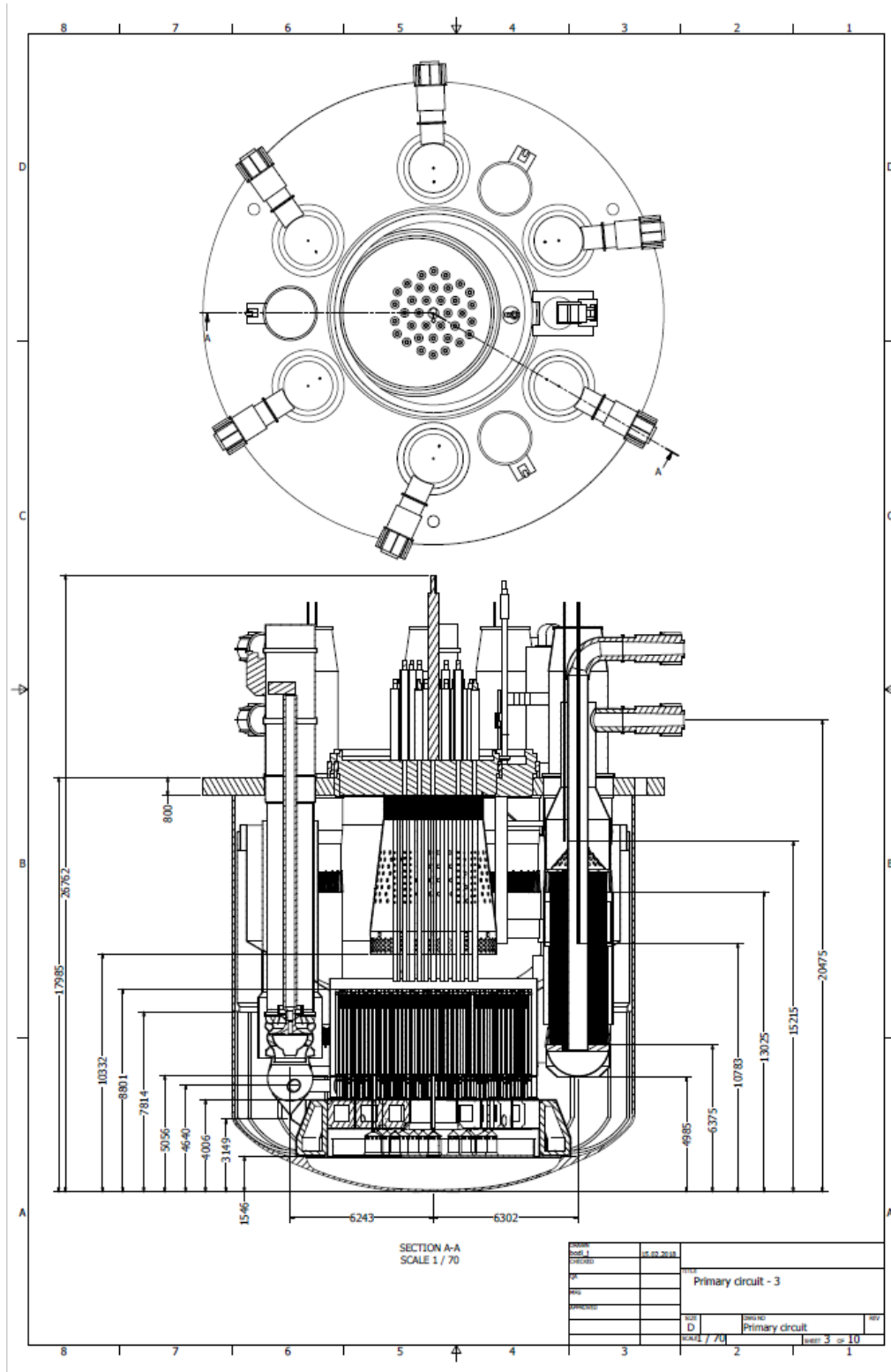
Appendix A - ESRF-SMART reactor concept main characteristics

General	
Thermal power (MWth)	3600
Net electrical power (MWe)	1500
Global efficiency (%)	42
Plant lifetime (years)	60
Availability target (%)	90
Mass of sodium in main vessel, t	2350
Total pressure losses in primary system, bar	4.5
Cover gas above primary sodium free level	Argon
Pressure of cover gas, bar	1.15
Core	
Core inlet / outlet temperatures, °C	395 / 545
Type of fuel	(U,Pu)O ₂
Core global geometry	Cylindrical, 3 layers of reflectors
Core Support	Strongback resting on primary vessel bottom
Core mass, t	~430
Core outside diameter, m	~8
Core flowrate, kg/s	~18700
Core bypass flowrate, kg/s	~900
Sodium supply	pump connection to diagrid
Diagrid and core support materials	316 L(N)
Diagrid mass, t	~70
Core pressure drop (including inlet and outlet), bar	3.8
Core support pressure drop (diagrid), bar	0.7
IHX	
Number of IHXs	6
Power of one IHX, MW	600
Type	Tubular, counterflow
Material	stainless steel
Pressure loss (primary), bar	0.25
Working fluids, primary / secondary	sodium / sodium
Mass of one IHX, t	127
Primary sodium temperature at IHX inlet / outlet, °C	545 / 395
Secondary sodium temperature at IHX inlet / outlet, °C	530 / 345
Primary pumps	
Number of primary pumps	3
Type	mechanical, radial admittance, axial exhaust, anti-reverse-flow diode
Mass of one pump with motor, t	~164
Location	in reactor vessel
Nominal rotational speed, rot/min	450
Net positive suction head, / available, m	13
Pressure head, bar	4.5
Nominal flowrate, kg/s	6512
Halving Time, s	~10
Min Time from 100% to 25% of nominal speed, s	30
Secondary loops	

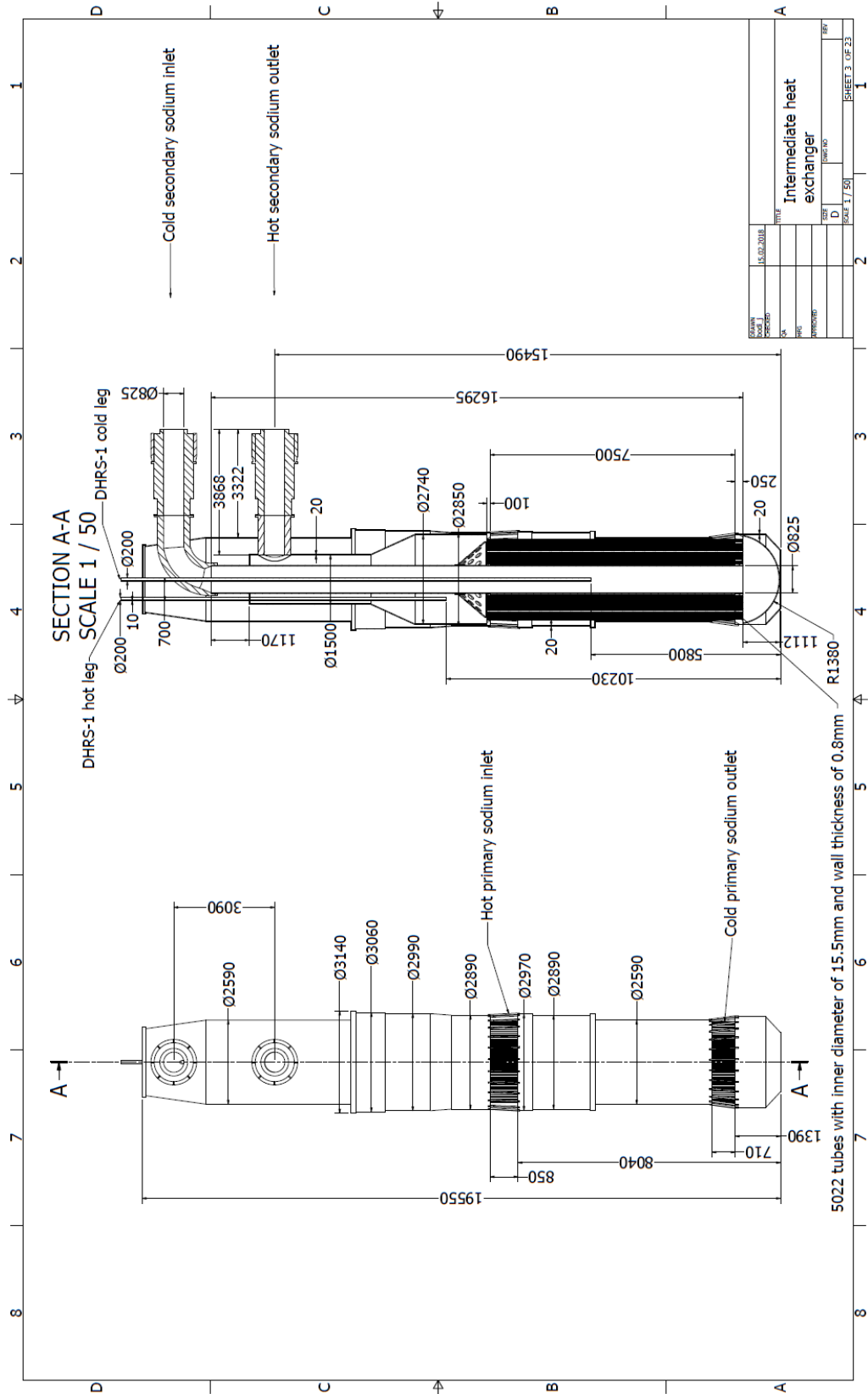
Number of secondary loops	6
Composition	1 IHX, 6 SGs, 1 secondary pump, 1 thermal pump, 1 purification system, 2 draining systems
Nominal flowrate per loop, kg/s	2541
Length of pipes with \varnothing 850 / \varnothing 350 mm per loop, m	~219 / ~90
Mass of secondary sodium per loop, t	~254
Steam generator	
Number of steam generators per secondary loop	6
Type	modular, tubular, counterflow
Mass of one SG, t	~50
Material	9Cr-1Mo modified
Working fluids, secondary / tertiary	sodium / water
Power of one SG, MW	100
Water inlet / steam outlet temperature, °C	240 / 528
Steam pressure, bar	185
Steam flowrate per secondary loop, kg/s	287

Table A-A-1. ESFR-SMART reactor concept main characteristics

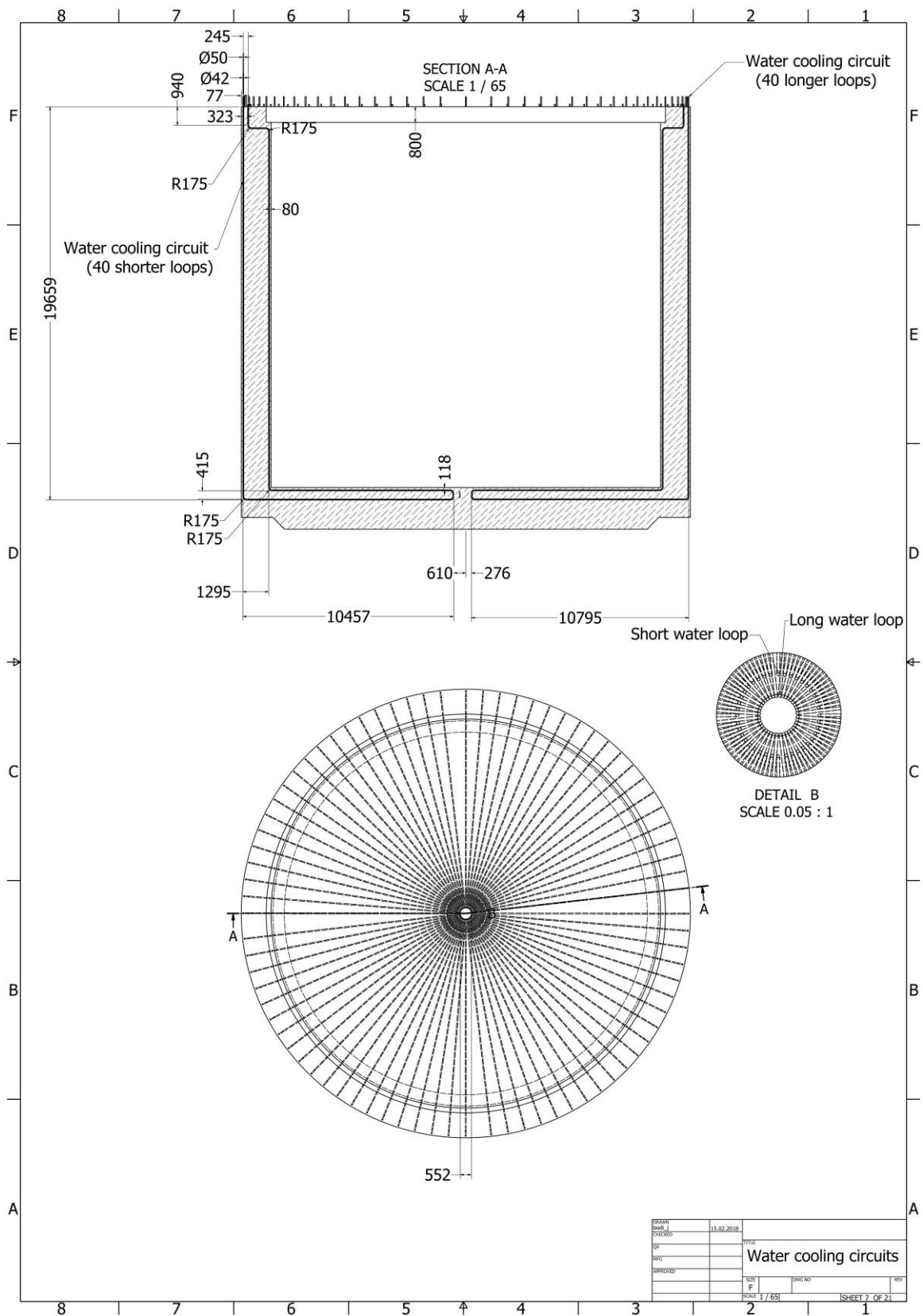
Appendix B - ESRF-SMART working drawings



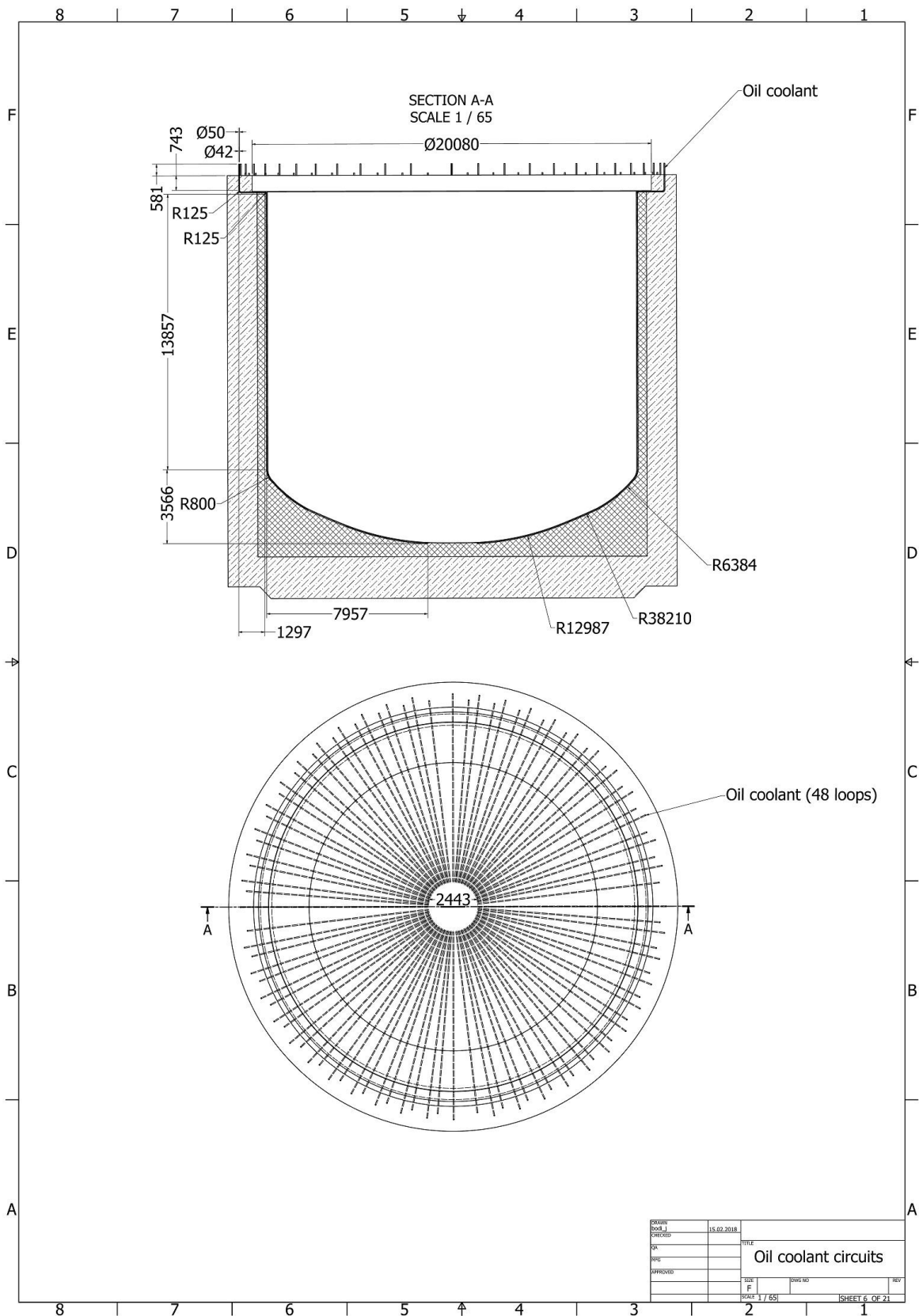
Drawing 1



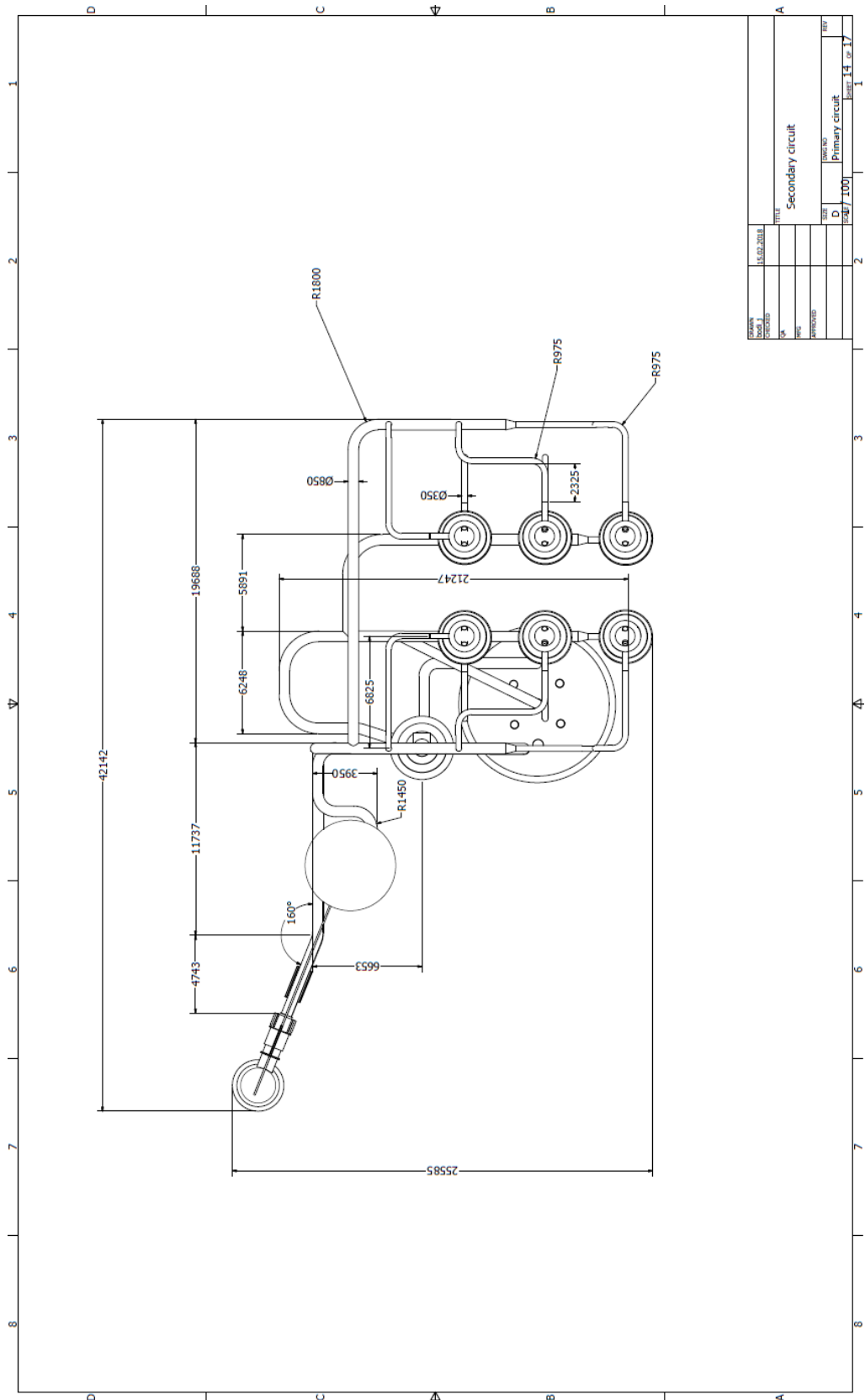
Drawing 3



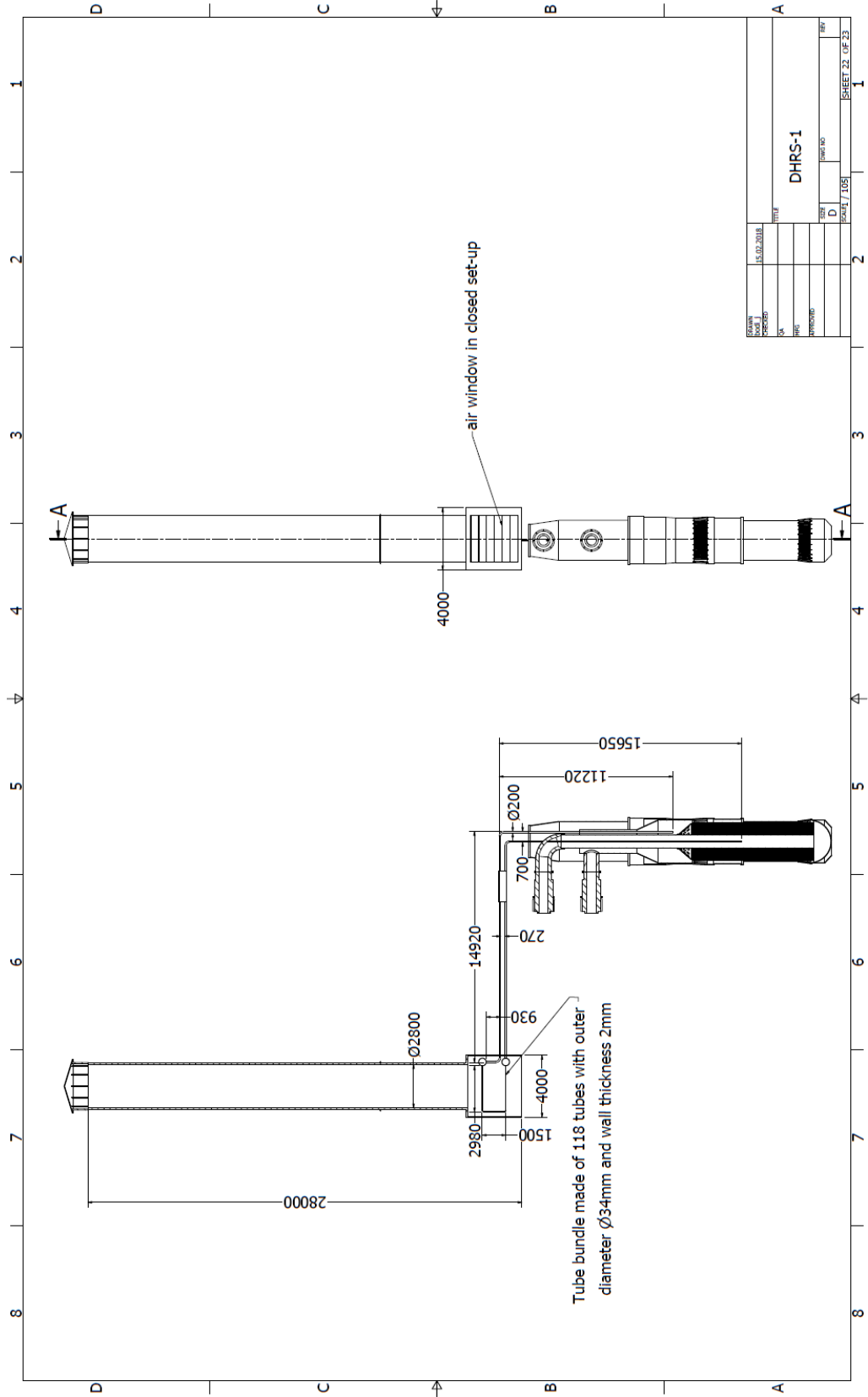
Drawing 7



Drawing 8



Drawing 9



Drawing 10

Appendix C - CEFR CRP modeling and results

Introduction and codes used

The current work presented in the paper is performed as part of an International Atomic Energy Agency organized Coordinated Research Project (CRP) dedicated to the static neutronic benchmark analysis of the Chinese Experimental Fast Reactor (CEFR) start-up tests. In the project, calculations are performed to measure the accuracy of the utilized neutronic tools and serve as a basis for validation work for the participants as experimental results have been supplied by the CRP organizers.

The CEFR is a pool-type, Sodium-cooled Fast Reactor (SFR) laying the foundation to the Chinese SFR technology development as it is its first building block. This reactor has a 65 MW_{th} power output generating 20 MW_e. The initially adopted fuel for the reactor core is uranium dioxide (UO₂), with 64.4 % enrichment. The core consists of 79 fuel assemblies, 8 control assemblies, 1 neutron source, 394 stainless steel reflector assemblies, and 230 shielding assemblies [A-D-1], shown in Figure A-C-1.

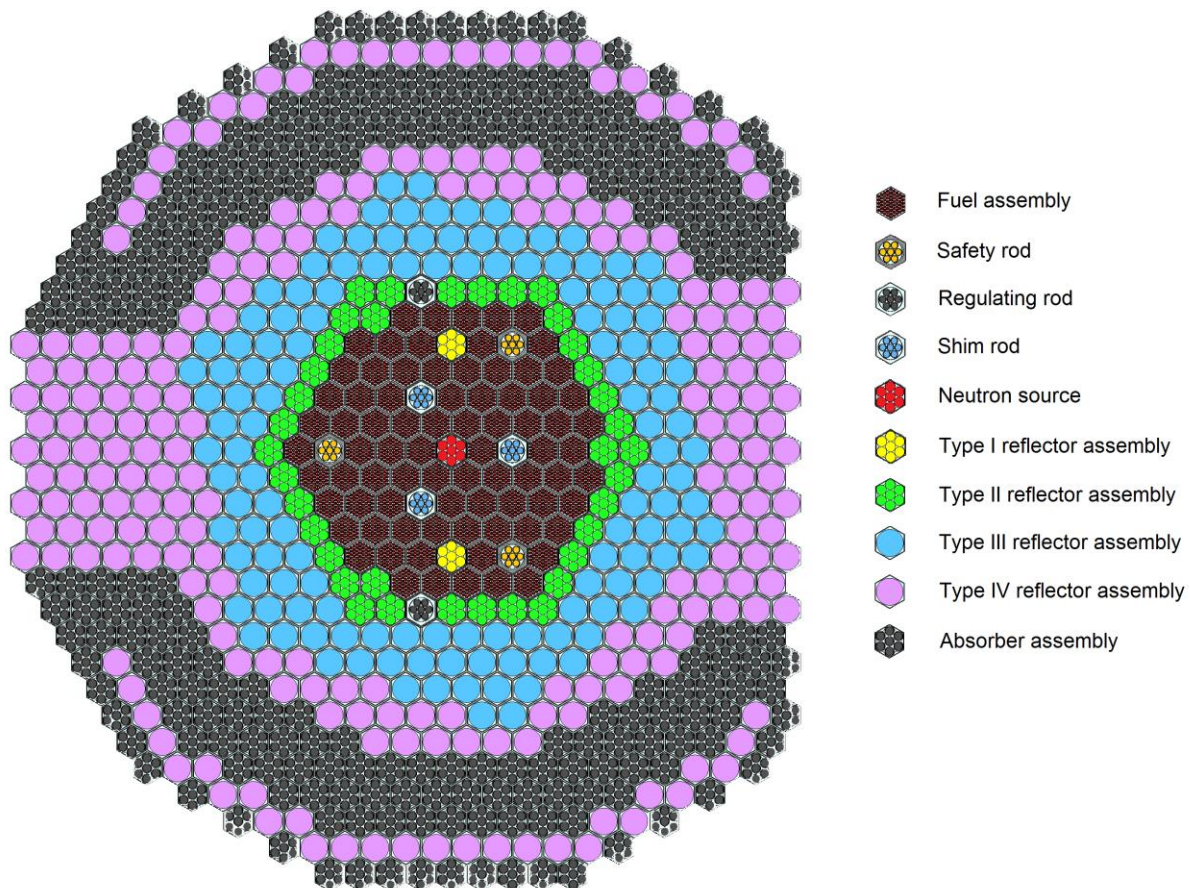


Figure A-C-1. CEFR reactor core arrangement

There are two main codes and an in-house script, at the Paul Scherrer Institut (PSI), used for the current analysis: 1) The first code is the Serpent 2 Monte Carlo code [A-D-2], which is a multi-purpose, continuous energy particle transport code developed by the VTT Technical Research Center in Finland. The Monte Carlo code is used to generate cross sections for the deterministic core calculator. 2) The deterministic

solution is obtained from **Purdue Advanced Reactor Core Simulator (PARCS)**, which is a US NRC reactor kinetics code [A-D-3]. 3) Lastly, an in-house script, called **sampling** [A-D-4], is used in conjunction with Serpent and PARCS to increase the consistency between the results of the two calculation routes, forming a hybrid hybrid spatial kinetics sampling method.

As part of the aforementioned CEFR start-up tests, a series of experiments have been conducted to obtain data regarding the fuel loading and criticality, control rod worth, reactivity coefficients, and foil activation. This data is accessible in the CRP to check the accuracy of the codes and validate the calculation methodology. The CRP is divided into two main stages: 1) The first stage consists of the model development of the participants having all the required data being provided by the China Institute of Atomic Energy (CIAE). Through the models, the experimental tests are replicated with the numerical simulation tools without knowing the actual experimental results. This stage is called the blind phase of the project. 2) In the second stage, the experimental results are released, and it is possible to check the model accuracy and to potentially increase the agreement of the results between the calculation and experiments.

In the blind phase of the CRP, the following calculations are performed by PSI:

- Fuel loading and criticality
- Sodium void reactivity
- Integral reactivity coefficient calculation

In the refined phase, where the experimental results are released, the simulations done by PSI are:

- Control rod worth
- Temperature reactivity
- Subassembly swap reactivity

By completing these simulations, all the models specified in the CRP description are generated and assessed except for the foil activation calculations, which are out of scope for PSI using the present methodology.

Geometry description

The geometry description utilized for the models can be divided into two separate sections. 1) In the first section, the Serpent model's geometry is discussed explaining the core modeling; 2) In the second section, the utilized PARCS geometry overview is presented with the simplifications involved in the models.

The Serpent geometry is based on the description provided in the CRP technical specifications. Every assembly is modeled individually, shown in Figure A-C-2, allowing to create separate universes for the different axial regions of each assembly (called universe) for which cross section can be generated separately. For the fuel assemblies in the core, every fuel pin is modeled, whereas the wire wrap is smeared into the cladding of the pin. A similar approach is used for the control rod modeling, where every absorbing pin is modeled individually, whereas the shielding region at the bottom is smeared into one cylindrical block surrounded by sodium and the wrapper. The stainless steel (SS) region, surrounding the fissile core, of type I and type II reflector assemblies have pin-wise geometry definition, whereas the

bottom and upper shielding are modeled as one block of steel. The same geometry definition is used for the absorber assemblies, whereas the type III and type IV reflector assemblies do not have pin-wise geometry definition at all, but the steel is smeared into one block everywhere being surrounded by sodium and wrapper.

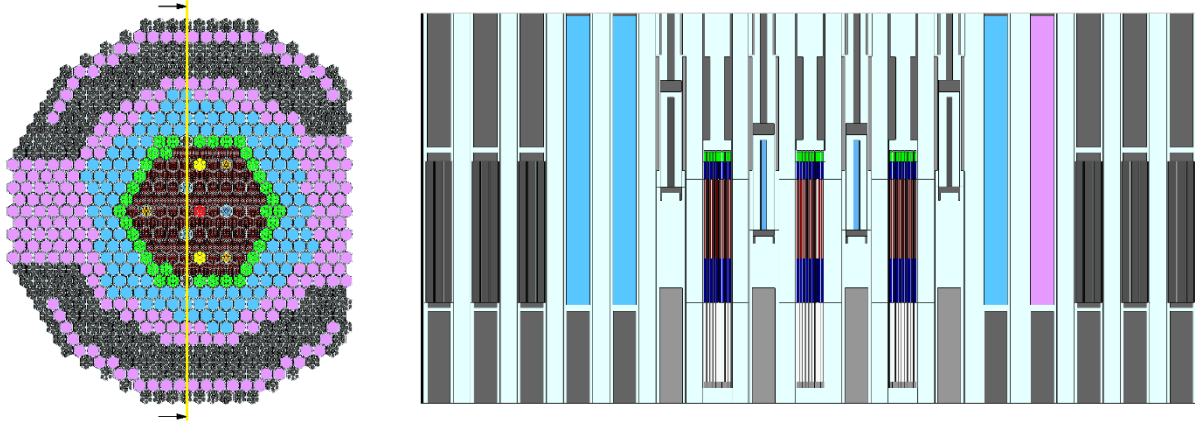


Figure A-C-2. Serpent geometry modeling of the CEFR

In the PARCS model, the simulated reactor core follows the arrangement of the Serpent input, i.e., every assembly is modeled individually in the core. Every time when there is a difference in the axial positions of the control rods between experimental set-ups, a new model is developed with corresponding axial divisions in PARCS, as only one type of nodalisation can be used for all of the assemblies in the core. The size of the nodes is kept close to 5 cm with certain deviations to be consistent with the different material region boundaries. Within one node of the model, the hexagonal assemblies are homogeneous, in accordance with the universe wise cross section generation in Serpent, where every universe corresponds to a separate axial material region within the assembly.

Neutronics methods and models

The neutronic methodology used for the calculations, starts with the 1 energy group cross section generation for the subsequent deterministic calculations, presented in Figure A-C-3. This cross section generation happens with the aid of the continuous energy Serpent Monte Carlo code with the aforementioned geometry description using JEFF 3.1.1. cross section library. Based on the same core set-up which is used in Serpent, the PARCS model is developed with the newly generated cross sections. Following this, a calculation is performed by PARCS in nodal diffusion mode, which gives calculated K_{eff} and flux distribution in the core. The PARCS generated values are then compared to the Serpent ones to assess the discrepancy, which is later decreased by using an in-house script called Sampling. Sampling uses the fact that the Monte Carlo calculation, by its nature, contains an error on the transport cross section value. In this way, the transport cross-section can be modified, in an iterative manner, by a small amount for every node of PARCS (up to 1.5 %/iteration), where after every iteration, the K_{eff} and flux distribution is compared to the Serpent results. When the errors on both K_{eff} and flux decrease between two iterations, the newly generated cross section value is used as the default for the next iteration. As 10000 iterations have been set to reach the required accuracy on the results, an upper limit for the transport cross section change has been set, allowing a maximum of 50 % deviation compared to the

original Serpent generated values. As the change in every iteration is random, this boundary is generally not reached. Nevertheless, it serves as a barrier to keep it within an acceptable limit.

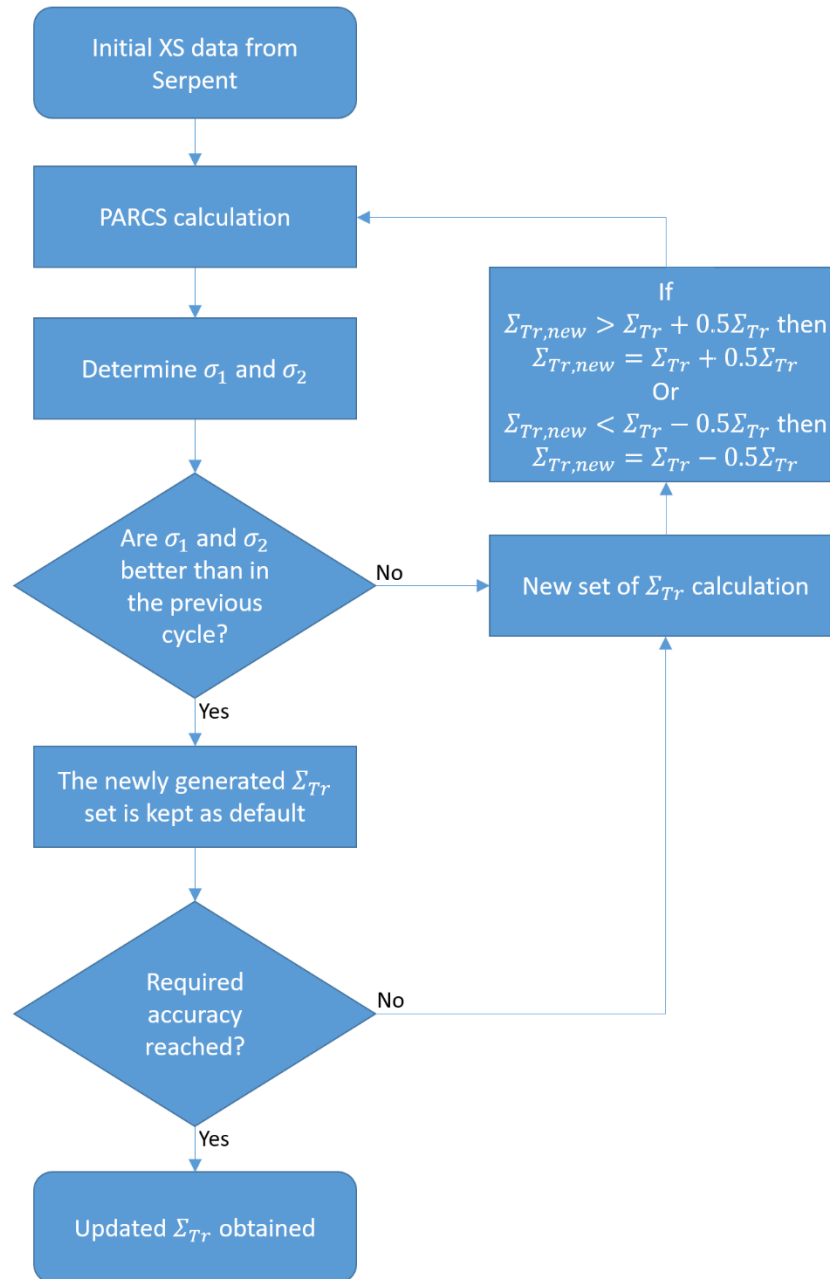


Figure A-C-3. Sampling methodology flowchart

Simulation results: blind, refined, and brief discussion

Fuel loading and criticality

The first calculation presented is the criticality calculation reproducing the start-up of the reactor, approaching criticality by first loading the fuel assemblies into the core and later withdrawing a regulating rod in steps to reach the K_{eff} of 1. In Figure A-C-4, the fuel region of the reactor core is shown in the

arrangement which was used to achieve criticality in the reactor. To reach the critical state, 72 fuel assemblies were loaded into the core compared to the 79 of the nominal set-up. In this way, at 7 fuel assembly positions, dummy assemblies were loaded for this experiment.

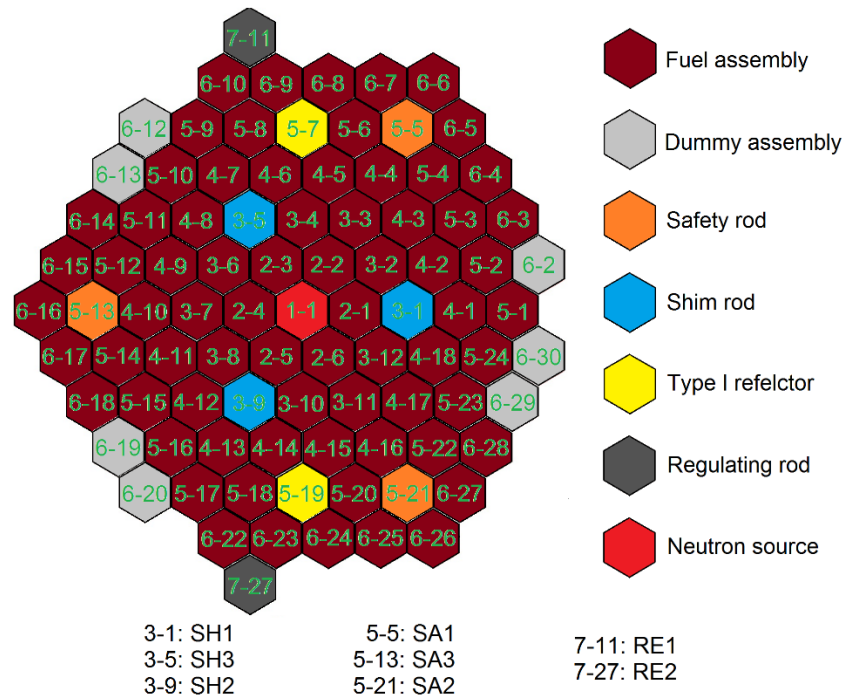


Figure A-C-4. Fuel assembly region of the core including the position numbering for every assembly and the naming scheme of the control rods

The simulation consists of 6 cases, corresponding to the final 6 steps of the experiments, shown in Table A-D-1. Case 1 includes only 70 fuel assemblies, which gives a subcritical core set-up. In the second case, the number of fuel assemblies is extended to 71, which results in the simulations in an already supercritical core, whereas it should be clearly still subcritical based on the experiment. In case 3, where the critical setting is achieved in the experiment, 72 assemblies are inserted into the core. From this point onward, the RE2 regulating rod is inserted in 4 steps to achieve the criticality. The results are plotted in Figure A-C-5, which shows that the overall calculation has a reasonable tendency but shifted upwards by around 600 pcm. This amount of discrepancy can be the result of the cross section library used [A-D-5], leading to a supercritical core, whereas the experimental results show a critical value. As the current method is mainly used for transient simulations, when it is coupled to a thermal-hydraulic code, the reactivity effect predictions are of higher importance, which are presented in the subsequent sections.

Case	RE2 Control Rod Position [mm]	k_{eff}
1	Out of Core	0.99939
2	Out of Core	1.00294
3	190	1.00626
4	170	1.00609
5	151	1.00605
6	70	1.00573

Table A-D-1. Criticality calculation K_{eff} and regulating rod positions

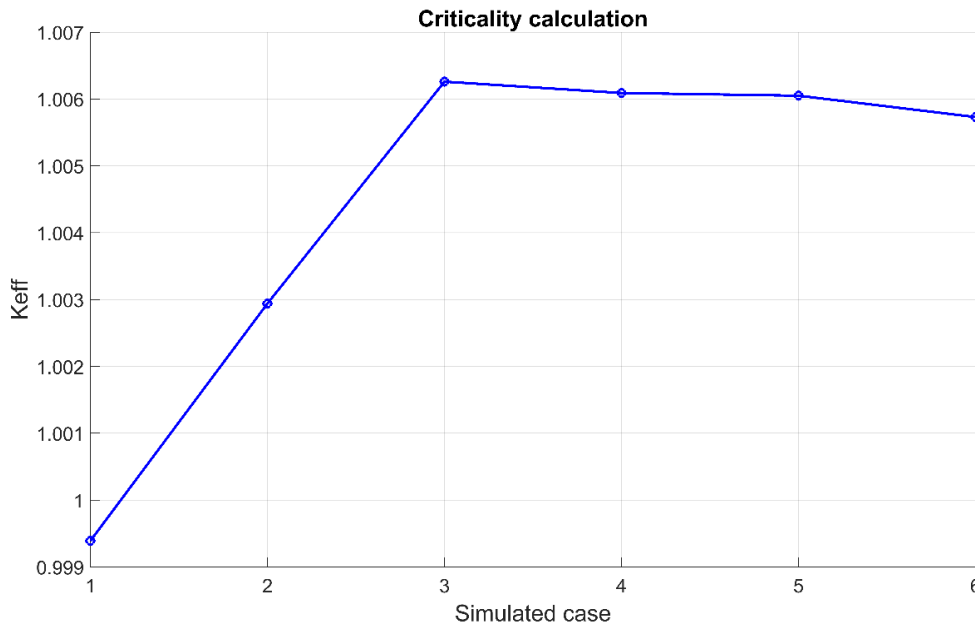


Figure A-C-5. Criticality approach predicted by the calculations

Sodium void reactivity evaluation

The second calculation achieved in the blind phase is the void reactivity prediction. This calculation is important to validate that the void reactivity can be predicted accurately, which is an important reactivity effect in a reactor transient. With the boiling of the sodium in the reactor core, the resulting void hardens the neutron spectrum leading to a potentially positive reactivity effect in the core, which can be hazardous.

To conduct the experiment, a special fuel assembly was inserted into certain locations of the reactor core, followed by the withdrawal of the regulating rods to compensate for the reactivity effect of the voided assembly. The position numbering is indicated in Table A-D-2, from which the actual assembly location can be found in Figure A-C-4. The safety rods were withdrawn from the core into the parking position, whereas the shim rods were inserted into the mid-core level. The fact that the regulating rods were withdrawn from the core to reach criticality shows that at the assessed locations, the voided assembly had a negative reactivity feedback effect, which is an important safety feature. This probably comes from the fact that CEFR has a relatively small core with high leakage. After the reactivity effect of the control rods has been quantified, the resulting void effect is shown in the Table.

In Figure A-C-6, the results from the calculation and the experiment are compared to each other. From this plot, it is clearly shown that the obtained reactivity effect matches well the experiment, and it is within the uncertainty margin everywhere except for the location at 6-13, where the simulation overpredicts the actual effect by about 12 pcm.

Measurement position in core		Control rod positions (mm)		Expected output			
		RE1	RE2	k_{eff}	CR reactivity [pcm]	Residual reactivity diff. [pcm]	Void reactivity [pcm]
(2-4)	Reference	277.6	277.3	1.00629	-41.5	-3	-44.5
	Voided	336.8	336.8	1.00626			
(3-7)	Reference	278	277.4	1.00628	-42	-2	-44
	Voided	337.9	337.9	1.00626			
(4-9)	Reference	277.7	277.6	1.00627	-42	6	-36
	Voided	338	337.6	1.00633			
(5-11)	Reference	278.4	276.2	1.00632	-42.3	-1	-43.3
	Voided	338	337.5	1.00631			
(6-13)	Reference	302.9	303.3	1.00654	-22.1	-23	-45.1
	Voided	338.1	337.8	1.00631			

Table A-D-2. Voided assembly and regulating rod position together with reactivity results

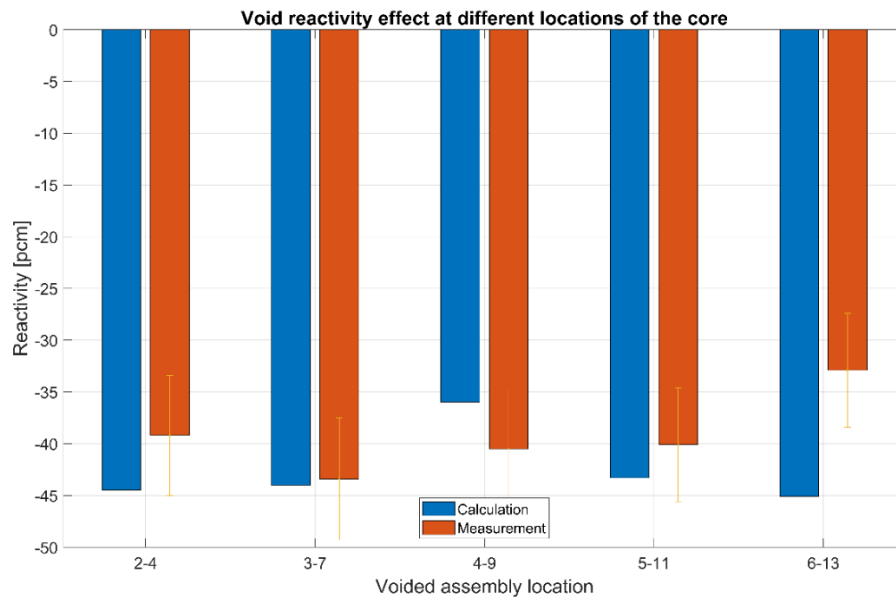


Figure A-C-6. Void reactivity effect result comparison between the calculations and the experiment

Reactivity coefficients determination

The last calculation which was performed in the blind phase of the CRP by PSI was the reactivity coefficient assessment. For this study, no experimental results are available, thus the accuracy cannot be validated. All the computed coefficients and their results are presented in Table A-D-3. The axial expansion is modeled by increasing 1% of the fuel height with a corresponding height decrease in the spring at the top of the fuel pin. The radial expansion includes a 1% fuel assembly pitch increase, modeled by the expansion of the diagrid. The fuel density effect and sodium density effect are accounted for by 1% material density increase, whereas for the steel density, 10% change is used. The Doppler effect is modeled by increasing the fuel temperature to 500 °C, which is a 250 °C increase compared to the fact that for all simulations, the reference core temperature is at 250 °C. At this point, it can be mentioned that the resulting coefficient is relatively low compared to other sodium fast reactors [A-D-6][A-D-7], but this probably can be attributed to the fact that the fissile U-235 content is very high in the core, and thus the Doppler effect is reduced by the reduced influence of the U-238 capture increase. The voided Doppler includes, on top of the temperature increase, the voiding of all the 79 fuel assemblies present in the core. Finally, the regulating rod and shim rod expansion coefficients are calculated, giving their differential reactivity worth by inserting them 10 cm from around the mid-core level.

Reactivity coefficient	Unit	Value
Axial expansion	pcm/% expansion	-360
Radial expansion	pcm/% expansion	-706
Fuel density	pcm/% density increase	548
Steel density	pcm/% density increase	33.6
Sodium density	pcm/% density increase	31
Doppler, normal	pcm/°C	-0.236
Doppler, voided	pcm/°C	-0.21
Regulating CR expansion	Pcm/cm insertion	-9.4
Shim CR expansion	Pcm/cm insertion	-155.2

Table A-D-3. Different reactivity coefficients of the CEFR

Control rod worth calculation

The first calculation performed in the refined phase is the control rod worth assessment. This study allows to subtract from all other studies the effect of the control rod movement to directly compare the reactivity effects rather than a cumulative effect of a reactivity change due to a measured quantity and the control rod movements. All the control rod positions for each case and the resulting K_{eff} and rod worth are presented in Table A-D-4, for which experimental measurement was also performed.

Measurement object	Rod or rod group		Control rod positions [mm]								k_{eff}	Rod worth [pcm]
			RE 1	RE 2	SH 1	SH 2	SH 3	SA 1	SA 2	SA 3		
Regulating rod worth	RE1	Before drop	50	10	24	24	23	49	50	50	1.006	-
			1	6	0	0	9	8	0	0	27	144.396

		After drop	-1	10 6	24 0	24 0	23 9	49 8	50 0	50 0	1.004 81	
	RE2	Before drop	10 6	49 9	24 0	24 0	23 9	49 8	50 0	50 0	1.006 33	- 157.254
		After drop	10 6	5	24 0	24 0	23 9	49 8	50 0	50 0	1.004 74	
Shim rod worth	SH1	Before drop	24 0	24 0	50 1	14 1	14 1	49 8	49 9	49 9	1.005 20	- 1899.14 4
		After drop	24 0	24 0	4	14 1	14 1	49 8	49 9	49 9	0.986 37	
	SH2	Before drop	23 9	24 0	15 1	49 8	15 1	49 8	50 0	50 0	1.005 79	- 1867.13 3
		After drop	23 9	24 0	15 1	-1	15 1	49 8	50 0	50 0	0.987 25	
	SH3	Before drop	24 0	23 9	14 8	15 0	49 8	49 8	50 0	50 0	1.005 47	- 1841.64 7
		After drop	24 0	23 9	14 8	15 0	7	49 8	50 0	50 0	0.987 19	
Safety rod worth	SA1	Before drop	24 0	23 9	24 0	24 0	24 1	49 8	49 9	49 9	1.006 17	- 876.910
		After drop	24 0	23 9	24 0	24 0	24 1	46	49 9	49 9	0.997 37	
	SA2	Before drop	24 0	24 0	24 0	24 0	24 0	49 8	49 9	49 9	1.006 13	- 869.943
		After drop	24 0	23 9	24 0	24 0	24 0	49 8	55	49 9	0.997 40	
	SA3	Before drop	24 0	23 9	24 0	24 0	24 0	49 8	49 9	49 9	1.006 11	- 935.362
		After drop	24 0	23 9	24 0	24 0	24 0	49 8	49 9	40	0.996 73	
Worth of 1st shutdown system	3*SH + 2*RE	Before drop	24 7	24 7	23 9	24 0	23 9	49 8	50 0	49 9	1.006 08	- 3045.49 9
		After drop	0	5	1	-1	7	49 8	50 0	49 9	0.976 17	

Worth of 1st shutdown system with SH1 stuck	SH2+	Before drop	24 7	24 8	50 1	14 1	14 1	49 8	50 0	49 9	1.005 26	- 997.486
	SH1+ 2*RE	After drop	-2	2	50 1	-3	16	49 8	50 0	49 9	0.995 28	
Worth of 2nd shutdown system	3*SA	Before drop	24 7	24 9	24 0	24 0	24 0	49 8	50 0	49 9	1.006 28	- 2802.52 5
		After drop	24 7	24 9	24 0	24 0	24 0	46	56	40	0.978 68	
Worth of 2nd shutdown system with SA3 stuck	SA1+	Before drop	24 7	24 8	24 0	24 0	24 0	49 8	50 0	50 0	1.006 09	- 1775.85 7
	SA2	After drop	24 7	24 8	24 0	24 0	24 0	45	54	50 0	0.988 43	
All control rods	2*RE +	Before drop	24 7	24 8	24 0	24 0	24 0	49 9	50 0	50 0	1.006 21	- 5980.14 3
	3*SA + 3*SA	After drop	0	3	2	-2	0	45	56	40	0.949 10	
All control rods with SH1 stuck	2*RE +	Before drop	24 8	24 8	50 0	14 1	14 1	49 8	50 0	49 9	1.005 27	- 3850.30 3
	SH2+ SH3+ 3*SA	After drop	-2	2	50 0	-3	7	45	55	40	0.967 81	

Table A-D-4. Control rod worth calculation based on the experimental control rod positions

In Figure A-C-7, the reactivity effect of the specified rod movements is compared to the experimental outcomes. This plot shows the accuracy of the model, and the calculation scheme, as all the measured cases are within the experimental uncertainty level.

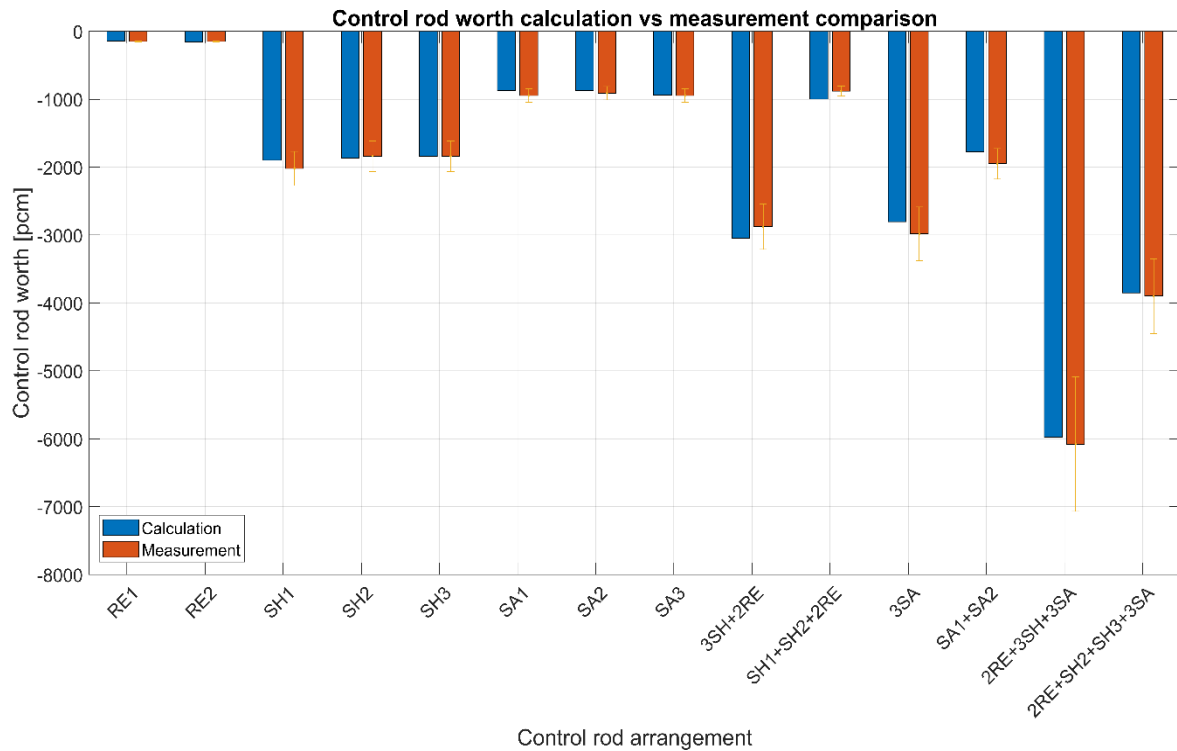


Figure A-C-7. Control rod movement reactivity effect comparison between simulation and experiment

A subsequent calculation arrangement is analyzed to obtain results about the integral control rod worth for every control rod and control rod bundles. The modification compared to the previously presented data is that in this calculation, all control rod, which does not take part in the analysis, is withdrawn completely from the active core region into the parking position (500 mm from the bottom of the fissile fuel). In Table A-D-5, the control rod arrangement and the resulting integral rod worth is shown. The results are plotted in Figure A-C-8, where it is clear that the same rod types have a reactivity worth of nearly identical to each other. Another effect, which can be understood from the Figure, is the fact that when the rod bundles are inserted together, their cumulative effect is close to identical to the addition of each individual rod worth.

Measurement object	Rod or rod group	Control rod positions [mm]								k_{eff}	Rod worth [pcm]
		RE1	RE2	SH1	SH2	SH3	SA1	SA2	SA3		
All control rods out of core	2*RE+									1.03515	-
	3*SH+	500	500	500	500	500	500	500	500		
	3*SA										
Regulating rod worth	RE1	0	500	500	500	500	500	500	500	1.03355	-149.550
	RE2	500	0	500	500	500	500	500	500	1.03354	-150.486
	2*RE	0	0	500	500	500	500	500	500	1.03193	-301.441
Shim rod worth	SH1	500	500	0	500	500	500	500	500	1.01606	-1815.028

	SH2	500	500	500	0	500	500	500	500	1.01651	- 1771.458
	SH3	500	500	500	500	0	500	500	500	1.01653	- 1769.523
	3*SH	500	500	0	0	0	500	500	500	0.97904	- 5536.516
Safety rod worth	SA1	500	500	500	500	500	0	500	500	1.02553	-906.199
	SA2	500	500	500	500	500	500	0	500	1.02556	-903.346
	SA3	500	500	500	500	500	500	500	0	1.02521	-936.635
Worth of 1st shutdown system	3*SH+ 2*RE	0	0	0	0	0	500	500	500	0.97610	- 5844.163
Worth of 1st shutdown system with SH1 stuck	SH2+ SH1+ 2*RE	0	0	500	0	0	500	500	500	0.99442	- 3956.774
Worth of 2nd shutdown system	3*SA	500	500	500	500	500	0	0	0	1.00492	- 2906.052
Worth of 2nd shutdown system with SA3 stuck	SA1+ SA2	500	500	500	500	500	0	0	500	1.01553	- 1866.392
All control rods	2*RE+ 3*SH+ 3*SA	0	0	0	0	0	0	0	0	0.94776	- 8907.587
All control rods with SH1 stuck	2*RE+ SH2+ SH3+ 3*SA	0	0	500	0	0	0	0	0	0.96639	- 6873.535

Table A-D-5. Integral control rod worth calculation arrangement and results

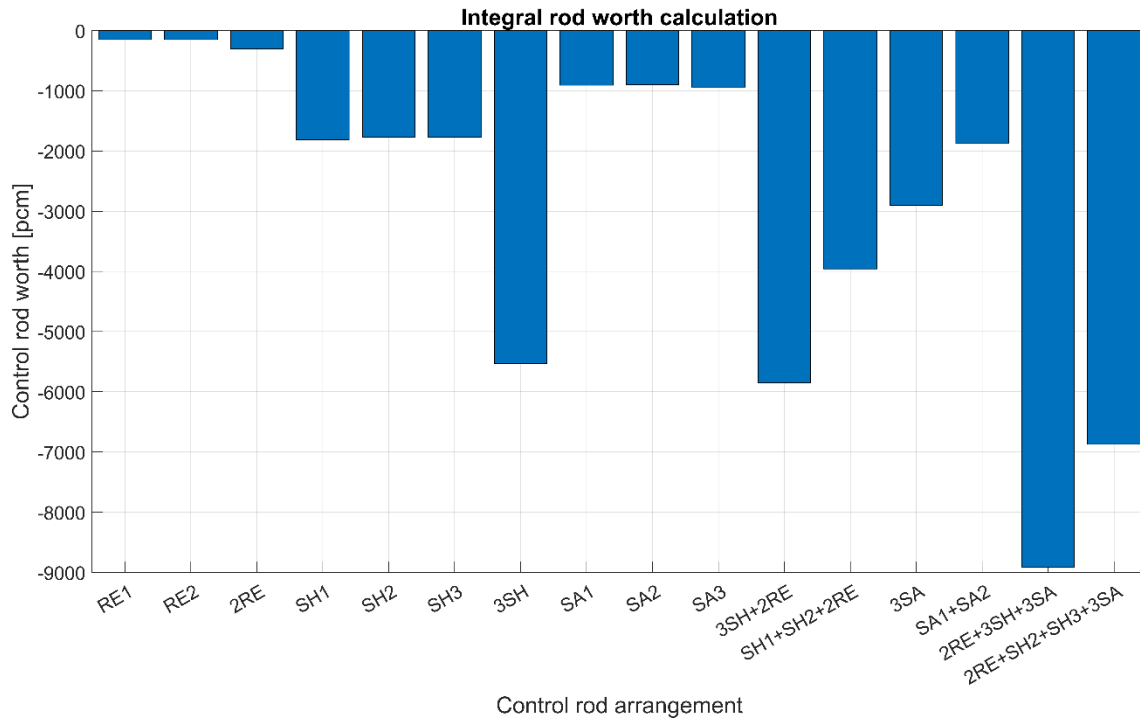


Figure A-C-8. Integral control rod worth reactivity effect

As was mentioned before, to calculate the reactivity effect in other calculations and to see the rod worth at different axial positions, the control rod worth S curve has been constructed, presented in Figure A-C-9. From the curve, the different rod types are clearly distinguishable, where the same types have a closely matching S curve pattern.

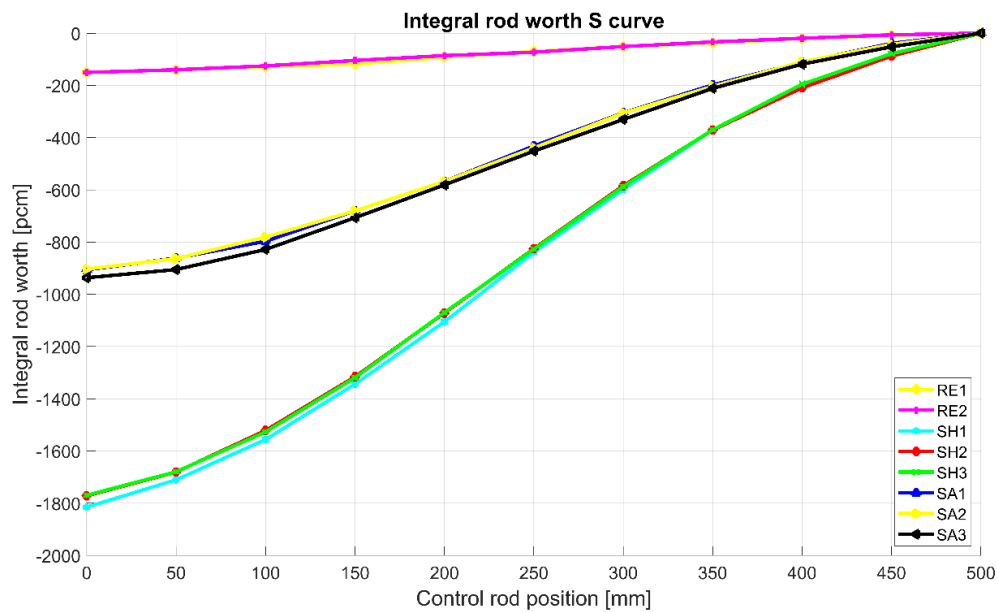


Figure A-C-9. Control rod S curves

From the S curve calculations, the differential rod worth has been constructed, shown in Figure A-C-10. This curve has been used for the control rod movement reactivity effect calculations in the other experimental set-ups. The lines do not always have a smooth change between the measured points, which probably comes from the fact that the cross sections are prepared by the stochastic Serpent 2 Monte Carlo code, and even with a matching deterministic solution, a few pcm inaccuracies are inherent in the results.

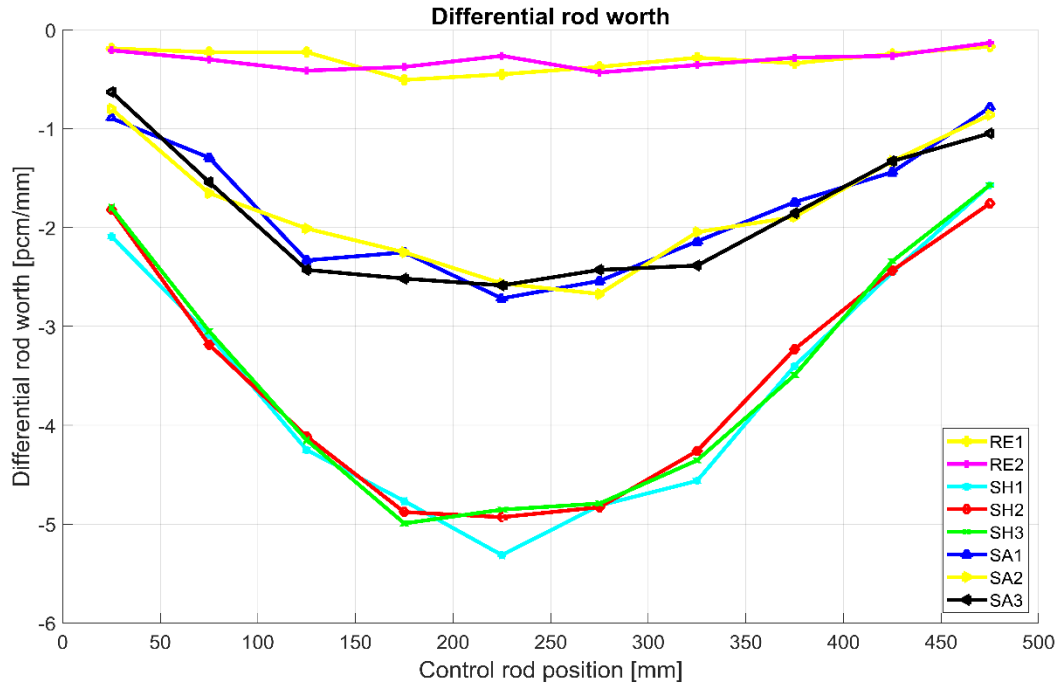


Figure A-C-10. Differential rod worth for each control rod at every measured axial position

Temperature reactivity effect

To calculate the temperature reactivity effect of the reactor core, an experiment has been performed, where the core was heated up to different isothermal temperature values between 250°C and 300°C. Two sets of measurements have been performed, one with increasing temperatures, measuring the count rates at each measured step, and another with decreasing temperatures using the same process. From the count rates, the criticality was calculated and thus the temperature reactivity effect. The process has been repeated by the simulation tools obtaining the K_{eff} value directly for each step.

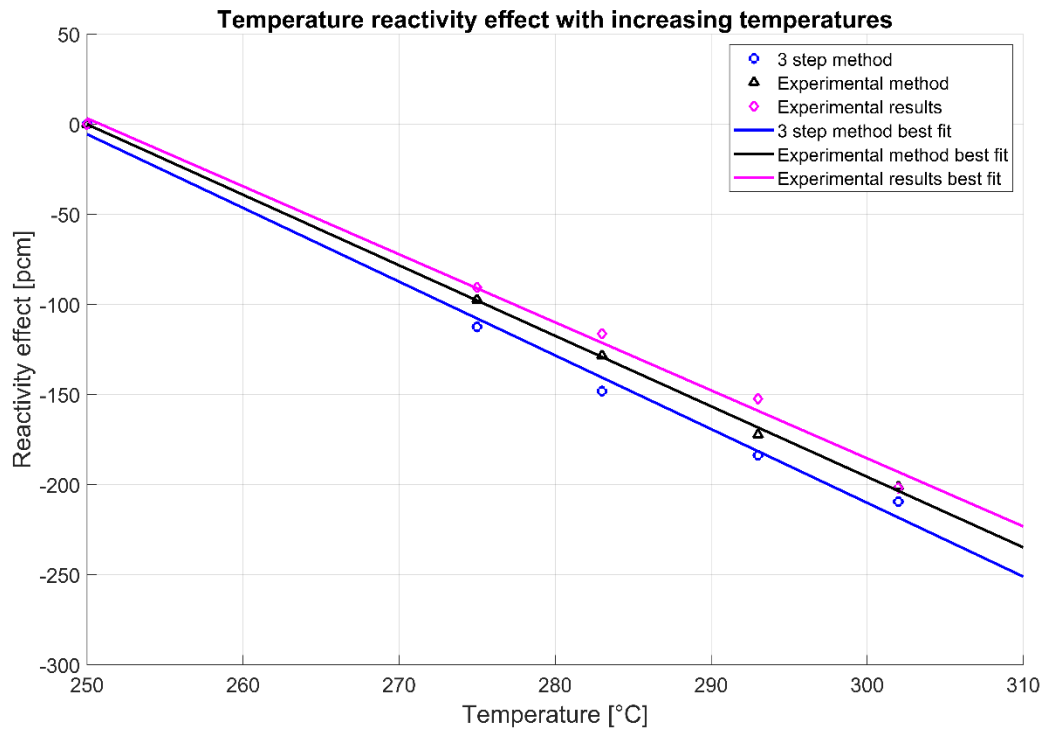


Figure A-C-11. Temperatures reactivity effect comparison of different calculation methods and the experimental result for increasing core temperatures

To determine the reactivity effect, two different calculation methods are used for both increasing and decreasing core temperatures. The first method is the experimental method, which follows everywhere the experimental process. In this sense, there is an initial measurement at the starting temperature with a set of control rod positions for which the K_{eff} is calculated. For the next point, the temperature is increased or decreased, depending on the set-up, coupled with a new set of control rod positions to keep the reactor approximately at the same criticality level during all the calculation points, matching to the experiments. By knowing the K_{eff} value for both points and calculating the reactivity effect of the control rod movements, the resulting temperature reactivity effect can be obtained. As for the 3 step method, the situation is different in the sense that before the temperature would be changed between two points, first the control rod position of the next point is implemented in the current measured temperature, thus there are always 2 calculations done for every temperature point. In this way, no control rod reactivity effect calculation is required. In Figure A-C-11 and Figure A-C-12, the increasing and decreasing temperature reactivity results are plotted, respectively. For both settings, the best-fit of the points shows good agreement thus, the simulation reproduces well the experiments. Furthermore, in Table A-D-6, the gradient of all best-fit lines are presented, providing the resulting temperature coefficients.

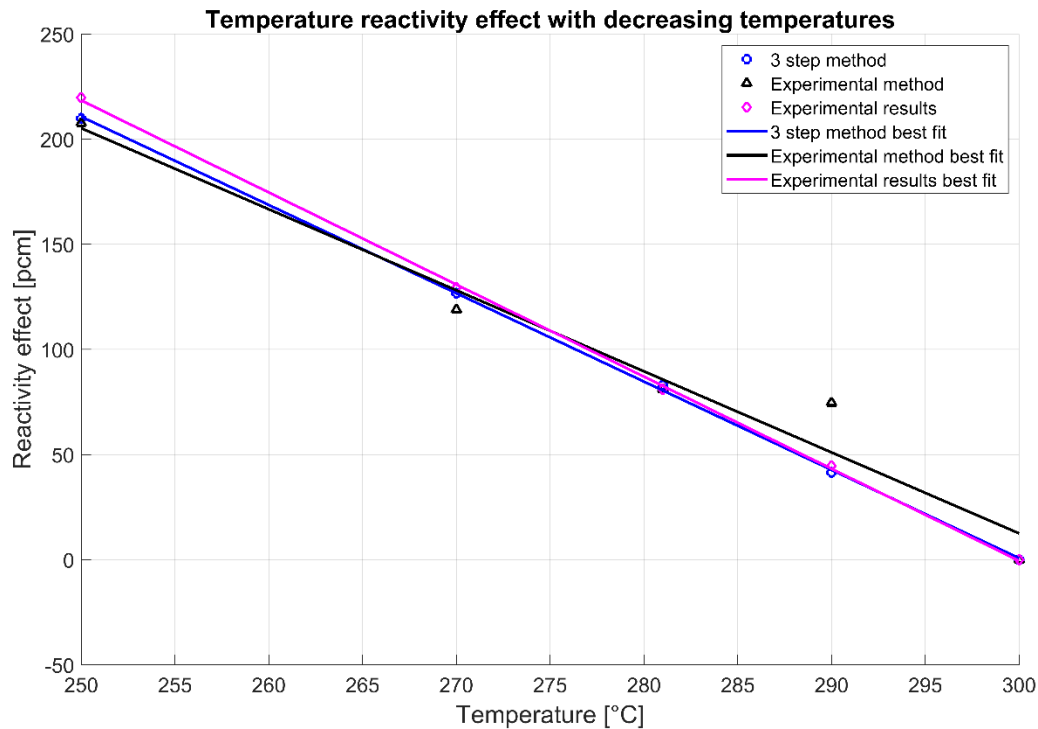


Figure A-C-11. Temperatures reactivity effect comparison of different calculation methods and the experimental result for decreasing core temperatures

Temperature coefficient	3 step method	Experimental method	Measured data
Determination method	[pcm/°C]	[pcm/°C]	[pcm/°C]
Increasing temperature	-4.091	-3.913	-3.759
Decreasing temperature	-4.199	-3.854	-4.384

Table A-D-6. Temperature reactivity coefficients according to the various calculation schemes compared to the experimental results

Assembly swap reactivity effect

The last effect which is analyzed in the paper is the assembly swap reactivity effect. In the experiments, fuel assemblies were exchanged with the type I reflector assemblies at specified locations, shown in Table A-D-7. The purpose of the exercise is to simulate the effect of an accidental swap of fuel assemblies during reactor refueling. Two different measurements were performed for the same arrangements. One with only moving a single control rod and another where multiple control rods were moved, thus the effect of different control rod positions affecting the swap reactivity could be quantified.

Position to be measured*	Assemblies Loaded After Swap							
	(2-6)	(3-11)	(4-17)	(5-23)	(6-29)	(5-22)	(7-31)	(5-19)
(2-6)	SS	Fuel	Fuel	Fuel	Fuel	Fuel	SS	SS
(3-11)	Fuel	SS	Fuel	Fuel	Fuel	Fuel	SS	SS
(4-17)	Fuel	Fuel	SS	Fuel	Fuel	Fuel	SS	SS
(5-23)	Fuel	Fuel	Fuel	SS	Fuel	Fuel	SS	SS
(6-29)	Fuel	Fuel	Fuel	Fuel	SS	Fuel	SS	SS
(5-22)	Fuel	Fuel	Fuel	Fuel	Fuel	SS	SS	SS
(7-31)	Fuel	Fuel	Fuel	Fuel	SS	Fuel	Fuel	SS
(5-19)	Fuel	Fuel	Fuel	SS	Fuel	Fuel	SS	Fuel

Table A-D-7. Swap cases with assembly specification at the chosen locations

The results of the swap reactivity are summarized in Table A-D-8, and for better visualization, it is plotted in Figure A-C-12 and Figure A-C-13. The simulation follows the experimental specifications, thus the core for the first 6 cases includes 79 fuel assemblies, which is reduced to 78 for the swapped set-up, therefore, results in a strong negative reactivity insertion. For the cases 7-31 and 5-19, the reference core layout includes only 78 fuel assemblies, and this number is kept for the swapped layout also, only changing the position of the 7-31 and 5-19 reflector assemblies to the position 6-29 and 5-23, respectively. As the results display, when only the reflector assembly is shuffled, it introduces a positive reactivity effect into the core.

From the results, at locations closer to the center of the reactor (the first number in the position refers to the radial ring number), a relatively high discrepancy is visible between the calculated and measured values for both multiple rod and single rod cases. As the swapped assembly location moves closer to the periphery of the reactor core, this discrepancy continuously decreases until the location 7-31, which is the outermost position measured in the experiment. Generally speaking, the calculation underestimates nearly everywhere the swap reactivity effect systematically, even when the 13% error on the measured data is accounted for. This can originate from certain modeling inaccuracies, which is more pronounced at the center of the core or from an error in the experimental measurement itself. Nevertheless, the tendency of the reactivity effect change, depending on the radial core position, is well kept in the calculation, thus the overall phenomenon is reproduced by the simulations. In this sense, when the assembly swap results in a fuel assembly being positioned closer to the core-periphery and hence a reflector closer to the center, a negative reactivity effect is introduced into the core.

Measurement position	Multiple rod measurement Swap reactivity [pcm]	Single rod measurement Swap reactivity [pcm]	Experimental Multiple rod Swap reactivity [pcm]	Experimental Single rod Swap reactivity [pcm]
(2-6)	-824.9	-839.1	-986.0	-984.4
(3-11)	-722.2	-726.4	-879.6	-875.1
(4-17)	-649.9	-641.7	-777.3	-771.6
(5-23)	-525.3	-513.7	-634.2	-639.5
(6-29)	-362.5	-344.1	-474.1	-476.4
(5-22)	-520.0	-525.8	-590.2	-585.8
(7-31)	210.7	229.0	209.7	209.9
(5-19)	532.4	533.0	582.2	581.9

Table A-D-8. Swap reactivity effect at variable assembly locations

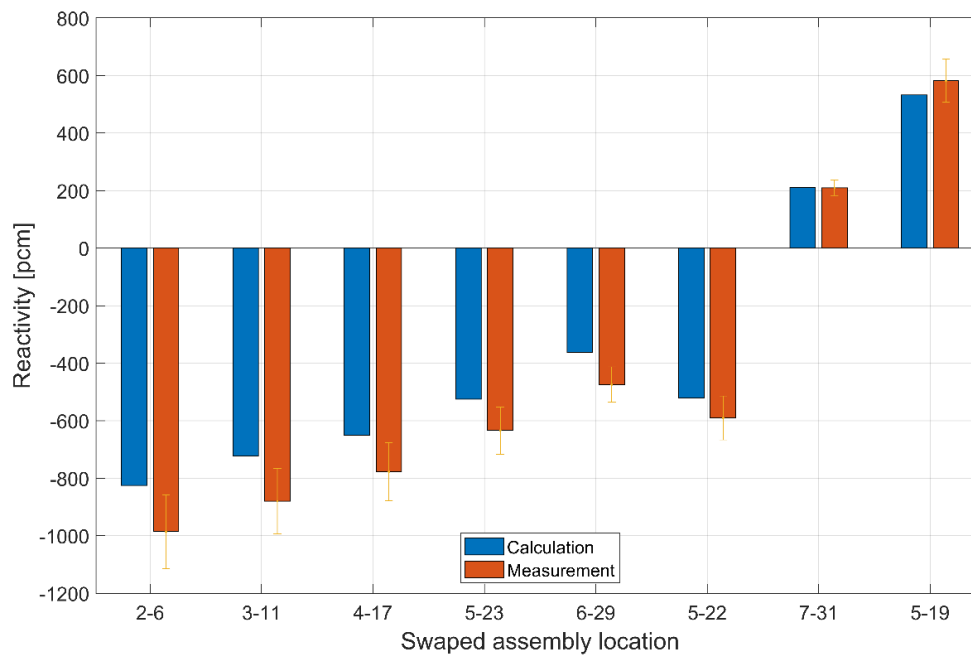


Figure A-C-12. Multiple rod swap reactivity effect calculation vs. measurement at different locations of the core

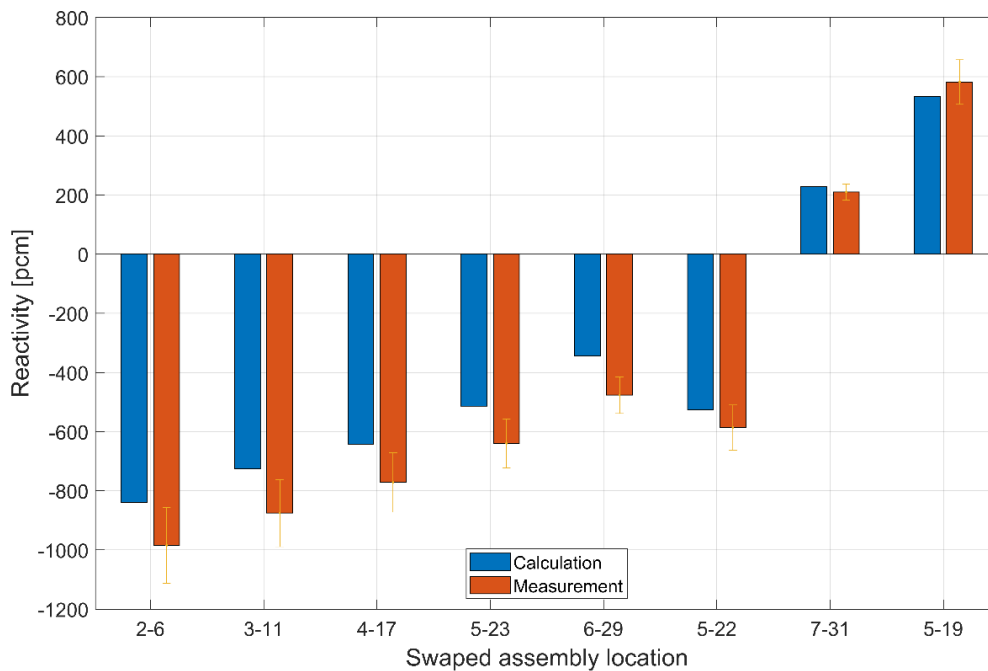


Figure A-C-13. Single rod swap reactivity effect calculation vs. measurement at different locations of the core

Conclusions

In the assessment, specific start-up experimental set-ups of the CEFR has been modeled with a hybrid spatial kinetics sampling approach. In this approach, the reactor core was modeled in Serpent to generate cross sections, which were used in PARCS with the aid of the Sampling in-house script. Through the CRP, it was possible to perform static neutronic analysis on 6 specific cases to reproduce the experimental results as close as possible. In this sense, calculations were performed on:

- Criticality approach
- Control rod reactivity worth
- Temperature reactivity effect
- Void reactivity effect
- Swap reactivity effect
- Specified reactivity coefficients

Based on the studied data set, the simulation methodology proved to be reliable in calculating the reactivity effect in a static calculation setting, providing the base for further transient simulations to validate its effectiveness in such conditions also.

REFERENCES

- [A-D-1] Huo, Xingkai; Hu, Y., Chen, X., Xu, L., Duan, T. (2018). Technical Specifications for Neutronics Benchmark of CEFRR Start-up Tests (CRP-I31032) V6.0. Beijing, China
- [A-D-2] Leppänen, J., 2013. Serpent – a Continuous-energy Monte Carlo Reactor Physics Burnup Calculation Code.
- [A-D-3] T. Downar, Y. Xu, V. Seker, N. Hudson, 2010. PARCS v3.0 – U.S. NRC core neutronics simulator. Theory Manual, Ann Arbor, MI. <<http://pbadupws.nrc.gov/docs/ML1016/ML101610117.pdf>
- [A-D-4] J. Bodi, A. Ponomarev, K. Mikityuk, “Hybrid stochastic-deterministic method of one-group cross-section generation applied to Sodium Fast Reactor” in International Congress on Advances in Nuclear Power Plants (ICAPP 2019), Juan Les Pins, France, 2019.
- [A-D-5] I. Duhamel, S. Eno, Benchmarking of the JEFF-3.1 library against critical integral experiments, International Conference on Nuclear Data for Science and Technology, (2007) 821-824, DOI: <https://doi.org/10.1051/ndata:07465>
- [A-D-6] A. Ponomarev, K. Mikityuk, L. Zhang, E. Nikitin, E. Fridman, F. Alvarez-Velarde, P. Romojaro Otero, A. Jimenez-Carrascosa, N. Garcia-Herranz, B. Lindley, U. Davies, A. Seubert, R. Henry, Large Sodium Fast Reactor Benchmark: Part I - Static Neutronics, Journal of Nuclear Engineering and Radiation Science, 2021
- [A-D-7] S. Bortot, F. Alvarez-Velarde, E. Fridman, I. Garcia Cruzado, N. Garcia Herranz, D. López, K. Mikityuk, A.-L. Panadero, S. Pelloni, A. Ponomarev, P. Sciora, A. Seubert, H. Tsige-Tamirat, A. Vasile, 2015, European benchmark on the ASTRID-like low-void-effect core characterization: neutronic parameters and safety coefficients. In Proceedings of 2015 international congress on advances in nuclear power plants (ICAPP 2015) (pp. 668-676).

Appendix D - Reactivity decomposition Figures from ULOF sensitivity study

Appendix D provides reactivity decomposition Figures from Section 4.1.6., ULOF sensitivity case assessment.

Influence of the SA shielding and reflector pin bundle design modification

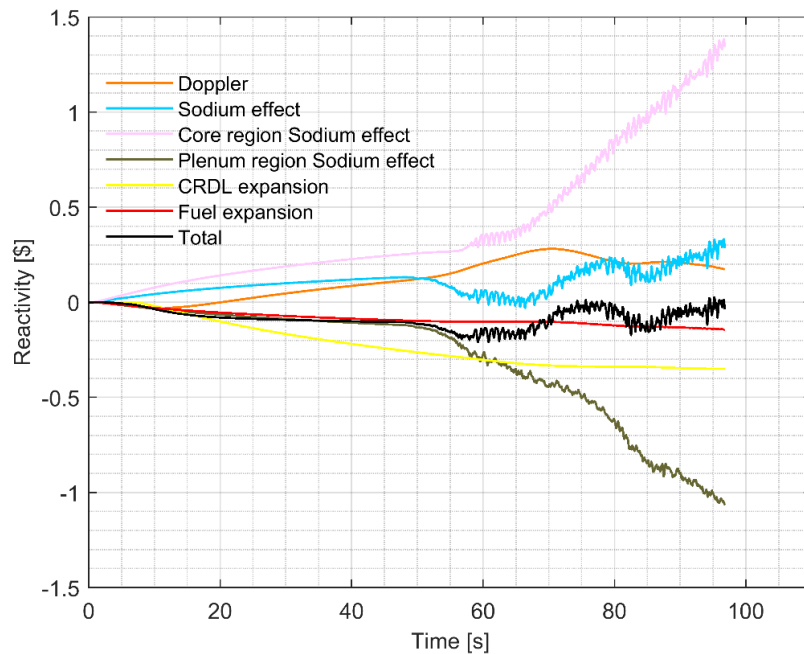


Figure A-D-1. Evolution of the reactivity components used in the point kinetics model vs. time

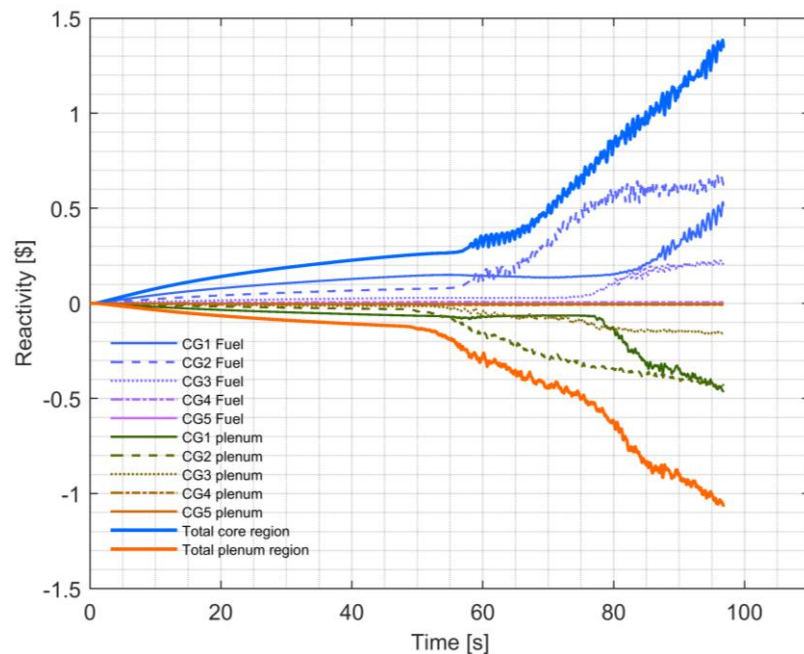


Figure A-D-2. Sodium reactivity effect evolution in time distributed amongst the different cooling groups and fuel/plenum regions

Influence of the cooling group flow distribution modification

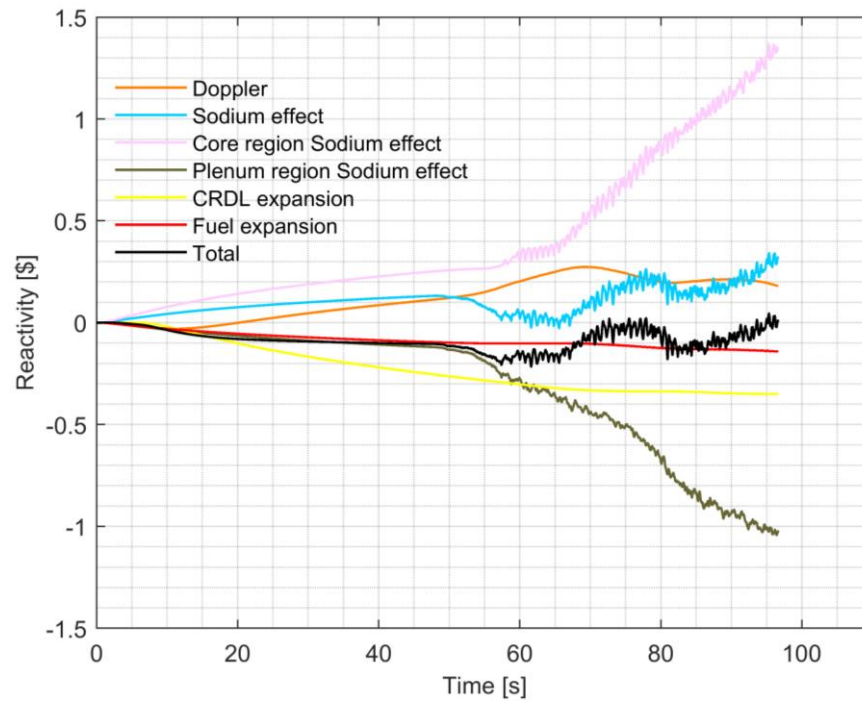


Figure A-D-3. Evolution of the reactivity components used in the point kinetics model vs. time

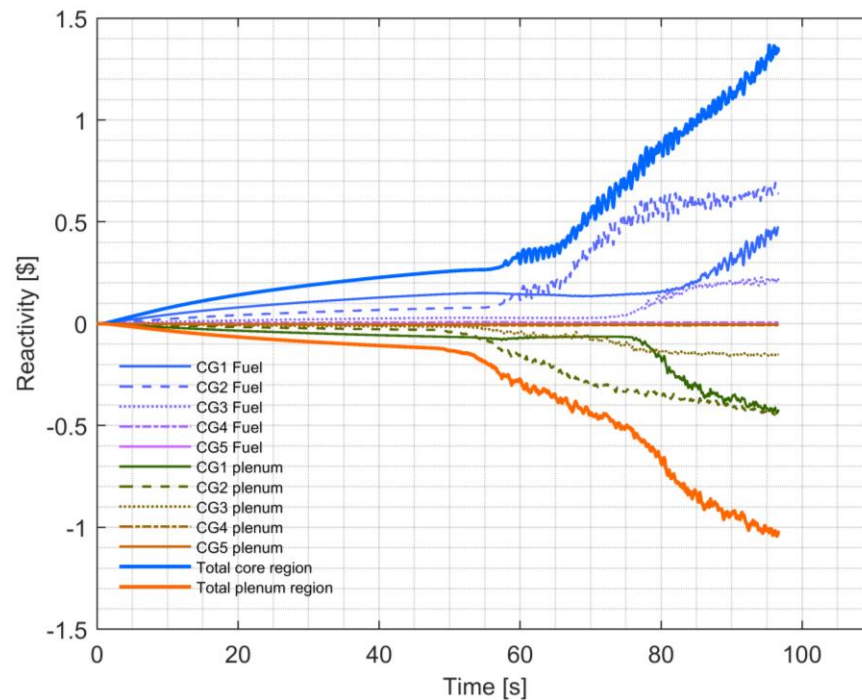


Figure A-D-4. Sodium reactivity effect evolution in time distributed amongst the different cooling groups and fuel/plenum regions

Influence of the fuel gap conductance modification

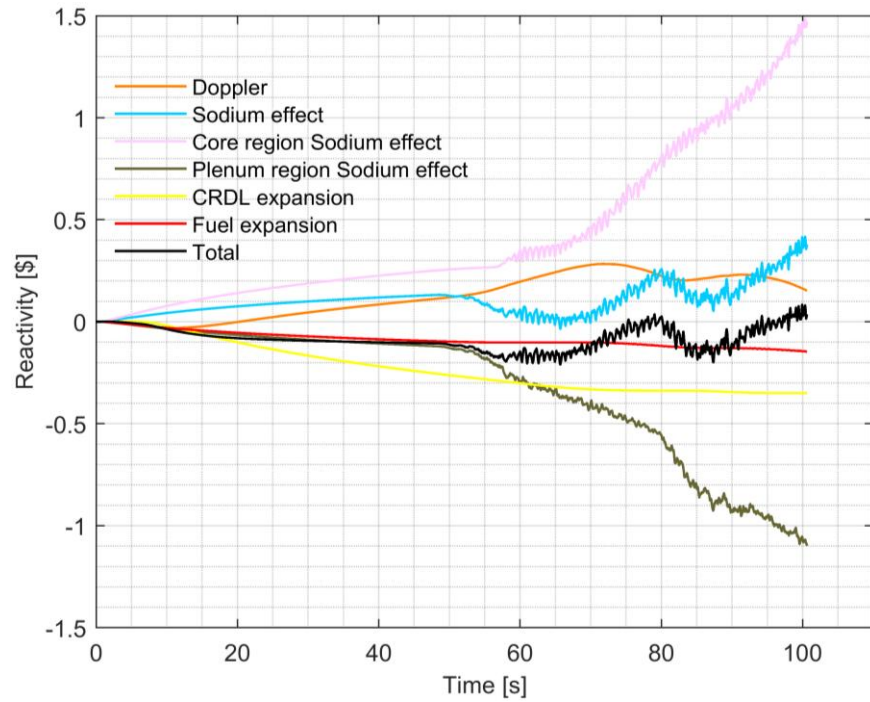


Figure A-D-5. Evolution of the reactivity components used in the point kinetics model vs. time

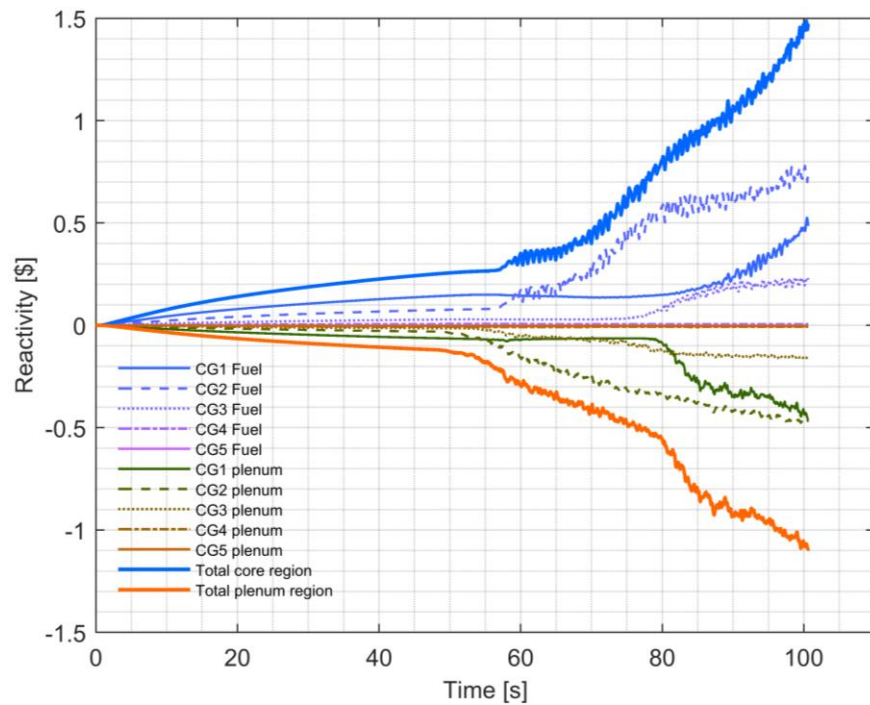


Figure A-D-6. Sodium reactivity effect evolution in time distributed amongst the different cooling groups and fuel/plenum regions

Influence of the sodium plenum reactivity worth modification

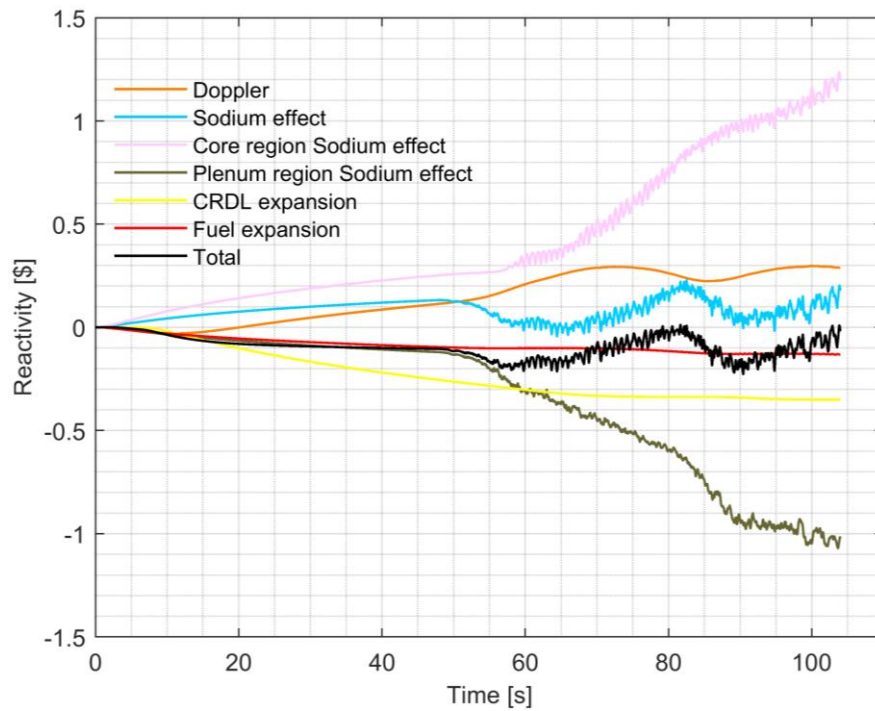


Figure A-D-7. Evolution of the reactivity components used in the point kinetics model vs. time

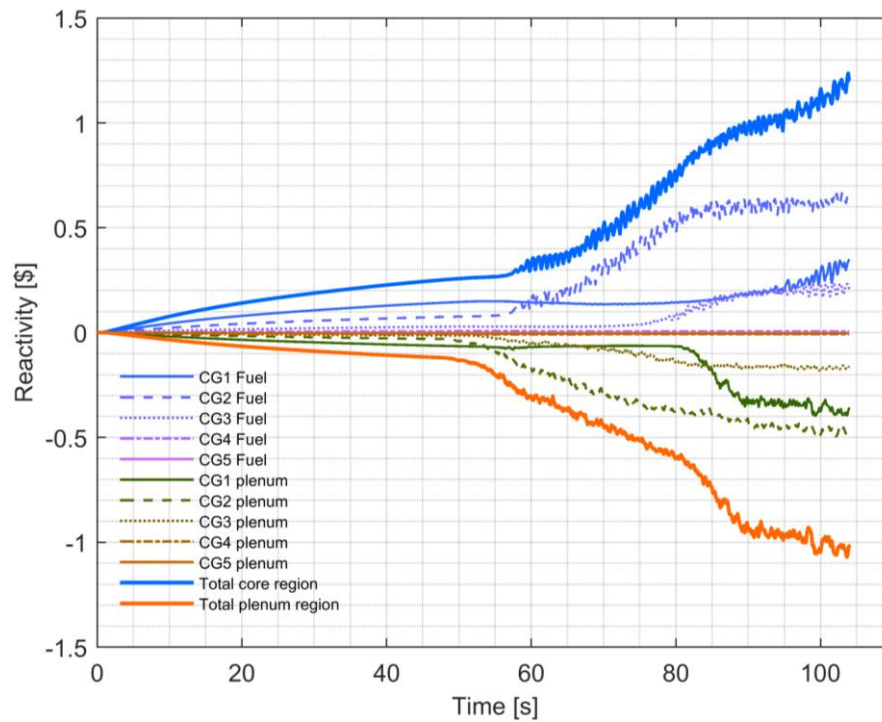


Figure A-D-8. Sodium reactivity effect evolution in time distributed amongst the different cooling groups and fuel/plenum regions

Bibliography

- [1] World Nuclear Association, 2022, *Plans For New Reactors Worldwide*, Available at: <https://world-nuclear.org/information-library/current-and-future-generation/plans-for-new-reactors-worldwide.aspx> (Accessed: Feb. 12, 2022.)
- [2] International Energy Agency (IEA), 2019, *Nuclear Power in a Clean Energy System*, IEA, Paris, Available at: <https://www.iea.org/reports/nuclear-power-in-a-clean-energy-system> (Accessed: Feb. 12, 2022.)
- [3] International Atomic Energy Agency (IAEA), 2021, *Energy, Electricity and Nuclear Power Estimates for the Period up to 2050*, Reference Data Series No. 1, IAEA, Vienna
- [4] International Atomic Energy Agency (IAEA), 2020, *IAEA Releases 2019 Data on Nuclear Power Plants Operating Experience*, Available at: <https://www.iaea.org/newscenter/news/iaea-releases-2019-data-on-nuclear-power-plants-operating-experience> (Accessed: Feb. 12, 2022.)
- [5] Gen IV International Forum (GIF), 2013, *Generation IV goals*, Available at: https://www.gen-4.org/gif/jcms/c_9502/generation-iv-goals (Accessed: Feb. 13, 2022.)
- [6] Gen IV International Forum (GIF), 2013, *Systems*, Available at: https://www.gen-4.org/gif/jcms/c_9353/systems (Accessed: Feb. 13, 2022.)
- [7] World Nuclear Association, 2021, *Fast Neutron Reactors*, Available at: <https://world-nuclear.org/information-library/current-and-future-generation/fast-neutron-reactors.aspx> (Accessed: Feb. 13, 2022.)
- [8] J. Guidez, J. Bodi, K. Mikityuk, E. Girardi, B. Carlucci, 2021, *New Reactor Safety Measures for the European Sodium Fast Reactor - Part I: Conceptual Design*, ASME. *ASME J of Nuclear Rad Sci.*, <https://doi.org/10.1115/1.4051364>
- [9] J. Guidez, 2013, *Phenix - The experience feedback*. France: EDP Sciences.
- [10] J. Guidez, G. Prele, 2017, *Superphénix. Technical and scientific achievements*, Atlantis press, ISBN 978-94-6239-245-8.
- [11] W. Marth, 1993, *The story of the European fast reactor cooperation (KFK--5255)*. Germany
- [12] L. Buiron, A. Vasile, R. Sunderland, 2013. CP ESFR: Collaborative Project for a European Sodium Fast Reactor Core studies. International Conference on Fast Reactors and Related Fuel Cycles: Safe Technologies and Sustainable Scenarios (FR13) Presentations, (p. v). International Atomic Energy Agency (IAEA): IAEA.
- [13] K. Mikityuk, E. Girard, J. Krepel, E. Bubelis, E. Fridman, A. Rineiski, N. Girault, F. Payot, L. Buligins, G. Gerbeth, N. Chauvin, C. Latge, J.-C. Garnier, 2018, *ESFR-SMART: new Horizon-2020 project on SFR safety*. Presented at the International Conference on Fast Reactors and Related Fuel Cycles: Next Generation Nuclear Systems for Sustainable Development (FR17), Yekaterinburg, Russia: Zenodo. <http://doi.org/10.5281/zenodo.1309193>

- [14] Nuclear Energy Agency (NEA), 2020, *Use and Development of Probabilistic Safety Assessments at Nuclear Facilities*, NEA/CSNI/R(2019)10, [https://www.oecd.org/officialdocuments/publicdisplaydocumentpdf/?cote=NEA/CSNI/R\(2019\)10&docLanguage=En](https://www.oecd.org/officialdocuments/publicdisplaydocumentpdf/?cote=NEA/CSNI/R(2019)10&docLanguage=En) (Accessed: Sept. 13, 2022.)
- [15] International Atomic Energy Agency (IAEA), 2016, *Safety of Nuclear Power Plants: Design*, IAEA Safety Standards Series No. SSR-2/1 (Rev. 1), IAEA, Vienna
- [16] CEA, 2016, "Sodium-Cooled Nuclear Reactors", A Nuclear Energy Division Monograph, Editions du Moniteur, ISBN 978-2-281-14055-2
- [17] I. Pakhomov, 2018, *BN-600 and BN-800 operating experience*, [PowerPointSlides], Gen IV International Forum, Accessed at: https://www.gen-4.org/gif/upload/docs/application/pdf/201901/gifiv_webinar_pakhomov_19_dec_2018_final.pdf
- [18] S. Bortot, F. Alvarez-Velarde, E. Fridman, I. Garcia Cruzado, N. Garcia Herranz, D. López, K. Mikityuk, A.-L. Panadero, S. Pelloni, A. Ponomarev, P. Sciora, A. Seubert, H. Tsige-Tamirat, A. Vasile, 2015, European benchmark on the ASTRID-like low-void-effect core characterization: neutronic parameters and safety coefficients. In *Proceedings of 2015 international congress on advances in nuclear power plants (ICAPP 2015)* (pp. 668-676).
- [19] N. Alpy, P. Marsault, M. Anderhuber, A. Gerschenfeld, P. Sciora, D. Kadri, J. Perez, R. Lavastre, 2016, Phenomenological investigation of sodium boiling in a SFR core during a postulated ULOF transient with CATHARE 2 system code: a stabilized boiling case, *Journal of Nuclear Science and Technology*, 53:5, 692-697, DOI: [10.1080/00223131.2015.1111778](https://doi.org/10.1080/00223131.2015.1111778)
- [20] K. Raskach, A. Volkov, D. Lemasson, N. Solomonova, A. Moryakov, A. Yakunin, 2021, 2D and 3D numerical investigations of sodium boiling in sodium cooled fast reactor with MOX fuel and low sodium void reactivity effect during unprotected loss of flow accidents, *Nuclear Engineering and Design*, Volume 372, ISSN 0029-5493, <https://doi.org/10.1016/j.nucengdes.2020.110961>.
- [21] E. Fridman, F. Álvarez Velarde, P. Romojaro Otero, H. Tsige-Tamirat, A. Jiménez Carrascosa, N. García Herranz, F. Bernard, R. Gregg, U. Davies, J. Krepel, S. Massara, S. Pomerouly, E. Girardi, K. Mikityuk, 2021, "Neutronic Analysis of the European Sodium Fast Reactor: Part I—Fresh Core Results." *ASME. ASME J of Nuclear Rad Sci.* April 2022; 8(1): 011301. <https://doi.org/10.1115/1.4048905>
- [22] K. K. Rajan, 2021, A study on sodium - the fast breeder reactor coolant. *IOP Conference Series: Materials Science and Engineering*. 1045. 012013. [10.1088/1757-899X/1045/1/012013](https://doi.org/10.1088/1757-899X/1045/1/012013).
- [23] U. Baker, M. Margulis, E. Shwageraus, E. Fridman, A. J. Carrascosa, N. García Herranz, O. Cabellos, R. Gregg, J. Krepel, 2021, "Evaluation of the ESFR End of Equilibrium Cycle State: Spatial Distributions of Reactivity Coefficients." *ASME. ASME J of Nuclear Rad Sci.* April 2022; 8(1): 011316. <https://doi.org/10.1115/1.4052121>
- [24] K. Mikityuk, A. Chenu, K. Sun. "A wrapper tube for a fuel subassembly of a nuclear reactor core and method for protecting fuel against overheating in case of coolant boiling", Patent WO 2013098079 A1, July 2013 <http://www.google.com/patents/WO2013098079A1>

- [25] K. Sun, A. Chenu, J. Krepel, K. Mikityuk & R. Chawla, 2013, Coupled 3-D Neutronics/Thermal-Hydraulics Optimization Study for Improving the Response of a 3600 MW(Thermal) SFR Core to an Unprotected Loss-of-Flow Accident, *Nuclear Technology*, 183:3, 484-503, DOI: [10.13182/NT13-A19436](https://doi.org/10.13182/NT13-A19436)
- [26] M. Ragheb, 2010, Experimental Breeder Reactor number I, EBR-I criticality accident, [online], Available at: <https://mragheb.com/NPRE%20457%20CSE%20462%20Safety%20Analysis%20of%20Nuclear%20Reactor%20Systems/Experimental%20Breeder%20Reactor%20Number%201%20%20EBRI%20Criticality%20Accident.pdf> (Accessed: Oct. 07, 2020.)
- [27] J. J. Grudzinski, C. Grandy, 2014, Fuel assembly bowing and core restraint design in Fast Reactors, Proceedings of the ASME 2014 International Mechanical Engineering Congress and Exposition, Montreal, Quebec, Canada, November 14-20, IMECE2014-38331
- [28] P. Dumaz, N. Alpy, D. Broc, M. Bucci, J. Cardolaccia, C. Guenaut, E. Hourcade, L. Martin, J. A. Jolly, P. Masoni, V. Pascal, N. Simon, N. Schmidt, 2012, New investigations of the Phenix negative reactivity events, ICAPP 2012, Chicago, USA, June 24-28, Paper 12456
- [29] F. Zylbersztejn, 2012, "Study of the Core Compaction Effects and Its Monitoring in Sodium Cooled Fast Reactors," [PowerPoint presentation] presented at Technical Mtg. Innovative Fast Reactor Designs with Enhanced Negative Reactivity Feedback Features, Vienna, Austria, April 27-29, Available at: https://inis.iaea.org/collection/NCLCollectionStore/_Public/45/084/45084452.pdf (Accessed: Oct. 07, 2020.)
- [30] C. Fiorina, I. Clifford, M. Aufiero, K. Mikityuk, 2015, GeN-Foam: A novel OpenFOAM® based multi-physics solver for 2D/3D transient analysis of nuclear reactors. *Nuclear Engineering and Design*, 294, 24-37. <https://doi.org/10.1016/j.nucengdes.2015.05.035>
- [31] W. Heo, Y. Kim, 2018, Diffusion-Based Finite Element Method to Estimate the Reactivity Changes due to Core Deformation in an SFR. *Nuclear Science and Engineering*, 189(1): p. 41-55.
- [32] J. F. Sauvage, 2004, Phenix 30 years of history: the heart of a reactor, CEA Valrhô. Chapter 4
- [33] International Atomic Energy Agency, 2021, "Limited Scope Sustainability Assessment of Planned Nuclear Energy Systems Based on BN-1200 Fast Reactors," IAEA, Vienna, Report No. IAEA-TECDOC-1959 accessed Oct. 20, 2021, <https://www.iaea.org/publications/14864/limited-scope-sustainability-assessment-of-planned-nuclear-energy-systems-based-on-bn-1200-fast-reactors>
- [34] J. Guidez, J. Bodi, K. Mikityuk, E. Girardi, 2021, "Optimization of the European Sodium Fast Reactor Secondary Sodium Loop as Part of the ESFR-SMART Project." ASME. *ASME J of Nuclear Rad Sci*. April 2022; 8(1): 011323. <https://doi.org/10.1115/1.4052589>
- [35] Autodesk, 2020, Autodesk Inventor Nastran Editor 2020 User's Manual, San Rafael, California, United States: Author
- [36] J.S. Genot, 2009, *ESFR Working Horse Pool Concept Description*, CP-ESFR Deliverable, ID: D-4.1.1.
- [37] ESFR-SMART, *ESFR-SMART: Introduction of main concepts*, YouTube, posted at: Sep 24, 2018, duration: 5 min 29 sec, Available at: <https://www.youtube.com/watch?v=Blay03wdoTI&t=199s>

- [38] U. S. R. Commission, TRACE - Theory Manual - Field Equations, Solution Methods, and Physical Models, Washington, DC 20555-0001: Version 5.0, 2011
- [39] K. Mikityuk, S. Pelloni, P. Coddington, E. Bubelis, R. Chawla, 2005, FAST: An advanced code system for fast reactor transient analysis. *Annals of Nuclear Energy* 32, 1613-1631.
- [40] J. K. Fink, L. Leibowitz, 1995, "Thermodynamic and transport properties of sodium liquid and vapour", Argonne National Laboratory, ANL/RE-95/2.
- [41] A. Chenu, 2011, "Single- and Two-Phase Flow Modelling for Coupled Neutronics/Thermal-Hydraulics Transient Analysis of Advanced Sodium-Cooled Fast Reactors", EPFL PhD Thesis, p.42, 2011, <http://dx.doi.org/10.5075/epfl-thesis-5172>.
- [42] K. Rehme, 1972, "Pressure Drop Performance of Rod Bundles in Hexagonal Arrangements", *International Journal of Heat and Mass Transfer*. Vol 15, pp. 2499-2517.
- [43] S.W. Churchill, 1977, "Friction Factor Equations Spans All Fluid-Flow Regimes," *Chemical Eng.*, November, 91-92.
- [44] K. Mikityuk, 2009, "Heat transfer to liquid metal: Review of data and correlations for tube bundles", *Nuclear Engineering and Design* 239, 680-687.
- [45] H. Ninokata, T. Okano, 1990, "SABENA: Subassembly boiling evolution numerical analysis", *Nuclear Engineering and Design* 120 349 – 367.
- [46] S. Perez-Martin, M. Anderhuber, L. Laborde, N. Girault, C. Lombardo, L. Ammirabile, K. Mikityuk, S. Mimouni, C. Péniguel, and W. Pfrang, 2021, "Evaluation of Sodium Boiling Models Using KNS-37 Loss of Flow Experiments." *ASME. ASME J of Nuclear Rad Sci.* January 2022; 8(1): 011310. <https://doi.org/10.1115/1.4050769>
- [47] E. Fridman, F. Álvarez Velarde, P. Romojaro Otero, H. Tsige-Tamirat, A. Jiménez Carrascosa, N. García Herranz, F. Bernard, R. Gregg, U. Davies, J. Krepel, B. Lindley, S. Massara, S. Pomerouly, E. Girardi, K. Mikityuk, 2021, "Neutronic Analysis of the European Sodium Fast Reactor: Part II—Burnup Results." *ASME. ASME J of Nuclear Rad Sci.* April 2022; 8(1): 011302. <https://doi.org/10.1115/1.4048765>
- [48] G. Efstratios Apostolakis, 1973, *Studies in nuclear reactor dynamics I. The accuracy of point kinetics II. The effect of delayed neutrons on the spectrum of the group-diffusion operator*, California Institute of Technology PhD Thesis, Available at: <https://thesis.library.caltech.edu/8534/1/Apostolakis%201973.pdf>
- [49] A. Ponomarev, 2017, *Improved methodologies for evaluation of severe transient conditions of sodium-cooled fast systems*, Karlsruher Institut für Technologie (KIT) PhD thesis, DOI: [10.5445/IR/1000069106](https://doi.org/10.5445/IR/1000069106)
- [50] E. Bubelis, M. Schikorr, K. Mikityuk, 2022, Evaluation of the passive reactor shutdown system performance in European sodium fast reactor. *Journal of Nuclear Engineering and Radiation Science*, 8(1), 011309 (8 pp.). <https://doi.org/10.1115/1.4050563>
- [51] D. Lemasson, A. Bretault, D. Schmitt, A. Ponomarev, S. Perez-Martin, 2013, New Methodology for Sodium Reactivity Feedback Modeling within the SAS-SFR Code for Fast Reactors Severe Accidents Analysis, Proceedings of ICAPP 2013, Jeju Island, Korea, April 14-18, Paper no. FF062

- [52] J. Bodi, A. Ponomarev, K. Mikityuk, 2019, Hybrid stochastic-deterministic method of generating one-group cross sections for transient analysis applied to Sodium Fast Reactor. 2019 International Congress on Advances in Nuclear Power Plants (ICAPP 19), Juan-les-Pins, France, <https://doi.org/10.5281/zenodo.3324179>
- [53] J. Leppänen, M. Pusa, T. Viitanen, V. Valtavirta, T. Kaltiaisenaho, 2015, The Serpent Monte Carlo code: Status, development and applications in 2013. *Ann. Nucl. Energy*, 82 (2015) p.142-150
- [54] E. Fridman, J. Leppänen, and C. Wemble, "Comparison of Serpent and HELIOS-2 as Applied for the PWR Few-Group Cross Section Generation," in *International Conference on Mathematics and Computational Methods Applied to Nuclear Science & Engineering (M&C 2013)*, American Nuclear Society, 2013.
- [55] R. Rachamin, C. Wemple, E. Fridman, 2013. Neutronic analysis of SFR core with HELIOS-2, Serpent, and DYN3D codes. *Annals of Nuclear Energy* 55, 194–204.
- [56] E. Nikitin, E. Fridman, K. Mikityuk, 2015. Solution of the OECD/NEA neutronics SFR benchmark with Serpent-DYN3D and Serpent-PARCS code systems. *Annals of Nuclear Energy* 75, 492–497.
- [57] J. Leppänen, On the Use of The Continuous-Energy Monte Carlo Method for Lattice Physics Applications, 2009 International Nuclear Atlantic Conference - INAC 2009 Rio de Janeiro, RJ, Brazil, September 27 to October 2, 2009
- [58] J. F. Briesmeister, MCNP6—A General Monte Carlo N-Particle Transport Code, Version 4C, LA-13709-M Manual, 18 December 2000
- [59] T. Downar, Y. Xu, V. Seker, N. Hudson, 2010. PARCS v3.0 – U.S. NRC core neutronics simulator. Theory Manual, Ann Arbor, MI. <http://pbadupws.nrc.gov/docs/ML1016/ML101610117.pdf>
- [60] J. Leppänen, Development of a New Monte Carlo Reactor Physics Code. PhD thesis, VTT Technical Research Centre of Finland, 2007.
- [61] E. Beltjens, Modelling of the low – void SFR core during ULOF with spatial kinetics, Ecole Polytechnique Federale De Lausanne, MS Thesis, 4 August 2017
- [62] A. Ponomarev, K. Mikityuk, 2021, "Modeling of Reactivity Effects and Transient Behavior of Large Sodium Fast Reactor." *ASME J of Nuclear Rad Sci.* April 2022; 8(1): 011313. <https://doi.org/10.1115/1.4051514>
- [63] J. Bodi, A. Ponomarev, K. Mikityuk, 2022, Coupled neutronics-mechanics analysis method for evaluation of reactivity change due to core distortion in sodium fast reactor. *Journal of Nuclear Engineering and Radiation Science*, 8(1), 011307 (7 pp.). <https://doi.org/10.1115/1.4050417>
- [64] B. Fontaine, G. Prulhière, A. Vasile, P. Masoni, P. Barret, D. Rochwerger, J. Gros, R. Dupraz, N. Moussallam, M. Chassignet, 2011, Description and preliminary results of PHENIX core flowering test, *Nuclear Engineering and Design* 241, p. 4143– 4151.
- [65] B. Fontaine, R. Eschbach, N. Tauveron, R. Bavière, 2013, Recent analysis of PHENIX end of Life Tests and perspectives, FR'13, Paris, France, T1-CN-199/237

- [66] J. M. Gere, B. J. Goodno, *Mechanics of Materials* (Eighth ed.). p. 1083–1087. ISBN: 978-1-111-57773-5.
- [67] IAEA Tecdoc Series, 2013, Benchmark analysis on the Natural Circulation Test Performed During the PHENIX End-of-Life experiments, No.1703, IAEA (International Atomic Energy Agency), Vienna, Austria
- [68] J. Séran, V. Lévy, D. Gilbon, A. Maillard, A. Fissolo, H. Tournon, R. Cauvin, A. Chalony, E. Le Boulbin, 1992, Behavior under Neutron Irradiation of the 15-15Ti and EM10 Steels Used as Standard Materials of the Phénix Fuel Subassembly, in *Effects of Radiation on Materials: 15th International Symposium*, ASTM STP 1125 p. 1209-1233.
- [69] IAEA Nuclear Energy Series, 2012, Structural Materials for Liquid Metal Cooled Fast Reactor Fuel Assemblies – Operational Behaviour, No. NF-T-4.3, IAEA (International Atomic Energy Agency), Vienna, Austria
- [70] LLC. MatWeb, www.matweb.com, [online], Available at:
<http://www.matweb.com/search/datasheet.aspx?bassnum=MS0001&ckck=1> (Accessed: Feb. 01, 2020.)
- [71] J. Bodi, A. Ponomarev, E. Bubelis and K. Mikityuk, 2021, "Analysis of ESFR Decay Heat Removal Systems in Protected Station Blackout." *ASME. ASME J of Nuclear Rad Sci.* January 2022; 8(1): 011315. <https://doi.org/10.1115/1.4052190>
- [72] K. A. Polzin, 2007, Liquid Metal Pump Technologies for Nuclear Surface Power, *Proceedings of Space Nuclear Conference 2007*, Boston, Massachusetts, June 24-28, Available at: <https://ntrs.nasa.gov/api/citations/20070032704/downloads/20070032704.pdf> (Accessed: 10 January 2021.)
- [73] J. Bittan, C. Bore, J. Guidez, 2021, Preliminary assessment of decay heat removal systems in the ESFR-SMART design: the role of natural air convection around Steam Generators outer shells in accidental conditions, *ASME. ASME J of Nuclear Rad Sci.* October 2021; 7(4): 041301, <https://doi.org/10.1115/1.4048991>
- [74] A. Walker, 2016, Natural Ventilation, *WBDG - Whole Building Design Guide*. National Institute of Building Sciences. Available at: <https://www.wbdg.org/resources/natural-ventilation> (Accessed: 12 January 2021.)
- [75] J. Bodi, A. Ponomarev, K. Mikityuk, 2022, Analysis of sodium boiling initiated by Unprotected Loss of Flow in European Sodium Fast Reactor core with different subassembly designs, *Nuclear Engineering and Design*, Currently under review
- [76] A. Rineiski, C. Mériot, M. Marchetti, J. Krepel, C. Coquelet-Pascal, H. Tsige-Tamirat, F. Álvarez-Velarde, E. Girardi, K. Mikityuk, 2021, "ESFR-SMART Core Safety Measures and Their Preliminary Assessment." *ASME. ASME J of Nuclear Rad Sci.* April 2022; 8(1): 011322. <https://doi.org/10.1115/1.4052588>
- [77] M.-S. Chenaud, N. Devictor, G. Mignot, F. Varaine, C. Venard, L. Martin, M. Phelip, D. Lorenzo, F. Serre, F. Bertrand, N. Alpy, M. Le Flem, P. Gavaille, R. Lavastre, P. Richard, D. Verrier, D. Schmitt, 2013, Status of the ASTRID core at the end of the pre-conceptual design phase 1, *Nuclear Engineering and Technology*, Volume 45, Issue 6, pg. 721-730, <https://doi.org/10.5516/NET.02.2013.519>.

- [78] V. M. Poplavsky, V. I. Matveev, V. A. Eliseev, I. A. Kuznetsov, A. V. Volkov, Y. E. Shvetsov, Y. S. Khomyakov, A. M. Tsiboulia, 2011, Studies on Influence of Sodium Void Reactivity Effect on the Concept of the Core and Safety of Advanced Fast Reactor, *Journal of Nuclear Science and Technology*, 48:4, 538-546, DOI: [10.1080/18811248.2011.9711731](https://doi.org/10.1080/18811248.2011.9711731)
- [79] V. M. Poplavsky, A. M. Tsiboulia, Y. S. Khomyakov, 2009, Core Design and Fuel Cycle of Advanced Fast Reactor with Sodium Coolant. Inter. Conf. on Fast Reactors and Related Fuel Cycles — Challenges and Opportunities (FR09), Kyoto, Japan, December 7–11.
- [80] S. Mambelli, Analytical and experimental study of chugging boiling instability: the CHUG project, MS Thesis, Zenodo. (2018, July 13). DOI:[10.5281/zenodo.1311464](https://doi.org/10.5281/zenodo.1311464)
- [81] K. Sun, 2012, "Analysis of Advanced Sodium-cooled Fast Reactor Core Designs with Improved Safety Characteristics", EPFL PhD thesis, <http://dx.doi.org/10.5075/epfl-thesis-5480>
- [82] A. Ponomarev, K. Mikityuk, E. Fridman, V.A. Di Nora, E. Bubelis, M. Schikorr, 2021, "Superphénix Benchmark Part II: Transient Results." *ASME. ASME J of Nuclear Rad Sci.* April 2022; 8(1): 011321. <https://doi.org/10.1115/1.4051877>
- [83] International Atomic Energy Agency (IAEA), 2014, Benchmark Analyses on the Control Rod Withdrawal Tests Performed during the PHÉNIX End-of-Life Experiments, IAEA-TECDOC-1742, IAEA, Vienna

Curriculum vitae

János Bódi

Feldblumenweg, 16
CH-5074 Eiken
Switzerland

Phone: +41 788745912
E-mail: bodjan1@gmail.com
Linkedin: <https://www.linkedin.com/in/janosbodi/>

Education

2017–2022	PhD , École Polytechnique Fédérale de Lausanne (EPFL), Doctoral Programme in Energy, Lausanne, Switzerland Thesis supervisor: Dr Konstantin Mikityuk, PSI, Villigen Thesis co-supervisor: Dr Alexander Ponomarev, HZDR, Dresden Thesis title: Advanced methodologies for modeling and assessment of SFR safety functions
2016-2017	MSc in Physics and Technology of Nuclear Reactors University of Birmingham, United Kingdom Master thesis title: “Development of CAD model for the European Sodium Fast Reactor for the use of TRACE thermal hydraulic code” Thesis supervisor: Dr. Paul Norman <i>Awarded the “School of Physics and Astronomy Scholarship” from the University of Birmingham</i>
2010–2015	BSc in Mechanical Engineering Óbuda University, Budapest, Hungary

Work experience

2022-present	Nuclear Fuel deployment planning Intern , Axpo Power AG, Baden, Switzerland
2017- 2022	PhD Candidate in Nuclear Physics and Engineering, Advanced Nuclear Systems Group , Paul Scherrer Institut, Villigen, Switzerland
2015-2016	Advanced Manufacturing and CAD engineer , Carrtech Engineering Ltd., Birmingham, United Kingdom

Publications

First author Journal Articles

Bodi, J., Ponomarev, A., Bubelis, E., & Mikityuk, K. (2022). Analysis of ESFR decay heat removal systems in protected station blackout. *Journal of Nuclear Engineering and Radiation Science*, 8(1), 011315 (18 pp.). <https://doi.org/10.1115/1.4052190>

Bodi, J., Ponomarev, A., & Mikityuk, K. (2022). Coupled neutronics-mechanics analysis method for evaluation of reactivity change due to core distortion in sodium fast reactor. *Journal of Nuclear Engineering and Radiation Science*, 8(1), 011307 (7 pp.). <https://doi.org/10.1115/1.4050417>

Bodi, J., Ponomarev, A., & Mikityuk, K., 2022, Analysis of sodium boiling initiated by Unprotected Loss of Flow in European Sodium Fast Reactor core with different subassembly designs, *Nuclear Engineering and Design*, Currently under review

Co-Authored journal articles

Grah, A., Tsige-Tamirat, H., Guidez, J., Gerschenfeld, A., Mikityuk, K., Bodi, J., & Girardi, E. (2022). Computational fluid dynamic analysis of the ESFR reactor pit cooling system in case of sodium leakage. *Journal of Nuclear Engineering and Radiation Science*, 8(1), 011314 (9 pp.). <https://doi.org/10.1115/1.4051292>

Guidez, J., Bodi, J., Mikityuk, K., Girardi, E., & Carlucci, B. (2022). New reactor safety measures for the European sodium fast reactor - part I: conceptual design. *Journal of Nuclear Engineering and Radiation Science*, 8(1), 011311 (17 pp.). <https://doi.org/10.1115/1.4051364>

Guidez, J., Bodi, J., Mikityuk, K., Girardi, E., Bittan, J., Grah, A., ... Carlucci, B. (2022). New reactor safety measures for the European sodium fast reactor—part II: preliminary assessment. *Journal of Nuclear Engineering and Radiation Science*, 8(1), 011312 (14 pp.). <https://doi.org/10.1115/1.4051723>

Guidez, J., Bodi, J., Mikityuk, K., & Girardi, E., 2022, Optimization of the European sodium fast reactor secondary sodium loop as part of the ESFR-SMART project. *Journal of Nuclear Engineering and Radiation Science*, 8(1), 011323 (10 pp.). <https://doi.org/10.1115/1.4052589>

Conference and Symposium papers

Bodi, J., Ponomarev, A., & Mikityuk, K., (2019, July 11). Hybrid stochastic-deterministic method of generating one-group cross sections for transient analysis applied to Sodium Fast Reactor. 2019 International Congress on Advances in Nuclear Power Plants (ICAPP 19), Juan-les-Pins, France. <https://doi.org/10.5281/zenodo.3324179>

Bodi, J., Mikityuk, K., Ponomarev, A., & Guidez, J. (2018). Use of CAD models in ESFR-SMART EU project. In 2018 GIF symposium proceedings (pp. 363-368). <https://doi.org/10.5281/zenodo.1479030>

Teaching

Teaching assistant for the course Physics of Nuclear Reactors II (MSc in Nuclear Engineering, ETH) 2018, 2019, 2020, 2021